

**RECEPTIVITY IN BOUNDARY-LAYER TRANSITION TO
TURBULENCE**

Final Technical Report
Full Award Period 10/15/93 - 5/14/96

SPONSOR AWARD # F49620-94-1-0021

Air Force Office of Scientific Research
AFOSR/NA
Bolling Air Force Base
Washington, DC. 20332

Attention:
Dr. James McMichael

AUGUST 1996

Submitted by

WILLIAM S. SARIC

Mechanical and Aerospace Engineering
College of Engineering and Applied Science
Arizona State University
Tempe, AZ 85287-6106

Janice D. Bennett, Director
Office of Research Creative Activity
(602) 965-8239

19970117 089

REPORT DOCUMENTATION PAGE

Form Approved
OMB No. 0704-0188

Public reporting burden for this collection of information is estimated to average 1 hour per response, including the time for reviewing instructions, searching existing data sources, gathering and maintaining the data needed, and completing and reviewing the collection of information. Send comments regarding this burden estimate or any other aspect of this collection of information, including suggestions for reducing this burden, to Washington Headquarters Services, Directorate for Information Operations and Reports, 1215 Jefferson Davis Highway, Suite 1204, Arlington, VA 22202-4302, and to the Office of Management and Budget, Paperwork Reduction Project (0704-0188), Washington, DC 20503.

1. AGENCY USE ONLY (Leave blank)	2. REPORT DATE	3. REPORT TYPE AND DATES COVERED
	August 1996	Final Technical Report 10/15/93-5/14/96
4. TITLE AND SUBTITLE		5. FUNDING NUMBERS
Receptivity in Boundary-Layer Transition to Turbulence		G F49620-94-1-0021, P00002
6. AUTHOR(S) Professor William S. Saric		
7. PERFORMING ORGANIZATION NAME(S) AND ADDRESS(ES) Arizona State University Professor William S. Saric Mechanical and Aerospace Engineering Box 876106 Tempe, AZ 85287-6106		
9. SPONSORING/MONITORING AGENCY NAME(S) AND ADDRESS(ES) AFOSR/NA Dr. James McMichael 110 Dundan Ave Suite B115 Bolling AFB, DC 20332-0001		10. SPONSORING/MONITORING AGENCY REPORT NUMBER NA P49620- 94-1-0021
11. SUPPLEMENTARY NOTES		

AFOSR-TR-96-97

CC 49

12a. DISTRIBUTION/AVAILABILITY STATEMENT Approved for public release; distribution unlimited	12b. DISTRIBUTION CODE
---	------------------------

13. ABSTRACT (Maximum 200 words)
Experiments are conducted in the Arizona State University Unsteady Wind Tunnel to investigate acoustic receptivity in the leading-edge region of a Blasius boundary layer. The experiment utilizes two different flat-plate models. One model has a leading edge with a special geometry that limits the receptivity mechanism to the leading edge. The second model is a tapered elliptical-leading-edge flat plate with a junction. A Blasius basic state isolates the instability mechanism to a Tollmien-Schlichting wave and symmetric flow around the leading edge is established for each model. The acoustic disturbances are digitally generated and broadcast into the test section creating sound pressure levels ranging from 90-130dB. Several techniques are examined for separating the Tollmien-Schlichting wave from the background noise. These include hot-wire signal separation in the complex plane, the Kendall differential microphone, a multiple-microphone technique, and a sound burst technique. Receptivity coefficients show the same focusing characteristics of the T-S wave amplitude for a narrow band of frequencies documented in previous experiments. This suggests that the focusing behavior is not due to the special geometry of the leading edge. Boundary-layer measurements indicate some spanwise variation that could contribute to the focusing behavior. The work is now extended to include very high disturbance levels.

14. SUBJECT TERMS	15. NUMBER OF PAGES 224		
16. PRICE CODE			
17. SECURITY CLASSIFICATION OF REPORT Unclassified	18. SECURITY CLASSIFICATION OF THIS PAGE Unclassified	19. SECURITY CLASSIFICATION OF ABSTRACT Unclassified	20. LIMITATION OF ABSTRACT U

NSN 7540-01-280-5500

Standard Form 298 (Rev 2-89)
Prescribed by ANSI Std Z39-18
298-102

ABSTRACT

Experiments are conducted in the Arizona State University Unsteady Wind Tunnel to investigate acoustic receptivity in the leading-edge region of a Blasius boundary layer. The experiment utilizes two different flat-plate models. One model has a leading edge with a special geometry that limits the receptivity mechanism to the leading edge. The second model is a tapered elliptical-leading-edge flat plate with a junction. A Blasius basic state isolates the instability mechanism to a Tollmien-Schlichting wave and symmetric flow around the leading edge is established for each model. The acoustic disturbances are digitally generated and broadcast into the test section creating sound pressure levels ranging from 90–130 dB. The amplitude and phase of the acoustic forcing are measured by a set of microphones designed specifically for wind-tunnel applications and the signals are processed using a cross-spectrum program.

Several techniques are examined for separating the Tollmien-Schlichting wave from the background noise. These include hot-wire signal separation in the complex plane, the Kendall differential microphone, and a multiple-microphone technique. Another method, which requires the introduction of sound bursts into the test section, has been preliminarily studied and appears quite promising. Receptivity coefficients obtained on the standard elliptical-leading-edge flat plate are high but show the same focusing characteristics of the T-S wave amplitude for a narrow band of frequencies documented in previous experiments. This suggests that the focusing behavior is not due to the special geometry of the leading edge. Boundary-layer measurements indicate some spanwise variation that could contribute to the focusing behavior. Freestream disturbance measurements show that disturbance levels are higher when the zero-pressure venting region is located in the plenum.

TABLE OF CONTENTS

	Page
LIST OF TABLES	x
LIST OF FIGURES	xi
NOMENCLATURE	xx
1 INTRODUCTION	1
1.1 Motivation	1
1.1.1 Boundary-Layer Transition	2
1.1.2 Transition and Receptivity	4
1.2 Theory	4
1.2.1 The Basic State	4
1.2.2 Linear-Stability Analysis	5
1.2.3 Receptivity	10
1.3 Review of Recent Research	12
1.3.1 Theoretical and Computational Analyses	12
1.3.2 Experimental Investigations	13
1.4 Experimental Objectives	15
1.5 Outline	15
2 EXPERIMENTAL FACILITY	17
2.1 Unsteady Wind Tunnel	17
2.2 Traverse and Sting	19
2.3 Computer Systems	19
2.4 Instrumentation	21
2.5 Sound-Generation Equipment	22
2.6 Sound- and Vibration-Detection Devices	24

	Page
3 MODEL CONFIGURATION	26
3.1 The Klebanoff Flat Plate	26
3.2 The VPI Flat Plate	28
4 SPECIAL CONSIDERATIONS	29
4.1 Wind-Tunnel Operation	29
4.2 Sound-Induced Vibration	31
5 EXPERIMENTAL TECHNIQUES	32
5.1 Hot-wire Signal Processing	32
5.1.1 Velocity Calibration	32
5.1.2 Temperature Compensation	33
5.2 Sound Generation	34
5.2.1 Digital-to-Analog Library Routines	34
5.2.2 Band-Passed Random Noise	35
5.3 Sound Detection	36
5.4 Hot-Wire Amplitude and Relative-Phase Measurements	37
5.5 Boundary-Layer Scans	38
5.6 Spanwise Constant-Y Scans	40
6 RESULTS - PART I. THE BASIC STATE	42
6.1 Special Considerations	42
6.2 Establishment of Blasius Flow	44
6.2.1 The Klebanoff Flat Plate	44
6.2.2 The VPI Flat Plate	45
6.3 Symmetric Flow	45
6.3.1 The Experimental Procedure	46
6.3.2 The VPI Flat Plate	49

	Page
7 RESULTS - PART II. FREESTREAM DISTURBANCE STATE	51
7.1 Acoustic-Forcing Measurements	51
7.1.1 Microphone Location	51
7.1.2 Microphone Phase Measurements	56
7.2 Freestream Disturbance Measurements	56
7.2.1 Transition Reynolds Number	56
7.2.2 Freestream-Turbulence Amplitude and Spectra	58
8 RESULTS-PART III. T-S WAVE MEASUREMENTS	67
8.1 Signal-Separation Techniques	67
8.1.1 The Complex-Plane Method	67
8.1.2 Dual Microphones as Spatial Filters	68
8.1.3 The Kendall Gauge	70
8.1.4 The Multiple-Microphone Technique	71
8.1.5 The Sound-Burst Technique	73
8.2 Receptivity Coefficients	75
8.2.1 Complex Polar Plots	76
8.2.2 Sound Amplitude at the Leading Edge	77
8.2.3 Receptivity Coefficient Focusing	81
8.3 Receptivity Coefficient Dependence on Frequency	82
8.3.1 Spanwise Variation of u'_{rms}	84
8.3.2 Induced v' at Leading Edge	86
9 CONCLUSIONS	88
9.1 Specific Results	88
9.1.1 Basic State	88
9.1.2 Disturbance State	88

	Page
9.1.3 T-S Amplitude Measurements	90
REFERENCES	92

LIST OF TABLES

Table	Page
2.1 Traverse system capabilities.	19
6.1 Shape factors at several plate locations.	45
7.1 Microphone locations for the frequency sweep shown in figure 7.2.	53
7.2 Microphone measurements with doors to the wind-tunnel area closed.	54
7.3 Microphone measurements with doors to the wind-tunnel area open.	55
7.4 Microphone measurements with the loading-dock door open.	55
7.5 Freestream disturbance measurements with the mixing region vented conducted by Mousseux (1988).	59
7.6 Freestream disturbance measurements with the plenum vented (Tektronix filters).	63
7.7 Freestream disturbance measurements with the plenum vented (Stewart filters).	64
7.8 Freestream disturbance measurements with the mixing region vented (Tektronix filters).	65
7.9 Freestream disturbance measurements with the mixing region vented (Stewart filters).	66
8.1 Focusing conditions from Wei (1994).	81
8.2 Focusing conditions from Rasmussen (1993).	82
8.3 Receptivity coefficient dependence on frequency (VPI flat plate).	83

LIST OF FIGURES

Figure	Page
1.1 Neutral Stability Curve For Blasius Flow	97
2.1 Plan view of the ASU Unsteady Wind Tunnel	98
2.2 Side view of traverse carriage	99
2.3 Front view of traverse carriage	100
2.4 Speaker arrangement on plenum wall	101
3.1 Blade- and stator-passing frequencies at each wind-tunnel speed	102
3.2 Power-spectral density of leading-edge response to random noise	103
6.1 Final position of the Klebanoff flat plate inside test section	104
6.2 Streamwise boundary-layer profiles for $U_{\infty} = 12$ m/s (Klebanoff Flat Plate)	105
6.3 Streamwise boundary-layer profiles for $U_{\infty} = 12$ m/s (VPI Flat Plate)	106
6.4 Streamwise boundary-layer profiles for $U_{\infty} = 8$ m/s (VPI Flat Plate)	107
6.5 Symmetric-flow measurements obtained with the dual Preston tube configuration mounted at $\hat{x} = 0.1$ m, $\hat{z} = 0.0$ m (Klebanoff Flat Plate)	108
6.6 Skin-friction coefficient vs. Reynolds number	109
6.7 Preston-tube skin-friction calibraton curve for different Reynolds number (Klebanoff Flat Plate)	110
6.8 Symmetric-flow measurements on the 67:1 ellipse test model using the leading-edge static pressure ports	111
6.9 Symmetric-flow measurements on the VPI flat plate using the top leading-edge static pressure ports	112
6.10 Symmetric-flow measurements on the VPI flat plate using the bottom leading-edge static pressure ports	113
7.1 Location of microphone ports on test-section perimeter	114

Figure	Page
7.2 Microphone relative-phase measurements for $U_\infty = 8.0 \text{ m/s}$ and $V_{sp} = 0.5 \text{ V}_{rms}$	115
7.3 Microphone relative-phase measurements for $f = 45\text{--}55 \text{ Hz}$, $U_\infty = 8.0 \text{ m/s}$, and $V_{sp} = 0.5 \text{ V}_{rms}$	116
7.4 Microphone relative-phase measurements for $f = 56\text{--}65 \text{ Hz}$, $U_\infty = 8.0 \text{ m/s}$, and $V_{sp} = 0.5 \text{ V}_{rms}$	117
7.5 Microphone relative-phase measurements for $f = 66\text{--}75 \text{ Hz}$, $U_\infty = 8.0 \text{ m/s}$, and $V_{sp} = 0.5 \text{ V}_{rms}$	118
7.6 Microphone relative-phase measurements for $f = 76\text{--}85 \text{ Hz}$, $U_\infty = 8.0 \text{ m/s}$, and $V_{sp} = 0.5 \text{ V}_{rms}$	119
7.7 Microphone relative-phase measurements for $f = 86\text{--}95 \text{ Hz}$, $U_\infty = 8.0 \text{ m/s}$, and $V_{sp} = 0.5 \text{ V}_{rms}$	120
7.8 Microphone relative-phase measurements for $f = 96\text{--}105 \text{ Hz}$, $U_\infty = 8.0 \text{ m/s}$, and $V_{sp} = 0.5 \text{ V}_{rms}$	121
7.9 Microphone relative-phase measurements for $f = 106\text{--}115 \text{ Hz}$, $U_\infty = 8.0 \text{ m/s}$, and $V_{sp} = 0.5 \text{ V}_{rms}$	122
7.10 Transition Reynolds number, $Re_{tr} = 2.6 \times 10^6$, obtained with a fixed hot wire at $\hat{x} = 1.8 \text{ m}$, $\hat{z} = 0.01 \text{ mm}$ (Klebanoff flat plate).	123
7.11 Transition Reynolds number, $Re_{tr} = 1.9 \times 10^6$, obtained with hot wire at $\hat{x} = 1.8 \text{ m}$, $\hat{z} = 0.01 \text{ mm}$ (VPI flat plate).	124
7.12 Freestream disturbance spectrum at $U_\infty = 5 \text{ m/s}$ with the plenum vented (DC coupled, band pass 0.1–1000 Hz, Tektronix filters).	125
7.13 Freestream disturbance spectrum at $U_\infty = 8 \text{ m/s}$ with the plenum vented (DC coupled, band pass 0.1–1000 Hz, Tektronix filters).	126
7.14 Freestream disturbance spectrum at $U_\infty = 10 \text{ m/s}$ with the plenum vented (DC coupled, band pass 0.1–1000 Hz, Tektronix filters).	127
7.15 Freestream disturbance spectrum at $U_\infty = 12 \text{ m/s}$ with the plenum vented (DC coupled, band pass 0.1–1000 Hz, Tektronix filters).	128
7.16 Freestream disturbance spectrum at $U_\infty = 15 \text{ m/s}$ with the plenum vented (DC coupled, band pass 0.1–1000 Hz, Tektronix filters).	129

Figure	Page
7.17 Freestream disturbance spectrum at $U_\infty = 18$ m/s with the plenum vented (DC coupled, band pass 0.1–1000 Hz, Tektronix filters)	130
7.18 Freestream disturbance spectrum at $U_\infty = 20$ m/s with the plenum vented (DC coupled, band pass 0.1–1000 Hz, Tektronix filters)	131
7.19 Freestream disturbance spectrum at $U_\infty = 21$ m/s with the plenum vented (DC coupled, band pass 0.1–1000 Hz, Tektronix filters)	132
7.20 Freestream disturbance spectrum at $U_\infty = 25$ m/s with the plenum vented (DC coupled, band pass 0.1–1000 Hz, Tektronix filters)	133
7.21 Freestream disturbance spectrum at $U_\infty = 5$ m/s with the plenum vented (AC coupled, band pass 2–1000 Hz, Tektronix filters)	134
7.22 Freestream disturbance spectrum at $U_\infty = 8$ m/s with the plenum vented (AC coupled, band pass 2–1000 Hz, Tektronix filters)	135
7.23 Freestream disturbance spectrum at $U_\infty = 10$ m/s with the plenum vented (AC coupled, band pass 2–1000 Hz, Tektronix filters)	136
7.24 Freestream disturbance spectrum at $U_\infty = 12$ m/s with the plenum vented (AC coupled, band pass 2–1000 Hz, Tektronix filters)	137
7.25 Freestream disturbance spectrum at $U_\infty = 15$ m/s with the plenum vented (AC coupled, band pass 2–1000 Hz, Tektronix filters)	138
7.26 Freestream disturbance spectrum at $U_\infty = 18$ m/s with the plenum vented (AC coupled, band pass 2–1000 Hz, Tektronix filters)	139
7.27 Freestream disturbance spectrum at $U_\infty = 20$ m/s with the plenum vented (AC coupled, band pass 2–1000 Hz, Tektronix filters)	140
7.28 Freestream disturbance spectrum at $U_\infty = 21$ m/s with the plenum vented (AC coupled, band pass 2–1000 Hz, Tektronix filters)	141
7.29 Freestream disturbance spectrum at $U_\infty = 25$ m/s with the plenum vented (AC coupled, band pass 2–1000 Hz, Tektronix filters)	142
7.30 Freestream disturbance spectrum at $U_\infty = 5$ m/s with the plenum vented (AC coupled, band pass 2–1000 Hz, Stewart filters)	143
7.31 Freestream disturbance spectrum at $U_\infty = 8$ m/s with the plenum vented (AC coupled, band pass 2–1000 Hz, Stewart filters)	144

Figure	Page
7.32 Freestream disturbance spectrum at $U_\infty = 10$ m/s with the plenum vented (AC coupled, band pass 2–1000 Hz, Stewart filters).	145
7.33 Freestream disturbance spectrum at $U_\infty = 12$ m/s with the plenum vented (AC coupled, band pass 2–1000 Hz, Stewart filters).	146
7.34 Freestream disturbance spectrum at $U_\infty = 15$ m/s with the plenum vented (AC coupled, band pass 2–1000 Hz, Stewart filters).	147
7.35 Freestream disturbance spectrum at $U_\infty = 18$ m/s with the plenum vented (AC coupled, band pass 2–1000 Hz, Stewart filters).	148
7.36 Freestream disturbance spectrum at $U_\infty = 20$ m/s with the plenum vented (AC coupled, band pass 2–1000 Hz, Stewart filters).	149
7.37 Freestream disturbance spectrum at $U_\infty = 21$ m/s with the plenum vented (AC coupled, band pass 2–1000 Hz, Stewart filters).	150
7.38 Freestream disturbance spectrum at $U_\infty = 25$ m/s with the plenum vented (AC coupled, band pass 2–1000 Hz, Stewart filters).	151
7.39 Freestream disturbance spectrum at $U_\infty = 5$ m/s with the plenum vented (AC coupled, band pass 35–1000 Hz, Stewart filters).	152
7.40 Freestream disturbance spectrum at $U_\infty = 8$ m/s with the plenum vented (AC coupled, band pass 35–1000 Hz, Stewart filters).	153
7.41 Freestream disturbance spectrum at $U_\infty = 10$ m/s with the plenum vented (AC coupled, band pass 35–1000 Hz, Stewart filters).	154
7.42 Freestream disturbance spectrum at $U_\infty = 12$ m/s with the plenum vented (AC coupled, band pass 35–1000 Hz, Stewart filters).	155
7.43 Freestream disturbance spectrum at $U_\infty = 15$ m/s with the plenum vented (AC coupled, band pass 35–1000 Hz, Stewart filters).	156
7.44 Freestream disturbance spectrum at $U_\infty = 18$ m/s with the plenum vented (AC coupled, band pass 35–1000 Hz, Stewart filters).	157
7.45 Freestream disturbance spectrum at $U_\infty = 20$ m/s with the plenum vented (AC coupled, band pass 35–1000 Hz, Stewart filters).	158
7.46 Freestream disturbance spectrum at $U_\infty = 21$ m/s with the plenum vented (AC coupled, band pass 35–1000 Hz, Stewart filters).	159

Figure	Page
7.47 Freestream disturbance spectrum at $U_\infty = 25$ m/s with the plenum vented (AC coupled, band pass 35–1000 Hz, Stewart filters).	160
7.48 Freestream disturbance spectrum at $U_\infty = 5$ m/s with the mixing region vented (DC coupled, band pass 0.1–1000 Hz, Tektronix filters). . .	161
7.49 Freestream disturbance spectrum at $U_\infty = 8$ m/s with the mixing region vented (DC coupled, band pass 0.1–1000 Hz, Tektronix filters). . .	162
7.50 Freestream disturbance spectrum at $U_\infty = 10$ m/s with the mixing region vented (DC coupled, band pass 0.1–1000 Hz, Tektronix filters). . .	163
7.51 Freestream disturbance spectrum at $U_\infty = 12$ m/s with the mixing region vented (DC coupled, band pass 0.1–1000 Hz, Tektronix filters). . .	164
7.52 Freestream disturbance spectrum at $U_\infty = 15$ m/s with the mixing region vented (DC coupled, band pass 0.1–1000 Hz, Tektronix filters). . .	165
7.53 Freestream disturbance spectrum at $U_\infty = 18$ m/s with the mixing region vented (DC coupled, band pass 0.1–1000 Hz, Tektronix filters). . .	166
7.54 Freestream disturbance spectrum at $U_\infty = 20$ m/s with the mixing region vented (DC coupled, band pass 0.1–1000 Hz, Tektronix filters). . .	167
7.55 Freestream disturbance spectrum at $U_\infty = 21$ m/s with the mixing region vented (DC coupled, band pass 0.1–1000 Hz, Tektronix filters). . .	168
7.56 Freestream disturbance spectrum at $U_\infty = 25$ m/s with the mixing region vented (DC coupled, band pass 0.1–1000 Hz, Tektronix filters). . .	169
7.57 Freestream disturbance spectrum at $U_\infty = 5$ m/s with the mixing region vented (AC coupled, band pass 2–1000 Hz, Tektronix filters). . . .	170
7.58 Freestream disturbance spectrum at $U_\infty = 8$ m/s with the mixing region vented (AC coupled, band pass 2–1000 Hz, Tektronix filters). . . .	171
7.59 Freestream disturbance spectrum at $U_\infty = 10$ m/s with the mixing region vented (AC coupled, band pass 2–1000 Hz, Tektronix filters). . . .	172
7.60 Freestream disturbance spectrum at $U_\infty = 12$ m/s with the mixing region vented (AC coupled, band pass 2–1000 Hz, Tektronix filters). . . .	173
7.61 Freestream disturbance spectrum at $U_\infty = 15$ m/s with the mixing region vented (AC coupled, band pass 2–1000 Hz, Tektronix filters). . . .	174

Figure	Page
7.62 Freestream disturbance spectrum at $U_{\infty} = 18$ m/s with the mixing region vented (AC coupled, band pass 2–1000 Hz, Tektronix filters). . .	175
7.63 Freestream disturbance spectrum at $U_{\infty} = 20$ m/s with the mixing region vented (AC coupled, band pass 2–1000 Hz, Tektronix filters). . .	176
7.64 Freestream disturbance spectrum at $U_{\infty} = 21$ m/s with the mixing region vented (AC coupled, band pass 2–1000 Hz, Tektronix filters). . .	177
7.65 Freestream disturbance spectrum at $U_{\infty} = 25$ m/s with the mixing region vented (AC coupled, band pass 2–1000 Hz, Tektronix filters). . .	178
7.66 Freestream disturbance spectrum at $U_{\infty} = 5$ m/s with the mixing region vented (AC coupled, band pass 35–1000 Hz, Stewart filters). . .	179
7.67 Freestream disturbance spectrum at $U_{\infty} = 8$ m/s with the mixing region vented (AC coupled, band pass 35–1000 Hz, Stewart filters). . .	180
7.68 Freestream disturbance spectrum at $U_{\infty} = 10$ m/s with the mixing region vented (AC coupled, band pass 35–1000 Hz, Stewart filters). . .	181
7.69 Freestream disturbance spectrum at $U_{\infty} = 12$ m/s with the mixing region vented (AC coupled, band pass 35–1000 Hz, Stewart filters). . .	182
7.70 Freestream disturbance spectrum at $U_{\infty} = 15$ m/s with the mixing region vented (AC coupled, band pass 35–1000 Hz, Stewart filters). . .	183
7.71 Freestream disturbance spectrum at $U_{\infty} = 18$ m/s with the mixing region vented (AC coupled, band pass 35–1000 Hz, Stewart filters). . .	184
7.72 Freestream disturbance spectrum at $U_{\infty} = 20$ m/s with the mixing region vented (AC coupled, band pass 35–1000 Hz, Stewart filters). . .	185
7.73 Freestream disturbance spectrum at $U_{\infty} = 21$ m/s with the mixing region vented (AC coupled, band pass 35–1000 Hz, Stewart filters). . .	186
7.74 Freestream disturbance spectrum at $U_{\infty} = 25$ m/s with the mixing region vented (AC coupled, band pass 35–1000 Hz, Stewart filters). . .	187
7.75 Freestream disturbance spectrum at $U_{\infty} = 5$ m/s with the mixing region vented (AC coupled, band pass 2–1000 Hz, Stewart filters). . .	188
7.76 Freestream disturbance spectrum at $U_{\infty} = 8$ m/s with the mixing region vented (AC coupled, band pass 2–1000 Hz, Stewart filters). . .	189

Figure	Page
7.77 Freestream disturbance spectrum at $U_\infty = 10$ m/s with the mixing region vented (AC coupled, band pass 2–1000 Hz, Stewart filters).	190
7.78 Freestream disturbance spectrum at $U_\infty = 12$ m/s with the mixing region vented (AC coupled, band pass 2–1000 Hz, Stewart filters).	191
7.79 Freestream disturbance spectrum at $U_\infty = 15$ m/s with the mixing region vented (AC coupled, band pass 2–1000 Hz, Stewart filters).	192
7.80 Freestream disturbance spectrum at $U_\infty = 18$ m/s with the mixing region vented (AC coupled, band pass 2–1000 Hz, Stewart filters).	193
7.81 Freestream disturbance spectrum at $U_\infty = 20$ m/s with the mixing region vented (AC coupled, band pass 2–1000 Hz, Stewart filters).	194
7.82 Freestream disturbance spectrum at $U_\infty = 21$ m/s with the mixing region vented (AC coupled, band pass 2–1000 Hz, Stewart filters).	195
7.83 Freestream disturbance spectrum at $U_\infty = 25$ m/s with the mixing region vented (AC coupled, band pass 2–1000 Hz, Stewart filters).	196
8.1 The Kendall gauge	197
8.2 Hot-wire and Kendall-gauge response with sound amplitude.	198
8.3 Time trace using sound-burst technique for $R = 1140, F = 56, f = 80$ Hz, and $\hat{x} = 1.8$ m.	199
8.4 Stokes wave and T-S wave growth with band-passed random noise for increasing sound amplitude.	200
8.5 Boundary-layer scan disturbance profile (raw signal). Measurements taken at $\hat{x} = 1.753$ m, $R = 1048, F = 55, U_\infty = 12$ m/s, $f = 75$ Hz, and SPL = 100 dB.	201
8.6 Boundary-layer scan disturbance profile after signal separation. Measurements taken at $\hat{x} = 1.753$ m, $R = 1048, F = 55, U_\infty = 12$ m/s, $f = 75$ Hz, and SPL = 100 dB.	202
8.7 Boundary-layer scan disturbance profile after signal separation. Measurements taken at $\hat{x} = 1.753$ m, $R = 1025, F = 50, U_\infty = 12$ m/s, $f = 68$ Hz, and SPL = 101 dB.	203
8.8 Complex polar plot obtained from streamwise scan. Measurements taken at $\hat{x}_{\text{avg}} = 1.763$ m, $R = 1115, F = 48, U_\infty = 13.9$ m/s, $f = 88$ Hz, and SPL = 89 dB.	204

Figure	Page
8.9 Complex polar plot obtained from streamwise scan. Measurements taken at $\hat{x}_{\text{avg}} = 1.763$ m, $R = 1105$, $F = 49$, $U_{\infty} = 13.9$ m/s, $f = 87$ Hz, and SPL = 89 dB.	205
8.10 Complex polar plot obtained from streamwise scan. Measurements taken at $\hat{x}_{\text{avg}} = 1.763$ m, $R = 1107$, $F = 50$, $U_{\infty} = 13.9$ m/s, $f = 90$ Hz, and SPL = 93 dB.	206
8.11 First configuration to correlate the hot-wire and microphone response at $\hat{x} = 0.5$ m.	207
8.12 Second configuration to correlate the hot-wire and microphone response at $\hat{x} = 0.5$ m.	208
8.13 Third configuration to correlate the hot-wire and microphone response at $\hat{x} = 0.5$ m.	209
8.14 Fourth configuration to correlate the hot-wire and microphone response at $\hat{x} = 0.5$ m.	210
8.15 Receptivity coefficients (at Branch I) as a function of dimensionless frequency and freestream speed.	211
8.16 Spanwise traverse-alignment scan for $\hat{x} = 1.73$ m, $F = 56$, and $U_{\infty} = 12.9$ m/s case.	212
8.17 Spanwise u'_{rms} variation for constant-y scans taken at $\hat{x} = 1.73$ m and $\hat{y} = 1.5$ mm, $F = 56$, $U_{\infty} = 12.9$ m/s.	213
8.18 Wavenumber spectrum of u'_{rms} spanwise variation taken at $\hat{x} = 1.73$ m and $\hat{y} = 1.5$ mm, $F = 56$, $U_{\infty} = 12.9$ m/s.	214
8.19 Spanwise traverse-alignment scan for $\hat{x} = 1.53$ m, $F = 85$, and $U_{\infty} = 8.0$ m/s case.	215
8.20 Spanwise u'_{rms} variation for constant-y scans taken at $\hat{x} = 1.53$ m and $\hat{y} = 1.78$ mm, $F = 85$, $U_{\infty} = 8.0$ m/s.	216
8.21 Wavenumber spectrum of u'_{rms} spanwise variation taken at $\hat{x} = 1.53$ m and $\hat{y} = 1.78$ mm, $F = 85$, $U_{\infty} = 8.0$ m/s.	217
8.22 Investigation of v' at the leading edge for $U_{\infty} = 8$ m/s and $V_{\text{sp}} = 0.5$ volts (rms).	218
8.23 Investigation of v' at the leading edge for $U_{\infty} = 12$ m/s and $V_{\text{sp}} = 0.5$ volts (rms).	219

Figure	Page
8.24 Investigation of v' at the leading edge for $U_{\infty} = 15$ m/s and $V_{sp} = 0.5$ volts (rms).	220
8.25 Investigation of v' at the leading edge for $U_{\infty} = 18$ m/s and $V_{sp} = 0.5$ volts (rms).	221
8.26 Investigation of v' at the leading edge for $U_{\infty} = 21$ m/s and $V_{sp} = 0.5$ volts (rms).	222
8.27 Investigation of v' at the leading edge for $U_{\infty} = 12$ m/s and $V_{sp} = 0.1$ volts (rms).	223
8.28 Investigation of v' at the leading edge for $U_{\infty} = 12$ m/s, $V_{sp} = 0.5$ volts (rms), and shutters rotated 30°	224

NOMENCLATURE

a, b	major and minor axes of an ellipse
a_j	complex amplitude of pressure wave j
a_∞	speed of sound [m/s]
A	norm of disturbance amplitude
A_o	amplitude at $R = R_o$, usually at Branch I
C_p	pressure coefficient
c	$= c_r + c_i$, complex wave speed; c_r is phase speed; αc_i is temporal growth rate
<i>c.c.</i>	denotes complex conjugate
D	$= d/dy$
F	$= \omega/R \times 10^6 = 2\pi f \nu / U_\infty^2 \times 10^6$, dimensionless frequency
f	frequency [Hz]
H	shape factor
k_{TS}	$= 2\pi\delta_r/\lambda_{TS}$, local dimensionless T-S wavenumber
k_1	wavenumber of downstream-travelling wave
k_2	wavenumber of upstream-travelling wave
K	$ u'_{TS} _I / u'_{AC} _{LE}$, receptivity coefficient referenced to Branch I
L	length scale, chord [m]
m, n	exponents in super-ellipse equation
M	$= U_\infty/a_\infty$, mach number
N	$= \ln(A/A_o)$, amplification factor; number of samples
p'	disturbance-state pressure

p'_{AC}	acoustic disturbance pressure
q'	disturbance-state dependent variable (i.e. u' , v' , w' or p')
R	$= \sqrt{Re_x} = U_\infty \delta_r / \nu$, boundary-layer Reynolds number
Re_x	$= U_\infty \hat{x} / \nu$, x-Reynolds number
t	time [s]
T	temperature [$^{\circ}\text{C}$]
U	basic-state chordwise boundary-layer velocity normalized by U_∞
U_e	boundary-layer edge streamwise velocity [m/s]
U_∞	freestream velocity [m/s]
V_{sp}	rms speaker voltage [volts]
u', v', w'	disturbance velocity components [m/s]
x, y, z	global test-section coordinates: x is streamwise coordinate, y is normal to the flat-plate model, z is spanwise coordinate from plate centerline (positive down)
$\hat{x}, \hat{y}, \hat{z}$	dimensional coordinates
$ u' $	rms of u' [m/s]
\hat{x}	chordwise distance from leading edge [m]
\hat{y}	normal coordinate to the flat-plate model, $\hat{y} = 0$ at the plate [m]
α	chordwise (x) wavenumber
Δ	change or difference, e.g., ΔT is a temperature difference
δ_F	trailing-edge flap deflection angle [$^{\circ}$]
δ_r	$= \sqrt{\nu \hat{x} / U_\infty}$, boundary-layer reference length (normalizing length) [m]
δ^*	displacement thickness [m]
η	$= \hat{y} / \delta_r = y$, boundary-layer coordinate

λ	wavelength [m]
λ_{TS}	Tollmien-Schlichting wavelength [m]
ν	kinematic viscosity [m^2/s]
σ	growth rate
θ	momentum thickness [m]
ρ	density [kg/m^3]
$\hat{\omega}$	$= 2\pi f$, dimensional circular frequency [rad/s]
ω	$= 2\pi f \delta_r / U_\infty = FR$, dimensionless circular frequency

Introduction

1.1 Motivation

A complete understanding of the process by which laminar flow is transformed to turbulent flow is vital in order to solve a variety of fluid-dynamic problems currently confronting scientists. Understanding this transition process can lead to the prediction and control of transition to turbulence which has many practical applications. For example, a reliable transition-prediction scheme could help to accurately predict airfoil-surface heat transfer and to cool the blades and vanes in gas-turbine engines. It has also been estimated that if laminar flow is maintained on the wings of a modern transport, fuel consumption can be reduced by 25% (Pfenninger 1977; Reshotko 1984; Thomas 1985; Saric 1996). In addition, heat-shield requirements on reentry vehicles and separation/stall characteristics on low-Reynolds-number airfoils and turbine blades strongly depend on whether the boundary layer is laminar, transitional, or turbulent.

Transition is the breakdown of laminar flow to turbulent flow due to external forcing disturbances. All of the aforementioned applications have *bounded shear flows* (boundary layers) with *open systems* (with different upstream or initial-amplitude conditions). Consequently, there are several different factors that may trigger transi-

tion which are not completely understood. These factors include a number of external disturbances (such as freestream turbulence and sound) that interact with passive elements of the geometry (such as surface shape, roughness, pressure gradients, and surface temperature variations) to cause transition. Saric (1996) discusses the many distinct transition mechanisms that have been found experimentally.

Understanding how each of these combinations affect transition is not a trivial matter. In fact, at the present time no mathematical model exists that can predict where transition will occur on a simple model such as the flat plate (Saric 1994). Moreover, this research focuses on understanding how one of these combinations, the interaction of sound with the leading edge of a flat plate, contributes to the transition process.

1.1.1 Boundary-Layer Transition

Conceptually, it is useful to describe the complicated transition process as occurring in three stages: (1) the entrainment of freestream disturbances into the boundary layer (2) linear amplification of these boundary-layer disturbances and (3) the nonlinear breakdown of the disturbances that eventually leads to transition. Morkovin (1969) defined the first stage of the transition process as *receptivity*. Freestream disturbances, such as sound and vorticity, enter the boundary layer as small fluctuations of the basic state. They provide the initial conditions of amplitude and frequency for the growth of unstable waves inside the boundary layer. This phase is the least understood of the transition process, but extremely important because it gives the intial condition on the disturbance amplitude. A variety of instabilities can occur and are dependent on Reynolds number, wall curvature, sweep, roughness, and initial conditions. In the case of Blasius flow over a flat plate, the unstable waves are of the Tollmien-Schlichting (T-S) type.

While all three stages have been appreciated for many years, most of the focus has

been on understanding the second phase, the growth of the entrained disturbances. The linearized, unsteady Navier-Stokes equations are solved to model the growth of the boundary-layer disturbances. For parallel flow over a flat plate, the equations reduce to the Orr-Sommerfeld equation which describes the behavior of T-S waves as a function of Reynolds number and frequency. Because linear stability theory can be calculated, transition-prediction schemes (the e^N method of Smith and Gamberoni 1956 and van Ingen 1956) are usually based on linear theory. However, since the transition process is initial-condition dependent, these prediction schemes work only between systems with similar geometry and environmental conditions.

The last stage of boundary-layer transition takes place when the instability waves grow in amplitude to a point where three-dimensional (3-D) and nonlinear interactions exist in the form of *secondary* instabilities. The 3-D disturbances arise from an instability of the basic state comprised of the original basic-state flow and the 2-D disturbances in the boundary layer. Secondary instabilities with T-S waves are characterized by peak-valley structures and include K-type (Klebanoff et al. 1962), C-type (Craik 1971), and H-type (Herbert 1983) instabilities. With the onset of secondary instabilities, the disturbance growth occurs very rapidly over a convective length scale and the breakdown to turbulence occurs.

For most cases, these three stages accurately depict the transition process. However, if the initial disturbances have large enough amplitudes, the second stage (linear amplification of the disturbances) may be bypassed. This occurs when there are high levels of freestream turbulence or sound, or the presence of large roughness. After being exposed to the large-disturbance source, the boundary-layer response may be forced to nonlinear levels and transition to turbulence occurs immediately. Morkovin (1993) and Reshotko (1994) further discuss this not well understood process.

1.1.2 Transition and Receptivity

Although much progress has been made in understanding the transition process, the literature remains rather incomplete in predicting transition. This is primarily because the type of transition that occurs is dependent on the spectral and amplitude characteristics of the disturbances that exist and grow inside the boundary layer. Consequently, there exists a motivation to understand the receptivity problem; i.e., how freestream disturbances transfer energy into the boundary layer at the appropriate amplitude, frequency, and phase for the growth of unstable waves.

Dating back to the earliest experiments on transition, such as the pipe experiments of Reynolds (1883), there is evidence of the importance of freestream disturbance levels (and hence receptivity) in the transition process. In addition, the success of the Schubauer and Skramstad experiments in 1943, which confirmed the existence of Tollmien-Schlichting waves in boundary-layer flow over a flat plate, can be attributed to their sensitivity to the receptivity problem. They took extra precautions (employed screens in the settling chamber) to significantly reduce the freestream turbulence level so that the evolution of T-S waves could be viewed in the early part of the transition process. However, after their confirmation of the presence of T-S waves inside the boundary layer, stage two of the transition process (the linear growth of the unstable waves) gained popularity. It has only been within the last twenty-five years that researchers have begun to realize that receptivity holds the key to better understanding the transition process.

1.2 Theory

1.2.1 The Basic State

Two-dimensional laminar boundary-layer flow past a flat plate under a zero pressure gradient is called Blasius flow. Blasius flow is often used as the basic state for ob-

serving T-S waves, primarily, because of its inherent simplicity. The dimensionless streamwise velocity, u/U_∞ , becomes a function of a single variable, $\eta = \hat{y}/\delta_r$. In addition, no inflection point exists in the velocity profile, so that the only instability is due to the viscous-instability mechanism. Moreover, using this basic state enables one to isolate the viscous instability without the competing influences of other instability mechanisms.

The governing equation for Blasius flow is a simplified form of the Falkner-Skan ordinary differential equation. The Falkner-Skan equation is presented in equation (1.1).

$$f''' + \frac{1}{2}ff'' + \frac{1}{2}\beta(1 - f'^2) = 0 \quad (1.1)$$

with boundary conditions:

$$f(0) = f'(0) = 0, f'(\infty) = 1$$

where $f = f(\eta)$, $f'(\eta) = U(y)/U_\infty$ and $\eta = \hat{y}/\delta_r$. The coefficient, β , defines the pressure gradient and is equal to zero for Blasius flow. This equation is easily solved using a Runge-Kutta method and a shooting scheme that iterates on the solution until the boundary conditions are satisfied. A program written in C computes the Blasius profile for comparison with the experiment. In addition, this solution is also used as the basic state in the Orr-Sommerfeld solver required for linear-stability analysis.

1.2.2 Linear-Stability Analysis

For flow over a flat plate, individual waves exist and propagate in the boundary layer parallel to the wall. These vorticity waves are often called Tollmien-Schlichting waves or *instability waves*. Depending on the Reynolds number R , the travelling waves are in one of three states: amplified, damped, or neutrally stable. The waves may be two

dimensional or oblique and have wavelength λ , and phase velocity c . As the wave travels downstream, the frequency, ω , is conserved but the wavenumber, $k = \frac{2\pi\delta_t}{\lambda}$, changes. In addition, the phase velocity is always less than the freestream velocity U_∞ so that at some location in the boundary layer, the mean velocity is c . This location is called the critical layer and the T-S wave's maximum amplitude usually occurs near this region.

The T-S wave is a viscous instability since the boundary-layer flow is stable in the inviscid limit and a decrease in viscosity (or an increase in Reynolds number) creates the instability wave. There are no dearth of books and papers that discuss this type of instability, such as Chandrasekhar (1961), Drazin and Reid (1981), Davis (1976), Reshotko (1976), Mack (1984), and Saric et al. (1994). The following discussion highlights some important aspects of the linear stability analysis to provide a better understanding of the stability behavior of T-S waves. The summary presented here follows that of Saric (1994).

The analysis begins by assuming that the basic state for the experiment is one-dimensional, incompressible, laminar flow over a flat plate. In the “local” analysis of the behavior of the T-S wave over the short scale, λ_{TS} , the dependence of the mean flow on x can be neglected. Therefore, the *parallel-flow* assumption can be applied. The basic state becomes $\mathbf{V} = (U(y), 0, 0)$ where $U(y)$ is described from equation (1.1) for Blasius flow. To investigate the stability of the flow, two-dimensional unsteady disturbances are superposed onto the basic state:

$$u = U + u'(x, y, t) \quad (1.2a)$$

$$v = v'(x, y, t) \quad (1.2b)$$

$$p = P + p'(x, y, t) \quad (1.2c)$$

Equations 1.2 are substituted into the Navier-Stokes equations which are made dimensionless by introducing the length scale, $L = \delta_r$. Because the basic-state terms satisfy the Navier-Stokes equations, these terms drop out and the linearized disturbance equations become

$$u'_x + v'_y = 0 \quad (1.3)$$

$$u'_t + U u'_x + U_y v' + p'_x - \nabla^2 u'/R = 0 \quad (1.4)$$

$$v'_t + U v'_x + p'_y - \nabla^2 v'/R = 0 \quad (1.5)$$

where subscripts denote partial differentiation and the equations have been appropriately nondimensionalized and $R = \sqrt{Re_x}$.

Equations (1.3)–(1.5) are reduced to ordinary differential equations with the introduction of the *normal mode*

$$q'(x, y, t) = q(y) e^{i(\alpha x - \omega t)} + c.c., \quad (1.6)$$

where *c.c.* denotes complex conjugate and q' represents any one of the real disturbance quantities. For the spatial stability problem, the wavenumber α is complex and the frequency ω is real. The normal-mode approximation is made because the coefficients (i.e., basic-state velocity) are a function of y only and the disturbance equations are linear.

Substituting equation (1.6) into equations (1.3)–(1.5) produces a system of first-order ordinary differential equations. This system can be combined into a single 4th-order equation known as the *Orr-Sommerfeld* equation:

$$\left\{ \left(D^2 - \alpha^2 \right)^2 - iR \left[(\alpha U - \omega) \left(D^2 - \alpha^2 \right) - \alpha \left(D^2 U \right) \right] \right\} \phi = 0, \quad (1.7)$$

where $D \equiv d/dy$, and $\phi = v$ represents the normal-mode amplitude function for the v' disturbance. This stability analysis investigates the behavior of the disturbances (i.e. T-S waves) in the absence of external forcing. Hence, homogeneous boundary conditions are applied at the wall and in the far field. The no-slip condition, $Dv = 0$, is also implemented producing

$$\phi(0) = D\phi(0) = 0 \quad \text{and} \quad \phi \xrightarrow[y \rightarrow \infty]{} 0. \quad (1.8)$$

Equations (1.7) and (1.8) are linear and homogeneous and thus form an eigenvalue problem. Solutions exist for only certain combinations of the parameters which is simply expressed as the dispersion relationship

$$\mathcal{F}(\alpha, \omega, R) = 0. \quad (1.9)$$

For the *spatial* stability problem, α is complex and it is often useful to rewrite the local normal mode in equation (1.6) as

$$q'(x, y, t) = q(y) e^{-\alpha_i x} e^{i(\alpha_r x - \omega t)} + c.c., \quad (1.10)$$

Employing this form, it is clear that the *spatial growth rate* of the disturbance is α_i and the phase speed is given by $c = \omega/\alpha_r$. Thus, as evident from equation (1.9), α (and hence the spatial growth rate) is a function of R and the dimensionless frequency, $F = \omega/R = 2\pi f\nu/U_\infty^2$. If $\alpha_i < 0$, the disturbances grow exponentially and the flow is unstable. For $\alpha_i > 0$, the disturbances decay exponentially and the flow is stable. Figure 1.1 shows the locus of R points where $\alpha_i = 0$ for different frequencies. This diagram is commonly called the *neutral stability curve*. The left side of the curve is referred to as Branch I and the right side of the curve is called Branch II. Therefore,

F and R combinations to the left of Branch I and to the right of Branch II produce damped disturbances and combinations between Branch I and Branch II produce amplified disturbances.

The disturbance amplitude ratio between two locations is computed by integrating the spatial growth rate, giving

$$\frac{A}{A_o} = e^N \quad (1.11)$$

where the amplification factor or the “ N -factor” is given by

$$N = \int_{x_o}^x -\alpha_i \, dx. \quad (1.12)$$

where $\alpha_i = \alpha_i(F, R)$ and x_o is the location at which the constant-frequency disturbance first becomes unstable (i.e. Branch I).

To obtain the stability characteristics of the flow for a particular experimental R , F , and \hat{x} , the linearized stability equations are numerically solved. The numerical approach follows the boundary-value method (BVM) of Malik et al. (1982) where the linearized disturbance equations are written as a system of first-order differential equations. The equations are reduced to a set of linear algebraic equations and are finite differenced using a fourth-order-accurate two-point Euler-MacClaurin formula. A block-tridiagonal matrix is obtained and the complex wavenumber, α , is iterated upon until the no-slip condition at the wall is satisfied. In order to avoid the trivial solution, non-homogeneous boundary conditions are imposed at the wall. Because the eigensolution is acceptable to within a multiplicative constant, the pressure perturbation at the wall is set to equal to one. This simply normalizes the eigensolution by the value of the pressure perturbation at the wall. The program is written in C++ to take advantage of the *complex class* which provides operator overloading for simple

operations (i.e., adding, subtracting, etc.) on complex numbers.

1.2.3 Receptivity

Linear stability analysis provides information on the growth and decay of disturbances inside the boundary layer. How these disturbances originate from external disturbances that provide the initial conditions of amplitude, phase, and frequency is the focus of the receptivity problem. Receptivity differs from the stability problem not only physically but mathematically (Reshotko 1984). Mathematically, the governing equations for the two problems are different. For the stability problem, the equations of motion have homogeneous equations with homogeneous boundary conditions. In contrast, the receptivity problem has either inhomogeneous equations or boundary conditions due to external forcing of the boundary layer. Therefore, receptivity is not an eigenvalue problem.

In an effort to describe the different receptivity mechanisms, receptivity sources are divided into two categories: forced receptivity and natural receptivity (Kerschen 1989). Forced receptivity refers to the introduction of short-scale unsteady disturbances directly into the boundary layer. The disturbances have wavelengths that are on the same order as the instability wavelength, thus providing a wavelength match. This wavelength matching enables a direct transfer of energy from the external disturbance to the instability wave inside the boundary layer. Unsteady wall suction/blowing, heating/cooling, and localized unsteady pressure fields are a few examples of forced-receptivity mechanisms.

Natural receptivity results from the introduction of energy from naturally-occurring disturbances to unstable waves inside the boundary layer through some wavelength-conversion process. Natural disturbances, such as freestream turbulence and sound, have much higher wavelengths than the unstable waves and require a wavelength conversion in order for an energy transfer to occur. Because a wavelength conversion is

necessary, the physical and theoretical formulations of the natural-receptivity process are less straightforward than for forced receptivity. As a result, only within the last fifteen years has significant progress been made in this area.

The regions where natural receptivity occurs can be separated into two classes: body leading-edge regions and areas where the boundary layer must adjust on a short streamwise scale. The latter class includes short-scale wall humps, suction strips, or areas where shock/boundary-layer interactions occur. Goldstein (1983) showed that in the leading-edge region (where the boundary-layer is thin and growing rapidly) the correct asymptotic approximation to the Navier Stokes equation is the linearized, unsteady, boundary-layer equation (LUBLE) rather than the O-S equation. Further downstream, the flow can be approximated by the classical large-Reynolds-number, small-wavenumber approximation to the O-S equation (OSE). Goldstein asymptotically matched these two regions and showed that the first Lam-Rott asymptotic eigensolution of the LUBLE, with coefficient C_1 , matches onto the T-S wave which becomes unstable further downstream in the OSE region. Hence, the amplitude of the T-S wave is linearly proportional to C_1 , which is called the *complex leading-edge coefficient*.

For the second class of receptivity mechanisms, the correct asymptotic approximation is the triple-deck structure. Goldstein (1985) discusses the triple-deck theory in detail where he shows that the viscous flow in the lower deck is also governed by the LUBLE. Moreover, the common thread for both of these classes is that natural receptivity occurs in regions where the mean flow changes rapidly in the streamwise direction. Consequently, non-parallel mean-flow effects must be considered because they provide the required wavelength-conversion mechanism.

1.3 Review of Recent Research

Reviews of earlier receptivity research are given by Reshotko (1984), Crouch (1994), Choudhari and Street (1994), and Saric et al. (1994). The reader is referred to these reviews and their references because they provide considerable insight into the history and progress of receptivity. Instead, some recent analyses, computations, and experiments are discussed to shed insight into the current experiment.

1.3.1 Theoretical and Computational Analyses

The most popular receptivity model for experiments is the flat plate with an elliptical leading edge. This is primarily due to the simple nature of the flow field when compared to complex geometries with 3-D flow fields. Consequently, it is reasonable that most computational and theoretical analyses use the same geometry. Murdock (1981) simplified the geometry even further when he studied the receptivity problem for incompressible flow over a flat plate with zero thickness. He examined the boundary-layer response due to a plane sound wave travelling parallel to the freestream. This study was unsuccessful because finite curvature was not included in the leading-edge region. The attachment line or stagnation region acts as a receptivity source as large mean-flow adjustments are made in this area, and an infinitely-thin plate features infinite vorticity in this region.

Numerical simulations that do not incorporate finite leading-edge curvature cannot resolve the resulting infinite vorticity which becomes a problem. Theoretical work by Hammerton and Kerschen (1994) shows that flow over a parabolic body with a sharp leading edge (smaller nose radius) is more receptive than flow over an infinitely-thin flat plate. Gatski and Grosch (1987) solved the full incompressible Navier Stokes equations for flow over an infinitely thin, semi-infinite flat plate and found no clear development of T-S waves. Casalis and Cantaloube (1994) also performed a direct

numerical simulation (DNS) on the same geometry and found the receptivity response to be an order of magnitude lower than asymptotic theory predictions. This may be due, in part, to the failure to apply finite curvature at the leading edge. Consequently, these computations do not fully capture the receptivity problem.

Lin et al. (1992) performed full Navier-Stokes computations in general curvilinear coordinates and included the finite thickness and curvature at the leading edge. The simulations showed that the T-S waves may be linked to freestream sound, and that the magnitude of the receptivity decreased with increasing leading-edge aspect ratio. In addition, a new leading edge geometry, based on a super ellipse, was examined where the leading-edge/flat-plate curvature discontinuity was removed. Simulations using the modified super ellipse (MSE) geometry showed a decrease in the receptivity magnitude when compared to geometries with a leading-edge/flat-plate juncture. This result agrees with numerical analyses by Goldstein (1985) and Goldstein and Hultgren (1987). Computational DNS studies are now underway by Fuciarelli and Reed (1994) to investigate the receptivity problem on a flat-plate with a modified-super-ellipse leading edge with aspect ratios of 6:1, 20:1, and 40:1.

1.3.2 Experimental Investigations

Numerical analyses performed by Goldstein and Hultgren (1989), Heinrich (1989), Kerschen (1989), Crouch (1992a) and Bodonyi et al. (1990) show that the coupling between the long-wavelength acoustic disturbance and the T-S wave occurs where the boundary layer adjusts locally. Crouch (1992b) also shows that the wavelength-conversion also takes place where the boundary-layer must adjust globally. This can occur at four positions on a flat-plate model: the leading edge, the leading-edge/flat-plate junction, in the presence of strong localized pressure gradients, and at any surface inhomogeneities. A plethora of experimental research has been conducted to examine the natural receptivity in these four regions.

Leehey and Shapiro (1980) found that a T-S wave is generated over a low-aspect-ratio leading edge (6:1) when a measurable pressure gradient exists at the leading edge. Aizin and Polyakov (1979) use a 60:1 leading edge and observe the coupling of an acoustic disturbance to the T-S wave due to a $10\mu\text{m}$, two-dimensional roughness element. No T-S waves were observed in the absence of roughness strips. Saric et al. (1991) performed sound experiments with roughness over a flat plate and demonstrated the linearity of the receptivity process with respect to roughness height. Kosorygin et al. (1994) examined the receptivity problem over a flat-plate model in the presence of 2-D roughness. They showed that the T-S wave amplitude can be decreased by the constructive-destructive interference of the roughness element with the travelling unstable waves.

The measurement techniques to extract the T-S wave from background noise have made significant progress in the last 10 years. Kendall (1990) successfully separated the T-S wave from freestream turbulence by means of a differential pressure sensor (Kendall gauge). Wlezien (1989) and Wlezien et al. (1990) used a complex-polar plot technique and a wavenumber spectrum based on streamwise scans to extract the T-S wave in their receptivity study of suction slots and leading edges. Spencer (1992) studied the receptivity of 3-D roughness elements by measuring the near-field disturbance patterns. The amplitude and phase of the hot-wire signal with and without the roughness was measured and subtracted in the complex plane to extract the T-S amplitude. Saric et al. (1995) isolated the receptivity mechanism to the leading edge by employing a 20:1 and 40:1 aspect-ratio modified super ellipse. They used the complex polar technique to separate the T-S wave and found some interesting features that cannot be explained by theory. For both leading edges, a wavelength focusing and narrow-frequency-band response of the T-S amplitude is observed. These interesting results provide some of the motivation for the current

experiment.

1.4 Experimental Objectives

The primary experimental objectives are the following: (1) to investigate new techniques for extracting the Tollmien-Schlichting wave from the background noise signal (2) to establish a Blasius basic state to limit the instability mechanism to a T-S wave (3) document the amplitude and spectra of the freestream disturbances which can contribute to the transition process (4) develop a robust sound generation and detection system for the acoustical forcing (5) further investigate the focusing behavior of the receptivity coefficient for a narrow band of frequencies shown in previous experiments and (6) obtain T-S wave amplitudes for different frequencies and freestream speeds on an elliptical-leading-edge flat plate with a juncture for comparison with coefficients obtained on a flat plate that limits the receptivity mechanism to the leading edge.

Of course, the objective for this report is to present the methodology and results of this experiment. However, because of the extremely sensitive nature of this work, the document also focuses, in detail, on the complexities encountered while performing the aforementioned tasks. In doing so, the author hopes to provide valuable information to future experimenters conducting research in this area.

1.5 Outline

The rest of this document describes the details of the experiment. Chapter 2 describes the ASU Unsteady Wind Tunnel facility, including the measurement devices used for data acquisition and sound generation/detection. The two different models employed in this experiment are discussed in chapter 3. Chapter 4 discusses some

special considerations taken into account before actual experimentation. The measurement techniques used to acquire and process the data are described in chapter 5. The process implemented to establish the basic state and symmetric flow around the model are discussed in detail in chapter 6. Chapter 7 provides amplitude and spectra documentation from the freestream turbulence measurements taken with the zero-pressure region of the tunnel located in the mixing region and plenum. This chapter also presents many of the difficulties encountered while surveying the acoustic field at the test-section entrance. A review of different signal-separation techniques investigated to extract the T-S wave from the background signal is discussed in chapter 8. Receptivity coefficients, as a function of different speed/frequency combinations, are documented. An investigation of the focusing behavior of the receptivity coefficient is also presented in this chapter. Finally, chapter 9 gives the conclusions and discusses new directions for future experiments.

CHAPTER 2

Experimental Facility

2.1 Unsteady Wind Tunnel

This experiment is conducted in the Arizona State University Unsteady Wind Tunnel. In 1970, Dr. Philip Klebanoff built the tunnel at the National Bureau of Standards (NBS) in Gaithersburg, Maryland for calibrating low-speed anemometers under atmospheric conditions. In 1984, parts of the tunnel were moved to Arizona State University under the direction of Dr. William Saric. During the reconstruction at ASU, major modifications were performed on the tunnel to improve the flow quality to make it suitable for both stability and receptivity experiments. The modified facility became fully operational in 1987. Figure 2.1 shows a plan view of the tunnel.

Saric (1992) gives a complete description of the facility and therefore only key features are described here. The tunnel is a closed-return tunnel within which oscillatory flows of air can be generated for the investigation of low-speed unsteady-flow problems. Unsteady-flow operation is achieved by a vertical array of rotating shutters located in a unique dual-duct arrangement. Air can be diverted from the primary duct (i.e. contraction cone and test section) to the secondary duct via the opening of a flow-separation panel located in the plenum. To create the unsteady flow, the set of rotating shutters in each duct are oscillated 90° out of phase. Flow oscillations in the test section range from 0.1 Hz to 25 Hz where the amplitude of the fluctuations can

be varied from near zero to 100%. The use of the secondary-duct design allows for improved performance over single-duct facilities because the unsteady inertial loads are confined to the two ducts. Consequently, the fan experiences a constant load at all times.

A 150 hp variable-speed DC motor powers the single-stage axial fan. The fan consists of nine adjustable blades which are 1.83 m in diameter and has 11 stators. A Mentor II digital DC drive controls the fan speed which is interfaced to the wind-tunnel computers for wind-tunnel-speed automation. To eliminate any motor vibrations from contaminating the experiment, the fan housing is mounted on a separate isolation pad. For this experiment, the wind tunnel is operated in the conventional steady-flow mode. When operated in steady mode, the tunnel has a speed range of 5 m/s to 35 m/s. For this configuration, the secondary duct is closed and the shutters in the primary duct are open.

The facility has two interchangeable 1.4 m × 1.4 m × 5 m test sections that can be mounted on casters for easy movement. Once the test section is properly placed in the wind-tunnel circuit, the casters are removed and flexible couplings attach the test section to the rest of the wind-tunnel. An isolated concrete pad is also located underneath the test section to help eliminate vibrations that can affect measurements inside the test section. Each test section allows the use of two different windows. One window is constructed for use with a 3-D traversing system (refer to section 2.2) for gaining access to the model for velocity measurements. The Plexiglas window is slotted and an adjustable opening for a sting is created by a zipper to minimize leakage. The other window is used for flow-visualization and for laser-doppler-velocimeter measurements.

2.2 Traverse and Sting

A traversing mechanism mounts to the exterior of the test section to avoid blockage and increased turbulence effects of an internally-mounted traverse system. Figures 2.2 and 2.3 provide side and front views of the traversing system. Connected to the traversing mechanism is a 45° forward swept, carbon-carbon composite sting that protrudes into the test section and supports two hot-wire sensors for velocity measurement. The sting is attached to an aluminum carriage (item 'd') and a microstepping motor drives the carriage in the Y (wall-normal) direction via a precision lead screw. The Y motion of the carriage is guided by two vertical rails and is supported by two vertical lead screws which are driven in the Z (spanwise) direction by two microstepping motors. When the sting moves in the spanwise direction, two additional microstepping motors move the Plexiglas window to provide synchronous sting motion. This entire traverse system rests on a stainless-steel platform and is driven by a 3.65 m precision lead screw (item 'b') which moves in the streamwise direction along two stainless-steel Thompson rails (item 'c'). All microstepping motors are made by Compumotor and digital-position feedback is provided by 1000-line Renco optical encoders. Table 2.1 shows the minimum step-size for each axis.

Table 2.1: Traverse system capabilities.

Direction	X	Y	Z
Total Travel	1.25 m	100 mm	175 mm
Minimum Step	12 μm	0.7 μm	1.3 μm

2.3 Computer Systems

Automating measurement procedures is considered standard practice. To integrate the many standard operations (tunnel operation, hot-wire calibration, data acquisition, etc), all of the procedures are controlled by a Sun SPARCstation 20 which is

equipped with two 60 MHz processors, each providing 167 MIPS and 36.6 MFLOPS. The system has a 20 inch monitor with 1024×768 resolution, 64 MB RAM, a 3.15 GB hard drive, and a 5 GB external tape drive. The SPARCstation runs Solaris version 2.4 which allows multiusers and is a multi-tasking environment that is ideal for the many simultaneous wind-tunnel operation activities. The computer is equipped with a National Instruments GPIB card for interfacing with external equipment such as D/A and A/D boards.

Several other computers are located in the control room and are connected to the Sun SPARCstation 20 via the Ethernet. A subnet router connects the wind-tunnel computers to the Arizona State University network which allows access to the world-wide Internet. A PC compatible, with a 50 MHz 80486DX microprocessor, is typically used as an xterm to the main workstation but also serves as the back-up data-acquisition system. If the need arises, the computer can communicate with all external D/A and A/D boards via a National Instruments AT-GPIB/TNT card. The computer has 20 MB of RAM, a 425 MB hard disk, and runs SCO UNIX which provides a multi-user environment. In addition, a 2 GB, 4 mm DAT drive furnishes additional storage for system backups and data archiving.

A DECstation 5000 running Ultrix serves as a workstation but is typically implemented as an xterm to the Sun SPARCstation 20. It is equipped with 16 MB RAM and a 2.4 GB hard disk which supplies additional data storage space.

In addition, a Macintosh Quadra 650 is available for word processing and drafting. The system runs the Macintosh OS with a 17-inch, 64k-color terminal. The computer has 8 MB RAM, a 230 MB hard disk, and is equipped with a 8 GB tape drive for nightly back-ups and additional storage space. Printing capabilities include a Hewlett-Packard HP4M 600 dpi PostScript laser printer and a Hewlett-Packard 1200C/PS 300 dpi PostScript inkjet printer provides color prints.

2.4 Instrumentation

A pitot-static tube, connected to a 10-torr differential pressure transducer (MKS model 398 HD), measures the test-section dynamic pressure. The pitot-static tube is positioned at the test-section entrance and is aligned parallel to the flow to minimize static-pressure errors associated with yaw (Rae and Pope 1984). A 1000 torr absolute pressure transducer (MKS model 390HA) measures the static pressure. Each transducer connects to a MKS 270B 14-bit signal conditioner with a digital display for monitoring. The dynamic and static pressures are acquired by the computer via a GPIB interface. A thin-film RTD measures the test-section temperature which is also acquired by the computer.

Hot-wire anemometry provides instantaneous mean and fluctuating velocity measurements inside the test section. Two Dantec 55P15 boundary-layer sensors (hot wires) mount onto the sting via two probe holders. The hot wires consist of $5 \mu\text{m}$ platinum-plated Tungsten wire welded between two supporting 8 mm probe tines which are 1.25 mm apart. Each sensor connects to a Dantec 55M01 constant-temperature anemometer using a 55M10 CTA standard bridge.

Typical AC measurements employ a 2-channel Stewart (model VBF44) filter to amplify and band pass the hot-wire signals with band-passing capabilities ranging 1–255,000 Hz. The device provides optimum filtering in the frequency or time domain with gains up to 70 dB per channel. An RS-232 line interfaces with the Sun SPARCstation 20 via a serial port to provide computer control to the filter.

A three-channel Tektronix AM502 differential amplifier provides additional signal amplification and filtering. Amplification ranges from 1-100,000 with a high-pass minimum of 0.1 Hz and a low-pass maximum of 1 MHz. This device is employed when DC-coupling and/or a 0.1 Hz high-pass cut off is required such as when taking freestream turbulence measurements.

A Stanford SR530 lock-in amplifier measures the amplitude and phase of the hot-wire signals allowing single-ended, true-differential, or current inputs. This device provides frequency tracking (see section 5.4) with band-pass, line-notch, and $2 \times$ -line-notch filtering capability. It is equipped with two D/A outputs with 13-bit resolution (± 10.24 V) and can be interfaced to the computer via an RS-232 connection.

Two IOtech (Model AD488/8SA) A/D converters digitize all analog signals and the digitized signal is sent to the data-acquisition computer. Each unit provides 8 16-bit differential input channels with simultaneous sample and hold capability. Discrete sampling rates ranging from 0.2 Hz to 100 kHz are possible with data transfer to the data-acquisition computer via a high-speed GPIB. When the two units are configured in a master/slave configuration, 16 channels can be acquired simultaneously with no data-acquisition time lag between the two boards. The device allows input signal voltages ranging from ± 1 to ± 10 volts with the ability to change the voltage range for optimum signal resolution.

2.5 Sound-Generation Equipment

An integral requirement for this experiment is a robust and reliable system for generating an acoustic-forcing field. Previous experiments (Wei 1994, Rasmussen 1993, and Saric et al. 1991) used a rather simple scheme for sound generation. This consisted of one to three speakers, an amplifier, and an analog signal generator for signal generation. Although quite functional, this system was modified to incorporate computer-controlled signal generation. This reduces time-consuming procedures such as performing frequency sweeps and acquiring signals at each frequency to a trivial task of executing a computer program. The program is constructed to change the frequency at a user-specified increment and acquire the appropriate signals from the A/D board. In addition, to enable the study of *bypass* mechanisms such as large-

amplitude sound, the system consists of nine speakers. Moreover, the sound signal is digitally generated and output via a D/A board, amplified by five two-channel amplifiers, and radiated into the tunnel by an array of speakers.

The acoustic signal is digitally generated and converted to an analog signal a 16-bit IOtech DAC488HR digital-to-analog (D/A) board. The D/A board has a maximum update rate of 100 kHz which allows the generation of signals with frequencies up to 33 kHz (three points per wave). The board also provides the capability to digitally produce single and arbitrary waveforms including random noise. The board is equipped with three output channels so that oblique waveforms may be radiated into the test section. This is accomplished by generating phase-lagged waveforms which are sent to the array of speakers.

The signal from the D/A board is sent to Five ADCOM GFA-555 amplifiers which amplify the signal approximately 32 times. The amplifiers provide 325 Watts of continuous power. The amplifiers are encased in an in-house constructed shelving unit with six small fans for cooling. During the initial experiment phase, amplifier overheating was a problem. To alleviate this, an auxiliary fan directed towards the back of the amplifiers provides additional cooling.

The acoustic disturbances are sent into the test section by an array of nine McCauley Sound speakers. To minimize blockage affects, the speakers are flush-mounted on the plenum wall as shown in figure 2.4. The speakers are 250 mm in diameter and have a maximum power capacity of 300 Watts. The speaker response is relatively flat in the frequency range 50–100 Hz, making them ideal for this experiment because this encompasses the range of frequencies where the T-S waves are most amplified. The maximum input to the amplifiers should not exceed 1.52 volts (rms) since this corresponds to the maximum speaker capability of 300 Watts.

2.6 Sound- and Vibration-Detection Devices

A robust acoustic-generation system is only as good as the system implemented to detect the generated signal. Previous experiments (Wei, 1994) employed a set of Radio Shack condenser microphones, type 270-090. The sound pressure level (SPL) threshold for these microphones limited the investigation of large-amplitude-sound affects ($SPL > 110$ dB). To better measure the initial amplitude and phase of the acoustic disturbance, new acoustic-detection devices were purchased and implemented. Moreover, this experiment uses the following set-up for measuring the incident sound field.

Six PCB 103A102 piezotronic microphones, developed specifically for wind-tunnel applications, are used for sound amplitude and phase measurement. The microphone is structured with ceramic crystal elements, contains a microelectronic amplifier, and has a built-in accelerometer to virtually cancel out vibration sensitivity. A thin, recessed Invar diaphragm and a bender-mode crystal element make it suitable for very low and high pressure measurements up to 198 dB. In addition, the microphone has an ultra-high sensitivity of 1500 mv/psi. The microphones have an outside diameter of 9.53 mm, a 3.1 mm diameter pressure orifice, and are flush-mounted on the walls of the test-section entrance so that they do not affect the flow field.

The microphone signals are powered and amplified by a PCB ICP 16-channel microphone signal conditioner (Model 584A). This device amplifies the microphone signal with set gains of 1, 10, or 100. To eliminate system electrical noise, the signal conditioner is battery powered by a PCB 073B10 portable AC power source. The signal conditioner is also equipped with an IEEE-488 interface for computer control.

Because model vibration contaminates the receptivity process (Leehey et al. 1984), any sound-induced vibration of the wind-tunnel structure or model must be detected and eliminated. A PCB piezoelectric U352B22 accelerometer is employed to investigate any sound-induced vibration of the wind-tunnel structure and model. The

accelerometer has a resolution of 0.0015 g, a voltage sensitivity of 9.55 mV/g, a frequency range of 5–8000 Hz, and a range of ± 400 g. The resonant frequency is 32 kHz, which is much higher than any frequencies that are of concern for this experiment. The device is also chosen for its small size (3.5 mm \times 6.4 mm \times 9.1 mm) and weight (0.5 grams).

CHAPTER 3

Model Configuration

This chapter discusses the two different flat-plate models employed in this experiment. One flat plate has a special leading-edge geometry making it ideal for investigating the leading-edge as a receptivity mechanism. The other model has a tapered elliptical leading edge with a leading-edge/flat-plate juncture. Consequently, each model is unique and is further discussed here.

3.1 The Klebanoff Flat Plate

This flat-plate model was originally built in 1971 by Dr. Klebanoff at the National Bureau of Standards for investigating 3-D roughness. The plate was then implemented at the Unsteady Wind Tunnel for the flow-quality improvement studies performed during the reconstruction phase (Mousseux 1988). The plate is constructed from a nickel-aluminum alloy and the surface is ground (not rolled) thus making it suitable for sensitive boundary-layer experiments where any surface discontinuities are known to act as a receptivity mechanism (Goldstein 1985). The model is 9.53 mm thick, 3.6 m in chord, 1.37 m in span, and has a 9% flap. The flat plate is mounted vertically in the test-section and ten adjustable brackets hold the model in place. The model is placed at a nominal distance of 0.762 m from the front wall of the test section splitting the flow 57%–43%. The surface of the plate is polished to $0.2\mu\text{m}$ rms to

eliminate surface roughness as a possible receptivity mechanism.

Each end of the flat plate is machined with a specially-designed leading edge (Lin et al. 1992) which eliminates the leading-edge/flat-plate juncture present on standard elliptical leading edges. The leading edge has the form of a modified super ellipse (Equation 3.1) whose curvature continuously goes to zero at the juncture.

$$\left(\frac{y}{b}\right)^2 + \left(\frac{(a-x)}{a}\right)^{2+\left(\frac{a}{x}\right)^2} = 1 \quad (3.1)$$

One end has a 20:1 aspect ratio ($a = 95.3$ mm, $b = 4.76$ mm) and the other end is contoured with a 40:1 aspect ratio ($a = 190.5$ mm) leading edge. This geometry has a nose radius similar to standard ellipses. For this experiment, the 20:1 aspect ratio leading edge is used and the 40:1 aspect ratio leading edge is sandwiched by contoured balsa woods and covered by tape and the trailing-edge plate attaches to this end.

For static-pressure measurements, the plate is equipped with 25 static pressure ports on each side of the centerline. Plastic tubing connects to each hole so that the pressure distribution along the plate can be measured. Static pressure measurements are often used in the initial stages of aligning the plate for Blasius flow.

A set of holes displaced ≈ 25 mm apart (one-half the wavelength of a 50 mm T-S wave) are located near Branch II for typical run conditions. There are total of 27 dual ports divided into three groups as discussed by Wei (1994). These dual ports were drilled into the plate to be used as spatial filters for measuring the T-S wave pressure. Refer to sections 8.1.2 and 8.1.3 for more information on their use. A trailing-edge flap attaches to the end of the plate to provide leading-edge separation control. Flap adjustment is performed to balance the blockage on each side of the plate. The flap is

0.5 m long with a sharp trailing edge that is adjusted via moveable brackets. Typical flap-angle values range from 1–4°. Section 6.3 discusses the role of the trailing-edge flap for creating symmetric flow around the leading edge.

3.2 The VPI Flat Plate

This model is constructed as a laminated panel that contains a 19 mm honeycomb core sandwiched between two 6061-T6 aluminum sheets. The overall dimensions of the plate are 1.4 m wide, 20.6 mm thick, and 3.7 m long. A 0.34 m × 1.4 m tapered leading-edge is mounted directly to the flat plate by mounting brackets and thread inserts. The 10 μm gap between the leading edge and plate is filled with Bondo and wet sanded with fine-grit paper to minimize any surface discontinuities. The leading edge has an elliptical profile with a ratio of major-to-minor axes of 67:1. This leading-edge aspect ratio minimizes the stagnation point pressure rise and is insensitive to leading-edge separation at slight angles-of-attack. This model also has inductance-probe ports near Branch I to monitor the oscillation amplitude and frequency of a vibrating ribbon and ports for a smoke-wire system. Consequently, the plate's overall surface is not as “smooth” as the Klebanoff plate.

The flat-plate is equipped with two rows of 24 static-pressure ports that are parallel to the plate centerline. Plastic tubing connects to each hole to provide pressure-coefficient information along the entire plate. These static pressure measurements are often used in the initial stages of aligning the plate for Blasius flow.

CHAPTER 4

Special Considerations

The extremely sensitive nature of boundary-layer receptivity requires a very conservative approach to the experimental set-up and measurements. Consequently, this chapter discusses some of the precautionary measures taken to ensure that environmental conditions are considered.

4.1 Wind-Tunnel Operation

When performing experiments that require several hours to complete, the test-section temperature can vary by as much as 20°C. Temperature compensation provides the necessary hot-wire voltage correction but temperature variations change the viscosity which, in turn, affect the Reynolds number, Re_x , and dimensionless frequency, F . To minimize viscosity variations, the tunnel is operated at a low velocity for most of this experiment. Typical velocities range from 8–15 m/s and most of the experimental work is conducted at 8 m/s and 12 m/s.

Because the freestream environment plays an active role in the stability and receptivity characteristics of this experiment, it is crucial to continuously monitor and control the wind tunnel environment. It is paramount that the tunnel is running at the desired speed at all times for a particular experiment. In addition, the appropriate velocity changes must be made to keep the tunnel operating at a constant

Reynolds number or dimensionless frequency to account for any temperature changes. A LabVIEW program, called “cruise control” is a virtual instrument that continually monitors the test-section temperature, static pressure, and fan rpm using the Sun SPARCstation data-acquisition computer. The wind tunnel can be operated in constant speed, constant Reynolds-number, or constant dimensionless-frequency mode. Moreover, to run at a particular Reynolds number or dimensionless frequency, the program makes the appropriate changes in the velocity to account for viscosity changes due to tunnel heating.

For all the experiments using radiated sound, the wind-tunnel cruise program is run with an active control on the dimensionless frequency, F . The dimensionless frequency is chosen rather than the Reynolds number for the following reasons. First, during a streamwise scan, the Reynolds number is changing continuously due to the different streamwise location of the hot-wire. Consequently, it is not desired to keep the Reynolds number constant. In addition, F is proportional to ν/U_∞^2 and a change in ν is compensated by a relatively small change in velocity. Moreover, keeping F constant is the most favorable test condition.

To provide further information about the freestream environment inside the test section, it is necessary to document the blade- and stator-passing frequencies. To ensure that disturbances at these frequencies do not contaminate the experiment, the wind-tunnel experiment parameters (speed and dimensionless frequency) are chosen far away from conditions where the blade- and stator-passing frequencies could play a role in the receptivity process. Figure 3.1 shows the blade- and stator- passing frequencies for tunnel velocities ranging from 5–25 m/s.

4.2 Sound-Induced Vibration

During preliminary experiments, sound from all nine speakers is projected into the test section. During these experiments, a frequency sweep is performed and the wind tunnel structure is examined for audible vibrations. At certain frequencies, several locations on the contraction cone resonated. To eliminate the vibrations, areas of the contraction cone are reinforced with 6.35 mm steel.

The natural frequency of the leading edge is also documented by mounting the PCB accelerometer (discussed in section 2.6) to the back of the leading edge. The accelerometer is located at the centerline of the flat plate and digitally-generated random noise (discussed in section 5.2.2) is broadcast into the test section. The accelerometer signal is amplified, band-passed 1–1000 Hz, and acquired by the A/D board at a 2 kHz sampling rate. Figure 3.2 shows the power spectral density of the accelerometer signal. The resonant frequency of the leading edge is approximately 21 Hz. To verify this measurement, the leading edge is lightly tapped with a rubber hammer to provide the impulse function, and the accelerometer signal is acquired. The power spectrum of the resulting signal closely matches the spectrum produced by the random noise.

This experiment focuses on the generation of T-S waves with frequencies ranging from 45–115 Hz, which are two to three times higher than the plate's natural frequency. Consequently, the flat plate acts as a natural low-pass filter and helps to dampen any high-frequency energy contributions. Accelerometer measurements at the leading edge are also performed for single-frequency sound. It is shown that peak-to-peak oscillations of the leading edge were $O(20)$ μm which are considered tolerable.

CHAPTER 5

Experimental Techniques

This chapter discusses the hot-wire signal-processing techniques that are used at the Unsteady Wind Tunnel. Many of these procedures are a result of several years of testing and modification. In addition, the sound-generation and detection techniques developed by the author are presented.

5.1 Hot-wire Signal Processing

Measurements of mean- and disturbance-flow quantities in the freestream and boundary layer are obtained from hot-wire anemometry. The primary focus in the analysis of the hot-wire signals at the Unsteady Wind Tunnel is to eliminate the need for external analog conditioning equipment by using computerized calibration and temperature-compensation techniques.

5.1.1 Velocity Calibration

As discussed in section 2.4, the hot-wire anemometry system employs constant-temperature anemometers. For incompressible flow, the wire's response is virtually only a function of velocity and thus a single overheat temperature is sufficient. The constant-temperature anemometer maintains the wire at a constant temperature by electrical resistance heating. As air flows over the wire and convects heat away, the

amount of current required to keep the wire at the given temperature changes. The current (and thus voltage) through the wire is changed to keep the wire at a constant resistance. This voltage change is calibrated against the velocity measured by the Pitot-static tube where the maximum and minimum obtainable tunnel velocities are covered for the calibration. The anemometer's velocity response can be modeled using King's Law (Perry 1982), but it is generalized to the best polynomial fit (usually a fourth-order fit is best) for use at the Unsteady Wind Tunnel. The calibration procedure is completely automated and usually takes less than 7 minutes to perform.

5.1.2 Temperature Compensation

The Unsteady Wind Tunnel does not have a cooling system (i.e. heat exchanger). Consequently, the tunnel temperature can increase by 20 °C during a high-Reynolds-number experiment or during an experiment that requires hours to complete. To account for hot-wire voltage drift with changing test-section temperature, the hot-wire signals are temperature-compensated. Reibert (1996a) and Radeztsky et al. (1993) provide a detailed discussion of the employed technique which assumes the square of the hot-wire anemometer voltage varies linearly with temperature for a fixed velocity. The hot-wire voltage, test-section temperature, and Pitot-static velocity are acquired while the tunnel is preheated to provide voltage, velocity, and temperature data. The slope of the linear model is the *compensation coefficient* which is a function of the tunnel velocity. The measured Pitot-static velocity provides the required voltage/velocity dependence. This speed dependence of the compensation coefficient is modeled with a 2nd-order polynomial least-squares curve fit. The compensation coefficients are obtained before the velocity calibration (discussed in section 5.1.1) which allows the velocity calibration to be corrected for any temperature changes. As a result, the temperature-compensated hot-wire voltage is an implicit function of the corresponding velocity and temperature where the velocity is a function of the

compensated hot-wire voltage. This temperature-compensated hot-wire voltage, in turn, is then used in the voltage/velocity calibration. The routines required for determining the temperature-compensated voltage and the corresponding velocity are provided as standard Unsteady Wind Tunnel library routines (Reibert 1996b) that can be efficiently implemented into all data-acquisition programs.

5.2 Sound Generation

5.2.1 Digital-to-Analog Library Routines

This experiment relies heavily on providing reliable and repeatable sound generation that can be incorporated into data-acquisition routines. As discussed in section 2.5, computer-controlled sound generation makes important procedures such as performing frequency sweeps and acquiring microphone/hot-wire signals a trivial task. To simplify the programming process for incorporating the sound generation into the data-acquisition process, a set of D/A board library routines were written. As a result, initializing the D/A board, or changing the sound amplitude or frequency, is reduced to a simple matter of calling a subroutine. The use of the D/A library routines provides complete automation of the sound signal generation which ensures that the same procedures are implemented each time. This eliminates any repeatability errors that are prominent when using an analog waveform generator that requires human intervention to change the frequency and amplitude.

The D/A library consists of the following routines. A procedure to initialize communication with the D/A board, a routine to stop the waveform output, and a procedure to close communication to the D/A board. Commands to generate a particular waveform type (square, triangle, or sine wave) of a specified amplitude and frequency are also controlled by a subroutine. Another routine provides the capability for phase-modulated sine waves, and a separate procedure handles the generation of

band-passed, random-noise output.

5.2.2 Band-Passed Random Noise

Band-passed random noise is digitally generated considering the maximum allowable input voltage to the amplifiers, the D/A update rate (which affects the output signal frequency), and the desired rms level of the final signal. In addition, because the GPIB must be free to acquire data while the speaker signal is radiated into the test section, the band-passed random signal cannot be generated and sent to the D/A board continuously. Therefore, a one-minute sample of the noise is generated, stored on the D/A board, and repeated. This does provide a 1 Hz frequency component in the signal but this frequency is low enough so that it is not a concern.

Generation of the band-passed noise consists of two primary steps. First, a set of random, Gaussian-distributed numbers (x_i) are generated using routines provided in Press et al. (1992). The routines are slightly modified to produce numbers ranging from ± 2 which is an acceptable voltage input range to the ADCOM amplifiers. To provide a relatively flat, band-passed signal to the speakers, the number set is filtered using a finite impulse response (FIR). The FIR technique is discussed by Cunningham (1992). The number of coefficients chosen depends on the number-set length and on the band pass, but typical values range from 500 to 2000 coefficients. The coefficients are simply determined from the inverse Fourier Transform of the desired frequency response. The fact that the total power in the frequency-response spectrum is the square of the rms of the time-domain signal is used for computing the coefficients. The coefficient calculation ensures that the resulting band-passed random signal sent to the amplifiers is approximately 1 volt rms, by assuming a constant power level S_o in the band-passed region and zero elsewhere.

The data is windowed keeping the many “trade-offs” of different window functions (Gibbs ripple, main lobe width, attenuation, etc.) as a primary concern. The

Blackman window function was chosen because it reduces the Gibbs phenomenon ripple better than, say, the Hamming and von Hann window, although the main lobe width is slightly increased in comparison. This window function also provides more attenuation between the main lobe and the first side lobe. The Blackman window attenuates approximately 60 dB, the Hamming window attenuates 40 dB, and the von Hann window provides 32 db attenuation. A power-spectrum was performed on the final signal to ensure that the desired band-passed signal is produced.

5.3 Sound Detection

Two different IOtech A/D boards are required when acquiring the environment conditions (pressure, temperature, and dynamic pressure), the microphone signals, and the hot-wire signals simultaneously. The acquired microphone signals provide information on the incoming sound signal that includes not only the sound amplitude, but the relative phase of the incoming signal (where one microphone is the reference). Consequently, it is crucial that no time lag exists between the two A/D boards so that the relative phase measurement between the microphones is correct. If the reference microphone signal is acquired by the first board, some microphone signals are acquired on the same board, and others are acquired on the second board, any time-lag between the two boards will yield erroneous phase differences between the signals.

To ensure that the boards are sampling simultaneously, the two boards are configured as a master/slave system. It is *essential* that the two boards are configured in this manner. Some initial tests are conducted to verify the need for this configuration and show relative phase differences up to 15° when the same signal is acquired on both boards when not in the master/slave configuration. In addition, the time-lag between the two boards is not a constant when repeated which compounds the importance of

using this configuration. Configuring the two boards as master/slave is quite simple. Particular digital I/O pins on each of the two boards are attached to each other to provide simultaneous triggering. Commands are sent to one board designating it as the master board and the other board is designated as the slave. Moreover, triggering the master board to start sampling automatically triggers the slave board to sample simultaneously via the I/O connection. Testing with the two boards configured in this manner showed no detectable time lag between the two boards.

5.4 Hot-Wire Amplitude and Relative-Phase Measurements

A Stanford Research lock-in amplifier simplifies signal analysis significantly. This device tracks, amplifies, and measures the component of a signal that travels at a user-specified frequency. Because the frequency of an external disturbance (such as sound) is preserved as the disturbance becomes entrained into the boundary layer, the T-S wave generated by an external disturbance has the same frequency. Consequently, this apparatus is useful when tracking the development of an unstable wave in the boundary layer due to some external forcing.

This device was primarily used to obtain boundary-layer amplitude relative-phase information where the driving speaker signal provides the reference signal. To obtain amplitude and relative phase information, the Stanford lock-in amplifier is operated in “ R/ϕ ” mode where R is the signal magnitude and ϕ is the signal phase. Initially, a shorting device is connected to input “A” to zero the magnitude output. Next, the reference signal (speaker signal) is connected to the “reference input” and “relative phase” button is pressed. The two “90°” buttons may also be pressed to rotate the internal coordinate axes to provide an initial zero relative phase. The boundary-layer signal is then attached to input “A” and the device now reads the true magnitude of the boundary-layer signal, and the phase output is measured relative to the reference

signal input. The phase output voltage is proportional to degrees and the magnitude output voltage is converted to a velocity fluctuation by means of the boundary-layer hot-wire calibration curve. It is important to note that the boundary-layer voltage is sent directly from the anemometer to the Stanford device, and *no* amplification is required since the device has amplification capability.

5.5 Boundary-Layer Scans

Traversing the boundary-layer to obtain the disturbance profile and/or the mean-flow profile is a completely automated procedure. To obtain the disturbance profile, the boundary-layer signal is acquired by the Stanford lock-in amplifier to provide amplitude and relative phase information. To provide an additional check, the AC hot-wire signals are band-passed, amplified using the Stewart filters, and acquired by the A/D board. When establishing the basic state, it is necessary to acquire only the mean-flow signal to obtain shape factors. Consequently, two different boundary-layer-scan programs are used. One program acquires only the mean-flow signal (DC hot-wire component) and another program obtains both the mean-flow and the disturbance (AC hot-wire component) profile.

Initially, the both wires are aligned parallel to the plate to measure the streamwise velocity u component. This requires moving the boundary-layer wire as close to the plate as possible and positioning the tines so that they are equidistant from the plate when viewed under magnification. Both hot-wires are then positioned outside the boundary layer and if a disturbance profile is desired, the hot-wire anemometer output is connected to the Stanford lock-in amplifier and Stewart filters for acquisition. If the disturbance profile with sound is desired, the sound signal (with the appropriate amplitude and frequency) is introduced into the test-section. The wind-tunnel speed is controlled using the cruise-control program which operates in either constant-velocity

or dimensionless-frequency mode, depending on the experiment. Hot-wire measurements are then taken at each \hat{y} location as the traverse steps through the boundary layer. The first acquired point provides a boundary-layer-edge-to-freestream-velocity factor that must be considered to ensure that the boundary-layer wire velocity is normalized with instantaneous edge velocity, U_e , and not the instantaneous freestream velocity. This scaling factor becomes important when the tunnel speed is adjusted due to heating affects when running with active control on the dimensionless frequency, F .

The initial step size outside the boundary-layer varies from 0.1 mm to 0.2 mm depending on the boundary-layer thickness at the streamwise location. As the wire moves through the boundary layer, the step size is continuously reduced where the new step size is computed from

$$\Delta y_{k+1} = \Delta y_k \times u_k(y)/U_e \quad (5.1)$$

When $u(y)/U_\infty < 0.30$, the new step size is halved so that the equation becomes

$$\Delta y_{k+1} = \frac{1}{2}(\Delta y_k \times u_k(y)/U_e) \quad (5.2)$$

In addition, when $u(y)/U_\infty < 0.30$, an estimate of the wire distance from the plate is computed for monitoring purposes. The distance is calculated using the last three acquired points and the best least-squares line is fit through these points. The \hat{y} intercept, or offset, is then subtracted from the current \hat{y} location, which is just some arbitrary traverse-coordinate position that is not referenced from the plate. This resulting value provides the approximate hot-wire distance from the plate. The boundary-layer scan is terminated when the velocity ratio reaches some nominal value which is the minimum $u(y)/U_e$ obtainable without the evidence of radiation heat transfer between the wire and flat plate. After the scan is completed, the best least-

squares line is fit through all points with velocity ratios less than 0.27. The offset from this fit is then subtracted from the arbitrary traverse \hat{y} location to provide the \hat{y} location relative to the flat-plate model. This new \hat{y} location, and all data for each boundary-layer point, are written to a file for post processing.

5.6 Spanwise Constant-Y Scans

To investigate the spanwise uniformity of u' , scans are taken at a constant- \hat{y} distance from the plate. The distance from the plate is typically chosen as the location of the T-S wave maximum. The T-S wave maximum is determined by performing several streamwise scans at different heights in the boundary layer and using the complex polar-plot technique to find the \hat{y} location corresponding to the T-S maximum. The spanwise span covers a distance of 150 mm which is slightly less than the maximum allowable distance that the traverse can move in the \hat{z} direction. This distance is large enough to resolve a typical T-S wavelength, and with 512 points taken along the span, the minimum wavelength resolved is 0.6 mm. To minimize variance in the spatial power spectrum, the data set is multiplexed into four averages and a Fast Fourier Transform is performed on each segment to provide the power-spectral-density estimate. The estimates are then averaged at each frequency to reduce the variance of the power-spectral-density by a factor of four.

To ensure that the hot-wire stays at a constant- \hat{y} distance from the flat-plate model, the traverse drift in the \hat{z} direction is considered. The traverse drift is obtained by taking 30 rough boundary layer scans over the entire spanwise distance of 150 mm to find the corresponding wall location. The wall location obtained from the first boundary-layer scan is used as the reference wall distance for the rest of the scans. The difference between the reference wall distance and the wall location obtained for the rest of the boundary-layer scans is the traverse-drift data. A fourth-order best-fit

curve through the drift data then provides the amount that the traverse drifts from the model, which is then accounted for when performing the spanwise scan.

CHAPTER 6

Results - Part I. The Basic State

Accurately establishing the basic state (Blasius flow) is crucial when conducting boundary-layer receptivity experiments, because a weak adverse or favorable pressure gradient can alter the stability characteristics significantly. Establishing a zero pressure gradient over a flat plate is no trivial task. Saric (1990,1996) discusses the problems associated with accurately measuring small changes in the pressure gradient and concludes that the measurement of the shape factor is more reliable than ΔC_p . Consequently, the alignment of the plate for Blasius flow consists of an iterative procedure between shape-factor measurements and model adjustment. Symmetric flow around the leading edge is also accomplished in order to compare results with theoretical and computational work.

6.1 Special Considerations

Global Pressure Gradient

Near the leading edge, a large pressure gradient exists and a recovery area is generated about the leading edge. After this recovery region, the boundary-layer begins to grow under the influence of a zero pressure gradient if Blasius-flow is established around the model. To account for this finite recovery region, a new reference location called the *virtual leading edge* is established. Errors as large as 20–30% in \hat{x} (10–15%

in R) may result if the virtual leading edge is not considered (Saric 1990). The location of the virtual leading edge is determined from a boundary-layer scan where the following equation is used

$$\hat{x}_v = \hat{x} - \frac{\theta^2 U_\infty \times 10^6}{0.441\nu} \quad (6.1)$$

where \hat{x} is the streamwise location of the boundary-layer scan, ν is the kinematic viscosity, and θ is the momentum thickness. All measurements in this experiment document and use the virtual leading edge as the reference location when appropriate.

Sampling Parameters

Because the basic state plays such an important role in the stability characteristics of a flow, a shape-factor repeatability check and boundary-layer-resolution issues ($\Delta\hat{y}$) should not be ignored. Shape-factor repeatability differences are minimized by sampling for 10 seconds at each point during the boundary-layer traverse. Although this appears unnecessary since DC measurements are taken, small fluctuations in the tunnel do occur and are thus averaged out with a longer sampling time. In addition, because of the simplicity and the complete automation of a typical boundary-layer scan, a detailed measurement of the boundary-layer profile is performed. For all boundary-layer scans, no less than 50 points are taken in the boundary-layer for accurately computing the shape factor.

Shape-Factor Dependence on Speed

An apparent shape-factor dependence with speed became prominent while performing the iteration procedure of obtaining shape factors and re-adjusting the flat plate to obtain Blasius flow. For example, obtaining a Blasius shape factor at all locations for a velocity of 12 m/s and increasing the speed to 18 m/s, produces a decrease in the shape factor (i.e. $H \approx 2.55$). Similarly, decreasing the speed to 8 m/s,

increases the shape factor slightly (i.e. $H \approx 2.62$). This effect is believed to be due to the increase/decrease in overall drag (and hence momentum thickness) with an increase/decrease in tunnel speed. Moreover, a “design” speed of 12 m/s is chosen and shape factors of $H = 2.59 \pm .04$ are considered acceptable around this design speed.

6.2 Establishment of Blasius Flow

Since the flat-plate mounting brackets provide the only means for moving the plate, mean boundary-layer velocity scans are taken near the streamwise locations corresponding to the position of the mounting brackets. Thus, any desired change in the measured shape factor is accomplished by adjusting the mounting-brackets located at approximately the same streamwise location. For each boundary-layer scan, the momentum thickness, θ , and displacement thickness, δ^* , are computed from

$$\theta = \int_0^\delta \frac{u}{U_e} \left(1 - \frac{u}{U_e}\right) dy$$

$$\delta^* = \int_0^\delta \left(1 - \frac{u}{U_e}\right) dy$$

where trapezoidal integration is used. The shape factor, $H = \delta^*/\theta$ is then computed and the plate is adjusted until the Blasius shape factor is obtained at all locations near the mounting brackets.

6.2.1 The Klebanoff Flat Plate

Blasius flow on the Klebanoff flat plate was established during the spring of 1995. Figure 6.1 shows the final placement of the plate inside the test section. A shape factor, $H = 2.59 \pm .04$, is obtained for all streamwise locations for the design speed of 12 m/s. Table 6.1 shows this result.

Velocity [m/s]	\hat{x} [m]	H [$\pm .04$]
12.0	0.5	2.58
12.0	0.75	2.57
12.0	1.20	2.58
12.0	1.50	2.58
12.0	1.80	2.59
8.0	0.50	2.61
8.0	1.80	2.62

Table 6.1: Shape factors at several plate locations.

Figure 6.2 shows a series of boundary-layer profiles at $U_\infty = 12.0$ m/s for different streamwise locations along with the theoretical Blasius solution.

6.2.2 The VPI Flat Plate

Blasius flow on this particular flat plate was accomplished in February 1996. A Blasius shape factor, $H = 2.59 \pm .04$, is obtained for all streamwise locations for a design speed of 12 m/s. Figure 6.3 shows a series of boundary-layer profiles at $U_\infty = 12.0$ m/s for different streamwise locations along with the theoretical Blasius solution. Figure 6.4 shows a series of boundary-layer profiles at $U_\infty = 8.0$ m/s for different streamwise locations along with the theoretical Blasius solution.

6.3 Symmetric Flow

Symmetric flow around the leading edge enables the comparison between computational and experimental results. The trailing-edge flap controls the position of the attachment line on the leading edge (and thus controls leading-edge separation) by balancing the wind-tunnel blockage between each side of the plate.

6.3.1 The Experimental Procedure

One achieves symmetric flow by adjusting the trailing-edge flap angle until the pressure on both sides of the leading edge is identical. Previous attempts (Rasmussen 1993, Wei 1994) to measure the differential pressure was by placing two Preston tubes on the plate at exactly the same streamwise location but on opposite sides of the leading edge. This procedure was first implemented to establish symmetric flow.

The two Preston tubes are first mounted on holders that allow for adjustable height placement and then the tube/holder configuration mounts onto the plate. The tubing from the pressure sensors connects to a 10 torr DataMetrics (now Edwards Vacuum Inc.) Barocel differential pressure sensor and the IOtech A/D board acquires the differential pressure measurement. The Preston tubes are constructed from stainless-steel hypodermic needles with an 0.41 mm inner diameter and a 0.71 mm outer diameter. Near the needle tips, the circular tubing becomes elliptic in shape with a minor axis of 0.15 mm. The minor axis is positioned perpendicular to the plate surface so that the tip mounts as close to the plate surface as possible and is inside the boundary layer. This is crucial, for if the Preston tubes are outside the boundary layer, the differential pressure is the same regardless of the flap setting and the measurement is useless. In addition, placing the probes far enough downstream from the leading edge ($\hat{x} = 0.1$ m) ensures that the boundary layer is thicker than the elliptic pitot-tube orifices. This technique was performed on the Klebanoff plate and figure 6.5 shows that a flap angle of 1.60° produces symmetric flow around the leading edge for all speeds.

Preliminary experiments show that the differential measurement between the two Preston tubes may not be the best method for establishing symmetric flow. The two probes placed in the same streamwise location ($\hat{x} = 0.5$ m) on the same side of the plate and displaced from each other in the spanwise direction (one probe was

positioned at $\hat{z} = 50$ mm and the other probe positioned at $\hat{z} = -50$ mm from the plate centerline) produce different total-pressure measurements. Since the flow is two-dimensional and the probes are located in the same streamwise location, the two total-pressure readings should be approximately identical. In addition, the angle of the Preston tube with respect to the incoming flow is found to significantly affect the readings. It is clear that small geometry differences and the angle-orientation of each tube can significantly affect the measured pressure. To minimize the inherent problems with this technique, a new method is established that uses the Preston-tube devices as calibrated skin-friction sensors.

Preston-Tube Calibration

Preston (1954) first determined the skin friction in a turbulent boundary layer by means of small pitot tubes. Preston showed that the local wall skin friction could be determined if the total pressure and the wall static pressure are measured. The total pressure was measured by a small pitot that touched the surface and the wall static pressure was measured by a static port close to the small pitot tube. He showed that the wall skin friction could be obtained from an empirical equation relating skin friction to the two measured pressures. Patel (1965) later modified the empirical equations for different shear-stress regions for an incompressible, isothermal flow.

Relating the total pressure measured by the Preston tube to the wall-skin friction becomes much easier for a laminar boundary layer. By definition, the shear stress at the wall is given by $\tau^* = \mu \left(\frac{\partial u}{\partial y} \right)_{y=0}$ and the skin-friction coefficient becomes $C_f = 2\tau^*/(\rho U_e)$. The slope of a boundary-layer profile at the wall provides the local shearing stress and simultaneous Preston-tube measurements provide the measured total pressure. Moreover, these two measurements provide a calibration curve expressing the measured Preston-tube pressure in terms of skin friction.

For the calibration, both Preston tubes are placed at the same streamwise location

($\hat{x} = 0.5$ m) but displaced 50 mm from the top and bottom of the plate centerline to eliminate any pressure influences between the two probes. The boundary-layer scans are performed with the hot wires at the same streamwise location as the Preston tubes but centered between the two tubes. The Preston-tube reading for different shear-stress measurements is obtained and plotted to use as a calibration curve for the Preston-tube measurements.

To obtain a complete calibration, the tunnel velocity is varied (and hence the Reynolds number) to thoroughly document the Preston-tube behavior in terms of the skin friction. Figure 6.6 shows the skin-friction coefficient in terms of Reynolds number (accounting for the virtual leading edge) along with the Blasius solution. Figure 6.7 shows the calibration curve relating the Preston-tube pressure to the local wall skin-friction coefficient. The new technique for establishing symmetric flow thus requires trailing-edge flap adjustment until the corresponding shear stress for each tube is identical.

Leading-Edge Static Pressure Ports

During the process of refining the Preston-tube calibration procedure, questions arose concerning the Preston-tube effect on the flow field on the model. Previous research has shown the sensitivity of the boundary-layer to roughness and surface discontinuities, especially near the leading edge. The affect of the probes has never been documented or investigated. The Preston probes, and the associated tubing leading to the pressure transducer, could act to trip the boundary layer and generate a turbulent flow field. To investigate this possibility, a strip of velcro is placed on the test side of the leading edge to ensure that the resulting flow field is turbulent. Preston-tube measurements show that the flap angle for the turbulent flow is approximately the same as the measurements taken without the velcro strip. This suggests two possibilities: (1) the Preston tube on the plate test-side is creating turbulent flow

on the test side of the plate, and thus the flap alignment for symmetrical flow is for a turbulent flow field rather than a laminar flow field or (2) small differences between the two different flow conditions (laminar/turbulent on the test side) cannot be detected by the differential pressure transducer. To completely eliminate the question of whether or not the Preston tube is generating turbulent flow, a non-obtrusive method for measuring the leading-edge static pressure on each side of the plate is employed.

A non-obtrusive differential pressure measurement is devised which requires that a small orifice (small enough to discount any roughness effects) is placed on each side of the leading edge, before the pressure minimum. The orifices are initially drilled into a 67:1 flat-plate test model and experiments are conducted to ensure that the pressure orifices are sensitive to trailing-edge flap adjustments to measure a changing differential pressure between the ports. Figure 6.8 shows the results from the preliminary testing. It is interesting to note that the setting for symmetric flow (and thus the blockage) appears to be the same for all speeds. Because the test-case proved successful, a 0.381 mm hole is drilled into each side of the leading-edge (top and bottom) for each of the two flat-plate models used for this experiment.

6.3.2 The VPI Flat Plate

Differential pressure measurements from the leading-edge static pressure ports provide the means for determining the trailing-edge flap angle for symmetric flow. The static pressure from each port connects to the 10 torr DataMetrics Barocel Pressure Transducer and the trailing-edge flap is adjusted from -1–5°. Differential pressure measurements are taken for both pair of ports located near the top and bottom of the plate. This ensures that the flap and plate is properly aligned vertically in the test section. Figure 6.9 shows the differential pressure as a function of trailing-edge flap position for the static-port pair near the top of plate. Similiarly, figure 6.10 shows

the differential pressure as a function of trailing-edge flap position for the static-port pair near the plate bottom. Both figures show that a flap angle of 0.75° produces symmetric flow about the leading edge. Note also that the flap angle for symmetric flow appears to be independent of tunnel speed.

Results - Part II. Freestream Disturbance State

Disturbance energy from freestream turbulence and acoustic waves comprise two sources of *natural* receptivity (Kerschen 1989). Because these environmental disturbances provide the initial conditions of amplitude and frequency for the growth of instability waves, full documentation of the amplitude and frequency spectrum of these disturbance energies is essential. In Nishioka and Morkovin (1986), the difficulties and flaws of several receptivity experiments are examined. With this caveat, this chapter discusses the documentation of the freestream disturbance state.

7.1 Acoustic-Forcing Measurements

7.1.1 Microphone Location

The PCB piezotronic microphones are flush mounted on the test-section walls to avoid obstructing the flow. Figure 7.1 shows the seven microphone-port locations along the perimeter of test-section entrance. A total of seven microphone locations exist, even though only three were initially purchased. Consequently, some of the documented results show measurements from three microphones. The microphones are installed in a manner that provides simple installation and removal. Moreover, the microphones

can be easily exchanged and moved to other port locations.

Initially, the ports were located in the plane of the leading edge. However, the leading edge was found to scatter the incoming sound wave creating an erroneous picture of the true sound field coming into the test section. This was determined by performing a frequency sweep between 45–115 Hz and taking freestream hot-wire measurements to measure the sound amplitude and relative phase of the incoming sound wave. A moveable wire was initially placed in the leading-edge plane at 660 mm from the test-section floor. A fixed wire, placed in the plane of the leading edge at $\hat{y} = 6.35$ mm and located at the same \hat{z} location as the other wire, was used as the reference wire for relative phase measurements. The cross-spectrum of these two wires provides relative-phase information where 16 averages are taken. The moveable hot wire was then moved upstream of the leading edge and the signal was acquired for the frequency sweep to obtain sound amplitude and relative-phase information. The hot wire was moved to different \hat{y} locations ($\hat{y} = -305$ mm, 32 mm, 356 mm, 533 mm, and 686 mm) to ensure that the sound field showed little change for other \hat{y} locations with upstream relocation of the hot wire. This procedure was performed until the moveable hot wire was placed at a streamwise location that showed little change in the measured sound field relative to its previous streamwise location. The measurements showed little differences in the sound field for distances larger than 75 mm upstream of the leading edge. Consequently, the final location of the microphones is 298 mm upstream of the leading edge. This location is far enough from the plate to reduce the problem of leading-edge scattering and far enough into the test section to provide a good measure of the incoming sound wave into the test section. Figure 7.2 shows relative-phase measurements for the frequency sweep and table 7.1 shows the respective microphone locations for the frequency sweep. Here, microphone 0 is the reference sensor, \hat{y} is referenced from the test-side wall, \hat{x} is referenced from the plate, and \hat{z} is referenced

from the test-section floor. Note that the relative-phase measurements change with frequency. This is addressed in more detail in section 7.1.2.

Microphone	\hat{x} [mm]	\hat{y} [mm]	\hat{z} [mm]
0	-298	1137	0.0
1	-298	540	0.0
2	-298	273	0.0
3	-298	273	1.4

Table 7.1: Microphone locations for the frequency sweep shown in figure 7.2.

Measurements in a Turbulent Boundary-Layer

During preliminary measurements, there was some concern about the turbulent boundary layer that exists on the test-section walls and how this might affect the microphone readings. Because the microphones are mounted flush on the test-section walls, they are exposed to this turbulent wall boundary-layer environment. This possible problem is acknowledged but no solution was found since the microphones need to be mounted non-obtrusively in order to prevent affecting the flow downstream on the plate. In order to ensure that the forced sound field is detected by the microphones and overpowers any turbulent boundary-layer affects, the sound pressure level (SPL) was increased to 105–110 dB. A range is specified because the SPL varies slightly for the range of frequencies (45–115 Hz) where the sound-field phase information is desired.

Microphone Sensitivity Check

Another problem considered is the possibility of external flow disturbances affecting the sound-field measurements. The wind tunnel vents to the atmosphere in the plenum which allows any external flow disturbances produced or brought inside the wind-tunnel building to affect the disturbance environment inside the test section (and affect sound relative-phase measurements). One solution is to keep all doors to the wind-tunnel area closed so that no gusts or changing pressure fields outside the

tunnel can affect the flow inside the test section. To determine if this precaution is necessary, relative-phase and amplitude measurements are taken with and without the doors closed to the wind-tunnel area and the measurements are compared. All measurements are taken with sound frequencies ranging 85-90 Hz with ≈ 108 dB SPL ($V_{sp} = 0.5 V_{rms}$) in the test-section. A cross-spectrum with 64 averages is used to compute the relative-phase measurements. Two runs are taken for each condition to determine the repeatability between runs at the same condition. Sound measurements are taken with two hot-wires and three microphones located on the test-section floor. Measurements are first taken with the doors from the control-room and the doors separating the insulated fan-housing space *closed* to the tunnel area. As shown in table 7.2, the repeatability of the relative phase between runs at the same condition is ± 2 degrees.

f [Hz]	Doors Closed					Doors Closed				
	Hw 0	Hw 1	Mc 0	Mc 1	Mc 2	Hw 0	Hw 1	Mc 0	Mc 1	Mc 2
85	0	-11	0	-2	-13	0	-10	0	-2	-13
86	0	3	0	-1	-6	0	4	0	0	-6
87	0	12	0	0	-2	0	12	0	0	-3
88	0	20	0	-1	-3	0	21	0	-2	-4
89	0	21	0	-2	-10	0	22	0	-2	-10
90	0	18	0	0	-15	0	18	0	0	-16

Table 7.2: Microphone measurements with doors to the wind-tunnel area closed. All measurements in degrees. A positive phase signifies that the sensor signal is leading the reference sensor.

Next, measurements are taken with the doors from the control-room and the doors separating the insulated fan-housing space *open* to the tunnel area. As shown in table 7.3, the relative phase readings encompass the previously obtained measurements with the doors closed when the repeatability error of ± 2 degrees is considered and no noticeable change in the sound amplitudes is detected.

f [Hz]	Doors Open					Doors Open				
	Hw 0	Hw 1	Mc 0	Mc 1	Mc 2	Hw 0	Hw 1	Mc 0	Mc 1	Mc 2
85	0	-8	0	-2	-14	0	-10	0	-2	-15
86	0	4	0	-1	-7	0	3	0	-1	-6
87	0	11	0	0	-3	0	12	0	0	-3
88	0	21	0	-2	-4	0	21	0	-2	-4
89	0	23	0	-3	-11	0	23	0	-3	-10
90	0	19	0	0	-15	0	19	0	0	-16

Table 7.3: Microphone measurements with doors to the wind-tunnel area open. All measurements in degrees. A positive phase signifies that the sensor leads the reference sensor.

As an added check, the doors are kept in their *open* position and the big door (which provides access to the loading ramp) is opened and sound measurements are taken. As shown in table 7.4, the relative phase readings encompass the previously obtained measurements when the repeatability error of ± 2 degrees is considered.

f [Hz]	Loading Door Open					Loading Door Open				
	Hw 0	Hw 1	Mc 0	Mc 1	Mc 2	Hw 0	Hw 1	Mc 0	Mc 1	Mc 2
85	0	-9	0	-2	-13	0	-8	0	-2	-13
86	0	3	0	-1	-5	0	2	0	-1	-7
87	0	10	0	1	-1	0	11	0	0	-4
88	0	21	0	-1	-2	0	21	0	-2	-5
89	0	23	0	-2	-9	0	23	0	-2	-11
90	0	20	0	0	-15	0	20	0	0	-16

Table 7.4: Microphone measurements with the loading-dock door open. All measurements in degrees. A positive phase signifies that the sensor leads the reference sensor.

Moreover, changes in the sound measurements do not change significantly between the three different conditions. This certainly does not suggest that external pressure changes are not slightly affecting the environment inside the test section. Rather, the measurements show that any changes are within the repeatability error. Therefore,

as a precautionary measure, the following sound-field measurements are conducted with all doors that access the wind-tunnel area closed.

7.1.2 Microphone Phase Measurements

Information about the sound inclination angle as a function of frequency is obtained by performing a 45–115 Hz frequency sweep (with a 40–120 Hz band pass) and acquiring the microphone response. Three microphones are placed on the test-section floor at the locations corresponding to the first three entries in table 7.1. The freestream velocity is set to $U_\infty = 8.0$ m/s and the speaker voltage is set to $V_{sp} = 0.5$ volts (rms) for the entire frequency sweep providing sound pressure levels ranging 105–110 dB. The microphone signals are acquired at 1 kHz for 8.192 seconds and the relative-phase measurements are computed using a cross-spectrum program with 8 averages. Figures 7.3–7.9 show the relative phase measurements from the frequency sweep. The reference microphone is located at $\hat{x}_o = -298$ mm, $\hat{y}_o = 540$ mm (recall that $\hat{y}_o = 0$ corresponds to the test-side wall), and $\hat{z}_o = 0$ mm. As apparent from the figures, the relative phase of the incoming sound wave depends on the sound frequency. The measurements were re-verified for a discrete-frequency set where the sampling time is increased to 16.384 seconds but approximately the same relative-phase readings are obtained. It appears as if the microphone positioned closest to the leading edge is detecting some upstream influence of the leading edge which affects the incoming-sound wave phase.

7.2 Freestream Disturbance Measurements

7.2.1 Transition Reynolds Number

In order to perform sensitive receptivity experiments, the freestream disturbance levels should be extremely low. One good indication of the flow quality in a wind

tunnel is the determination of the transition Reynolds number, Re_{tr} . The transition Reynolds number is determined by placing a calibrated wire approximately 1 mm above the plate's surface and one calibrated wire in the freestream. The wires are placed at an approximate \hat{x} -location of 2 meters from the leading edge. The wire location is variable but should be placed far back enough on the plate so that at some speed transition occurs there. The tunnel speed (and thus Re_x) is incremented and the velocity ratio u/U_∞ is plotted as a function of Re_x . The ratio increases slightly with increasing Re_x and a dramatic increase is observed at the onset of transition. Since transition occurs over a range of Re_x , the Re_{tr} corresponds to the intersection of the two lines with different slopes when the velocity ratio is plotted as a function of Re_x .

The transition-Reynolds-number measurement was performed during the initial stage of this experiment on the Klebanoff flat plate. As shown in figure 7.10, the transition Reynolds number is 2.6×10^6 . This value is quite high and is in good agreement with the Re_{tr} documented by Rasmussen (1993) in her experiments. However, this transition Reynolds number is significantly lower than $Re_{tr} = 3.5 \times 10^6$ which is the value obtained on the same plate (different leading edge) during the initial calibration of the tunnel (Mousseux 1988). It is clear that something is different between the two experiments, and either two things are possible: (1) The tunnel's freestream disturbances levels are much higher which affects transition and/or (2) there is some inherent difference between the two models (leading edge) that is creating the large difference in Re_{tr} .

During the final stage of this experiment, the second possibility was further investigated. Blasius flow was established on the VPI flat plate and the transition Reynolds number was determined. As shown in figure 7.11, $Re_{tr} = 1.9 \times 10^6$. This is considerably lower than the value quoted by Mousseux. Moreover, the next logical

step is to perform freestream disturbance measurements to compare the disturbance levels with those obtained during the initial calibration of the tunnel.

7.2.2 Freestream-Turbulence Amplitude and Spectra

Freestream disturbance measurements must include amplitude and spectrum information for a quoted band pass. Freestream disturbance amplitude measurements are often stated without the band pass and as such, render the measurements meaningless. These measurements yield no information about the frequency range where the largest contribution of the disturbance energy originates. In addition, the measurements are often performed with a 2 Hz high pass and for most low-speed tunnels, there is often a large energy contribution in frequencies less than 2 Hz. Therefore, it is important to use a high pass of least 0.1 Hz to obtain an accurate measurement of a tunnel's freestream disturbance levels. Refer to Mousseux (1988) for a more detailed discussion.

Freestream disturbance measurements are conducted for the following three band-pass ranges: (1) 0.1–1000 Hz (2) 2–1000 Hz and (3) 35–1000 Hz. These ranges are chosen to provide information about the amount of disturbance energy present in the low, mid, and T-S amplified frequencies. In addition, the first two band-pass ranges are chosen for comparison with the freestream disturbance levels quoted by Mousseux. Table 7.5 shows the freestream disturbance levels documented by Mousseux for two different band-pass ranges. These measurements are performed with the mixing region vented.

Freestream Changes with Speed

Because the freestream environment changes with tunnel velocity, freestream levels are documented for speeds ranging from 5–25 m/s. All data is obtained from 2-minute samples and the spectra are averaged 128 times and 64-times smoothed. Initial measurements are conducted with the tunnel configuration the same as during

U_∞ [m/s]	Band Pass 0.1–1000 Hz	Band Pass 2.0–1000 Hz
	u'/U_∞ [%]	u'/U_∞ [%]
5.0	0.069	0.018
10.0	0.088	0.030
15.0	0.085	0.038
20.0	0.091	•
25.0	0.092	0.067

Table 7.5: Freestream disturbance measurements with the mixing region vented conducted by Mousseux (1988).

the current experiment i.e., with the plenum vented. Table 7.6 shows the freestream disturbance levels as a function of speed for two different band passes. These measurements are performed with the same filters (Tektronix AM502 Differential Amplifier) used in Mousseux's experiments for amplifying and band passing the anemometer signals. Measurements included documenting u'/U_∞ and $u'_{\text{pk-pk}}/U_\infty$ [%] levels since these measurements succinctly describe the u' fluctuations.

As apparent from table 7.6, the u' fluctuations are significantly higher than those quoted in table 7.5. Note also that the 2–1000 Hz band-passed data are approximately half the 0.1–1000 Hz band-passed data. This again demonstrates the importance of stating the band pass in conjunction with the freestream disturbance levels. Figures 7.12–7.20 show the power-spectral density of the u' component for tunnel velocities of 5, 8, 10, 12, 15, 18, 20, 21, and 25 m/s using the Tektronix filters and a 0.1–1000 Hz band pass. For all measurements, the spectra are presented for these speeds so that a detailed investigation of disturbance changes with speed can be observed. Figures 7.21–7.29 show the power-spectral density of the u' component for the same speeds and filter but with a 2–1000 Hz band pass. Of interest, is the large contribution of disturbance energy in the low frequencies. In addition, the maximum normalized peak-to-peak velocity changes, $u'_{\text{pk-pk}}/U_\infty$, during the two-minute sampling interval are as much as 1.7%. One possible reason for the higher u' fluctu-

ations is that during the initial tunnel calibration, the tunnel's zero-pressure venting region was located in the mixing region *not* in the plenum region. At that time, it was conjectured that venting in the mixing region causes the area downstream of the test section to dampen out low-frequency disturbances. Consequently, venting in the mixing region reduces the low-frequency u' -disturbance contributions and the overall freestream disturbance level.

These measurements are also performed with the Stewart filters. Table 7.7 shows the freestream disturbance levels with the plenum region vented for two different band-pass settings. This measurement is conducted to investigate the different filter characteristics of the Tektronix and Stewart filters. For the band-passed 2–1000 Hz case, the Stewart-filtered measurements show an overall lower disturbance amplitude. The power spectra provides some explanation for this behavior. Figures 7.30–7.38 show the power-spectral density of the u' component using the Stewart filters with a 2–1000 Hz band pass. From the spectra, it is apparent that the high-pass characteristics are different between the two filters. The Tektronix filter captures more of the disturbance energy for frequencies less than 2 Hz which contributes to the higher u'_{rms} values. There appears to be a “roll-off” associated with the Tektronix filter at 2 Hz rather than a steep “cut-off” at 2 Hz which the Stewart filter provides. Figures 7.39–7.47 show the power-spectral density of the u' component for the same speeds and filter but with a 35–1000 Hz band pass. The 35–1000 Hz band-passed signals are significantly lower than the 2–1000 Hz band-passed signals which is useful information because this is the range where the T-S waves are most amplified.

During the first sound-receptivity experiments conducted at the Unsteady Wind Tunnel , the zero-pressure venting region was moved to the plenum where the speakers are located so that the speakers function at atmospheric pressure. At the time, freestream disturbance levels did not appear to increase significantly. However, the

current experiments show a significant increase in the u' levels that may be due to venting location. To verify this, the zero-pressure region was moved to the mixing region and freestream disturbance levels were again documented. Table 7.8 shows the freestream disturbance levels using the Tektronix filters for two different band passes.

Figures 7.48–7.56 show the power-spectral density of the u' component for various tunnel speeds using the Tektronix filters with a 0.1–1000 Hz band pass. Figures 7.57–7.65 show the power-spectral density of the u' component for the same speeds and filter but with a 2–1000 Hz band pass. Although still higher than the freestream disturbance levels quoted in table 7.5, the values are smaller than those quoted in table 7.6 when the plenum is vented. Moreover, although venting in the plenum causes the speaker system to work more efficiently, venting in the mixing region may be necessary to reduce the low-frequency disturbance levels.

The measurements are also performed with the Stewart filters with the mixing region vented. Table 7.9 shows the freestream disturbance levels for two different band-pass settings. Figures 7.66–7.74 show the power-spectral density of the u' component for various velocities using the Stewart filters with a 35–1000 Hz band pass. Figures 7.75–7.83 show the power-spectral density of the u' component for the same speeds and filter but with a 2–1000 Hz band pass. These measurements also show that the disturbance levels are lower when the mixing region is vented.

The freestream disturbance measurements indicate several important features. First, for all speeds, the disturbance levels are higher when venting in the plenum versus venting in the mixing region. This indicates that future receptivity experiments should be conducted with the mixing region vented. Secondly, for a 2–1000 Hz band pass, the Stewart-filtered data show smaller u'_{rms} levels than the Tektronix-filtered data. The power-spectrum indicate that the Tektronix filter does not have a sharp cut-off at the 2 Hz high pass and the values are higher due to the energy contribution

at frequencies less than 2 hz. Because the power-spectrum data obtained using the Stewart filters show a distinct 2 Hz high-pass cut off, these Stewart-filtered measurements are a better estimate of the disturbance levels for a 2-1000 Hz band pass. In addition, the measurements show that a significant amount of disturbance energy occurs at frequencies less than 2 Hz because the disturbance levels are significantly higher (more than double) for a 0.1-1000 Hz band pass than for a 2-1000 Hz band pass. Finally, for the 35-1000 Hz band-passed data, the disturbance levels are the lowest indicating that little external disturbance energy exists in the T-S amplified range.

U_∞ [m/s]	Band Pass 0.1–1000 Hz		Band Pass 2.0–1000 Hz	
	u'/U_∞ [%]	$u'_{\text{pk-pk}}/U_\infty$ [%]	u'/U_∞ [%]	$u'_{\text{pk-pk}}/U_\infty$ [%]
5.0	0.147	1.081	0.045	0.439
6.0	0.162	1.184	0.044	0.411
7.0	0.160	1.241	0.051	0.472
8.0	0.164	1.248	0.051	0.483
9.0	0.185	1.364	0.050	0.428
10.0	0.204	1.385	0.052	0.449
11.0	0.206	1.239	0.051	0.470
12.0	0.210	1.491	0.054	0.462
13.0	0.209	1.523	0.059	0.514
14.0	0.204	1.458	0.062	0.522
15.0	0.218	1.476	0.067	0.594
16.0	0.204	1.359	0.068	0.639
17.0	0.213	1.550	0.074	0.593
18.0	0.206	1.403	0.078	0.683
19.0	0.210	1.412	0.081	0.663
20.0	0.223	1.591	0.086	0.729
21.0	0.227	1.653	0.091	0.758
22.0	0.231	1.712	0.096	0.778
23.0	0.230	1.724	0.099	0.823
24.0	0.238	1.608	0.105	0.827
25.0	0.227	1.697	0.109	0.922

Table 7.6: Freestream disturbance measurements with the plenum vented (Tektronix filters).

U_∞ [m/s]	Band Pass 2–1000 Hz		Band Pass 35–1000 Hz	
	u'/U_∞ [%]	$u'_{\text{pk-pk}}/U_\infty$ [%]	u'/U_∞ [%]	$u'_{\text{pk-pk}}/U_\infty$ [%]
5.0	0.025	0.208	0.010	0.072
6.0	0.028	0.226	0.010	0.074
7.0	0.034	0.268	0.010	0.080
8.0	0.038	0.287	0.010	0.079
9.0	0.038	0.307	0.010	0.086
10.0	0.038	0.289	0.010	0.089
11.0	0.041	0.355	0.011	0.099
12.0	0.041	0.329	0.012	0.106
13.0	0.045	0.343	0.013	0.131
14.0	0.048	0.369	0.015	0.132
15.0	0.051	0.438	0.015	0.133
16.0	0.055	0.473	0.016	0.149
17.0	0.058	0.490	0.018	0.172
18.0	0.065	0.534	0.020	0.173
19.0	0.067	0.578	0.021	0.192
20.0	0.071	0.536	0.023	0.202
21.0	0.076	0.625	0.025	0.224
22.0	0.081	0.655	0.027	0.257
23.0	0.085	0.697	0.028	0.250
24.0	0.093	0.771	0.031	0.277
25.0	0.096	0.778	0.031	0.264

Table 7.7: Freestream disturbance measurements with the plenum vented (Stewart filters).

U_∞ [m/s]	Band Pass 0.1–1000 Hz		Band Pass 2.0–1000 Hz	
	u'/U_∞ [%]	$u'_{\text{pk-pk}}/U_\infty$ [%]	u'/U_∞ [%]	$u'_{\text{pk-pk}}/U_\infty$ [%]
5.0	0.090	0.700	0.033	0.367
6.0	0.094	0.660	0.038	0.362
7.0	0.103	0.803	0.041	0.428
8.0	0.105	0.911	0.044	0.391
9.0	0.103	0.748	0.042	0.380
10.0	0.098	0.713	0.038	0.351
11.0	0.101	0.751	0.037	0.332
12.0	0.097	0.702	0.036	0.308
13.0	0.127	0.925	0.038	0.333
14.0	0.121	0.895	0.037	0.335
15.0	0.121	0.856	0.039	0.323
16.0	0.119	0.869	0.038	0.342
17.0	0.118	0.841	0.040	0.341
18.0	0.122	0.846	0.043	0.404
19.0	0.129	0.924	0.044	0.357
20.0	0.126	0.865	0.047	0.387
21.0	0.128	1.080	0.047	0.388
22.0	0.151	1.171	0.050	0.441
23.0	0.141	1.133	0.053	0.545
24.0	0.142	1.035	0.056	0.469
25.0	0.143	1.051	0.058	0.499

Table 7.8: Freestream disturbance measurements with the mixing region vented (Tektronix filters).

U_∞ [m/s]	Band Pass 2–1000 Hz		Band Pass 35–1000 Hz	
	u'/U_∞ [%]	$u'_{\text{pk-pk}}/U_\infty$ [%]	u'/U_∞ [%]	$u'_{\text{pk-pk}}/U_\infty$ [%]
5.0	0.020	0.168	0.012	0.154
6.0	0.021	0.176	0.011	0.119
7.0	0.028	0.219	0.010	0.110
8.0	0.032	0.253	0.009	0.143
9.0	0.030	0.250	0.009	0.097
10.0	0.025	0.219	0.009	0.084
11.0	0.022	0.190	0.010	0.114
12.0	0.023	0.208	0.010	0.097
13.0	0.024	0.201	0.010	0.101
14.0	0.024	0.218	0.011	0.104
15.0	0.025	0.204	0.012	0.107
16.0	0.025	0.229	0.013	0.121
17.0	0.027	0.225	0.014	0.121
18.0	0.029	0.251	0.015	0.132
19.0	0.032	0.294	0.016	0.146
20.0	0.045	0.313	0.018	0.152
21.0	0.036	0.313	0.020	0.162
22.0	0.038	0.330	0.021	0.208
23.0	0.041	0.373	0.023	0.210
24.0	0.044	0.376	0.023	0.206
25.0	0.047	0.400	0.025	0.206

Table 7.9: Freestream disturbance measurements with the mixing region vented (Stewart filters).

CHAPTER 8

Results-Part III. T-S Wave Measurements

8.1 Signal-Separation Techniques

Accurately measuring the T-S wave in the boundary layer is a difficult task. Before the work of Kendall (1990), Wlezien (1989), and Wlezien et al. (1990), acoustic receptivity experiments lacked accurate measurements of the T-S wave amplitude. This is primarily for two reasons. First, the T-S wave amplitude near Branch I is extremely small, $O(10^{-6})$, and therefore it is difficult to isolate and measure. Second, for sound receptivity experiments, the measured disturbance signal consists of not only the T-S wave but also contains any sound-induced probe-support vibrations and an induced Stokes wave due to the oscillating pressure field. The disturbance signal that is not the T-S wave, is often referred to as *background noise*.

8.1.1 The Complex-Plane Method

A method proposed by Wlezien (1989) and (Wlezien et al. 1990) uses polar plots to separate the long-wavelength acoustic component from the short-wavelength T-S signal. The polar plot is made by acquiring the magnitude and phase of the boundary-layer disturbance signal in the streamwise direction so that a distance that corresponds to one T-S wavelength of interest is covered. The streamwise scan is performed at a constant height in the boundary layer and at a constant spanwise location. Over

this distance, the phase of the acoustic signal varies only slightly ($\approx 5^\circ$) while the phase of the T-S wave varies approximately 360° . When the boundary-layer disturbance signal from the streamwise scan is plotted in the complex plane, the polar plot resembles a spiral. The plot is a spiral instead of a circle because the T-S wave grows or decays slightly in amplitude over the streamwise distance. For obtaining the background and T-S amplitudes, however, the spiral is approximated by the best least-squared-fit circle. The background signal (which consists of acoustic and sting-vibration fluctuations) is the vector from the origin to the circle center. The radius of the circle then provides the amplitude of the T-S wave.

To aid in detecting the T-S wave, the measurements are taken near Branch II to take advantage of the exponential growth of the T-S wave predicted by linear stability theory. This procedure is performed at several \hat{y} locations in the boundary layer to provide a complete T-S amplitude profile. The resulting profile compares considerably well with O-S theory.

8.1.2 Dual Microphones as Spatial Filters

If the pressure perturbation of the T-S wave can be isolated and measured, the u'_{rms} of the T-S wave is easily obtained using linear theory. In principle, this idea is much more appealing than using hot-wire anemometry. There is no need to perform detailed boundary-layer scans to find the peak of the eigenfunction to capture the maximum T-S amplitude. Instead, the maximum u'_{rms} is directly computed from the p'_{TS} measurement and the Orr-Sommerfeld equation. In addition, if the microphone apparatus is mounted non-obtrusively, no wake is produced so that disturbances can be tracked in the streamwise direction by other flush-mounted microphones placed downstream.

No technique is ever perfect, however, and isolating the T-S pressure perturbation is no easy task. When examining acoustically-forced T-S waves, the pressure perturbation acquired by a microphone consists of the acoustic fluctuation and the

T-S wave. The acoustic pressure fluctuation, however, is two orders of magnitude greater than the T-S pressure perturbation because p'_{AC} is proportional to the speed of sound (≈ 350 m/s) and p'_{TS} is proportional to the freestream speed. Consequently, isolating the small T-S pressure component from the large total pressure signal is not a trivial matter. However, since λ_{TS} is much smaller than λ_{AC} , the signals from two microphones displaced one-half the T-S wavelength of interest apart (where $\lambda_{TS} \ll \lambda_{AC}$) could simply be subtracted to obtain p'_{TS} , since the acoustic amplitude is approximately a constant over the small distance.

Cohn (1992) first attempted to acquire the T-S pressure perturbation using dual microphones as a spatial filter. The streamwise spacing of the microphones was chosen to be 15 mm, which corresponds to one-half the wavelength of the most-amplified T-S wave such that $\lambda_{TS} \ll \lambda_{AC}$. With this configuration, the signals from the two microphones are electronically subtracted to obtain p'_{TS} directly, since the acoustic amplitude is approximately a constant over the small distance. The signals acquired by the microphones are sent to a control-loop circuit in which each signal is amplified and band-pass filtered. A difference amplifier (TL071 Op Amp) subtracts the two signals to isolate the T-S perturbation. Cohn documents some problems encountered while conducting his experiment. For example, the response of the individual microphones to an identical pressure fluctuation is significantly different. Attempts to “tune” the microphones by varying the amplification of each microphone so that the response of the microphones is identical lead to several other problems. In addition, the apparent temporal extension of the T-S wavepacket and the spatial filtering which amplified some frequency components more than others, provides some limitations to the dual-microphone technique. The most prominent problem *not* discussed anywhere in his report is that the technique is inherently corrupt. The total pressure signal (acoustic disturbance and T-S wave) are acquired by both microphones and therefore

the electronically-differenced signal is still contaminated by the large acoustic component. This important, yet unmentioned, problem was discovered while attempting to apply the dual-microphone technique to this experiment.

8.1.3 The Kendall Gauge

Kendall (1991) was the first to successfully invent a differential microphone gauge that accurately measures T-S perturbations produced by freestream turbulence. Figure 8.1 shows a front view of the differential pressure sensor. The gauge consists of an electret microphone configured as a differential pressure sensor which affixes to the back of a model. The sensor has two ports displaced approximately one-half the T-S wavelength of interest. Thus, the acoustic waves and other pressure disturbances of longer wavelength at equal frequency are rejected while the sensitivity to the T-S waves is doubled. The gauge attaches to the back of the model so that the two gauge ports are placed over the two similarly spaced pressure ports on the model. Thus, the two pressures from each port on the model are channeled to the two ports on the gauge, and the resulting gauge signal is the true pressure difference between the two pressure orifices. The differenced pressure signal is converted to a voltage signal which is then acquired.

Measurements with Sound

The Kendall gauge was affixed to the current model to obtain T-S amplitude measurements near Branch II. The measurements are taken near Branch II because T-S pressure ports (refer to section 3.1) exist in this region to take advantage of the amplified T-S wave. The T-S waves are generated by sending single frequency sound into the test-section. Sound pressure levels ranging from 88 dB to 120 dB are created to examine both low and high amplitude acoustic forcing. The measurements, however, did not provide accurate measurements of the T-S wave pressure disturbance. Even for the low amplitude sound (88 dB), the large acoustic pressure field in the test

section contaminated the gauge measurement. Figure 8.2 shows the hot-wire signal and the Kendall-gauge signal for increasing sound amplitude. It is clear that the Kendall gauge is still sensing some of the acoustic signal also measured by the hot wire. Consequently, the differenced pressure signal from the gauge (which should consist of only the small-amplitude T-S pressure signal) is contaminated by some of the acoustic pressure signal. A personal exchange with Kendall verified that the sensor is successful when extracting T-S waves generated by freestream turbulence (because $p'_{\text{TURB}} \approx p'_{\text{TS}}$) but contamination becomes a problem (even for high common-mode rejection ratios) when the disturbance pressure field is large in magnitude compared to the T-S amplitude. Since $p'_{\text{AC}} \approx 100 p'_{\text{TS}}$, a Kendall gauge with a common-mode ratio of 100:1 still contains $O(1)$ errors.

8.1.4 The Multiple-Microphone Technique

Another technique examined was the use of N pressure sensors affixed on the plate spaced some distance apart and the associated N equations that describe the wall pressure, $p'(x, t)$ at each sensor location. Since the problem yields three equations and three unknowns, a unique solution should exist. A feasibility investigation is performed numerically with three microphones.

It is known that when T-S waves are generated using acoustic forcing, the resulting flow field consists of three superposed waves: one downstream travelling sound wave, one upstream-travelling sound wave reflected from the diffuser, and a downstream-travelling Tollmien-Schlichting wave. Thus, the wall pressure takes the form:

$$p'(x, t) = a_1 \exp^{i(k_1 x_j - \omega t)} + a_2 \exp^{i(k_2 x_j + \omega t)} + a_{\text{TS}} \exp^{\int_1^j \sigma dx} \exp^{i(k_{\text{TS}} x_j - \omega t)} + c.c. \quad (8.1)$$

where $j = 1, 2, 3$.

The location of the microphone ports are chosen so that the distance between the first and second port is the half-wavelength of the T-S wave of interest. The position of the third port is detuned away from the first and second port, so that $p'(x_3, t)$ is much different from $p'(x_1, t)$ and three independent equations exist. Thus, the sensor locations are initially chosen as follows:

$$x_2 = x_1 + \frac{\lambda_{\text{TS}}}{2}; \quad x_3 = x_2 + \frac{2}{3}\lambda_{\text{TS}} \quad (8.2)$$

Eliminating time and assuming that the local T-S growth rate is essentially constant yields

$$p'(x, t) = a_1 \exp^{i(k_1 x_j)} + a_2 \exp^{i(k_2 x_j)} + a_{\text{TS}} \exp^{i(k_{\text{TS}} x_j)} + c.c. \quad (8.3)$$

For three microphone locations, there are three complex equations and three complex unknowns. This yields a unique solution for the system of equations.

The solution can be further simplified by assuming the complex amplitude of the three waves takes the form $a_j = A_j \exp^{i\beta_j}$ for $j = 1, 2$, and TS. Where

$$A_j = \text{wave amplitude (real)} \quad \text{and} \quad \beta_j = \text{wave phase (real)}$$

and substitution gives

$$p'(x, t) = A_1 \exp^{i(k_1 x_j + \beta_1)} + A_2 \exp^{i(k_2 x_j + \beta_2)} + A_{\text{TS}} \exp^{i(k_{\text{TS}} x_j + \beta_{\text{TS}})} + c.c. \quad (8.4)$$

Choosing typical values $A_1 \approx 100$, $A_2 \approx 10$, and $A_{\text{TS}} \approx 1$, and solving the system of equations (8.4) shows that detuning p' from an exact measurement by as little as 1%, yields large errors in A_{TS} . This is because the matrix system is stiff and thus any

small errors in the pressure value lead to large errors in the amplitudes. Consequently, this numerical analysis, conducted before actual experiment implementation, shows that this method does not work for isolating the T-S wave amplitude.

8.1.5 The Sound-Burst Technique

A new technique was successfully developed and appears promising in measuring the amplitude of the T-S wave. The technique is simple and effective and lends itself to understanding the behavior of the T-S wave. From linear theory, the maximum of the T-S wave propagates at approximately one-third the freestream velocity. Therefore, a T-S wave generated by an acoustic wave has a slower propagation speed than the acoustic disturbance. Using this fact, the travelling T-S wave is isolated from the acoustic disturbance and associated Stokes wave by sending bursts of sound into the test section. The initial sound burst is first measured and fractions of a second later after the sound wave and associated Stokes wave has passed, the slower-travelling T-S wave (initiated by the sound burst) is measured. The following experimental procedure is developed during the preliminary testing of this technique.

Bursts of single-frequency sound are digitally generated and broadcasted into the test section. The time interval between bursts is chosen so that the acoustically-forced T-S wave has passed the hot wires before another sound burst is emitted. The hot wires are placed near Branch II to take advantage of the amplified T-S wave in this region. The boundary-layer wire is placed at $u/U_\infty = 0.3$ (approximate location of the maximum) and the other wire is placed in the freestream at the same streamwise and spanwise location. To measure only the sound signal and the acoustically-forced T-S wave, both wires are narrow-band passed (± 3 Hz) around the forcing frequency. Figure 8.3 shows a time trace depicting the sound-burst wave sensed by both wires and the trailing T-S wave sensed only by the boundary-layer wire for $R = 1140$, $F = 56$, $f = 80$ Hz, and $\hat{x} = 1.8$ m.

This procedure is successful when trying to isolate the sound wave and associated Stokes wave from the forced T-S wave and should be especially useful for broad-band sound (noise) and large-amplitude signals. To examine this technique for use with broad-band sound, bursts of digitally-filtered noise (refer to section 5.2.2) with a 65–110 Hz band pass are broadcasted into the test-section. Because time traces are essentially acquired on both channels, the amount of data acquired for one burst is significant. Consequently, only data required for four ensemble averages are acquired and stored. Figure 8.4 shows the T-S wave and Stokes wave amplitude with increasing noise amplitude. There is much scatter in the data and more ensemble averages should be taken for complete certainty on the T-S wave behavior.

Sound-Burst Problems

Moreover, the sound-burst technique is developed and successfully implemented but requires further testing. During the initial testing of the technique, several problems were encountered that warrant some discussion.

One encountered problem is the inherent “ringing” present in the sound burst signal acquired by both wires. The sound burst consists of three complete sine waves of the desired frequency yet more than three waves are detected by the hot wires. Figure 8.3 shows this “ringing” behavior. One possibility is that since the speakers are composed of a diaphragm membrane, the diaphragm experiences some residual vibrations after broadcasting the three-wave sound burst. This residual vibration creates a small pressure fluctuation in the test section which is sensed by the hot wires. To dampen out any residual vibrations, a 1 kHz continuous waveform is broadcasted by the speakers between the sound bursts. The apparent “ringing” in the acquired signal is still present. Two other frequencies (2 kHz and 500 kHz) are placed in the interim yet the residual sound waves are still present on hot-wire time traces. Another possible reason for the residual sound wave is a reflection of the sound burst from the

diffuser which is sensed by the hot-wires.

As discussed earlier, an ensemble average of the T-S wave packets should be taken to account for any low-frequency oscillations in the test section and to minimize error. Consequently, the data acquired for an ensemble-averaged T-S wave amplitude is quite large. A means for minimizing data space and simplifying the signal processing should be implemented. One possible procedure is to set up a special acquisition process where the A/D board monitors the sound bursts measured on the freestream wire. When the freestream wire senses the sound burst, the A/D board is triggered to start sampling the boundary-layer wire after a specified time delay to ensure that the sound burst has passed. Moreover, the sound burst and the accompanying Stokes wave are not acquired on the boundary-layer wire, and only the T-S wave is obtained and processed.

One disadvantage of this technique is that if the maximum T-S wave amplitude is desired, a series of boundary-layer profiles still need to be taken to find the location of the maximum. Linear theory provides an estimate of the location of the maximum but the exact location should be found experimentally.

8.2 Receptivity Coefficients

One experimental goal for this work is to examine the receptivity problem on the VPI flat plate. This includes the comparison of Tollmien-Schlichting wave amplitudes in terms of receptivity coefficients with measurements obtained on the Klebanoff plate (Rasmussen 1993 and Wei 1994). As discussed in chapter 3, the VPI plate has a higher leading-edge aspect ratio which should decrease leading-edge receptivity to sound and yet it does have several mechanisms (flat-plate/leading-edge juncture and surface roughness) which should enhance receptivity. To allow for direct comparison with receptivity coefficients obtained by Rasmussen (1993) and Wei (1994) the same signal-

separation method is used. Thus, the complex-polar plot technique is implemented for separating the T-S wave from the associated Stokes wave and sting vibration.

8.2.1 Complex Polar Plots

As discussed earlier, a typical boundary-layer scan provides only limited information of an acoustically-forced T-S profile due to contamination of the associated Stokes wave and induced sting vibrations. Figure 8.5 shows a typical profile obtained from performing a boundary-layer scan. Therefore, the first step when obtaining receptivity coefficients is to isolate the T-S amplitude from the background noise. The complex polar plot signal-separation technique provides a suitable means for obtaining the T-S amplitude.

T-S Disturbance Profile

To ensure that the complex-polar plot accurately isolates the T-S wave amplitude, several streamwise scans at different heights in the boundary layer are taken to obtain a “complete” picture of the T-S profile. To obtain a T-S amplitude at a particular boundary-layer height, a complex polar plot is generated from the streamwise scan as discussed in section 8.1.1 and the radius of the best-fit circle that fits through the data points is computed. This radius corresponds to the amplitude of the T-S wave at that particular height in the boundary layer. The T-S wave amplitude for several heights in the boundary layer is then compared with the Orr-Sommerfeld solution (section 1.2.2). Figure 8.6 shows the T-S wave amplitude at different heights in the boundary layer along with the Orr-Sommerfeld solution for $R = 1048$, $F = 55$, $U_\infty = 12$ m/s and SPL= 100 dB. As shown in the figure, the complex-polar technique described in section 8.1.1 provides a good approximation of the actual T-S profile. Another typical profile after performing the signal separation is shown in Figure 8.7 for $R = 1025$, $F = 50$, $U_\infty = 12$ m/s and SPL = 101 dB.

The maximum T-S amplitude is used when determining receptivity coefficients.

Thus, the next step after isolating the T-S signal from the background noise is to obtain the location that corresponds to the T-S maximum. A boundary-layer scan gives a rough estimate of the T-S maximum location and several streamwise scans are performed above and below the maximum in the raw boundary-layer profile. Complex polar plots are generated for each scan and a T-S amplitude for each plot is obtained. The maximum T-S amplitude is documented along with the corresponding height above the plate and the $u(y)/U_\infty$. Figures 8.8–8.10, show complex polar plots taken at the location of the T-S maximum for $F = 48\text{--}50$, $U_\infty = 13.9$ m/s, and $\hat{x}_{\text{avg}} = 1.766$ m.

8.2.2 Sound Amplitude at the Leading Edge

Because it is very difficult to experimentally measure the T-S wave (even after it has been amplified at Branch II) it is practically impossible to measure the T-S wave amplitude during its embryonic stage at the leading edge. Consequently, the T-S amplitude at Branch I is normalized with the sound amplitude at the leading edge. This normalized quantity defines the receptivity coefficient i.e.

$$K_{\text{LE}} = \frac{|u'_{\text{TS}}|_I}{|u'_{\text{AC}}|_{\text{LE}}} \quad (8.5)$$

Several different procedures are tested to measure the acoustic amplitude at the leading edge. Difficulty arises since it is desired to obtain a simultaneous leading-edge sound amplitude measurement while performing a streamwise scan with the hot wires located at Branch II. A hot-wire placed at the leading edge and some distance off the plate (so that it is in the freestream) measures the leading-edge sound amplitude. However, this hot-wire probe affects the flow and yields erroneous measurements acquired by the hot-wires placed at Branch II. Rasmussen (1993) and Wei (1994) worked around the difficulty by taking measurements at the leading edge for different frequen-

cies and sound pressure levels and documenting the u'_{AC} rms levels. The streamwise scans were then performed later or on another day and the acquired T-S amplitudes were normalized with the documented u'_{AC} rms levels previously obtained. This technique is adequate, but certainly not ideal because the speaker behavior (and hence the broadcasted sound amplitude) strongly depends on temperature. Consequently, the sound output not only changes throughout the day due to outside temperature variations but also changes during a streamwise scan when the tunnel and the speakers heat up due to use. Moreover, different techniques for measuring the sound amplitude at the leading edge are examined.

Microphone and Hot-Wire Correlation at the Leading Edge

One technique for measuring the leading-edge sound amplitude is by means of a flush-mounted microphone. If a flush mounted microphone is calibrated to yield u'_{rms} values at the leading edge before hand, then the microphone signal can be acquired simultaneously during the streamwise scan and yield the actual leading-edge sound amplitude. Since dp/dy is approximately a constant throughout the boundary layer, the forced pressure field outside and inside the boundary layer should be identical. Thus, u'_{rms} ($= p'_{rms}/\rho a_\infty$ for a planar sound wave) measured by the hot wire should show a similar response as the microphone but differ in magnitude to account for the speed of sound.

From the discussion in section 7.1, it is not surprising that this technique, based on a somewhat simple principle, is not simple to implement. The microphone is first installed on the test-section floor at the leading edge. A hot wire placed at the same streamwise location but 660 mm above the microphone is simultaneously acquired to compare with the microphone signal. The response from the microphone is significantly different from the hot-wire signal. The significant differences could be due to the wall boundary layer sensed only by the microphone. In addition,

further testing showed that the hot-wire stand used to mount the hot-wire has an influence on the microphone and thus could affect the microphone response. Also, the leading-edge effect of scattering the sound wave also could be contributing to significant differences between the microphone and hot-wire response. To eliminate some of these problems, the microphone is flush-mounted on the plate near Branch I ($\hat{x} = 0.5$ m) and the u'_{rms} measured by two different hot wires placed at the same streamwise location is obtained. One wire is 150 mm from the plate and the other wire is placed 12 mm over the microphone and two boundary-layer thicknesses from plate (so there is no influence due to the embryonic T-S waves). The frequency of the radiated sound is swept from 45 Hz to 115 Hz in 1 Hz increments at ≈ 100 dB and the response of the hot wires and microphone are obtained. Figure 8.11 shows that the hot-wire responses are almost identical. The microphone response, however, is much different from the hot-wire response. To ensure that the microphone is working properly, another microphone is used and the same response is obtained. In addition, a microphone is hooked up to pressure ports located at the same streamwise location and the response is the same. To eliminate any possible nonlinear affects due to high-amplitude sound, the sound pressure level is reduced to 90 dB and provided identical results.

To ensure that sting vibration is not affecting the hot-wire response, a fixed wire is attached to the plate. The fixed hot wire (Hw1) is offset from the microphone by 25.4 mm and another wire (Hw0) is placed on the sting outside the boundary layer. Figure 8.12 shows the hot-wire and microphone response. The response from the fixed wire and the wire on the sting is almost identical which shows that the possibility of sting vibration affecting the hot-wire response is eliminated. In addition, the hot-wire and microphone response still differ significantly.

A hot wire (Hw1) is then placed as close to the flush-mounted microphone as pos-

sible (≈ 0.5 mm of the plate, directly over the microphone). Another hot-wire is kept outside the boundary layer to compare with the hot-wire inside the boundary layer. Assuming that the T-S waves are $O(10^{-6})$, the hot-wire signal inside the boundary layer should not significantly change due to the embryonic T-S wave. Figure 8.13 shows the microphone and each hot-wire response for the frequency sweep between 45 and 115 Hz. The response of the hot-wire inside the boundary layer over the microphone is much different from the freestream hot-wire signal. However, the hot-wire signal mounted close to the microphone sensor still shows a different response from the microphone. There does appear to be some agreement at 67 and 81 Hz which is not seen with the freestream hot-wire. To further verify that there must be some T-S wave and Stoke's wave contribution which is creating the differences in the hot-wire and flush-mounted microphone measurements, a hot-wire is placed at $u/U_\infty = 0.3$ (≈ 1 mm above the plate) which corresponds to the approximate location of the T-S wave maximum. This hot-wire is placed directly over the microphone and another hot-wire is placed in the freestream. Figure 8.14 shows the microphone and each hot-wire response for the frequency sweep. The response of the hot-wire placed at the T-S wave maximum is higher than the previous case and is much different from the freestream hot-wire response. In addition, both hot-wire responses are different from the microphone response. Clearly, there must be some T-S wave and Stoke wave contribution which is causing the difference between the microphone and hot-wire response. This technique is abandoned and a simpler method is employed for measuring the sound amplitude at the leading edge which completely eliminates these problems.

Fixed Hot-wire at the Leading Edge

In order to obtain simultaneous leading-edge sound-amplitude measurements while performing streamwise scans to obtain the T-S wave amplitude, a hot-wire is mounted in the plane of the leading edge at 180 mm from the test-side wall. The hot-wire is

located at the same spanwise location (-10 mm from plate centerline) where the streamwise scans are performed. Therefore, with this configuration, a sound measurement in the leading-edge plane can be obtained simultaneously while streamwise scans are performed. Moreover, the sensor is mounted near the test-side wall so that it is far enough from the flat plate so as to not affect flow measurements conducted further downstream on the plate. This leading-edge sound measurement is taken for all of the streamwise scans to use in the normalization process to obtain receptivity coefficients.

8.2.3 Receptivity Coefficient Focusing

One of the experiment objectives is to further investigate some interesting receptivity features found by Rasmussen (1993) and Wei (1994) that cannot be explained by the theory. The experiments were conducted with two different leading-edge aspect ratios (40:1 and 20:1, respectively) yet both show that the receptivity coefficient has a narrower frequency band than the typical amplified T-S wave at particular freestream speed. Tables 8.1 and 8.2 documents their focusing conditions.

U_∞ [m/s]	F	R	T [C]	ν [m ² /s]	f [Hz]	a_∞ [m/s]	λ_{ac} [mm]
8.0	84	792	27.5	16.4e-6	52.2	347.5	6661
12.0	54	1099	27.4	16.3e-6	75.9	347.5	4576
15.0	43	1232	30.6	16.7e-6	92.2	349.3	3788
18.0	36	1331	36.7	17.3e-6	107.3	352.8	3287

Table 8.1: Focusing conditions from Wei (1994).

Despite differences in the pressure distribution, nose radius, and the pressure-minimum location, the magnitude of the receptivity coefficient is relatively unchanged and the narrow-band of frequencies are essentially the same. In addition, the most amplified T-S wave is 50 mm, regardless of the unit Reynolds number. Some questions raised from these measurements include whether the the special modified-super-ellipse

U_∞ [m/s]	F	R	T [C]	ν [m ² /s]	f [Hz]	a_∞ [m/s]	λ_{ac} [mm]
8.06	84	812	26.0	16.0e-6	54.3	346.6	6386
12.0	54	1129	27.0	16.3e-6	75.9	347.2	4573
15.0	43	1268	28.0	16.6e-6	92.7	347.8	3749
18.0	35	1357	31.8	16.9e-6	106.8	349.9	3277

Table 8.2: Focusing conditions from Rasmussen (1993).

leading-edge geometry could somehow be causing the focusing behavior, or is some inherent tunnel feature creating this characteristic. Historical measurements conducted on a 6:1 aspect-ratio standard ellipse that had a curvature discontinuity at the leading-edge/flat plate juncture did not show such focusing behavior. However, Lin et al. (1992) show that the curvature discontinuity accounts for 50% of the receptivity in a 6:1 standard ellipse. Consequently, this curvature discontinuity may have broadened the response. In an attempt to further investigate the focusing behavior, the receptivity problem was examined on the VPI flat plate which has an elliptical leading edge with a juncture.

8.3 Receptivity Coefficient Dependence on Frequency

To determine the dependence of the receptivity on frequency, tests are conducted at each speed and the non-dimensional frequency is varied around the original frequency. T-S wave amplitudes at Branch II are obtained using the complex polar technique described in section 8.1.1. In addition, the T-S amplitude at Branch I is computed as described in section 1.2.3 and the leading-edge sound amplitude is measured by the method described in section 8.2.2. Moreover, receptivity coefficients for several frequencies at speeds of 8, 12, 12.9, and 13.9 m/s are shown in Table 8.3. The first two speeds are chosen to compare with Rasmussen (1993) and Wei (1994) and the last two speeds are chosen to detune from the previous speeds. Figure 8.15 shows a plot of these results along with the measurements obtained by Rasmussen

U_∞ [m/s]	F	R	N	$(u'_{TS})_R$	$(u'_{TS})_{R_I}$	$u'_{AC})_{LE}$	$(K_s)_I$
8.0	83	795	2.25	2.49e-4	2.62e-5	3.65e-4	0.072
	85	792	2.19	2.20e-4	2.46e-5	3.19e-4	0.089
	87	791	2.12	1.99e-4	2.38e-5	3.72e-4	0.064
	89	790	2.04	1.74e-4	2.26e-5	4.37e-4	0.052
	89	785	2.04	1.76e-4	2.28e-5	4.19e-4	0.054
	91	792	1.94	1.12e-4	1.60e-5	2.95e-4	0.046
	93	791	1.81	7.90e-5	1.29e-5	4.19e-4	0.031
	95	789	1.69	6.87e-5	1.26e-5	6.14e-4	0.022
	97	787	1.54	5.57e-5	1.19e-5	6.95e-4	0.017
12.0	50	1011	3.44	6.01e-4	1.92e-5	5.21e-4	0.037
	51	1008	3.46	5.52e-4	1.73e-5	3.25e-4	0.053
	52	1004	3.49	5.47e-4	1.66e-5	2.70e-4	0.062
	53	1003	3.53	5.17e-4	1.51e-5	2.78e-4	0.055
	54	1001	3.55	4.50e-4	1.29e-5	2.71e-4	0.048
	55	1000	3.58	3.77e-4	1.05e-5	2.97e-4	0.035
	56	1003	3.63	2.72e-4	7.20e-6	2.87e-4	0.025
12.9	48	1067	3.89	7.60e-4	1.55e-5	2.36e-4	0.066
	49	1074	4.02	9.31e-4	1.67e-5	2.28e-4	0.073
	50	1072	4.09	9.34e-4	1.56e-5	1.89e-4	0.082
	51	1073	4.09	1.15e-3	1.92e-5	2.120e-4	0.090
	52	1074	4.12	1.14e-3	1.85e-5	1.880e-4	0.098
	53	1067	4.07	1.08e-3	1.84e-5	1.740e-4	0.107
	54	1062	4.04	9.62e-4	1.69e-5	1.410e-4	0.120
	55	1062	4.01	1.08e-3	1.95e-5	1.350e-4	0.140
	56	1062	3.98	1.05e-3	1.96e-5	1.040e-4	0.187
13.9	46	1107	4.18	1.09e-3	1.66e-5	1.71e-04	0.097
	47	1112	4.36	9.29e-4	1.18e-5	1.33e-4	0.089
	48	1113	4.35	1.29e-3	1.66e-5	1.21e-4	0.137
	49	1105	4.31	1.09e-3	1.46e-5	1.13e-4	0.130
	50	1107	4.34	1.59e-3	2.07e-5	1.80e-4	0.116
	51	1105	4.32	1.66e-3	2.20e-5	1.97e-4	0.114

Table 8.3: Receptivity coefficient dependence on frequency (VPI flat plate).

(1993) and Wei (1994). Clearly, the focusing behavior is also occurring on the VPI flat plate. The receptivity coefficients, however, are significantly higher than those obtained by the previous experiments. This may be due, in part, to the possible constructive/destructive interference between the travelling waves and the leading-edge/flat-plate juncture. Receptivity coefficients at 12.9 m/s are obtained for a wide range of frequencies to provide more insight into the focusing behavior. Clearly, the receptivity coefficient increases gradually to the maximum. These results do indicate that the leading-edge geometry is *not* creating the focusing behavior. While conducting these experiments, however, it was noted that the T-S maximum is consistently at an η location much higher than that predicted by theory. This increase in the \hat{y} may indicate some three dimensionality in the boundary layer. The possibility is discussed in the next section.

8.3.1 Spanwise Variation of u'_{rms}

Spanwise constant- \hat{y} scans are taken to determine if a three-dimensional boundary layer exists. The scans are taken at the \hat{y} location corresponding to the maximum of the T-S wave. The maximum is found by taking a series of streamwise scans and using the complex polar plot technique to separate the T-S wave from the background noise. Once this \hat{y} location is determined, a spanwise scan is performed, accounting for any traverse drift as discussed in section 5.6. A total of 512 points are taken over the 150 mm in the spanwise direction yielding a step size of 0.29 mm in the z direction. To compute the traverse drift, 30 boundary-layer profiles are taken over the 150 mm span and a fourth-order curve fit is used to describe the drift.

The constant- \hat{y} scan is first performed at the $F = 56$, $U_\infty = 12.9$ m/s, $x = 1.73$ m, and $R = 1073$ case where the T-S wave shows significant amplification. The hot-wire response is band-passed (81–91 Hz) around the forcing frequency of $f = 86$ Hz. The average sound pressure level over the entire scan is 102 dB ($V_{\text{sp}} = 0.1 V_{\text{rms}}$). The

constant- \hat{y} scan is performed at $y = 1.5$ mm above the plate which corresponds to the maximum T-S location. Figure 8.16 shows the traverse drift for the scan, which is as much as 0.7 mm at the end of the scan. Figure 8.17 presents u'_{rms} normalized with the mean u'_{rms} . This figure shows that there is some sinusoidal variation of u'_{rms} in the spanwise direction. To determine the wavelength of the u'_{rms} variation, the data was multiplexed (discussed in section 5.6) into four individual data sets so that four averages are obtained for spectral analysis. From the wavenumber spectrum presented in Figure 8.18, the wavelength of the spanwise variation is approximately 61 mm, which corresponds to the wavelength of the T-S wave in the streamwise direction.

Another constant- \hat{y} scan is taken for the $F = 85$, $U_{\infty} = 8.0$ m/s, $x = 1.53$ m, and $R = 797$ case. The hot-wire response is band-passed (48–51 Hz) around the forcing frequency of $f = 51$ Hz. The average sound pressure level over the entire scan is 96 dB ($V_{\text{sp}} = 0.1V_{\text{rms}}$). The constant- \hat{y} scan is performed at $y = 1.78$ mm above the plate which corresponds to the maximum T-S location. Figure 8.19 shows the traverse drift for the scan and Figure 8.20 presents u'_{rms} normalized with the mean u'_{rms} . Similiarly, this figure shows some sinusoidal variation of u'_{rms} in the spanwise direction although it is not as pronounced as in the previous case. This could be due to the lower overall magnitude of the receptivity coefficient when compared with the previous case. To determine the wavelength of the u'_{rms} variation, the data is multiplexed into four individual data sets so that four averages are obtained for spectral analysis. From the wavenumber spectrum presented in Figure 8.21, the wavelength of the spanwise variation is approximately 90 mm, which is larger than the wavelength of the T-S wave in the streamwise direction (≈ 60 mm).

This apparent three-dimensionality of the boundary layer creates the peak-valley structure. The peaks and valleys correspond to the spanwise regions of enhanced

and reduced disturbance growth. One interesting feature of this spanwise variation is that in Figure 8.17, the u'_{rms} varies by as much as 50% in the spanwise direction. This may shed some light on what is causing the focusing behavior. When the frequency is slightly detuned from the focusing frequency giving the maximum receptivity coefficient, the effect is that the spanwise variation shifts in the spanwise direction. Moreover, accompanying this “shift” is a decrease in u'_{rms} which would decrease the receptivity coefficient.

8.3.2 Induced v' at Leading Edge

A v' component at the leading edge enhances the receptivity at the leading edge which could also cause the focusing behavior. Nishioka and Morkovin (1986) and Saric et al. (1994) discuss the effect of a weak v' component at the leading edge. A v' component can be induced at the leading edge by the vortex shedding of the trailing-edge flap. This shedding causes a weak unsteady circulatory flow around the plate. To determine if a weak v' component is causing the focusing, the presence of any unsteady circulatory flow around the plate is investigated.

To detect any oscillating circular flow around the plate, two hot wires are placed on opposing sides of the model at an \hat{x} location of 1.7 m. A frequency sweep is performed between 35–125 Hz with a frequency increment of 1 Hz and the two hot-wire signals are obtained for each frequency. The difference between the two u'_{rms} signals yields the out-of-phase component. Figures 8.22–8.26 show the out-of-phase component as a function of dimensionless F for wind-tunnel velocities of 8 m/s, 12 m/s, 15 m/s, 18 m/s, and 21 m/s. The speaker output voltage is 0.5 volts (rms) for all cases. The figures show a “peaky” structure that becomes even more prevalent at the higher speeds. However, the peaks do not occur at the frequencies where the focusing of the receptivity coefficient takes place. Further experiments show that the peak structure is not dependent on the sound amplitude. Figure 8.27 shows the out-

of-phase component at $U_{\infty} = 12$ m/s when the speaker voltage output is decreased to 0.1 volts (rms). In addition, the shutters (located downstream of the test-section) are rotated 30° to investigate any dependence of the out-of-phase component on shutter orientation. Figure 8.28 shows the resulting output which is almost the same as figure 8.23. Moreover, there are definitely peaks in the out-of-phase component for certain frequencies but they don't correspond to the focusing conditions.

CHAPTER 9

Conclusions

9.1 Specific Results

9.1.1 Basic State

A Blasius basic state isolates the instability mechanism to a Tollmien-Schlichting wave, and this flow condition is carefully established for two different flat-plate models. Adjustment of the trailing-edge flap provides stagnation line control and alignment for symmetric flow about the leading edge supplies a basic-state flow condition for comparison with computations. This experiment abandons the use of Preston tubes near the leading edge, which can trip the boundary layer and create turbulent flow, and employs leading-edge static-pressure ports for aligning the trailing-edge flap for symmetric flow.

9.1.2 Disturbance State

The Sound Field

A computer-integrated system provides reliable sound generation inside the test section, and a set of microphones are flush mounted around the perimeter entrance of the test-section to provide sound-field information. Measuring the phase of the incoming sound signal with the microphones posed some difficulties which may be attributed to wall boundary-layer effects and the leading-edge scattering of the in-

coming sound wave. Relative sound-incidence angle measurements are computed using a cross-spectrum and show that the sound field close to the model's leading edge is quite complicated. In addition, the sound incidence angle is a function of frequency. However, it is unclear at this time how much the turbulent boundary layer affects the phase measurements. Microphone-sensitivity measurements indicate that the external wind-tunnel environment does not significantly affect the microphone phase measurements when venting to the atmosphere in the plenum.

Attempts are made to correlate the microphone p'_{rms} with the hot wire u'_{rms} but no direct correlation is found. A hot-wire, mounted in the plane of the leading edge on the test-section side wall, provides a sound u'_{rms} measurement required for computing receptivity coefficients. This set-up allows the incoming sound amplitude to be measured simultaneously while measuring the T-S wave at Branch II, which is an improvement over previous techniques. Leading-edge accelerometer measurements also show that the peak-to-peak oscillations of the leading edge are $O(20)\mu\text{m}$ which is considered tolerable.

Freestream Disturbance Measurements

Freestream disturbance measurements are conducted for wind tunnel velocities ranging from 5–25 m/s. Both amplitude and power-spectral-density plots are given for several wind tunnel speeds with band passes of 0.1–1000 Hz, 2–1000 Hz, and 35–1000 Hz. The measurements show that when the zero-pressure state is located in the plenum (which is the configuration for this experiment), the streamwise freestream disturbance levels are much greater than when the mixing region is vented. Because the freestream disturbance levels affect the transition process, the results suggest that the zero-pressure state should be moved to the mixing region for future receptivity experiments. In addition, the measurements reveal that the disturbance levels are higher than what is quoted by (Mousseux 1988) which could explain why the

transition Reynolds number is also lower.

For a 2-1000 Hz band pass, the Tektronix-filtered measurements are higher than the Stewart-filtered data. From the power-spectral-density plots, it is apparent that the high-pass characteristics between the two filters are different. The Tektronix filter captures more of the disturbance energy for frequencies less than 2 Hz which contributes to the higher u'_{rms} and u'_{pk-pk} values. There appears to be a “roll-off” associated with the Tektronix filter at 2 Hz rather than a steep “cut-off” at 2 Hz which the Stewart filter provides. Because the Stewart filters provide a steep high-pass cut-off, the Stewart-filtered measurements are a better estimate of the disturbance levels for a 2-1000 Hz band pass. In addition, the measurements show that a significant amount of disturbance energy occurs at frequencies less than 2 Hz because the disturbance levels are significantly higher (more than double) for a 0.1-1000 Hz band pass than for a 2-1000 Hz band pass. Finally, for the 35-1000 Hz band-passed data, the disturbance levels are the lowest indicating that little external disturbance energy exists in the T-S amplified range.

9.1.3 T-S Amplitude Measurements

Signal-Separation Techniques

The complex-polar technique, the Kendall gauge, a multiple-microphone technique, and a sound-burst method are examined for extracting the T-S wave from the sound-induced sting-vibration/Stokes wave. The complex-polar technique is successful but requires several hundreds of measurements to obtain a T-S profile. Wind-tunnel heating and extended speaker use becomes a problem for this technique. The Kendall gauge successfully separates the T-S wave from background freestream disturbance but cannot separate the sound-induced T-S wave from the associated Stokes wave. The disturbance pressure field is large in magnitude when compared to the T-S amplitude and contamination becomes a problem even for high common-mode rejec-

tion ratios. Since $p'_{AC} \approx 100 p'_{TS}$, a Kendall gauge with a common-mode ratio of 100:1 still contains $O(1)$ errors. A simple three-microphone/three-equation analysis shows that the multiple-microphone technique does not work for isolating the T-S wave amplitude. The resulting matrix system is stiff and small measurement errors in p' produce a large error in the T-S amplitude. The sound-burst technique, which relies on the fact that the induced T-S wave travels at a slower phase speed than the associated Stokes wave, shows promising results. A procedure is successfully developed that requires that bursts of sound are radiated into the test section and the boundary-layer hot wire is monitored for the associated Stokes wave and the slower-travelling T-S wave.

Receptivity Coefficients

Receptivity coefficients are obtained on the VPI flat-plate model which has an elliptical leading edge with a junction. The measured receptivity coefficients are quite high but show the same focusing characteristics of the T-S amplitude for a narrow band of frequencies documented in previous experiments. This suggests that the focusing behavior is not due to any special geometry of the leading edge. The coefficients may be higher than expected because the leading-edge junction may constructively/destructively interfere with the travelling waves as indicated by Kosorygin et al. (1994). In addition, spanwise scans indicate some peak-valley structure of the u'_{rms} which could provide some explanation for the focusing of the receptivity coefficient. When the frequency is slightly detuned from the focusing frequency giving the maximum receptivity coefficient, the effect is that the spanwise variation shifts in the spanwise direction. Moreover, accompanying this “shift” is a decrease in u'_{rms} which decreases the receptivity coefficient for a fixed hot-wire location.

REFERENCES

- Aizin, L. and M. Polyakov. 1979. Acoustic generation of T-S waves over local uneveness of surface immersed in streams (in russian). *Preprint 17, ITPM, Akad. Nauk USSR, Siberian Div.* see Nishioka and Morkovin, 1986.
- Bodonyi, R., W. Welch, P. Duck, and M. Tadjfar. 1990. A numerical study of the interaction between unsteady freestream disturbances and localized variations in surface geometry. *J. Fluid Mech.* 209.
- Casalis, G. and B. Cantaloube. 1994. Receptivity by direct numerical simulation.
- Chandrasekhar, S. 1961. *Hydrodynamic and Hydromagnetic Stability*. New York: Oxford University Press.
- Choudhari, M. and C. Street. 1994. Theoretical predictions of boundary-layer receptivity. AIAA Paper 94-2223.
- Cohn, R. K. 1992. *Active Control of Boundary Layer Instabilities*. M.S. thesis, Churchill College, Cambridge University.
- Craik, A. 1971. Nonlinear resonant instability in boundary layers. *J. Fluid Mech.* 50.
- Crouch, J. 1992a. Localized receptivity of boundary layers. *Phys. Fluids* 4:1408.
- Crouch, J. 1992b. Non-localized receptivity of boundary layers. *J. Fluid Mech.* 244:567.
- Crouch, J. 1994. Receptivity of boundary layers. AIAA Paper 94-2224.
- Cunningham, E. 1992. *Digital Filtering: An Introduction*. Boston: Houghton Mifflin Company.
- Davis, S. 1976. The stability of time-periodic flows. *Ann. Rev. Fluid Mech.* 8:57.
- Drazin, P. and W. Reid. 1981. *Hydrodynamic Stability*. New York: Cambridge University Press.
- Fuciarelli, D. and H. Reed. 1994. Direct numerical simulations of leading-edge receptivity to freestream sound. In *Application of Direct and Large Eddy Simulation to Transition and Turbulence*, AGARD RCP-551. Loughton, Essex: Specialised Printing Services Ltd.

- Gatski, T. and C. Grosch. 1987. Numerical experiments in boundary-layer receptivity. In *Proceedings of the Symposium on the Stability of Time-Dependent and Spatially Varying Flows*, pp. 82–96. Springer-Verlag.
- Goldstein, M. 1983. The evolution of T-S waves near a leading edge. *J. Fluid Mech.* 127:59.
- Goldstein, M. 1985. Scattering of acoustic waves into T-S waves by small streamwise variations in surface geometry. *J. Fluid Mech.* 154:485.
- Goldstein, M. and L. Hultgren. 1987. A note on the generation of T-S waves by sudden surface-curvature change. *J. Fluid Mech.* 181:519.
- Goldstein, M. and L. Hultgren. 1989. Boundary-layer receptivity to long-wave disturbances. *Ann. Rev. Fluid Mech.* 21:137.
- Hammerton, P. and E. Kerschen. 1994. Boundary-layer receptivity for a parabolic leading edge. *J. Fluid Mech.* 181.
- Heinrich, R. 1989. *Flat-Plate Leading-Edge Receptivity To Various Freestream Disturbance Structures*. Ph.D. dissertation, University of Arizona.
- Herbert, T. 1983. Subharmonic three-dimensional disturbances in unstable plane shear flows. AIAA Paper 83-1759.
- Kendall, J. 1990. Boundary layer receptivity to freestream turbulence. AIAA Paper 90-1504.
- Kendall, J. 1991. Studies on laminar boundary-layer receptivity to freestream turbulence near a leading edge. In *Boundary-Layer Stability and Transition to Turbulence, FED-Vol. 114* (eds. D. Reda, H. Reed, and R. Kobayashi). ASME.
- Kerschen, E. 1989. Boundary layer receptivity. AIAA Paper 89-1109.
- Klebanoff, P., K. Tidstrom, and L. Sargent. 1962. The three-dimensional nature of boundary-layer instability. *J. Fluid Mech.* 12.
- Kosorygin, V., R. R.H. Jr, and W. Saric. 1994. Laminar boundary layer sound receptivity and control. In *Laminar-Turbulent Transition Vol IV* (ed. R. Kobayashi). Proc. IUTAM Symp., Sendai, Japan.
- Leehey, P. and P. Shapiro. 1980. Leading edge effect in laminar boundary layer excitation. In *Laminar-Turbulent Transition*, p. 321. Springer-Verlag.

- Leehey, P., C. Gedney, and J. Her. 1984. The receptivity of a laminar boundary layer to external disturbances. In *Proc. IUTAM Symp. on Laminar-Turbulent Transition*, pp. 233–242. Springer-Verlag.
- Lin, N., H. Reed, and W. Saric. 1992. Effect of leading edge geometry on boundary-layer receptivity to freestream sound. In *Stability, Transition, and Turbulence* (eds. M. Hussaini, A. Kumar, and C. Streett), New York. Springer-Verlag.
- Mack, L. M. 1984. Boundary-layer linear stability theory. In *Special Course on Stability and Transition of Laminar Flows*, AGARD R-709.
- Malik, M., S. Chuang, and M. Hussaini. 1982. Accurate numerical solution of compressible, linear stability equations. vol. 33, pp. 189–200.
- Morkovin, M. V. 1969. On the many faces of transition. In *Viscous Drag Reduction* (ed. C. S. Wells), pp. 1–31. New York: Plenum.
- Morkovin, M. V. 1993. Bypass-transition research: Issues and philosophy. In *Instabilities and Turbulence in Engineering Flows* (eds. D. Ashpis, T. Gatski, and R. Hirsh). Kluwer Academic.
- Mousseux, M. 1988. *Flow-Quality Improvements In The Arizona State University Unsteady Wind Tunnel*. M.S. thesis, Arizona State University.
- Murdock, J. 1981. The generation of T-S wave by a sound wave. *Proc. R. Soc. Lond. A* 372:517.
- Nishioka, M. and M. Morkovin. 1986. Boundary-layer receptivity to unsteady pressure gradients: Experiments and overview. *J. Fluid Mech.* 171.
- Patel, V. 1965. Calibration of the preston-tube and limitations on its use in pressure gradients. vol. 23, pp. 185–208.
- Perry, A. E. 1982. *Hot-wire Anemometry*. New York: Oxford University Press. ISBN 0-19-856327-2.
- Pfenninger, W. 1977. Laminar flow control—laminarization. In *Special Course on Concepts for Drag Reduction*, AGARD R-654.
- Press, W. H., S. A. Teukolsky, W. T. Vetterling, and B. P. Flannery. 1992. *Numerical Recipes in C: The Art of Scientific Computing*. New York: Cambridge University Press, 2nd ed. ISBN 0-521-43108-5.
- Preston, J. 1954. The determination of turbulent skin friction by means of pitot tubes. vol. 58, pp. 109–121.

- Radeztsky, R. H. Jr., M. S. Reibert, and S. Takagi. 1993. A software solution to temperature-induced hot-wire voltage drift. In *Proc. Third International Symposium on Thermal Anemometry*, vol. 167, pp. 49–55. ASME-FED.
- Rae, W. H. Jr. and A. Pope. 1984. *Low-Speed Wind Tunnel Testing*. New York: John Wiley & Sons, 2nd ed. ISBN 0-471-87402-7.
- Rasmussen, B. K. 1993. *Boundary-Layer Receptivity: Freestream Sound On An Elliptical Leading Edge*. M.S. thesis, Arizona State University.
- Reibert, M. S. 1996a. *Nonlinear Stability, Saturation, and Transition in Crossflow-Dominated Boundary-Layers*. Ph.D. dissertation, Arizona State University.
- Reibert, M. S. 1996b. *Standard C Libraries and Codes: A Guide to Programming at the ASU Unsteady Wind Tunnel*. Arizona State University. Unsteady Wind Tunnel Internal Documentation.
- Reshotko, E. 1976. Boundary-layer stability and transition. vol. 8 of *Ann. Rev. Fluid Mech.*, p. 311.
- Reshotko, E. 1984. Environment and receptivity. In *Special Course on Stability and Transition of Laminar Flow*, AGARD R-709. Loughton, Essex: Specialised Printing Services Ltd.
- Reshotko, E. 1994. Boundary-layer instability, transition, and control. AIAA Paper 94-0001.
- Reynolds, O. 1883. An experimental investigation of the circumstances which determine whether the motion of water shall be direct or sinuous, and of the law of resistance in parallel channels. vol. 174, pp. 935–982.
- Saric, W., J. Hoos, and R. Radetzsky. 1991. Boundary-layer receptivity of sound with roughness. In *Boundary-Layer Stability and Transition to Turbulence, FED-Vol. 114* (eds. D. Reda, H. Reed, and R. Kobayashi). ASME.
- Saric, W., H. Reed, and E. Kerschen. 1994. Leading edge receptivity to sound: Experiments, dns, and theory. AIAA Paper 94-2222.
- Saric, W., W. Wei, B. Rassmussen, and T. Krutckoff. 1995. Experiments on leading edge receptivity to sound. AIAA Paper 95-2253.
- Saric, W. S. 1990. Low-speed experiments: Requirements for stability measurements. In *Instability and Transition* (eds. M. Y. Hussaini and R. G. Voight), vol. 1, pp. 162–174. New York: Springer-Verlag. ISBN 0-387-97323-0.
- Saric, W. S. 1992. The ASU transition research facility. AIAA Paper 92-3910.

- Saric, W. S. 1994. Physical description of boundary-layer transition: Experimental evidence. In *Special Course on Progress in Transition Modelling*, AGARD R-793. Loughton, Essex: Specialised Printing Services Ltd. ISBN 92-835-0742-8.
- Saric, W. S. 1996. Low-speed boundary-layer transition experiments. In *ICASE Report*.
- Smith, A. M. O. and N. Gamberoni. 1956. Transition, pressure gradient, and stability theory. ES 26388, Douglas Aircraft Company, El Segundo, California.
- Spencer, S. A. 1992. *Boundary-Layer Receptivity: Freestream Sound With Three-Dimensional Roughness*. M.S. thesis, Arizona State University.
- Thomas, A. S. W. 1985. Aircraft drag reduction technology—a summary. In *Special Course on Aircraft Drag Prediction and Reduction*, AGARD R-723. Loughton, Essex: Specialised Printing Services Ltd. ISBN 92-835-1507-2.
- van Ingen, J. L. 1956. A suggested semi-empirical method for the calculation of the boundary-layer transition region. VTH 71 & 74, Dept. Aero. Eng., Univ. of Techn., Delft, Netherlands.
- Wei, W. 1994. *Boundary-Layer Receptivity: Freestream Sound On A 20:1 Elliptical Leading Edge*. M.S. thesis, Arizona State University.
- Wlezien, R. 1989. Measurement of boundary layer receptivity at suction surfaces. AIAA Paper 89-1006.
- Wlezien, R., D. Parekh, and T. Island. 1990. Measurement of acoustic receptivity at leading edges and porous strips. *Appl. Mech. Rev.* 43.

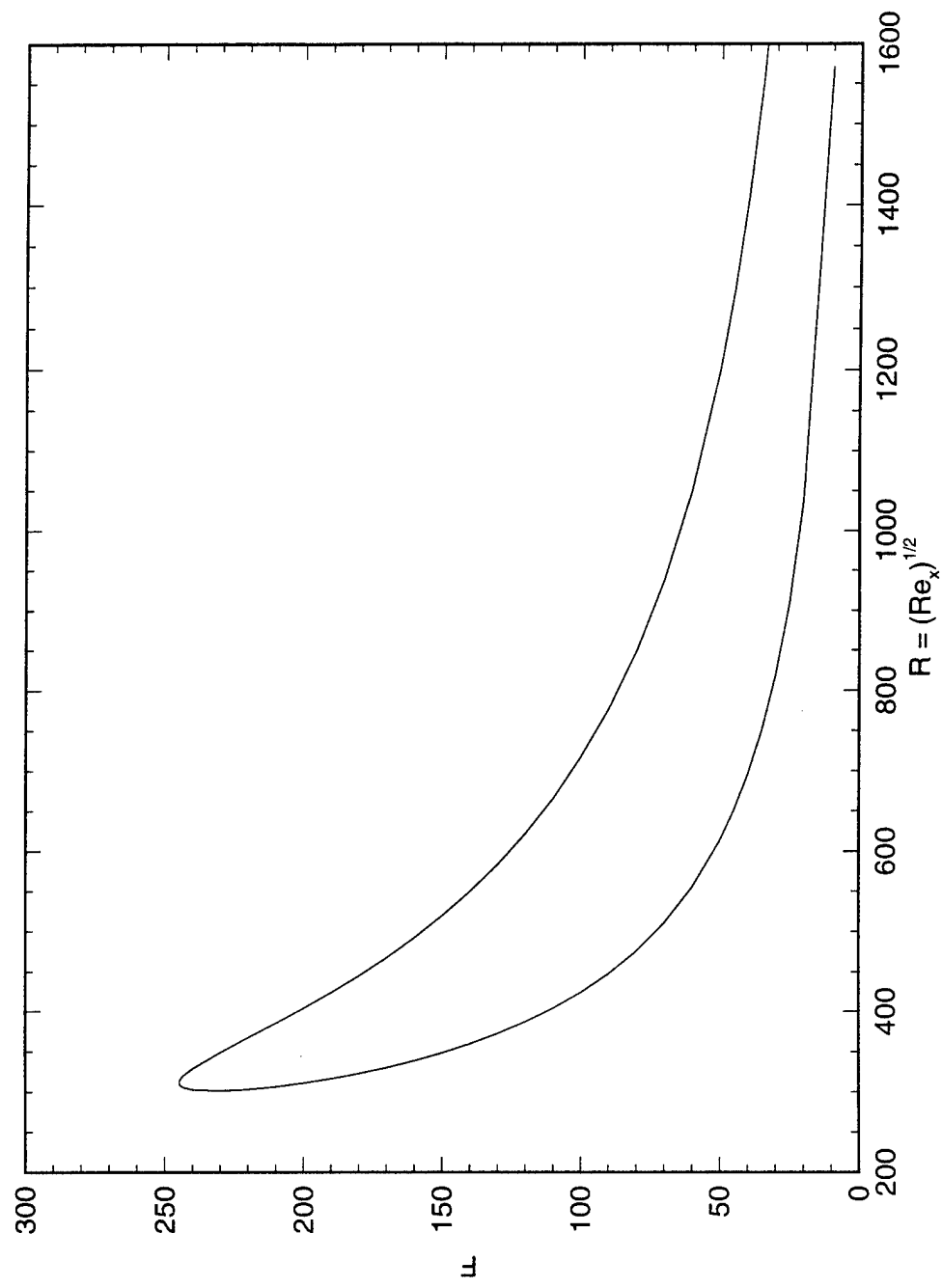


Figure 1.1: Neutral Stability Curve For Blasius Flow.

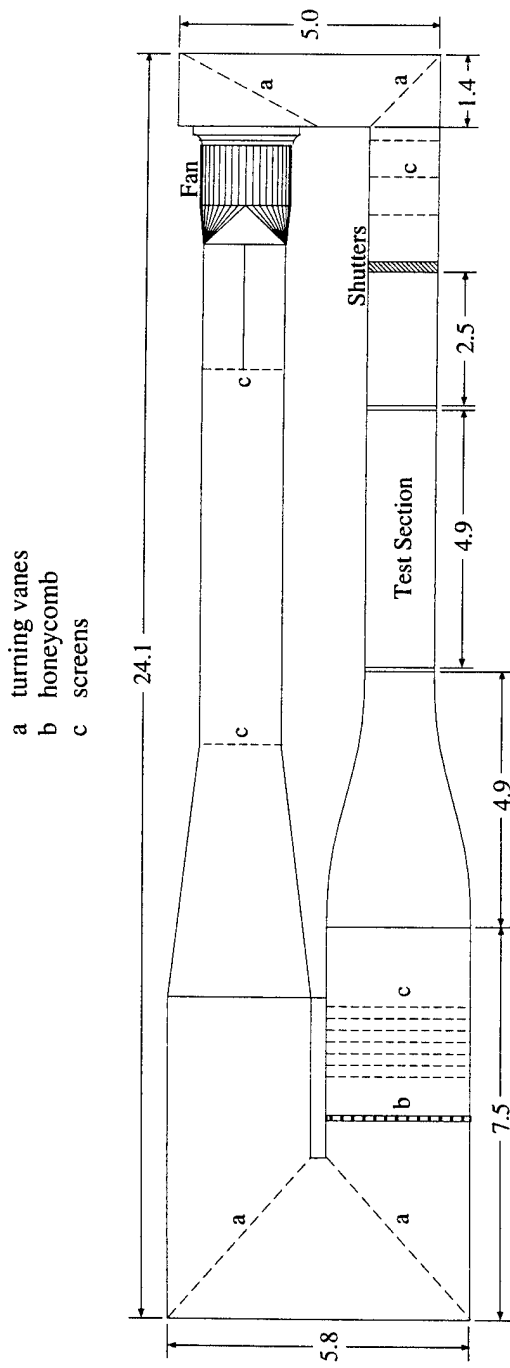


Figure 2.1: Plan view of the ASU Unsteady Wind Tunnel. All dimensions in meters.

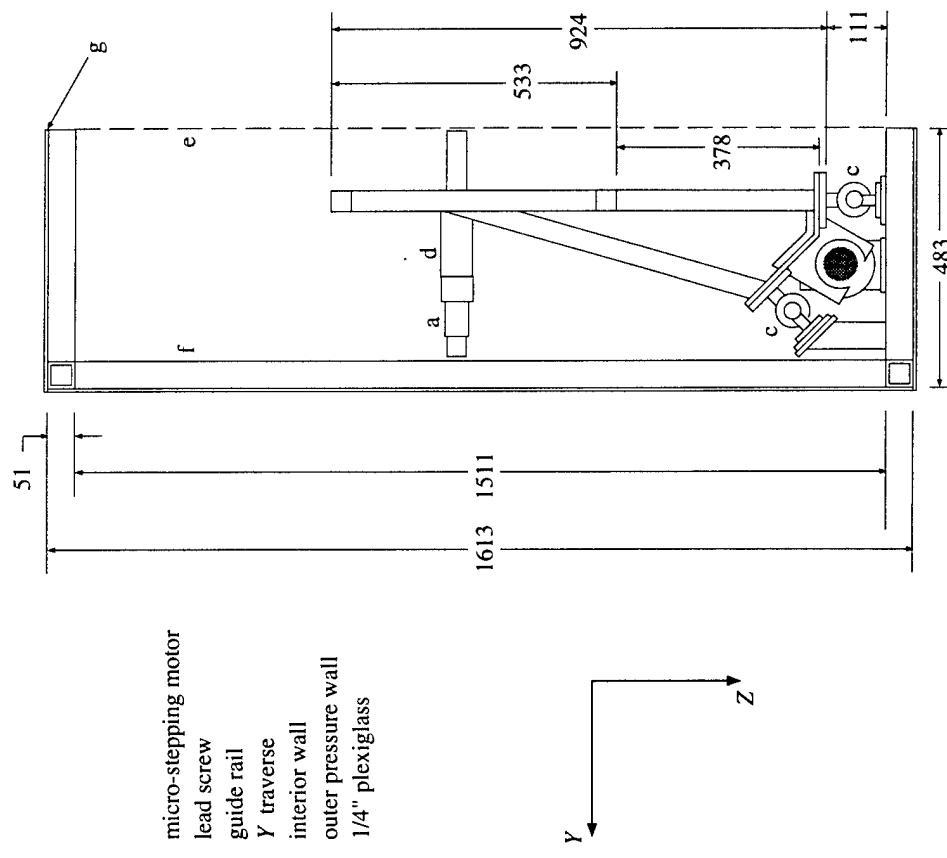


Figure 2.2: Side view of traverse carriage. All dimensions in millimeters.

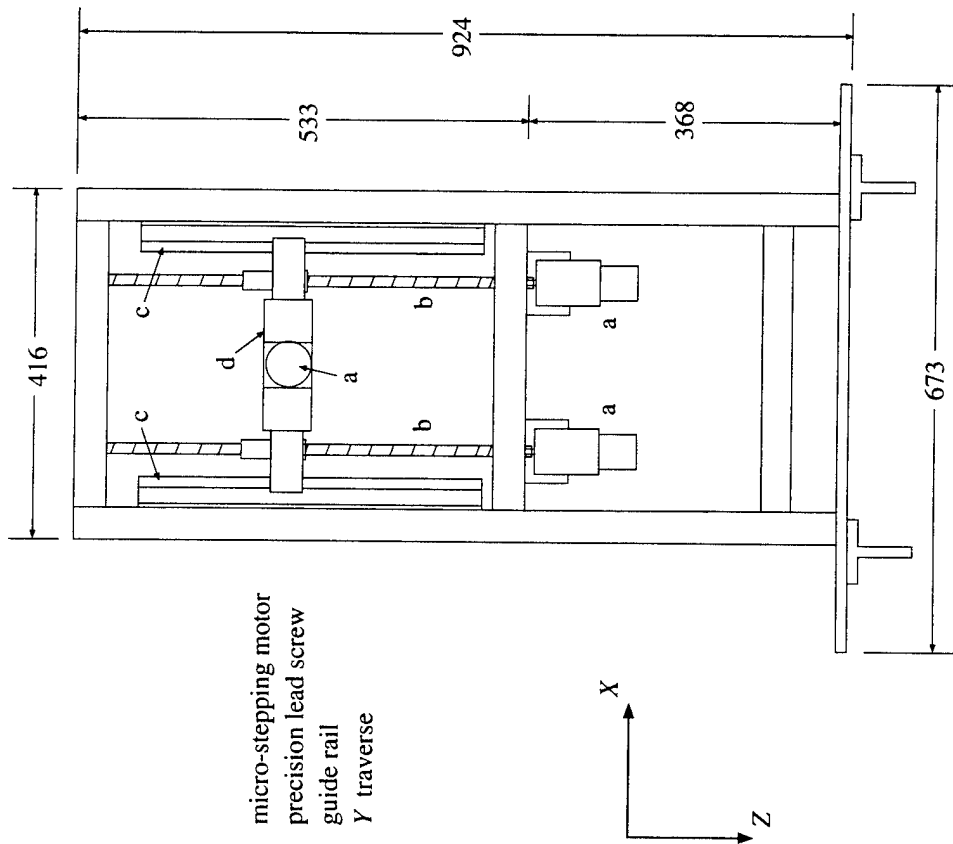


Figure 2.3: Front view of traverse carriage. All dimensions in millimeters.

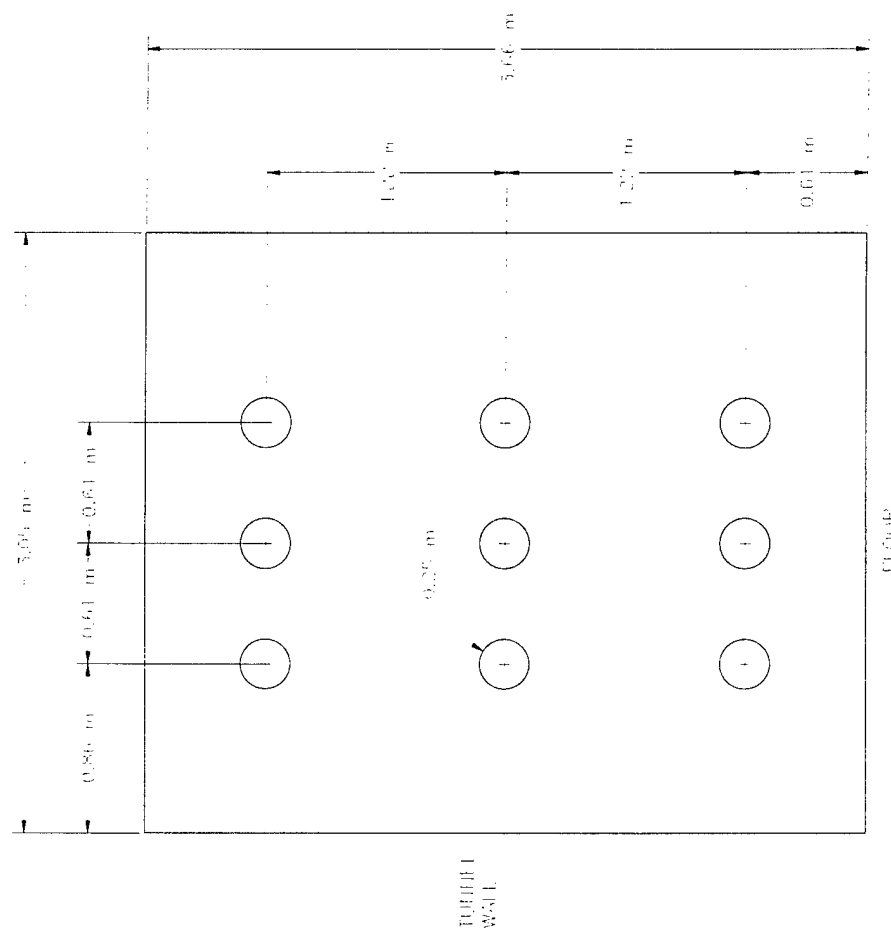


Figure 2.4: Speaker arrangement on plenum wall. All dimensions in meters.

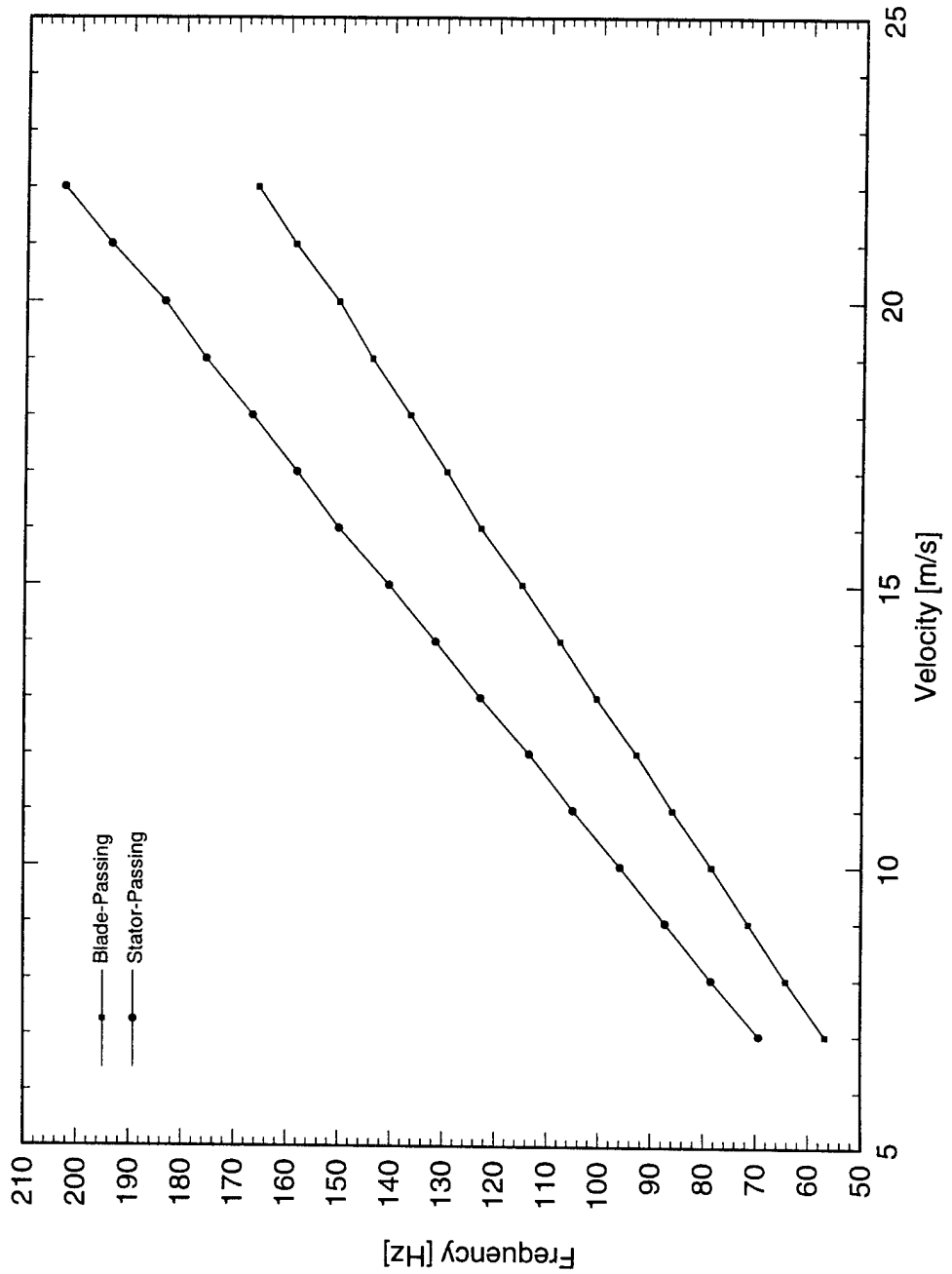


Figure 3.1: Blade- and stator-passing frequencies at each wind-tunnel speed.

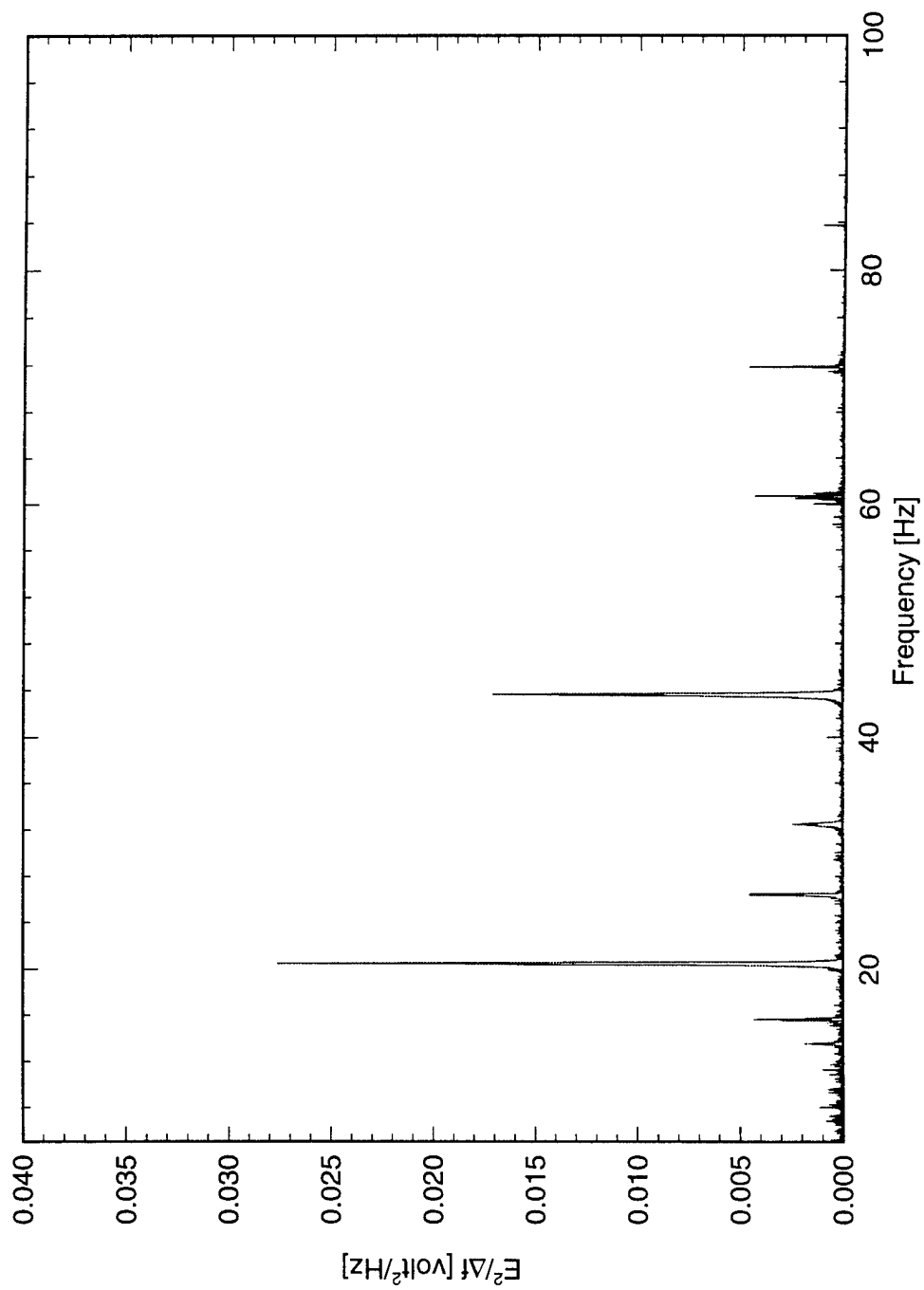


Figure 3.2: Power-spectral density of leading-edge response to random noise.

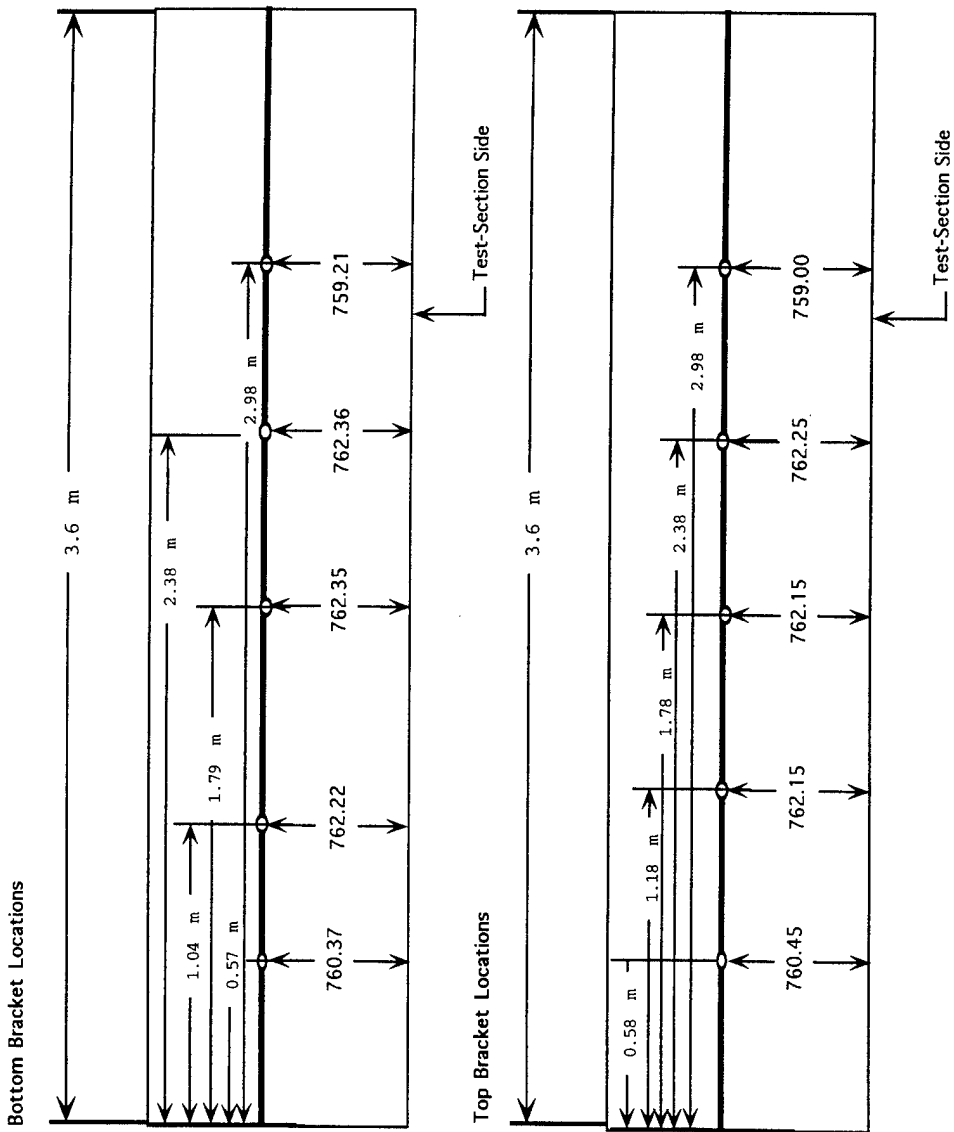


Figure 6.1: Final position of the Klebanoff flat plate inside test section. All unspecified measurements in mm.

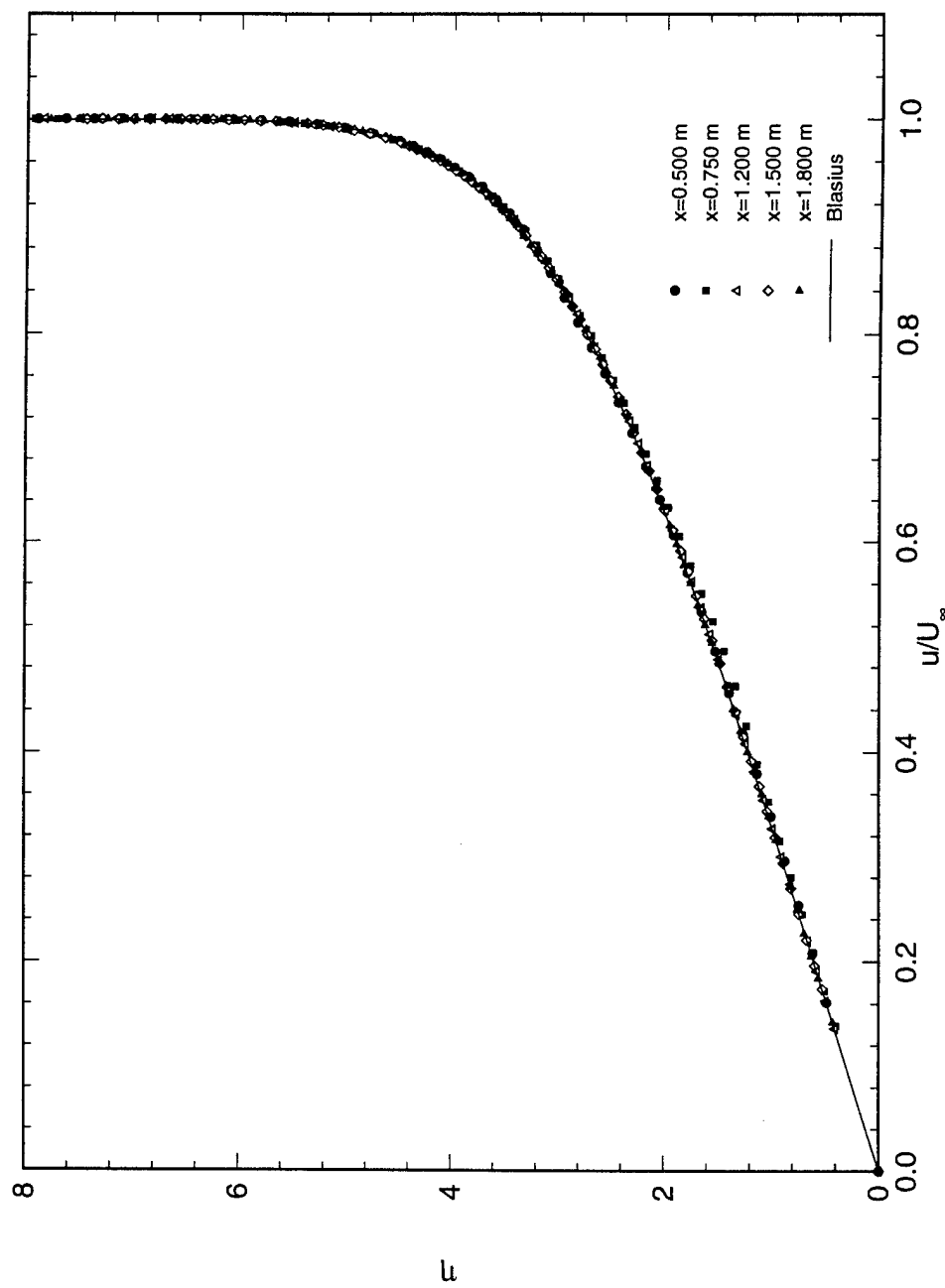


Figure 6.2: Streamwise boundary-layer profiles for $U_\infty = 12 \text{ m/s}$ (Klebanoff Flat Plate).

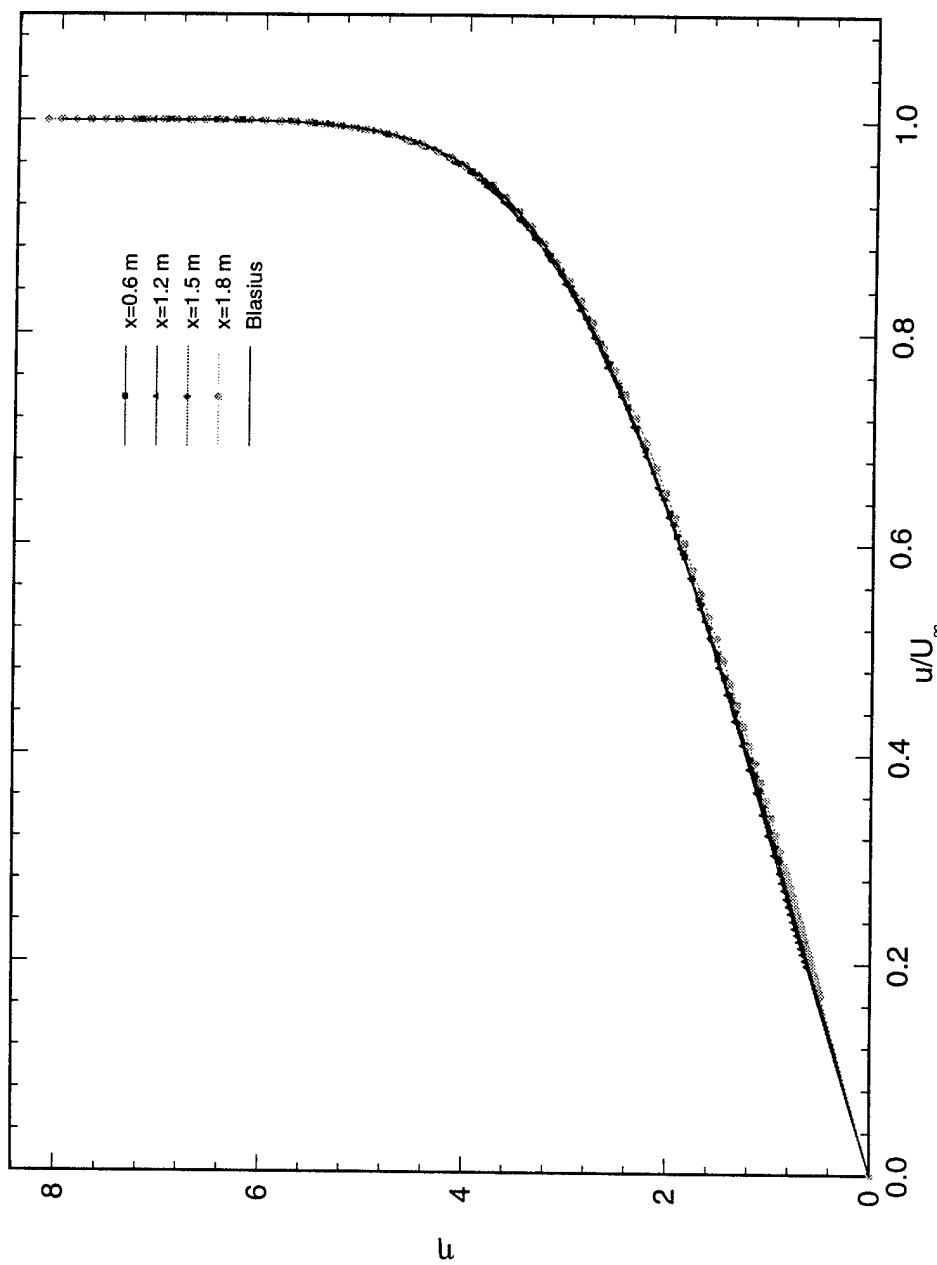


Figure 6.3: Streamwise boundary-layer profiles for $U_\infty = 12 \text{ m/s}$ (VPI Flat Plate).

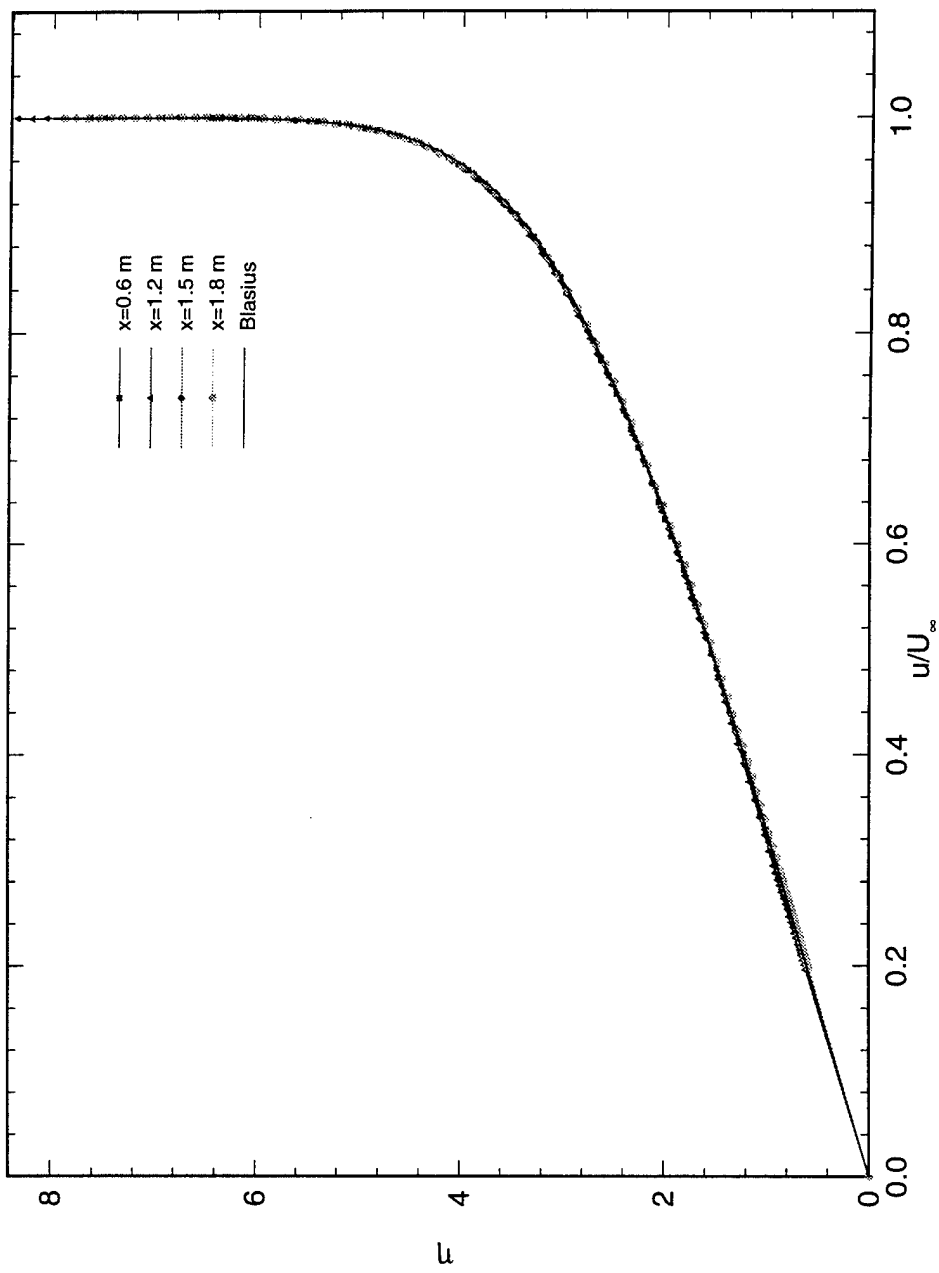


Figure 6.4: Streamwise boundary-layer profiles for $U_\infty = 8 \text{ m/s}$ (VPI Flat Plate).

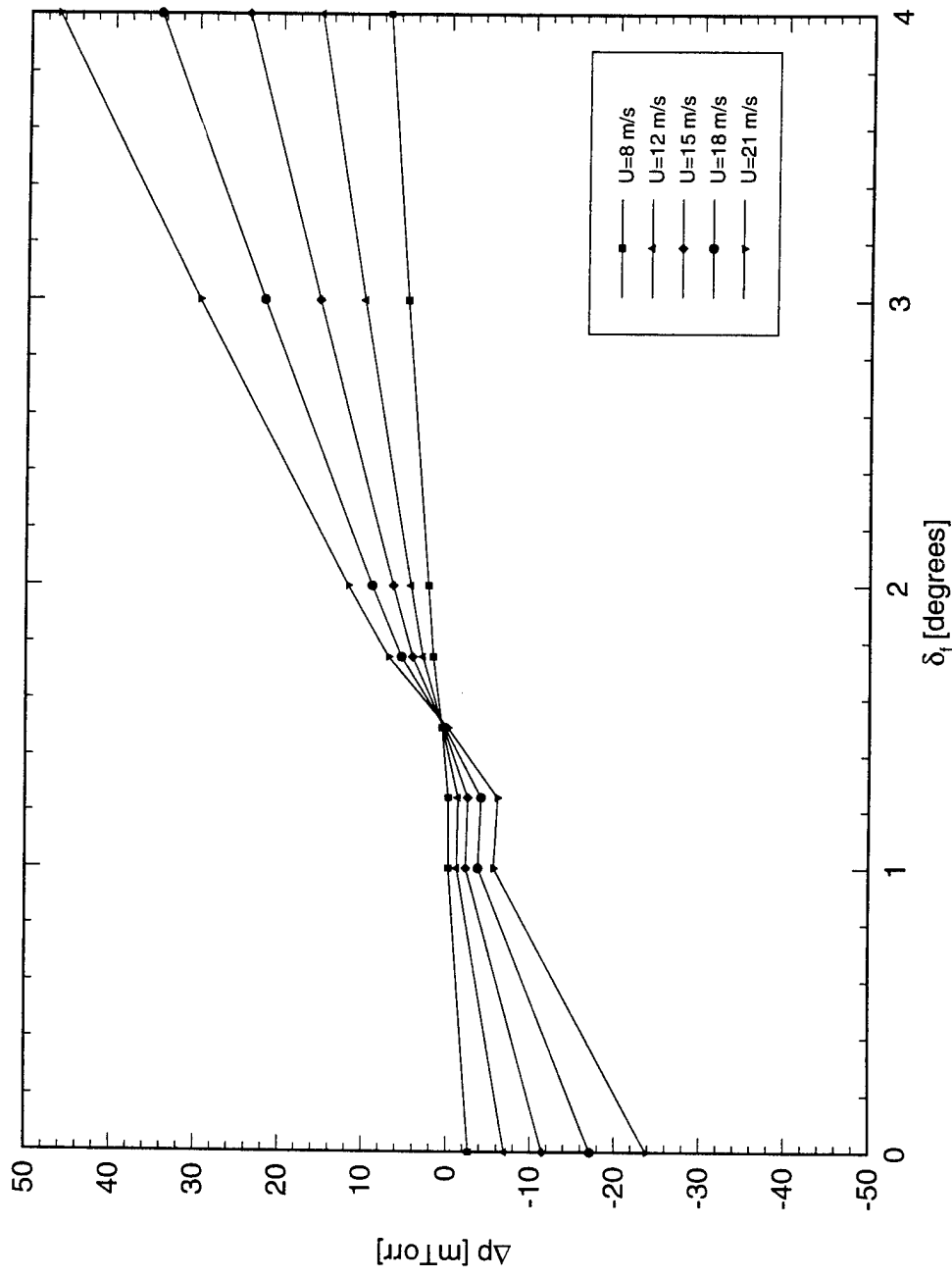


Figure 6.5: Symmetric-flow measurements obtained with the dual Preston tube configuration mounted at $\hat{x} = 0.1$ m, $\hat{z} = 0.0$ m (Klebanoff Flat Plate).

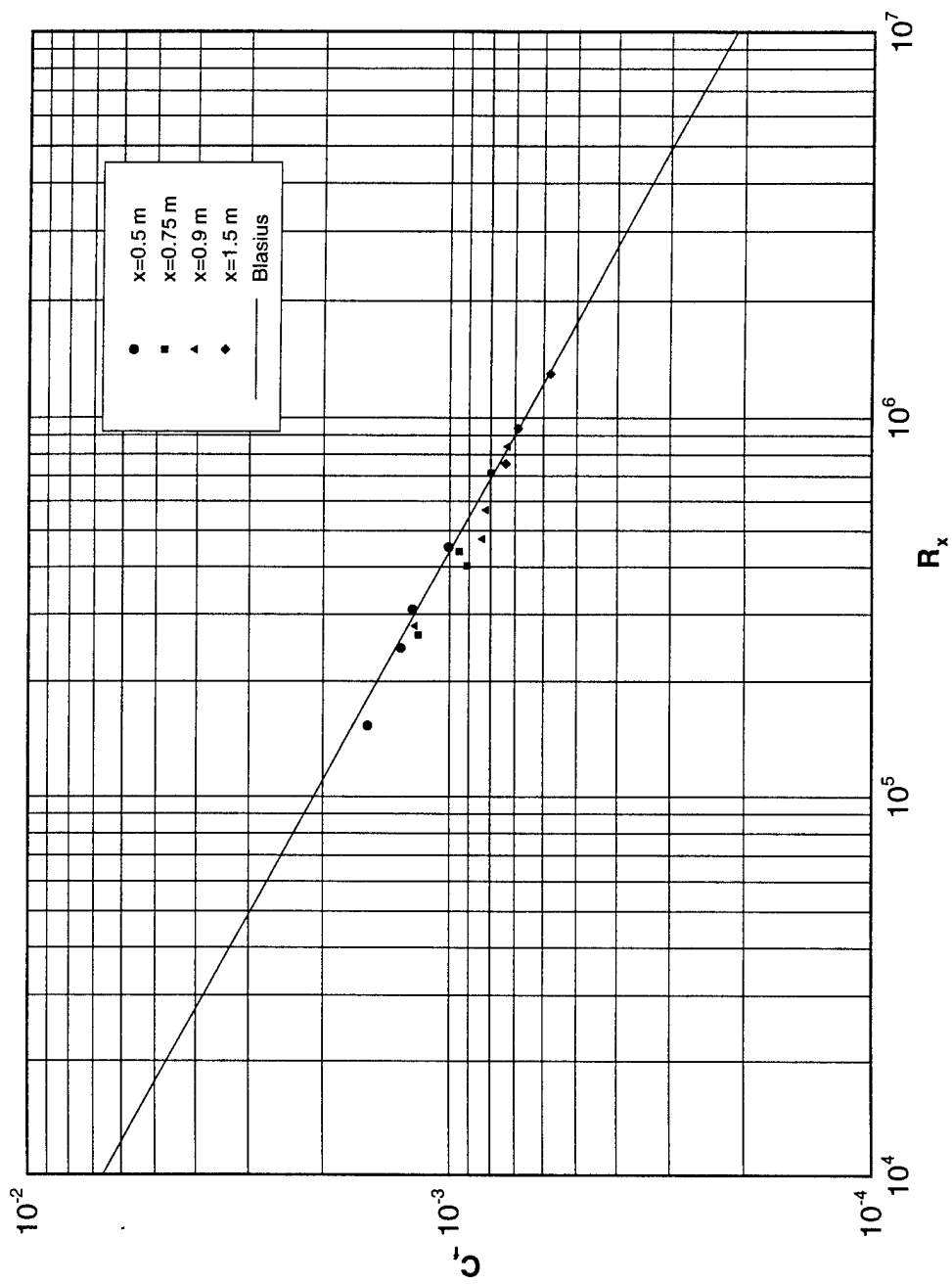


Figure 6.6: Skin-friction coefficient vs. Reynolds number.

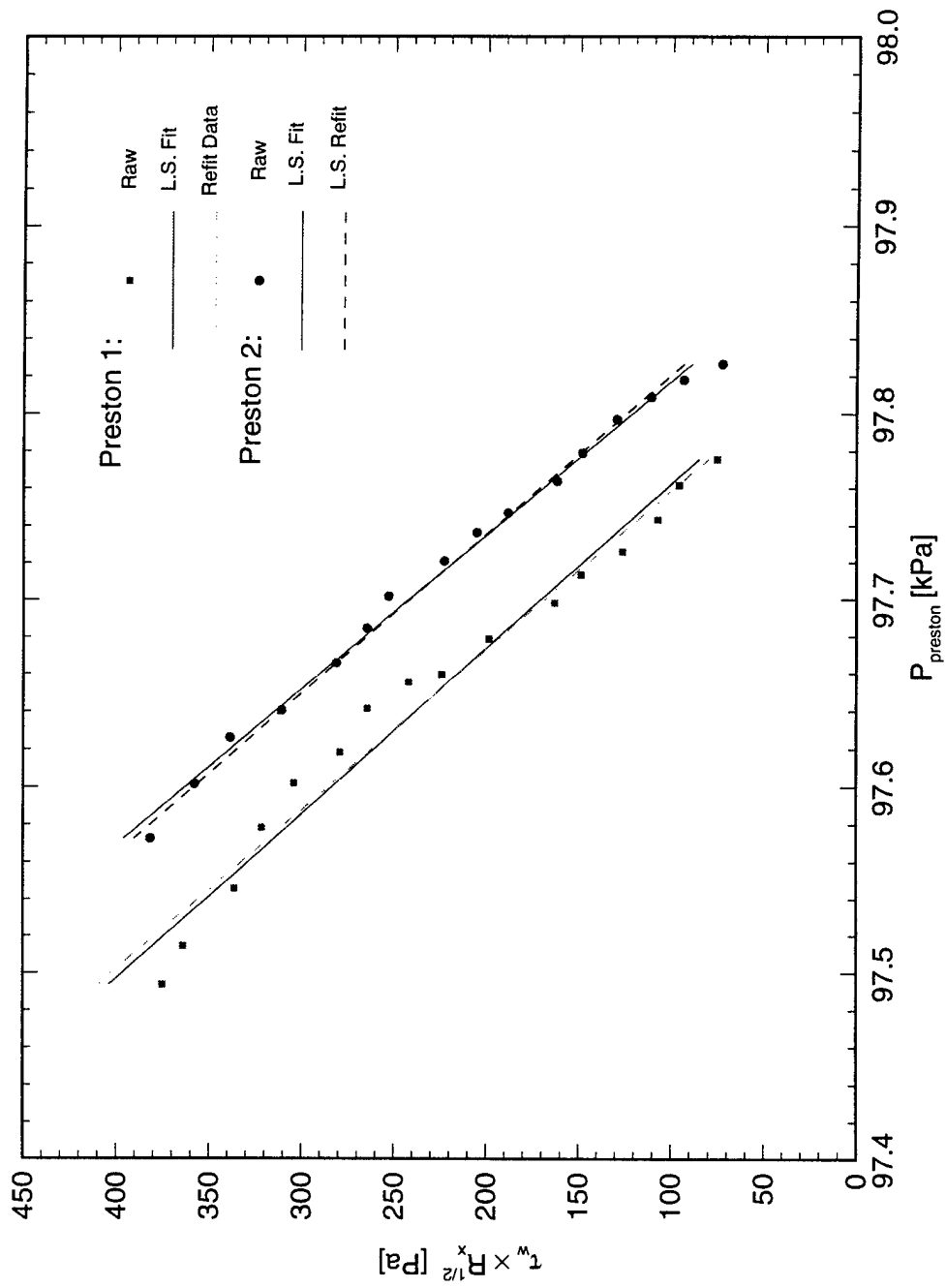


Figure 6.7: Preston-tube skin-friction calibration curve for different Reynolds number (Klebanoff Flat Plate).

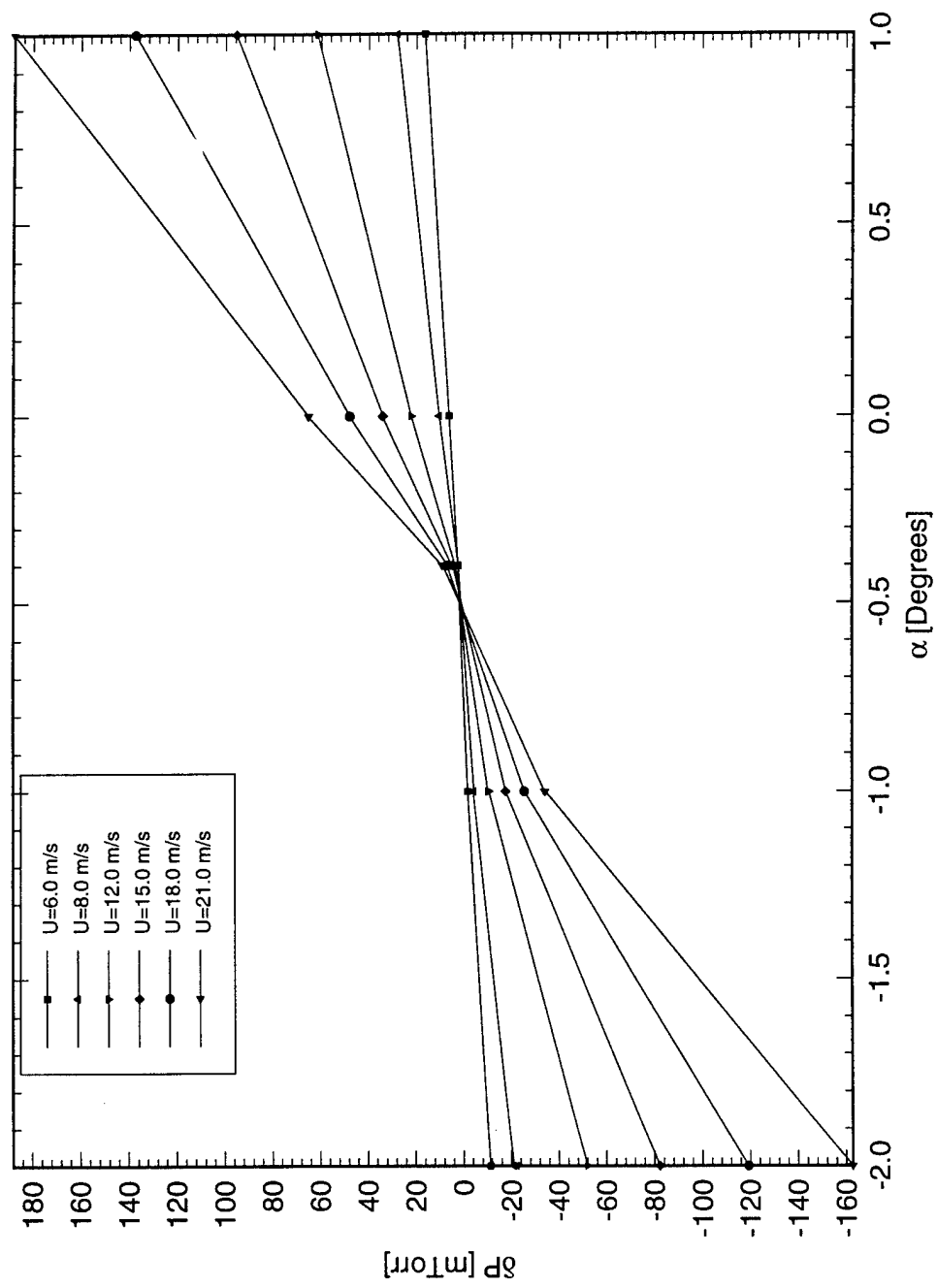


Figure 6.8: Symmetric-flow measurements on the 67:1 ellipse test model using the leading-edge static pressure ports.

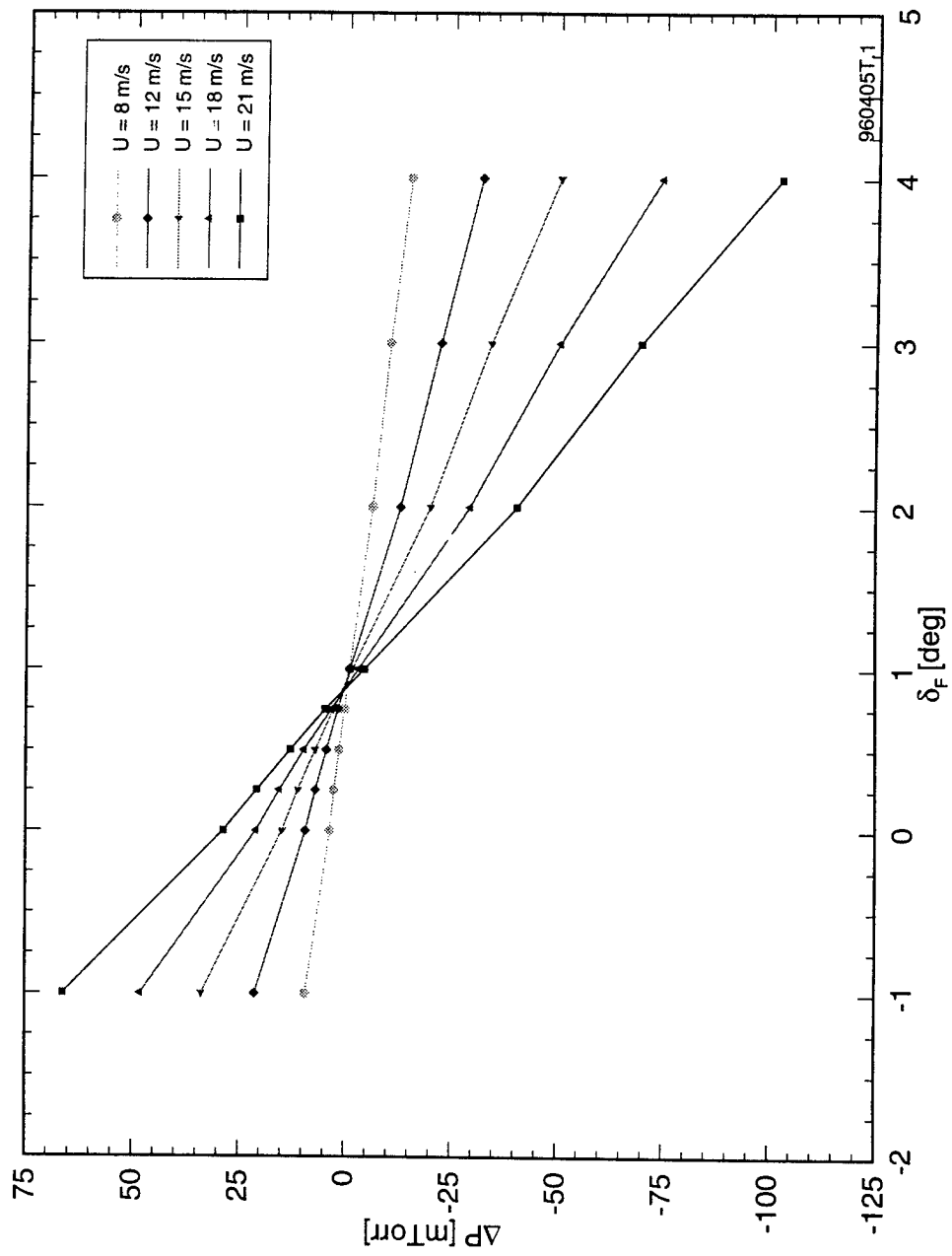


Figure 6.9: Symmetric-flow measurements on the VPI flat plate using the top leading-edge static pressure ports.

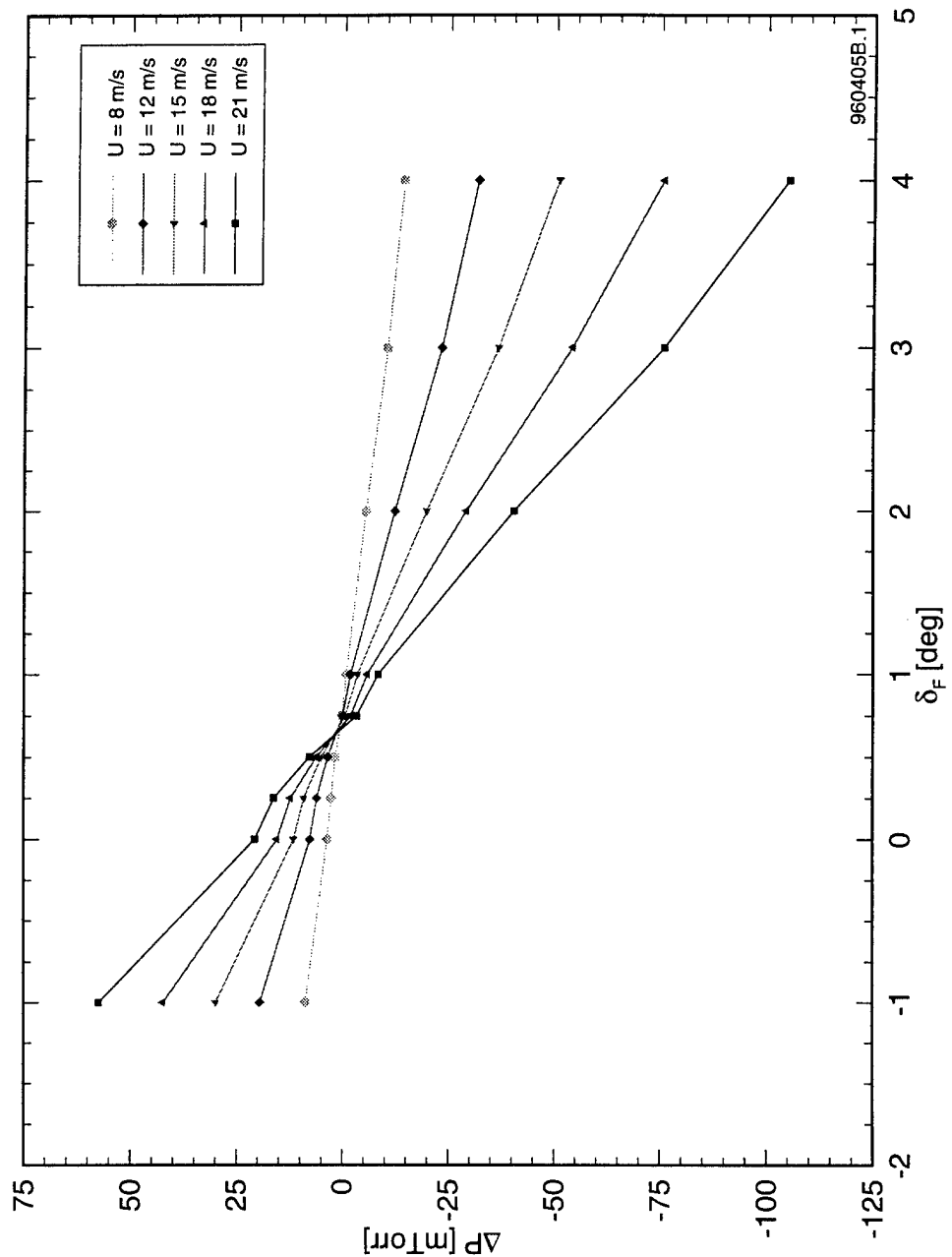


Figure 6.10: Symmetric-flow measurements on the VPI flat plate using the bottom leading-edge static pressure ports.

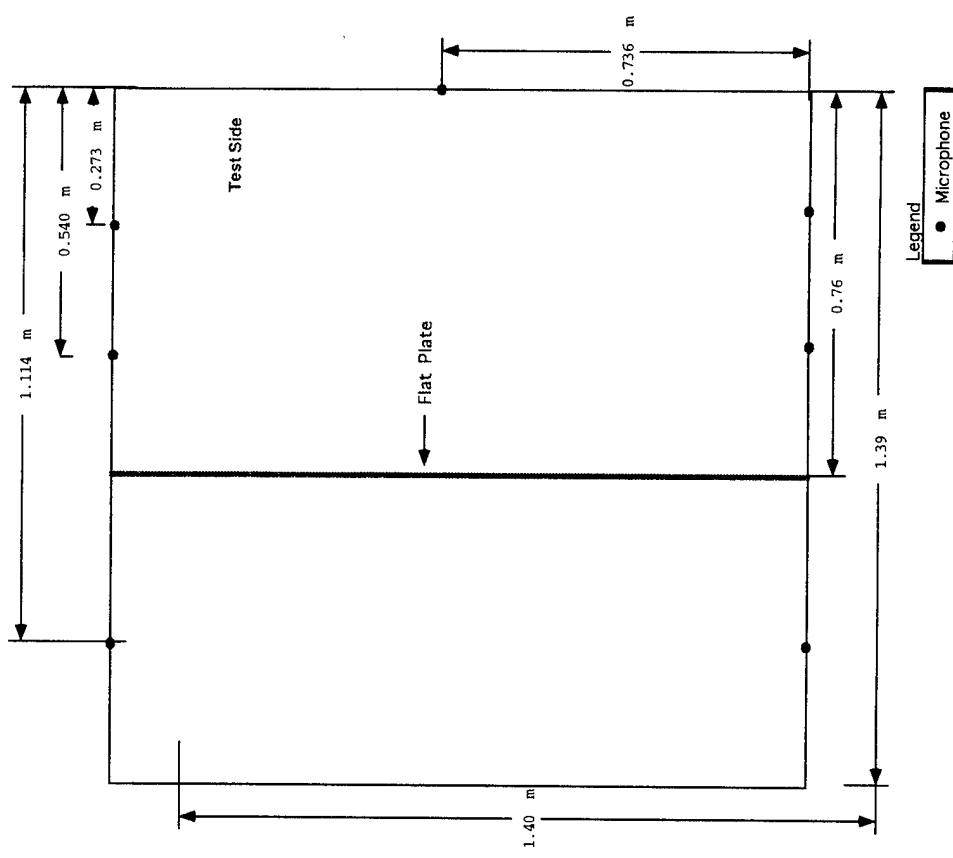


Figure 7.1: Location of microphone ports on test-section perimeter

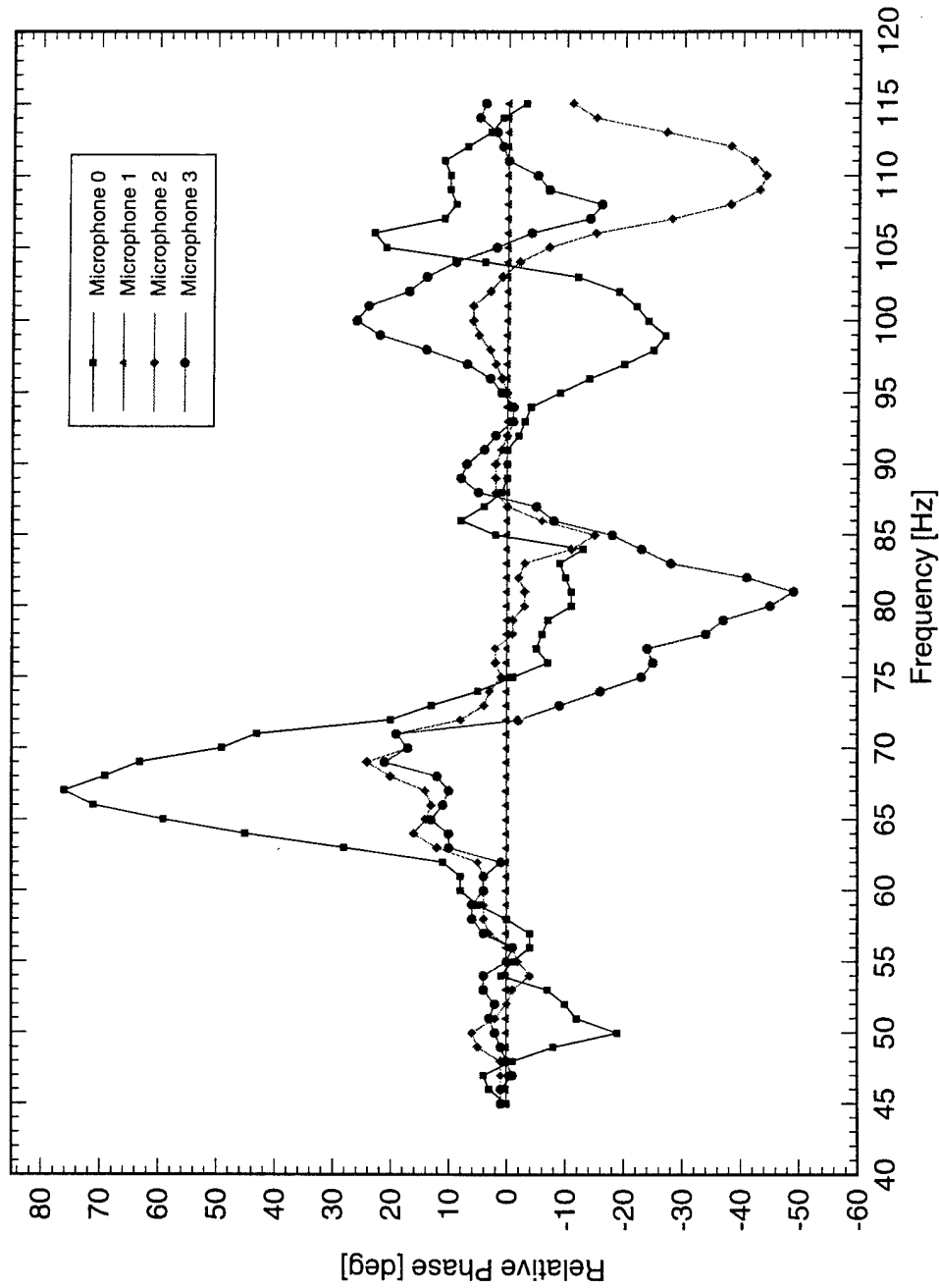


Figure 7.2: Microphone relative-phase measurements for $U_{\infty} = 8.0$ m/s and $V_{sp} = 0.5$ V_{rms}. Relative microphone placed at $\hat{x}_o = -298$ mm, $\hat{y}_o = 540$ mm, and $\hat{z}_o = 0$ mm.

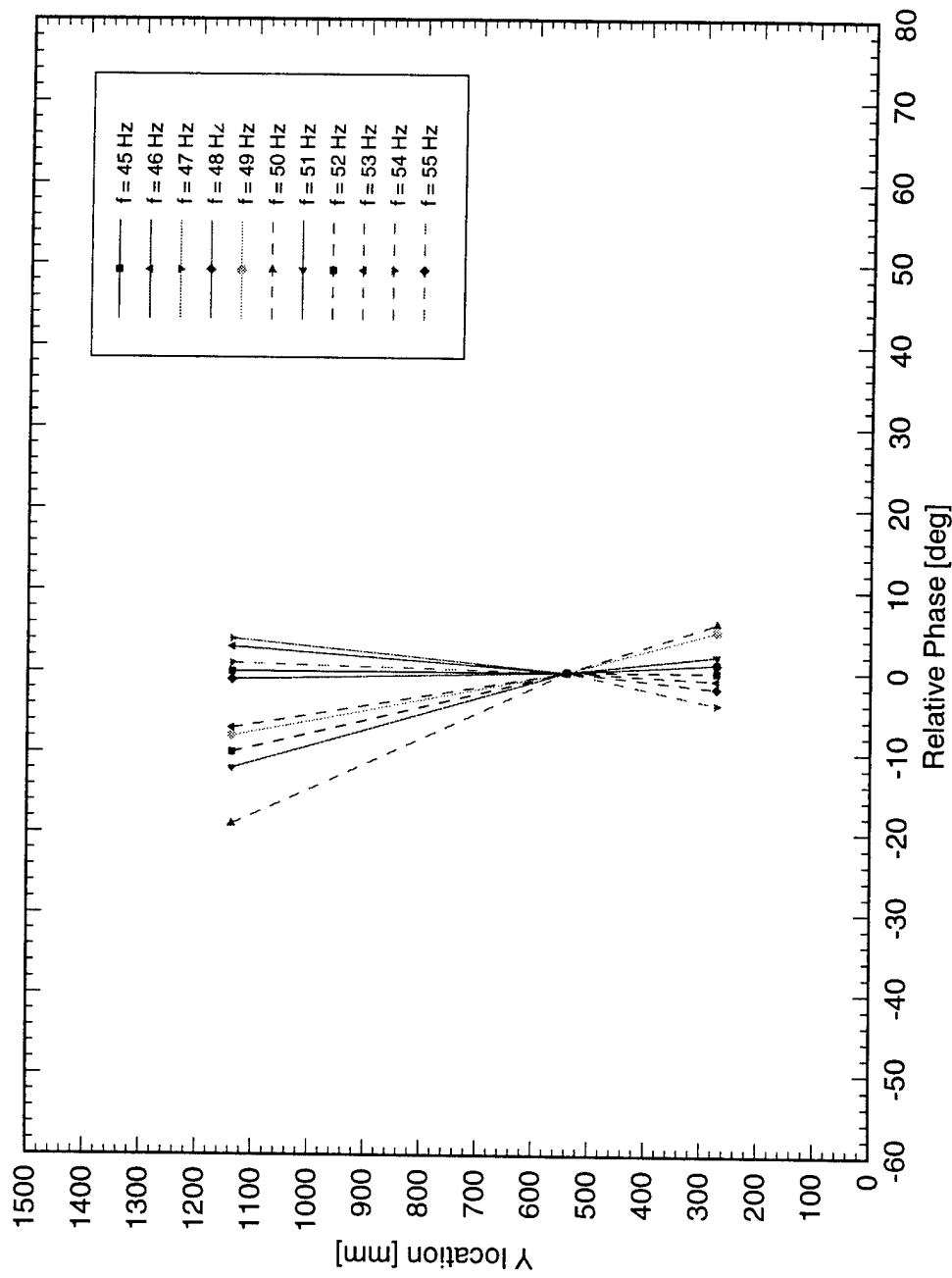


Figure 7.3: Microphone relative-phase measurements for $f = 45\text{--}55$ Hz, $U_\infty = 8.0$ m/s, and $V_{sp} = 0.5$ V_{rms}. Relative microphone placed at $\hat{x}_o = -298$ mm, $\hat{y}_o = 540$ mm, and $\hat{z}_o = 0$ mm.

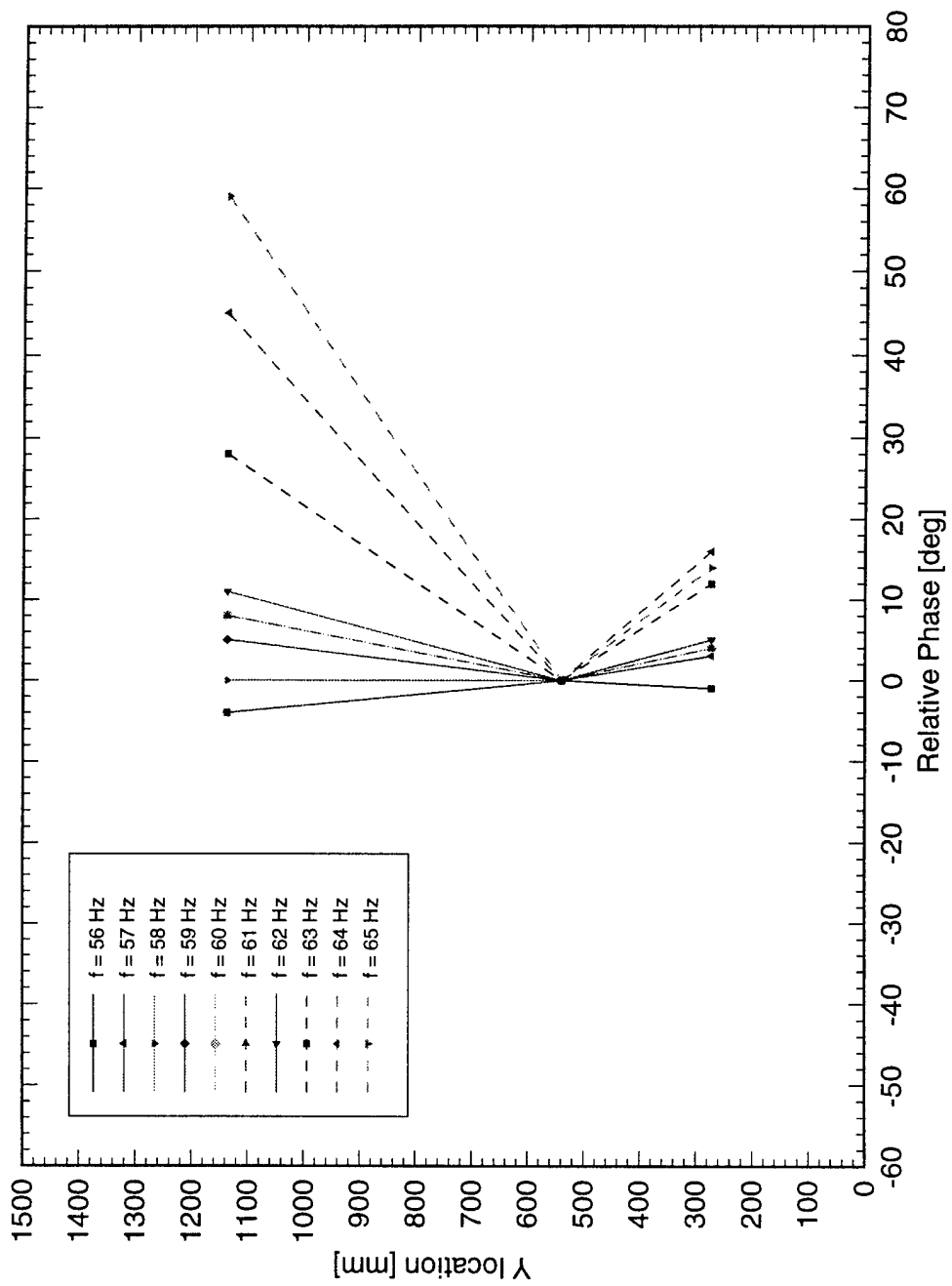


Figure 7.4: Microphone relative-phase measurements for $f = 56\text{--}65 \text{ Hz}$, $U_\infty = 8.0 \text{ m/s}$, and $V_{sp} = 0.5 \text{ V}_{rms}$. Relative microphone placed at $\hat{x}_o = -2985 \text{ mm}$, $\hat{y}_o = 540 \text{ mm}$, and $\hat{z}_o = 0 \text{ mm}$.

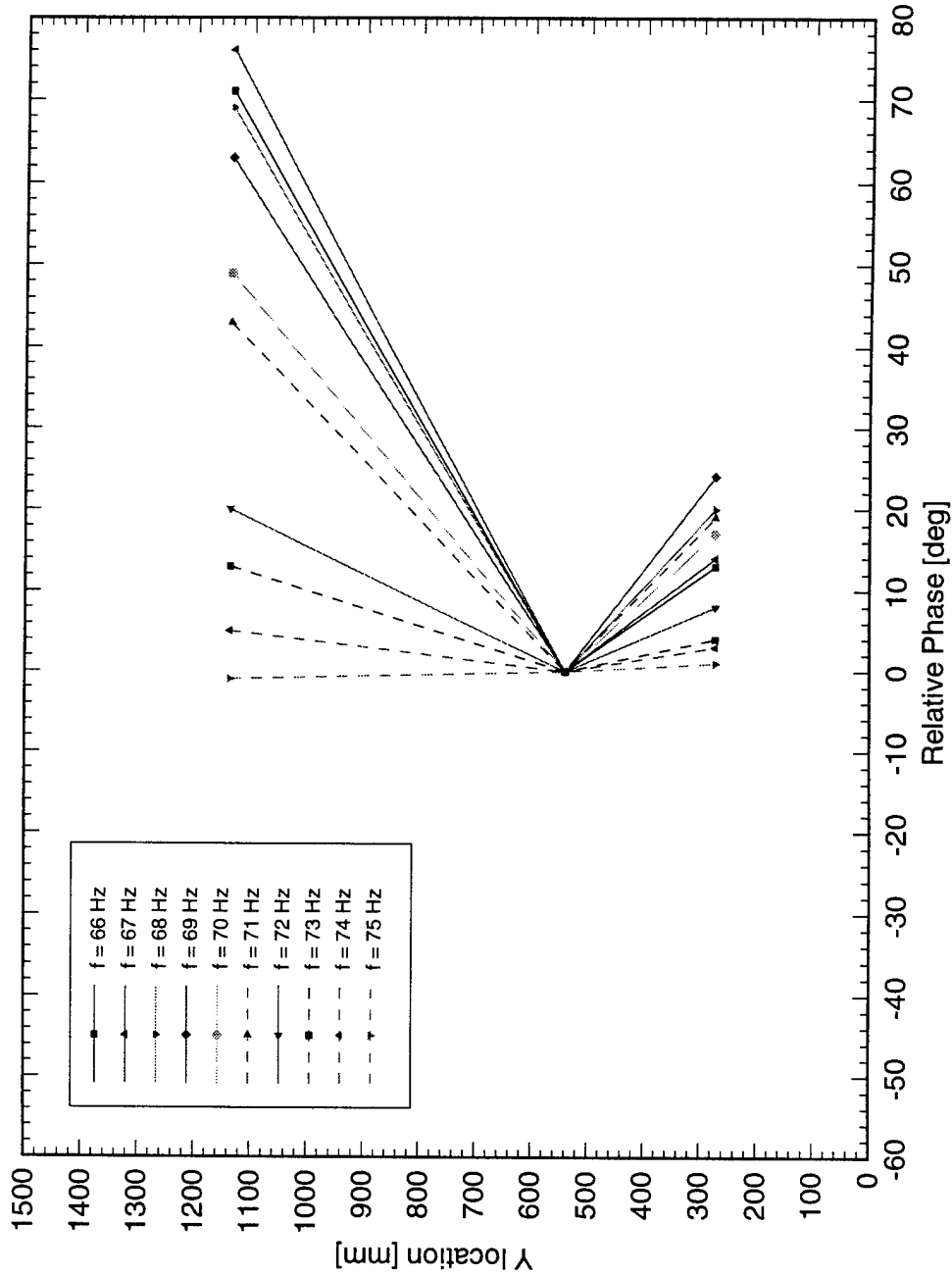


Figure 7.5: Microphone relative-phase measurements for $f = 66\text{--}75$ Hz, $U_\infty = 8.0$ m/s, and $V_{sp} = 0.5 V_{rms}$. Relative microphone placed at $\hat{x}_o = -298$ mm, $\hat{y}_o = 540$ mm, and $\hat{z}_o = 0$ mm.

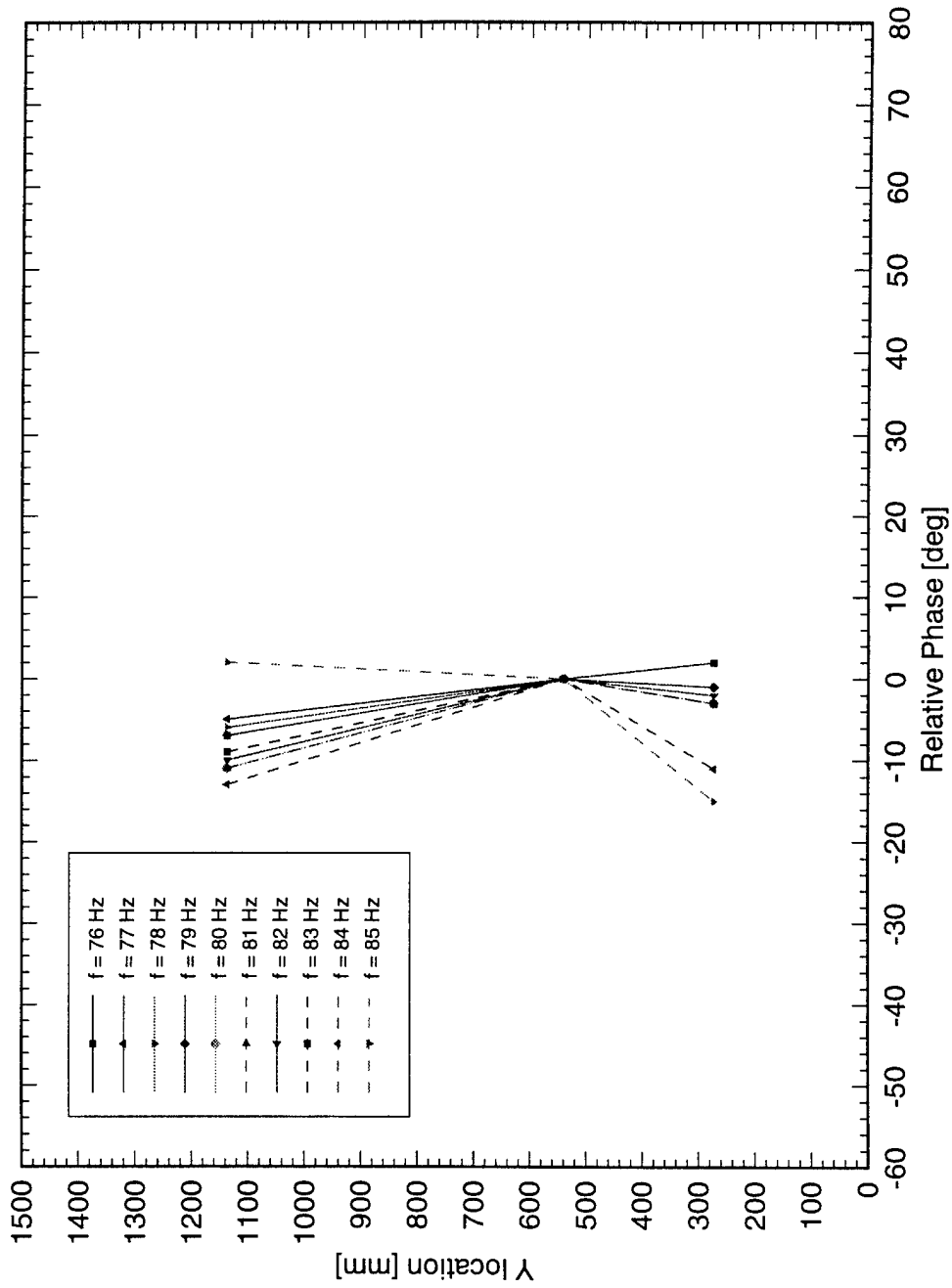


Figure 7.6: Microphone relative-phase measurements for $f = 76\text{--}85 \text{ Hz}$, $U_\infty = 8.0 \text{ m/s}$, and $V_{sp} = 0.5 \text{ V}_{rms}$. Relative microphone placed at $\hat{x}_o = -298 \text{ mm}$, $\hat{y}_o = 540 \text{ mm}$, and $\hat{z}_o = 0 \text{ mm}$.

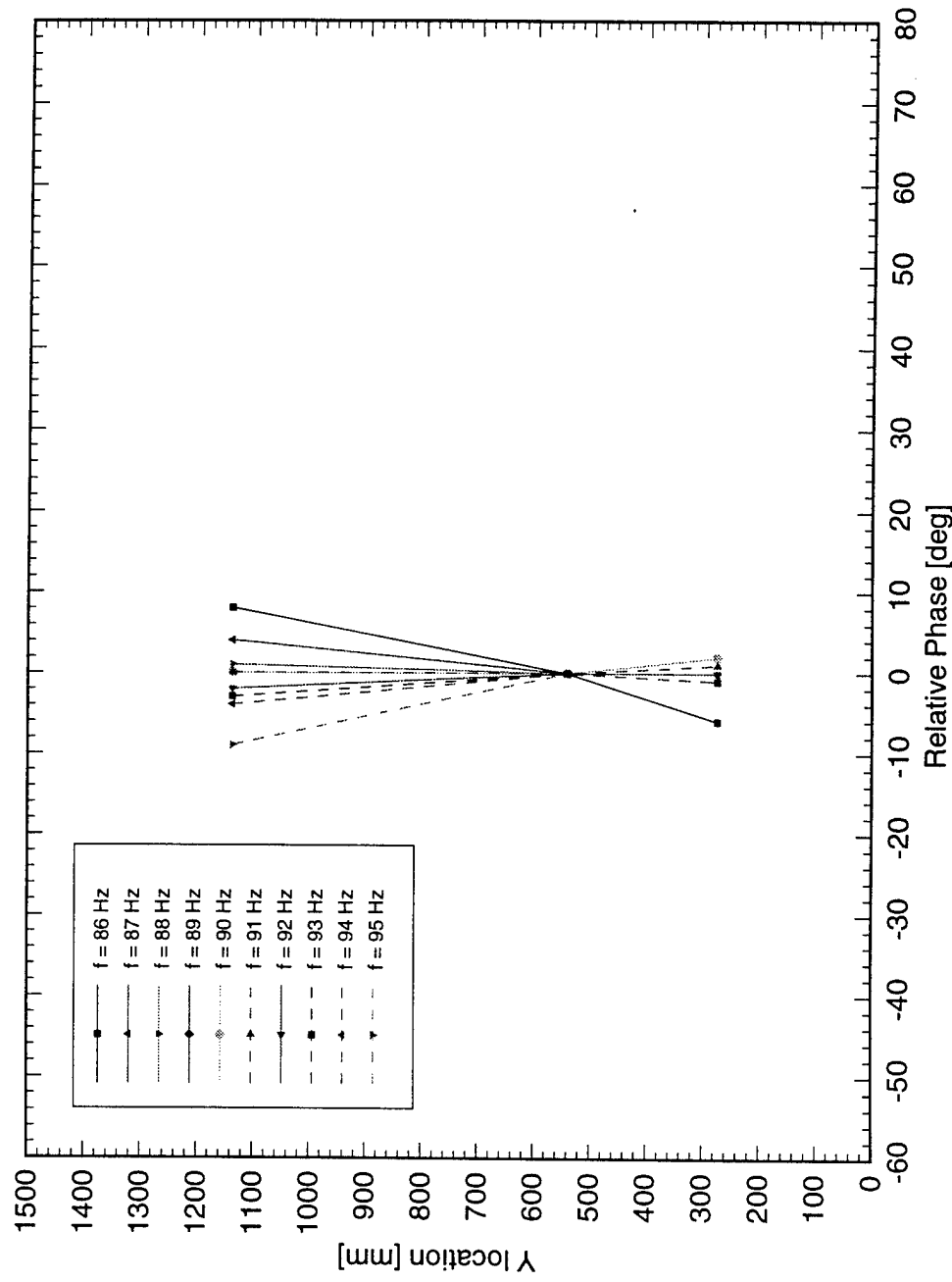


Figure 7.7: Microphone relative-phase measurements for $f = 86\text{--}95 \text{ Hz}$, $U_\infty = 8.0 \text{ m/s}$, and $V_{sp} = 0.5 V_{rms}$. Relative microphone placed at $\hat{x}_o = -298 \text{ mm}$, $\hat{y}_o = 540 \text{ mm}$, and $\hat{z}_o = 0 \text{ mm}$.

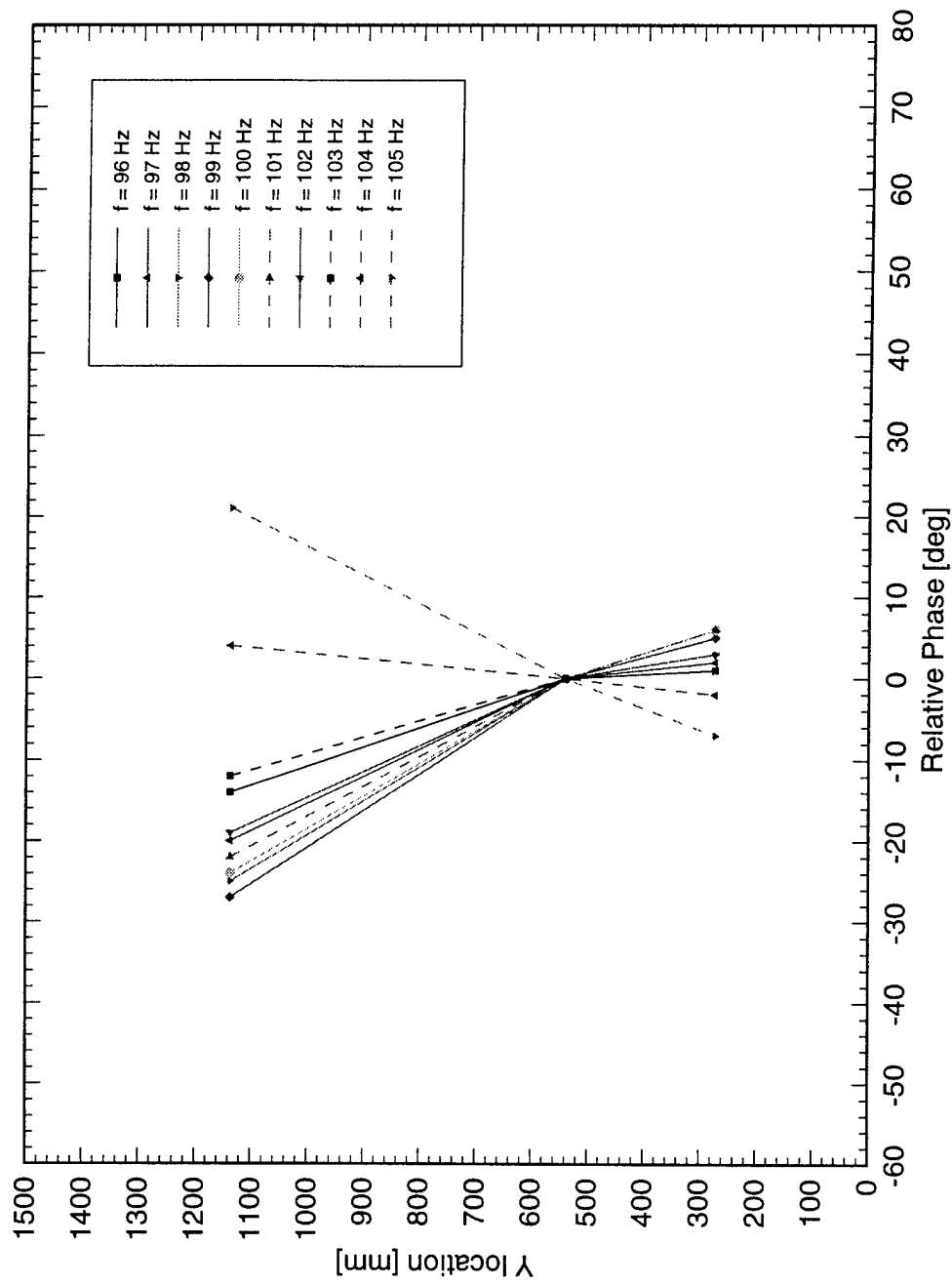


Figure 7.8: Microphone relative-phase measurements for $f = 96\text{--}105\text{ Hz}$, $U_{\infty} = 8.0\text{ m/s}$, and $V_{sp} = 0.5\text{ V}_{rms}$. Relative microphone placed at $\hat{x}_o = -298\text{ mm}$, $\hat{y}_o = 540\text{ mm}$, and $\hat{z}_o = 0\text{ mm}$.

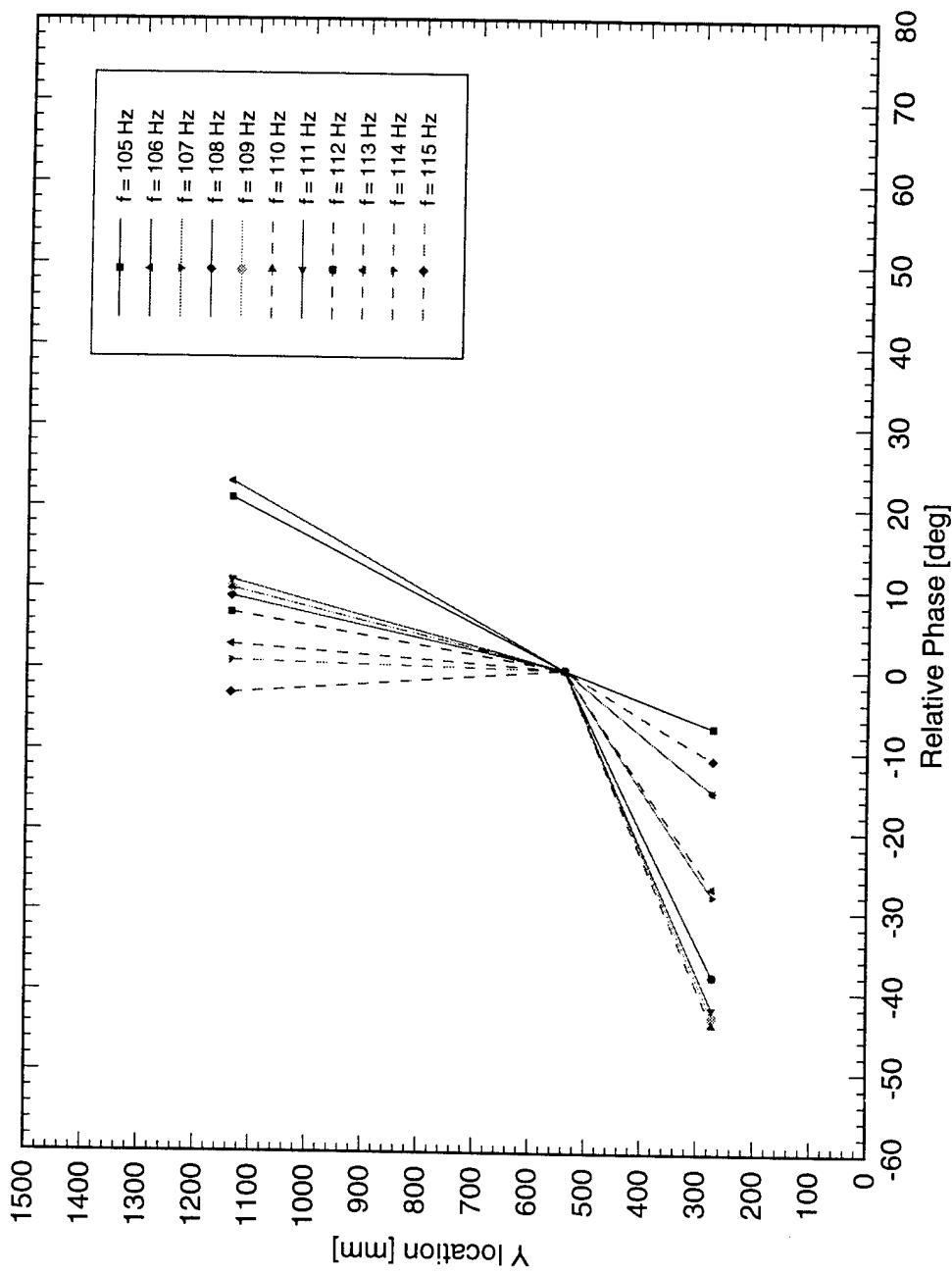


Figure 7.9: Microphone relative-phase measurements for $f = 106\text{--}115 \text{ Hz}$, $U_\infty = 8.0 \text{ m/s}$, and $V_{sp} = 0.5 V_{rms}$. Relative microphone placed at $\hat{x}_o = -298 \text{ mm}$, $\hat{y}_o = 540 \text{ mm}$, and $\hat{z}_o = 0 \text{ mm}$.

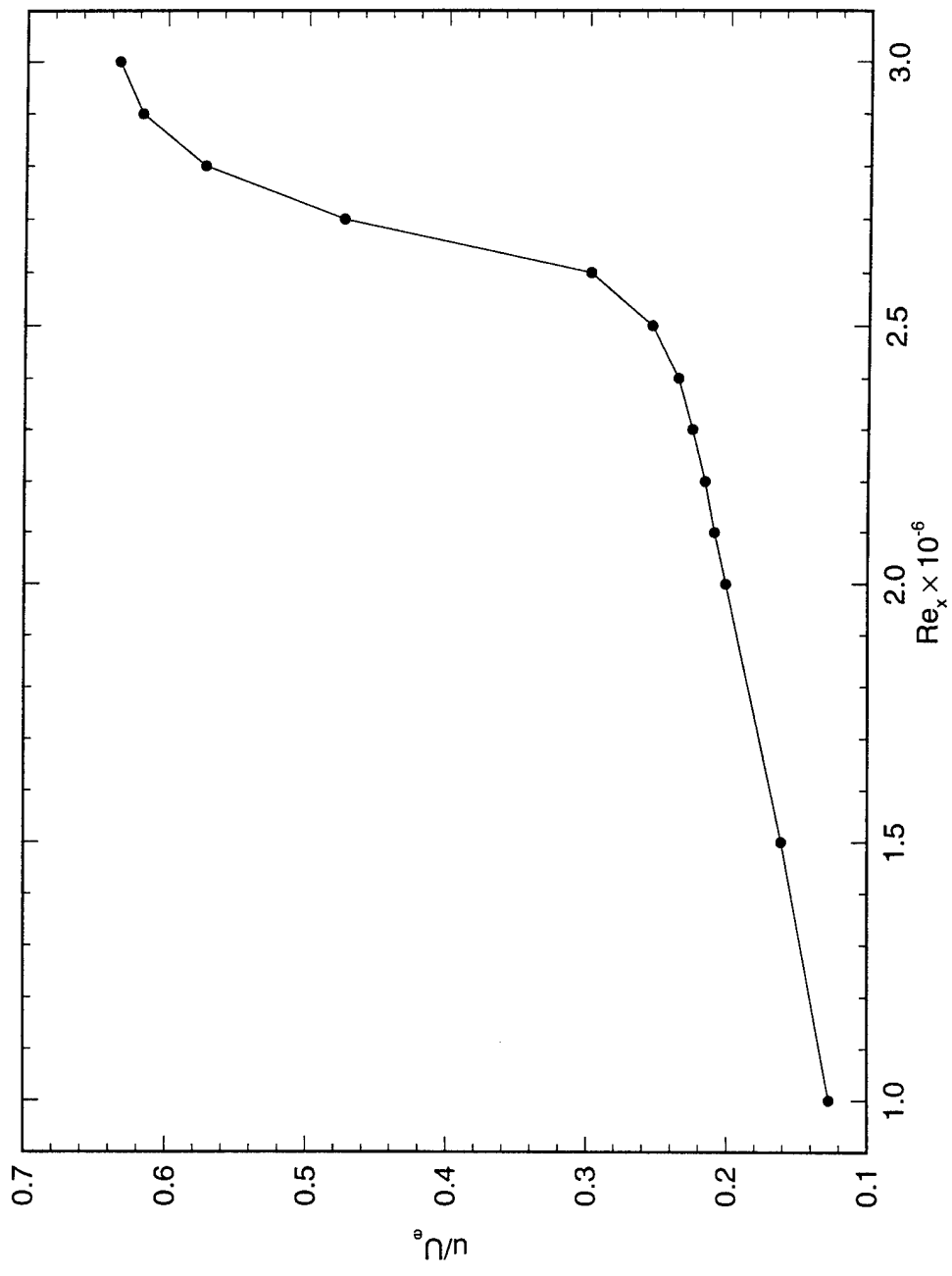


Figure 7.10: Transition Reynolds number, $Re_{tr} = 2.6 \times 10^6$, obtained with a fixed hot wire at $\hat{x} = 1.8$ m, $\hat{z} = 0.01$ mm (Klebanoff flat plate).

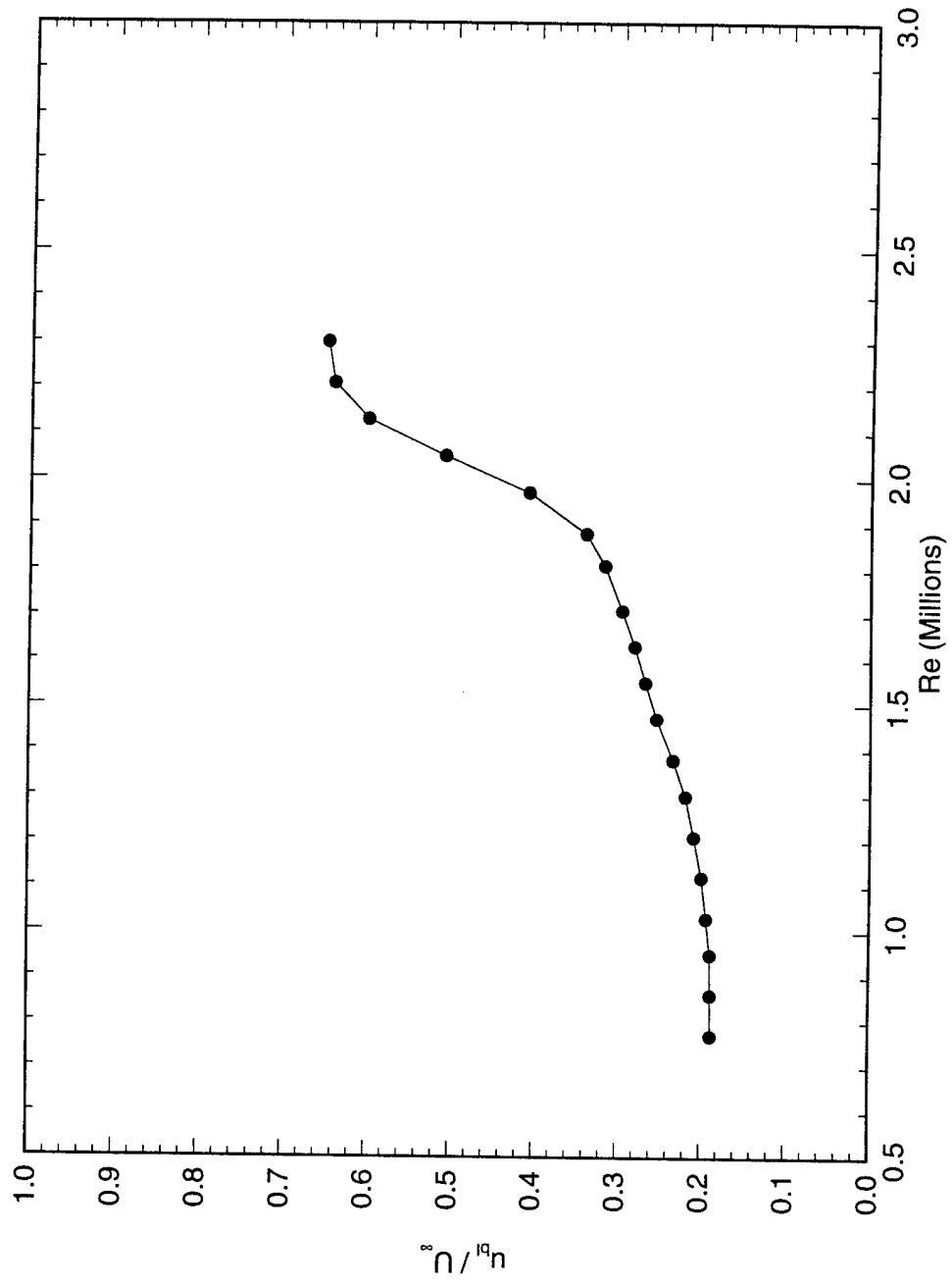


Figure 7.11: Transition Reynolds number, $Re_{tr} = 1.9 \times 10^6$, obtained with hot wire at $\hat{x} = 1.8$ m, $\hat{z} = 0.01$ mm (VPI flat plate).

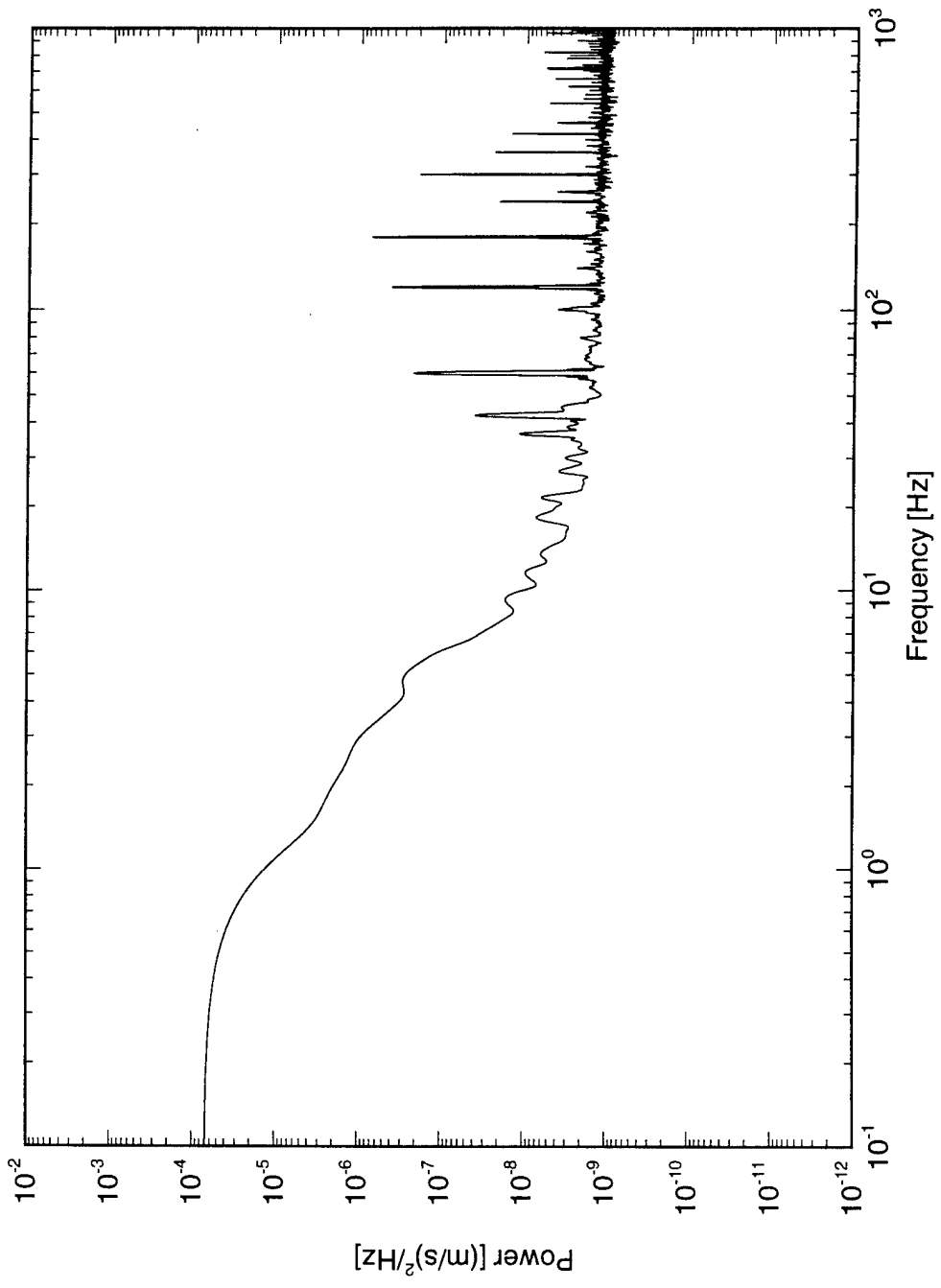


Figure 7.12: Freestream disturbance spectrum at $U_\infty = 5 \text{ m/s}$ with the plenum vented (DC coupled, band pass 0.1–1000 Hz, Tektronix filters). Measurements taken at $\hat{x} = 1.0 \text{ m}$.

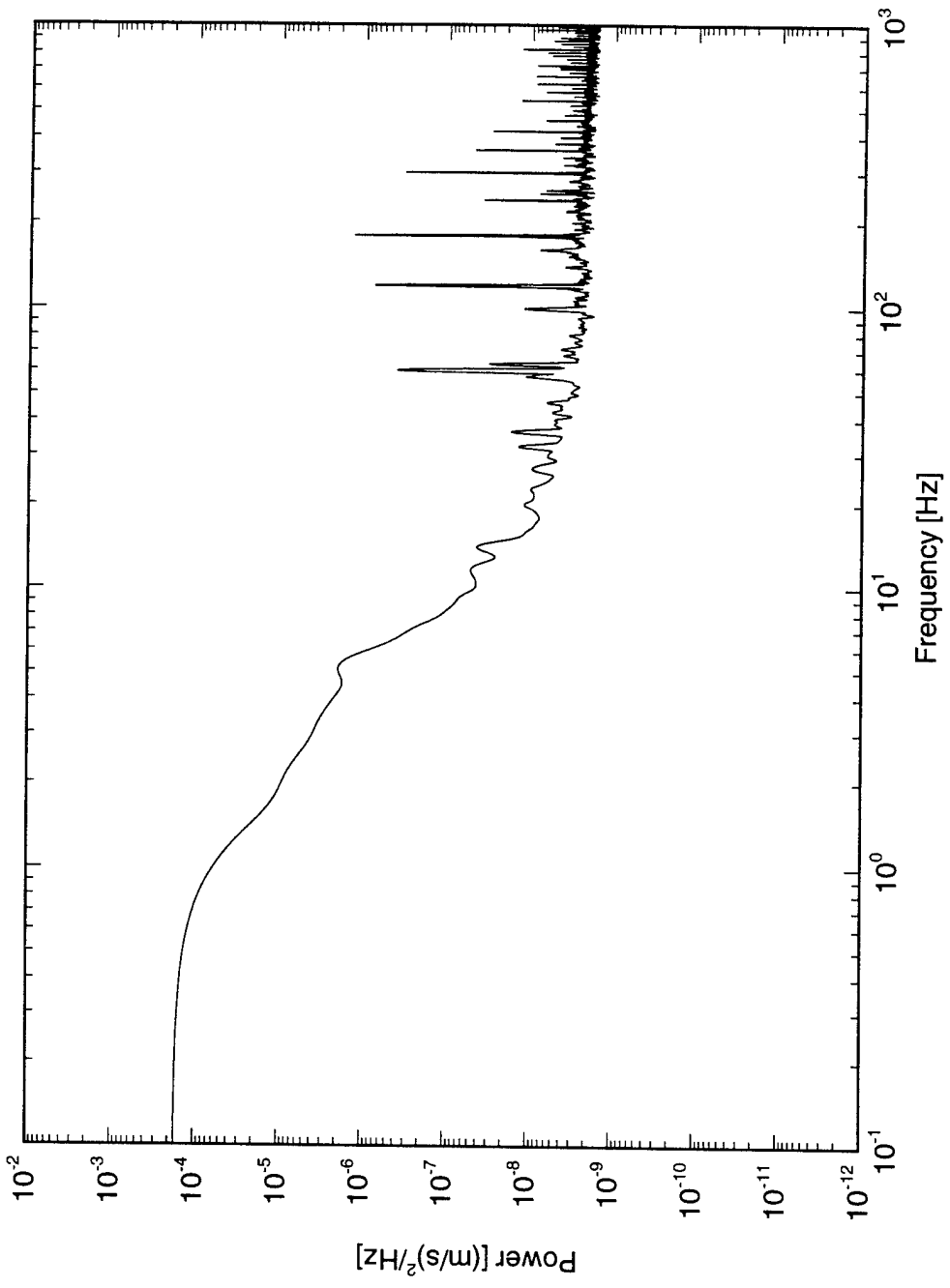


Figure 7.13: Freestream disturbance spectrum at $U_\infty = 8 \text{ m/s}$ with the plenum vented (DC coupled, band pass 0.1–1000 Hz, Tektronix filters). Measurements taken at $\hat{x} = 1.0 \text{ m}$.

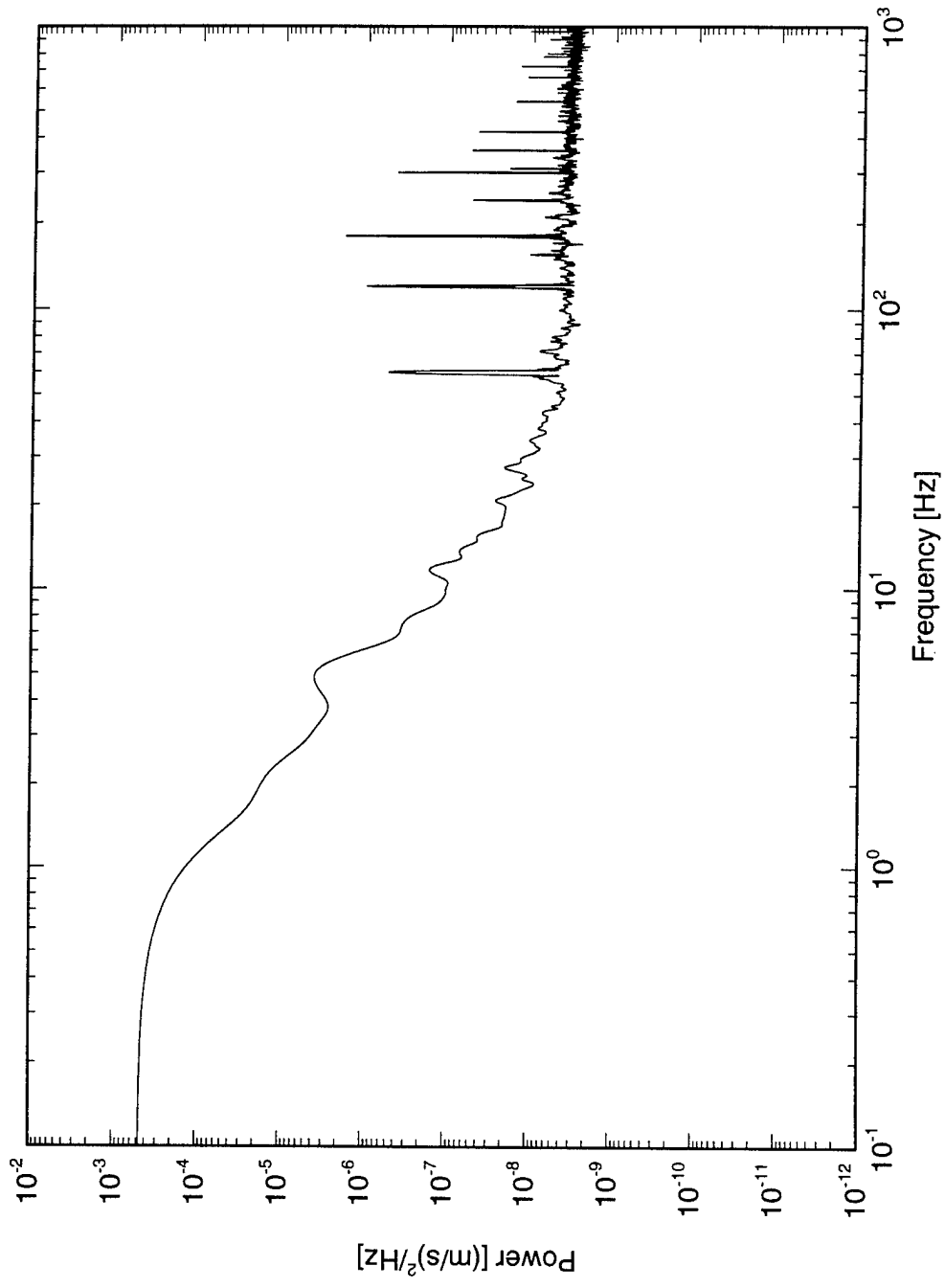


Figure 7.14: Freestream disturbance spectrum at $U_\infty = 10 \text{ m/s}$ with the plenum vented (DC coupled, band pass 0.1–1000 Hz, Tektronix filters). Measurements taken at $\hat{x} = 1.0 \text{ m}$.

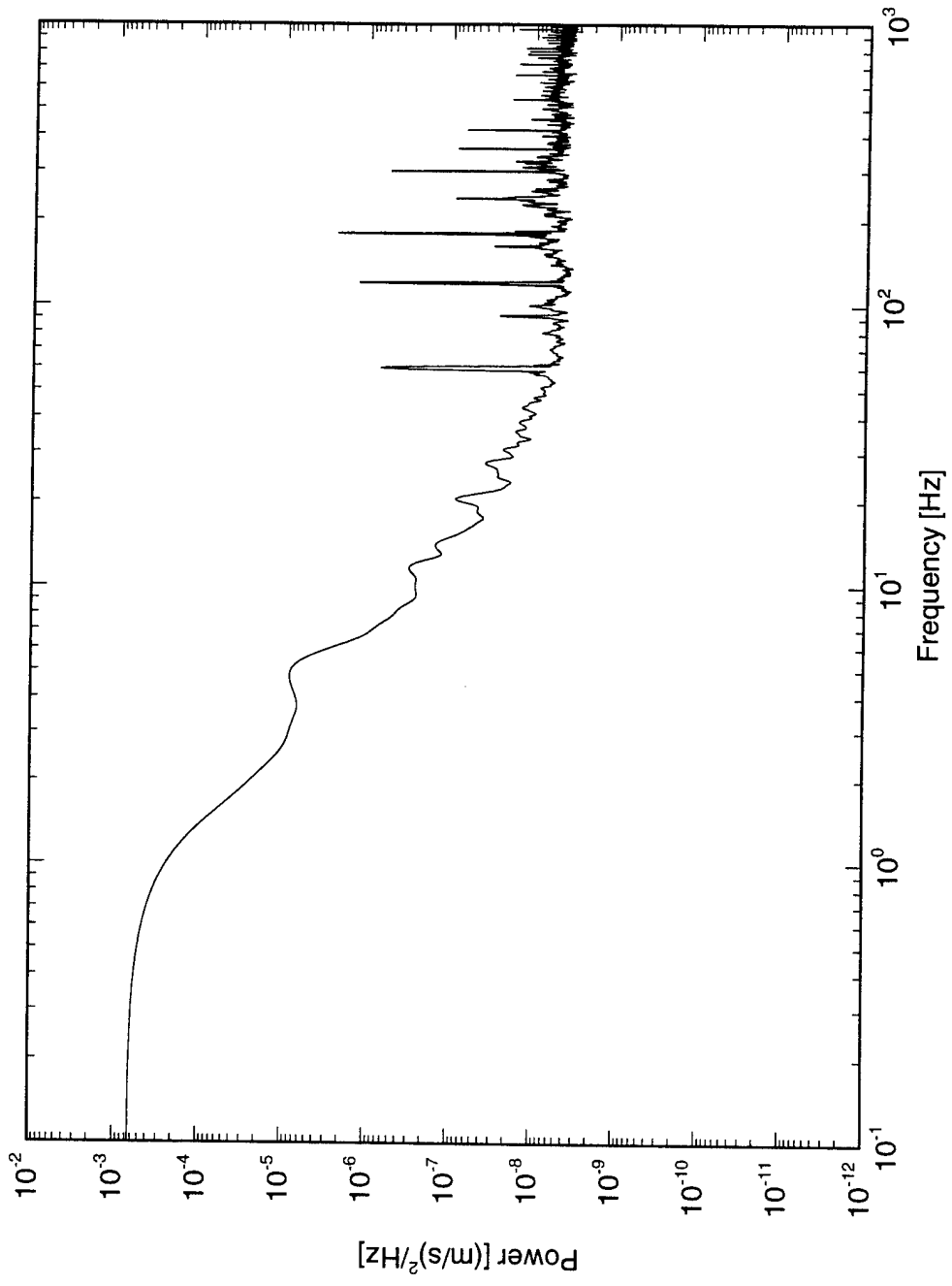


Figure 7.15: Freestream disturbance spectrum at $U_\infty = 12 \text{ m/s}$ with the plenum vented (DC coupled, band pass 0.1–1000 Hz, Tektronix filters). Measurements taken at $\hat{x} = 1.0 \text{ m}$.

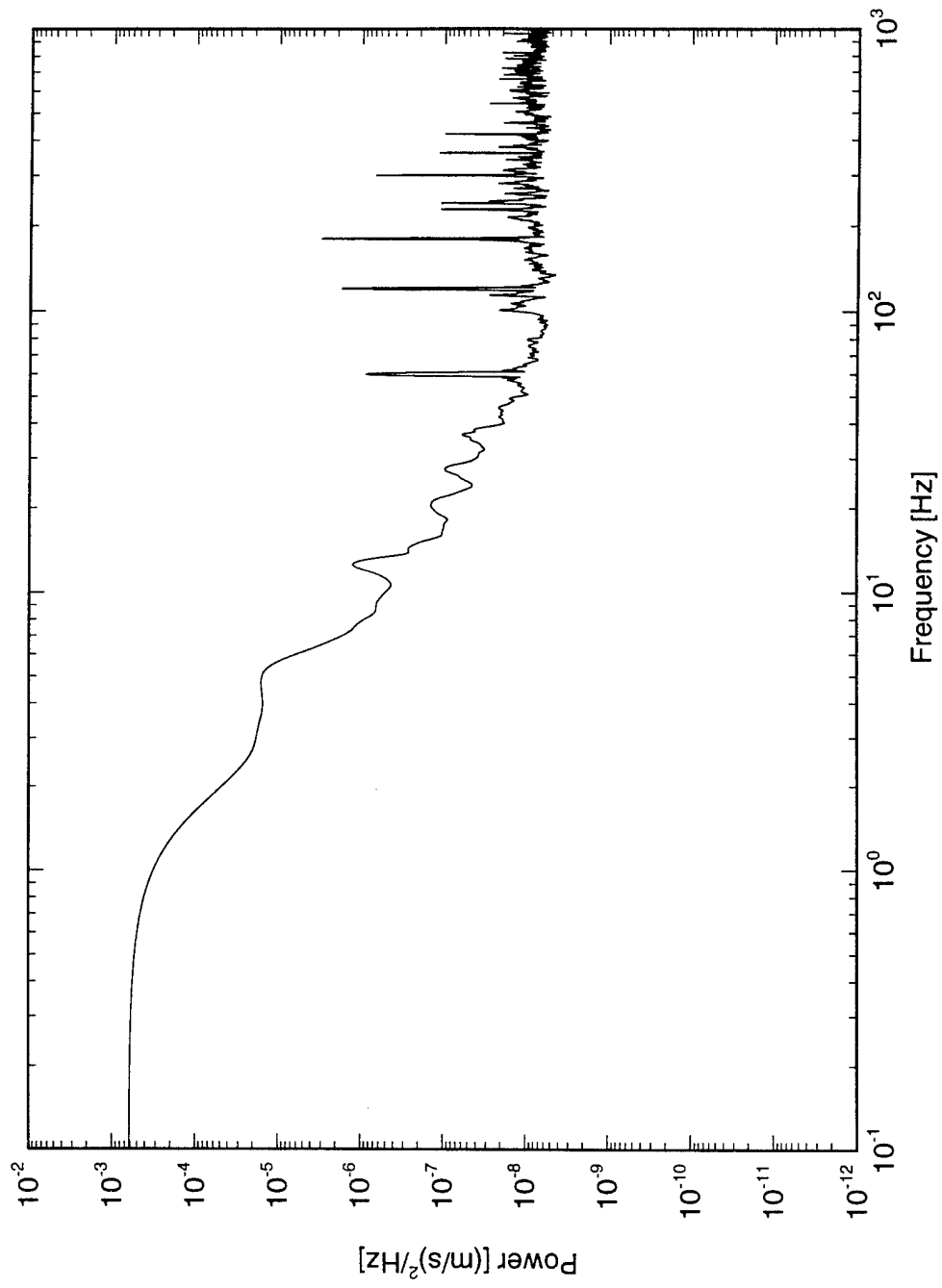


Figure 7.16: Freestream disturbance spectrum at $U_\infty = 15 \text{ m/s}$ with the plenum vented (DC coupled, band pass 0.1–1000 Hz, Tektronix filters). Measurements taken at $\hat{x} = 1.0 \text{ m}$.

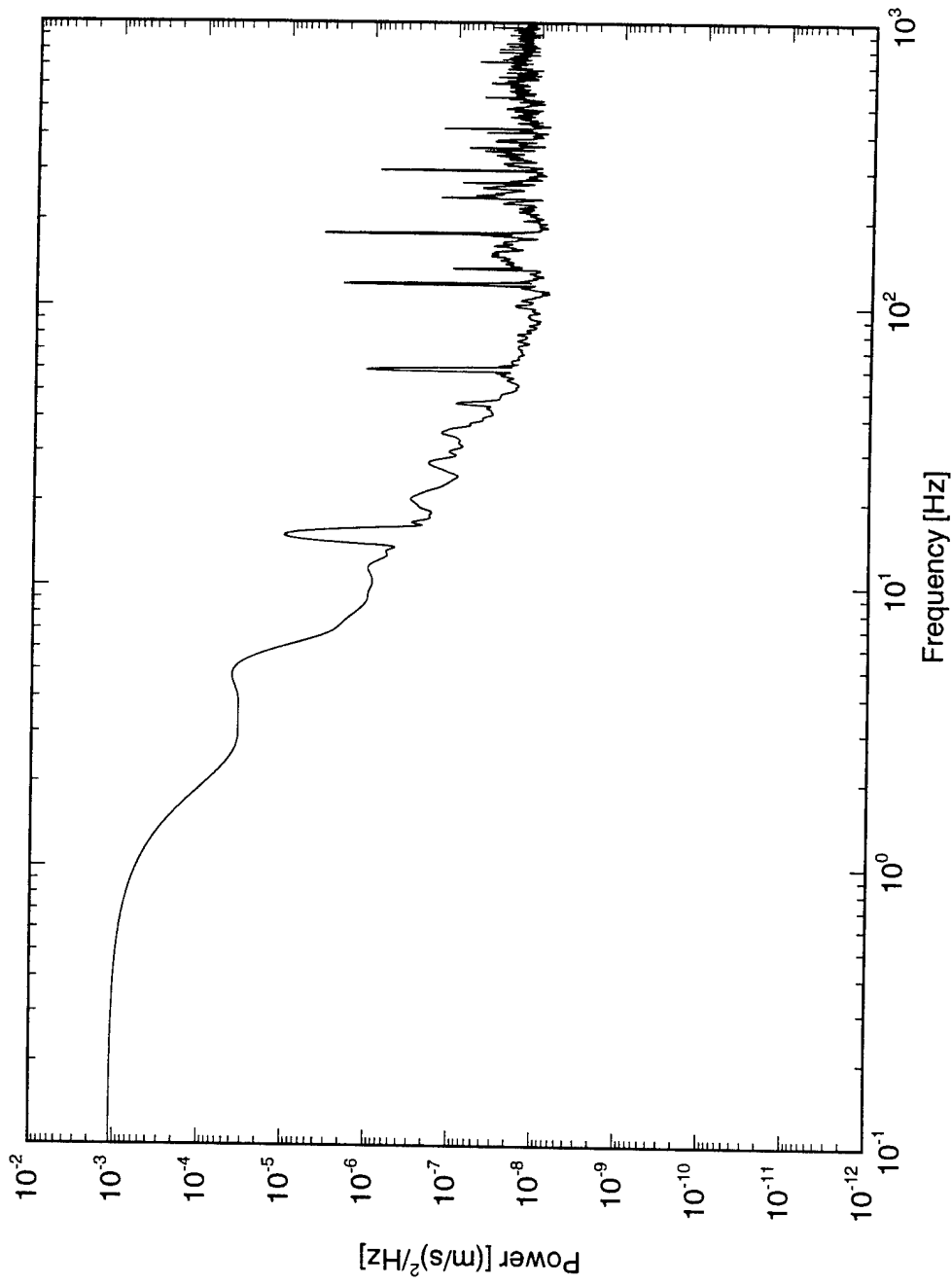


Figure 7.17: Freestream disturbance spectrum at $U_\infty = 18$ m/s with the plenum vented (DC coupled, band pass 0.1–1000 Hz, Tektronix filters). Measurements taken at $\hat{x} = 1.0$ m.

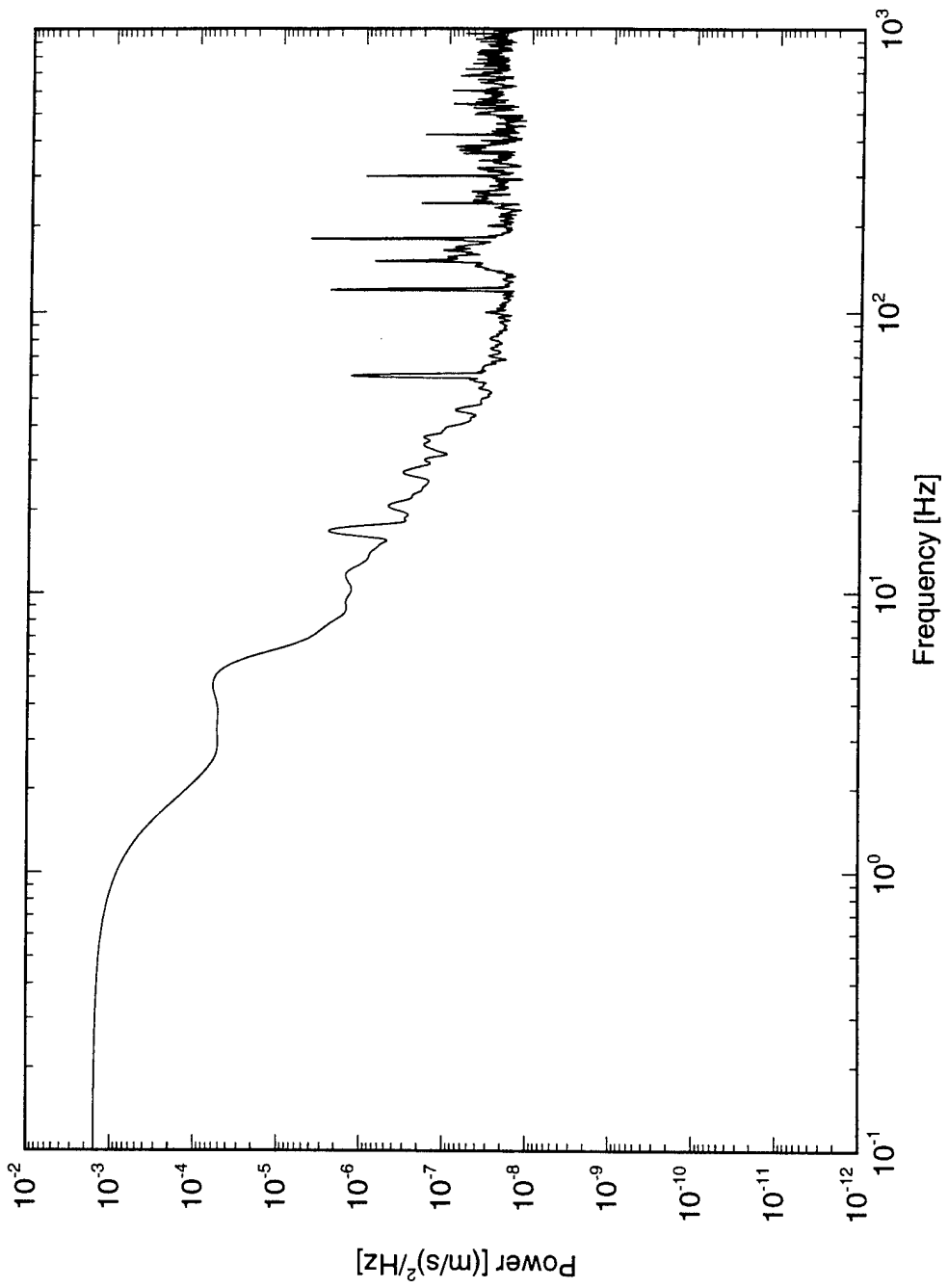


Figure 7.18: Freestream disturbance spectrum at $U_{\infty} = 20$ m/s with the plenum vented (DC coupled, band pass 0.1–1000 Hz, Tektronix filters). Measurements taken at $\hat{x} = 1.0$ m.

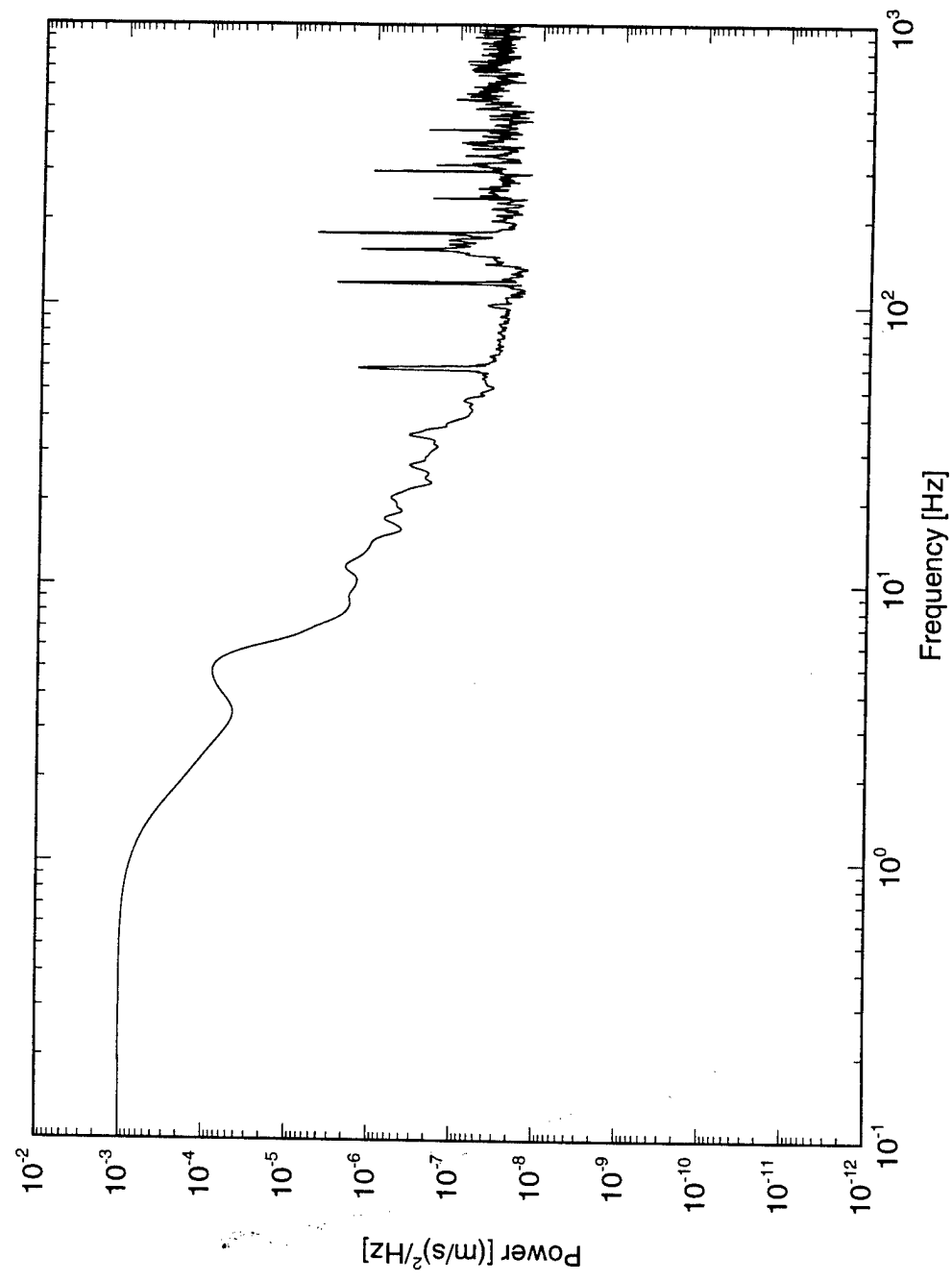


Figure 7.19: Freestream disturbance spectrum at $U_\infty = 21$ m/s with the plenum vented (DC coupled, band pass 0.1–1000 Hz, Tektronix filters). Measurements taken at $\hat{x} = 1.0$ m.

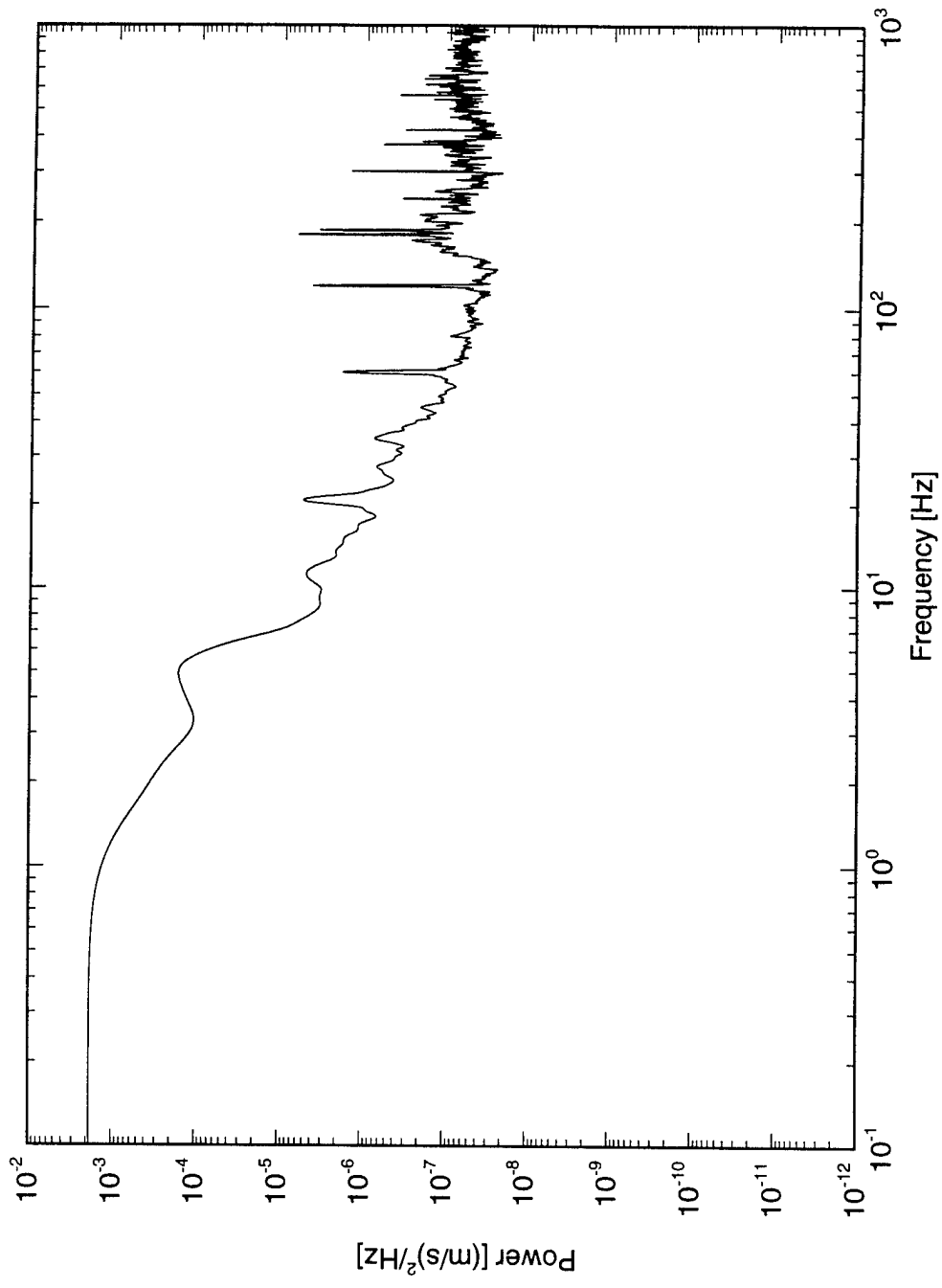


Figure 7.20: Freestream disturbance spectrum at $U_\infty = 25$ m/s with the plenum vented (DC coupled, band pass 0.1-1000 Hz, Tektronix filters). Measurements taken at $\hat{x} = 1.0$ m.

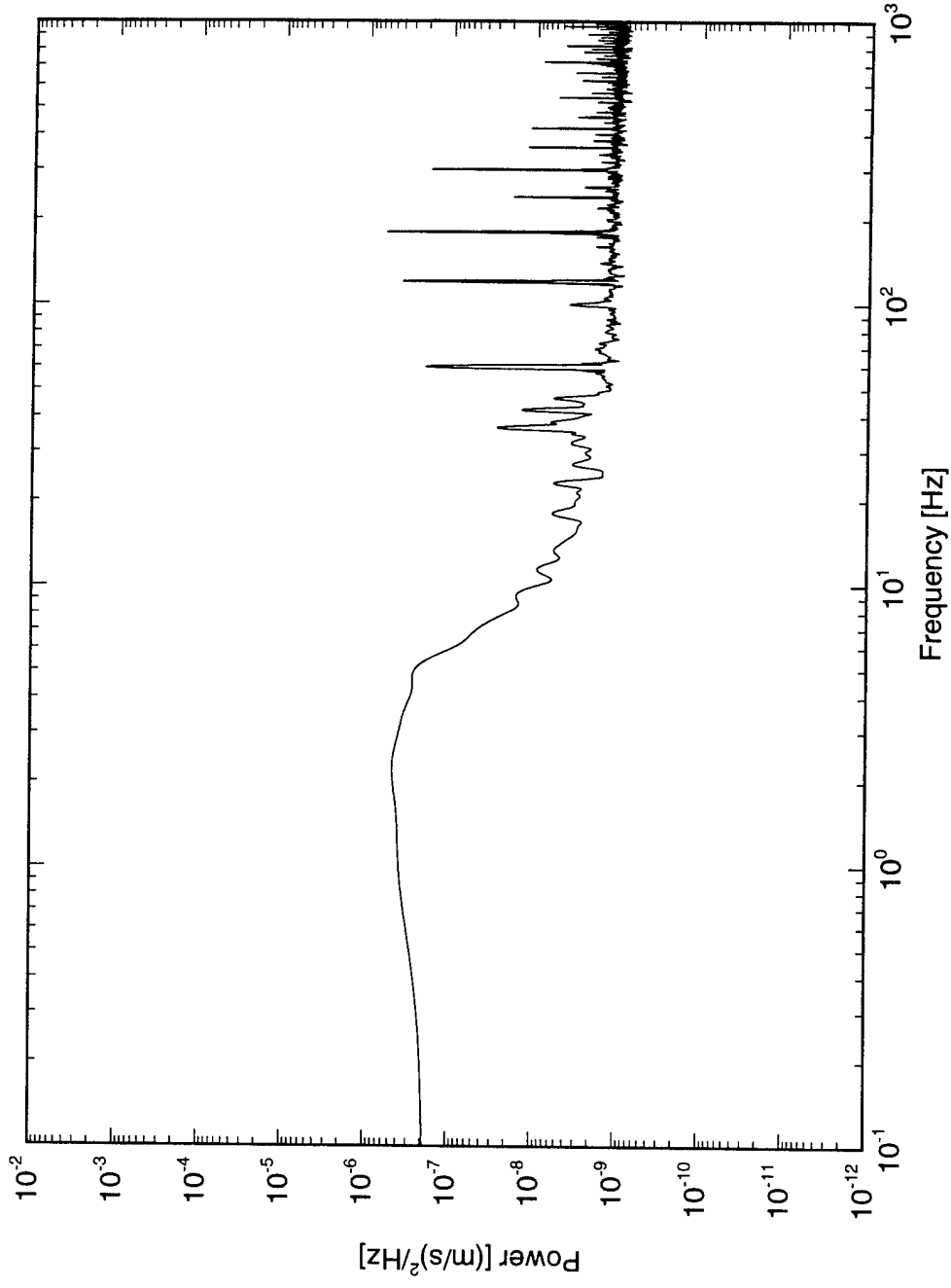


Figure 7.21: Freestream disturbance spectrum at $U_\infty = 5$ m/s with the plenum vented (AC coupled, band pass 2–1000 Hz, Tektronix filters). Measurements taken at $\hat{x} = 1.0$ m.

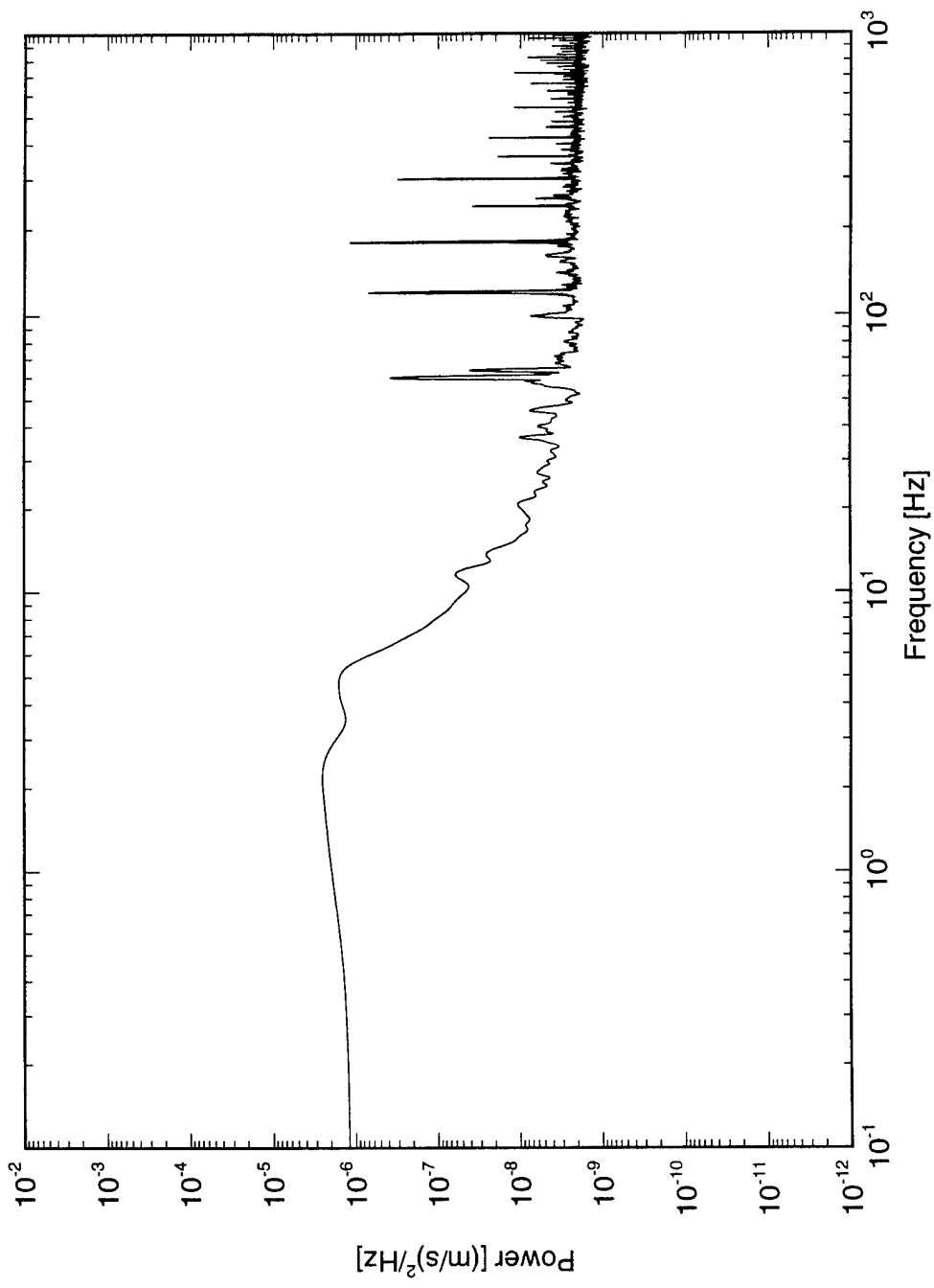


Figure 7.22: Freestream disturbance spectrum at $U_\infty = 8 \text{ m/s}$ with the plenum vented (AC coupled, band pass 2–1000 Hz, Tektronix filters). Measurements taken at $\hat{x} = 1.0 \text{ m}$.

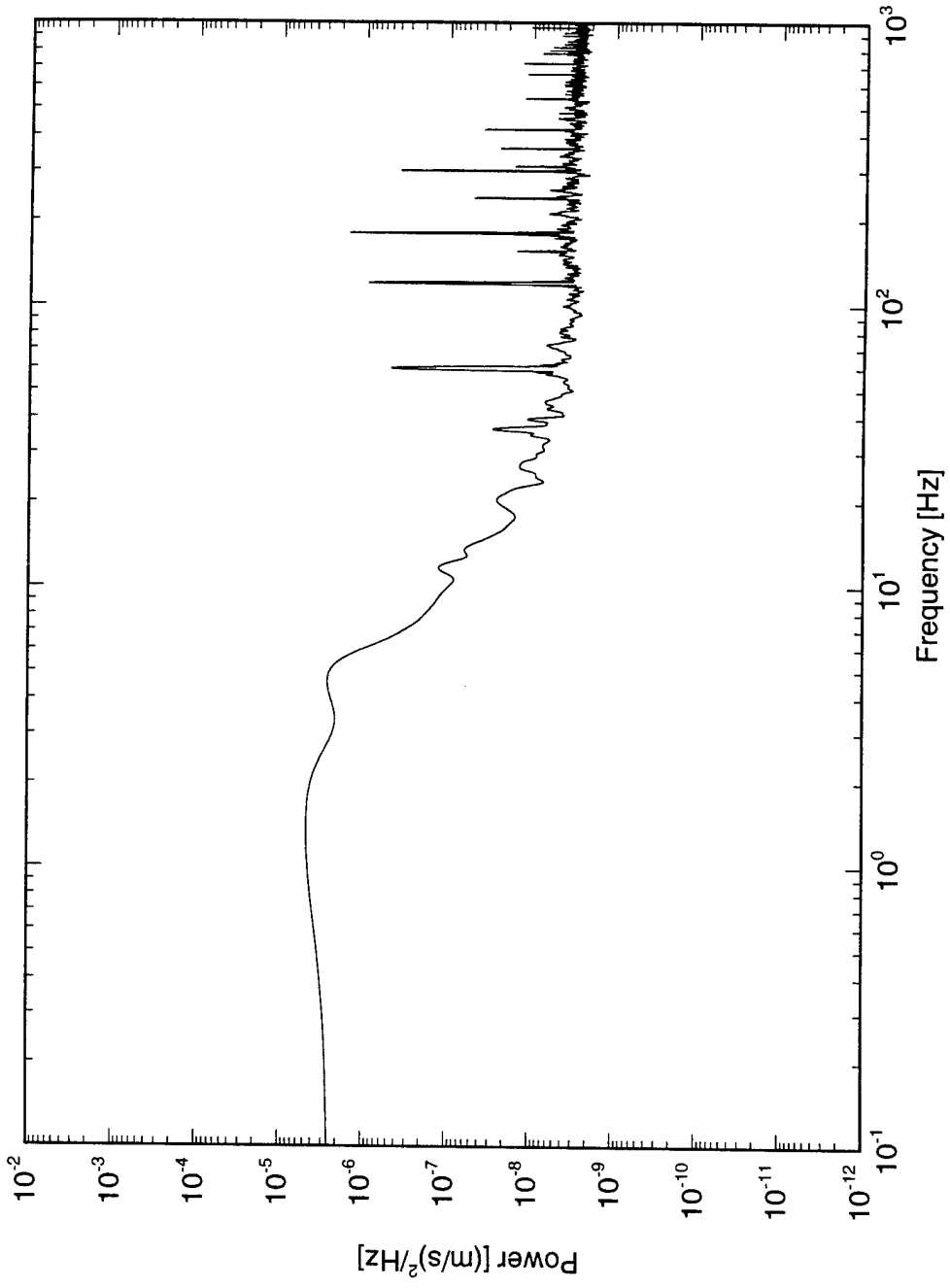


Figure 7.23: Freestream disturbance spectrum at $U_\infty = 10 \text{ m/s}$ with the plenum vented (AC coupled, band pass 2–1000 Hz, Tektronix filters). Measurements taken at $\hat{x} = 1.0 \text{ m}$.

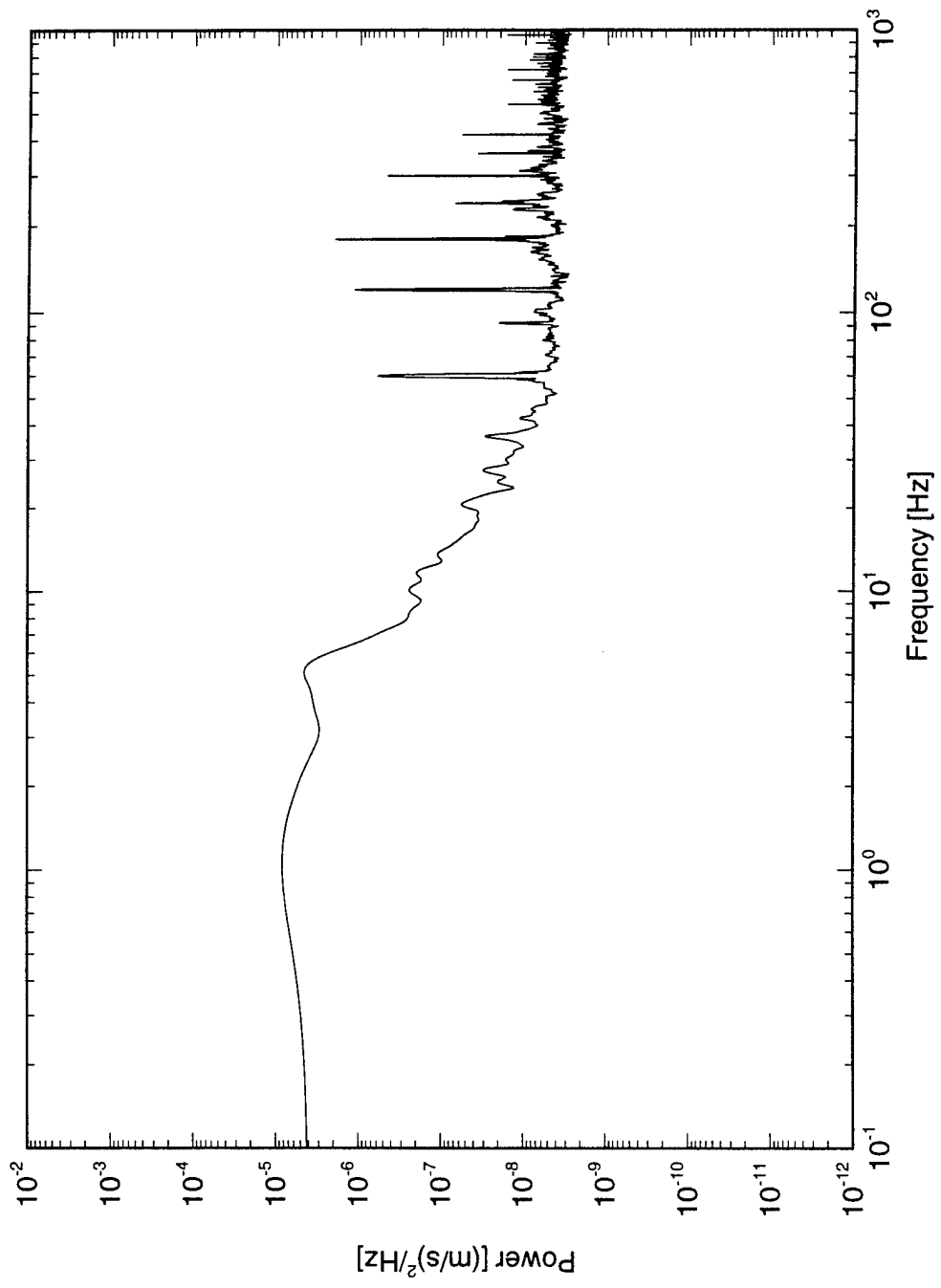


Figure 7.24: Freestream disturbance spectrum at $U_\infty = 12 \text{ m/s}$ with the plenum vented (AC coupled, band pass 2–1000 Hz, Tektronix filters). Measurements taken at $\hat{x} = 1.0 \text{ m}$.

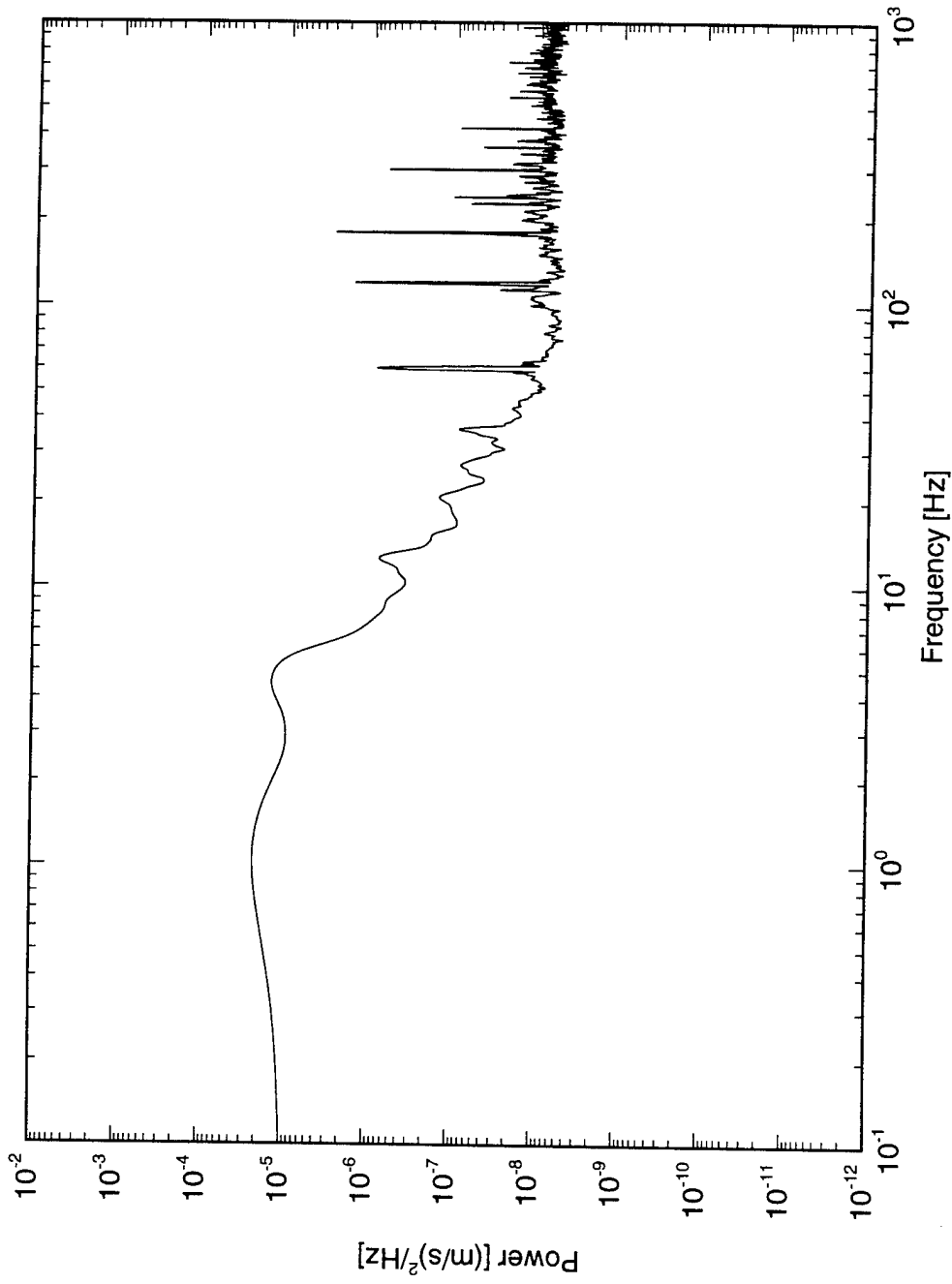


Figure 7.25: Freestream disturbance spectrum at $U_\infty = 15 \text{ m/s}$ with the plenum vented (AC coupled, band pass 2–1000 Hz, Tektronix filters). Measurements taken at $\hat{x} = 1.0 \text{ m}$.

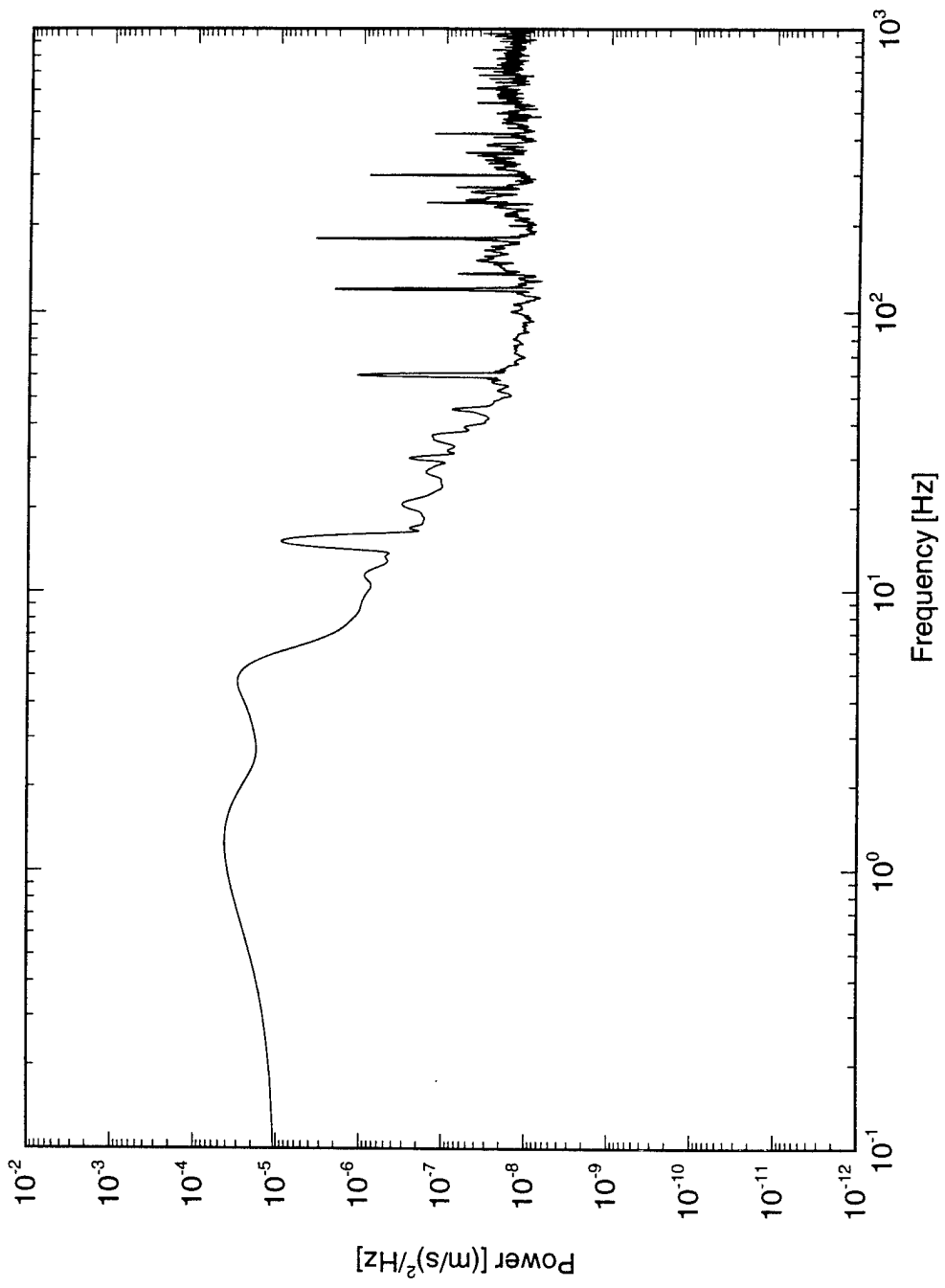


Figure 7.26: Freestream disturbance spectrum at $U_\infty = 18$ m/s with the plenum vented (AC coupled, band pass 2–1000 Hz, Tektronix filters). Measurements taken at $\hat{x} = 1.0$ m.

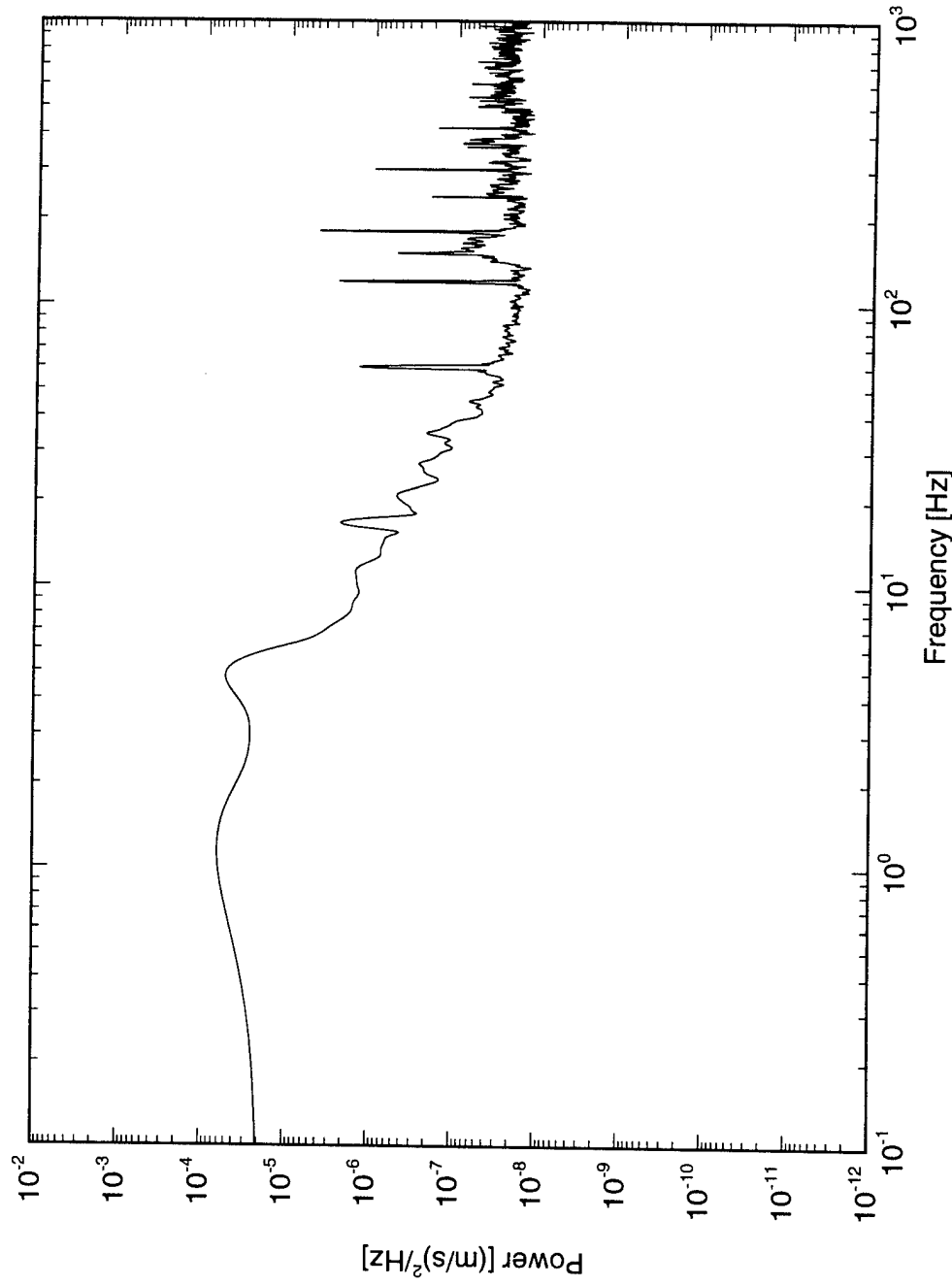


Figure 7.27: Freestream disturbance spectrum at $U_\infty = 20 \text{ m/s}$ with the plenum vented (AC coupled, band pass 2–1000 Hz, Tektronix filters). Measurements taken at $\hat{x} = 1.0 \text{ m}$.

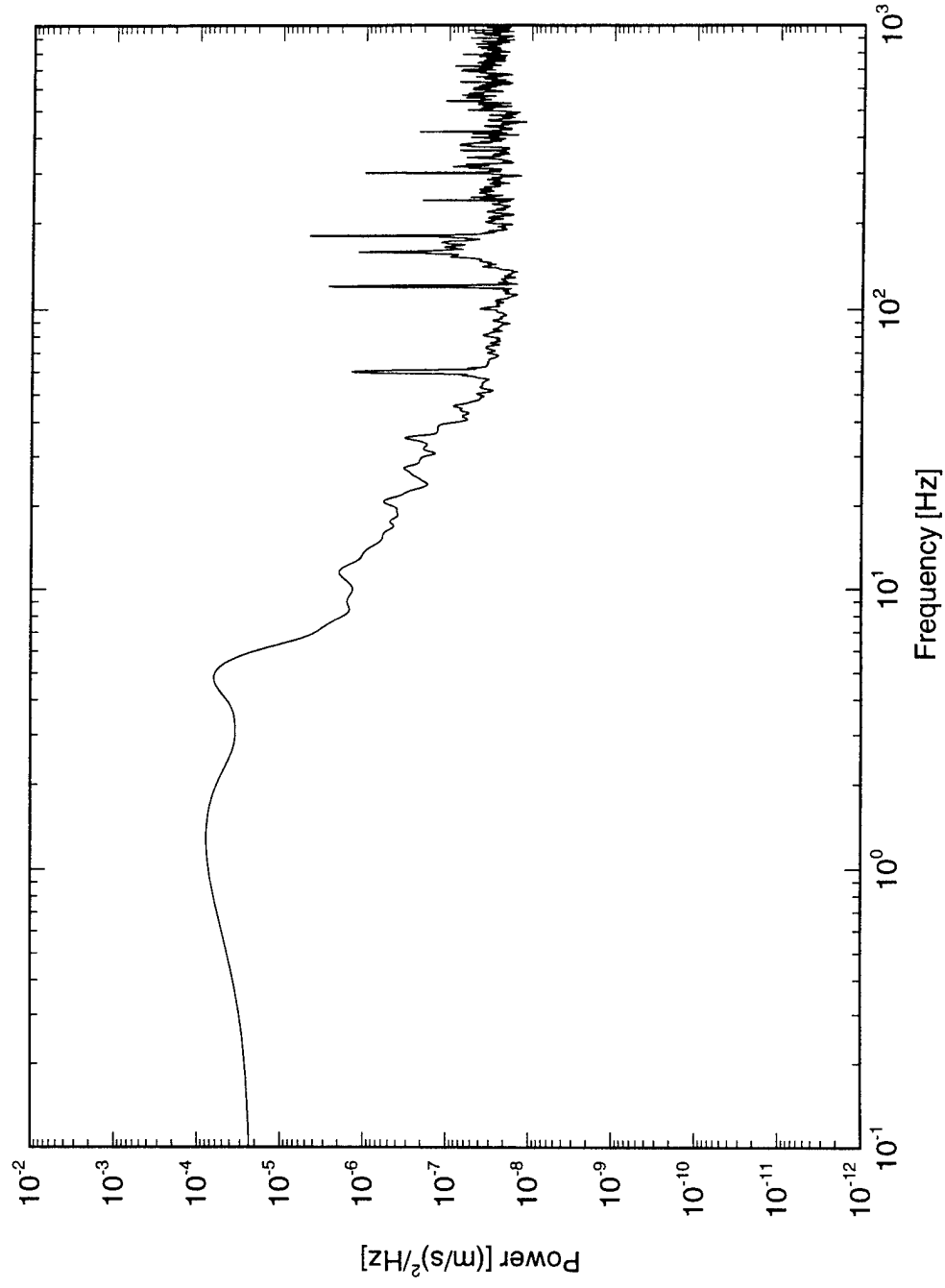


Figure 7.28: Freestream disturbance spectrum at $U_\infty = 21 \text{ m/s}$ with the plenum vented (AC coupled, band pass 2–1000 Hz, Tektronix filters). Measurements taken at $\hat{x} = 1.0 \text{ m}$.

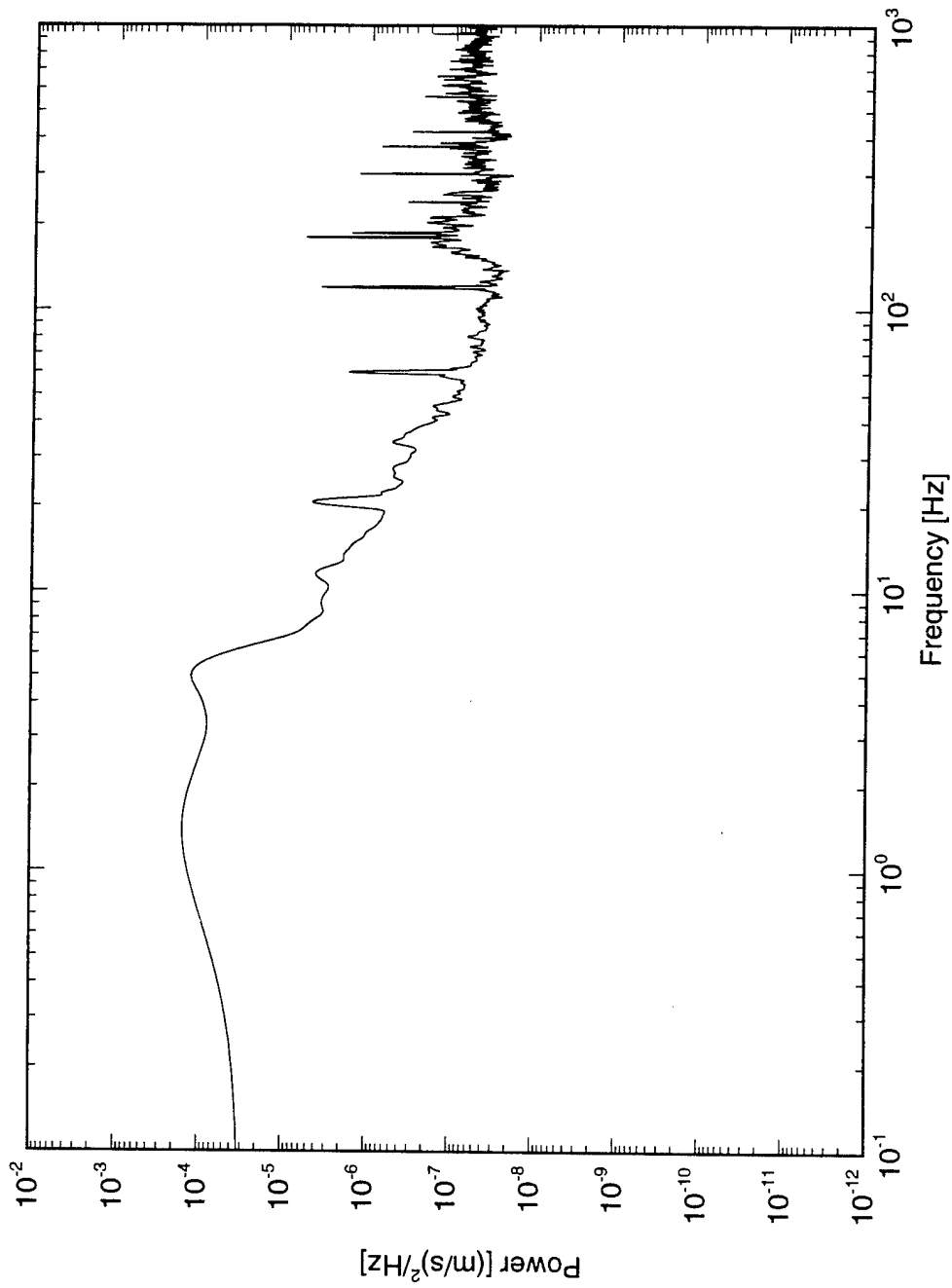


Figure 7.29: Freestream disturbance spectrum at $U_\infty = 25 \text{ m/s}$ with the plenum vented (AC coupled, band pass 2–1000 Hz, Tektronix filters). Measurements taken at $\hat{x} = 1.0 \text{ m}$.

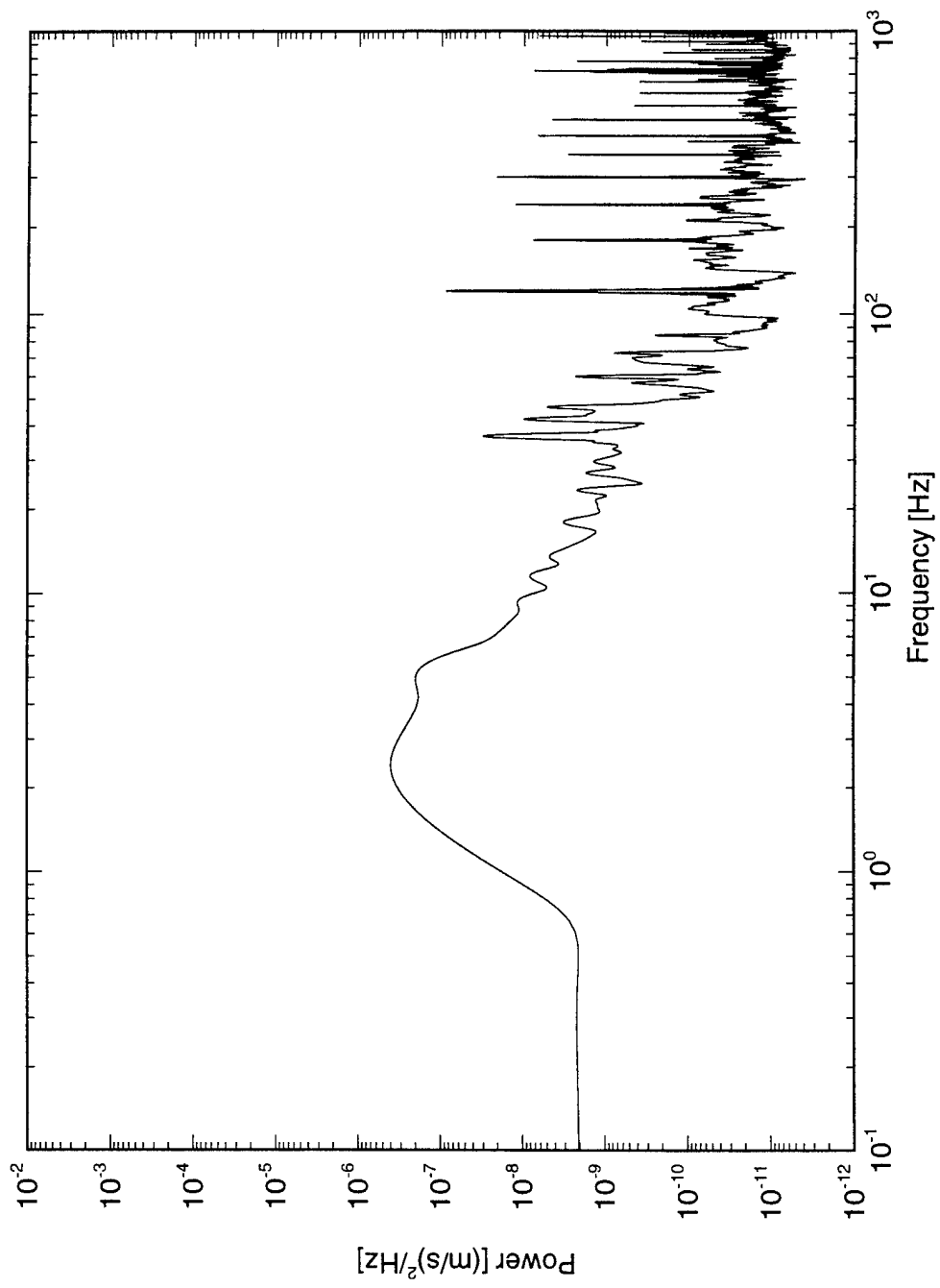


Figure 7.30: Freestream disturbance spectrum at $U_\infty = 5$ m/s with the plenum vented (AC coupled, band pass 2–1000 Hz, Stewart filters). Measurements taken at $\hat{x} = 1.0$ m.

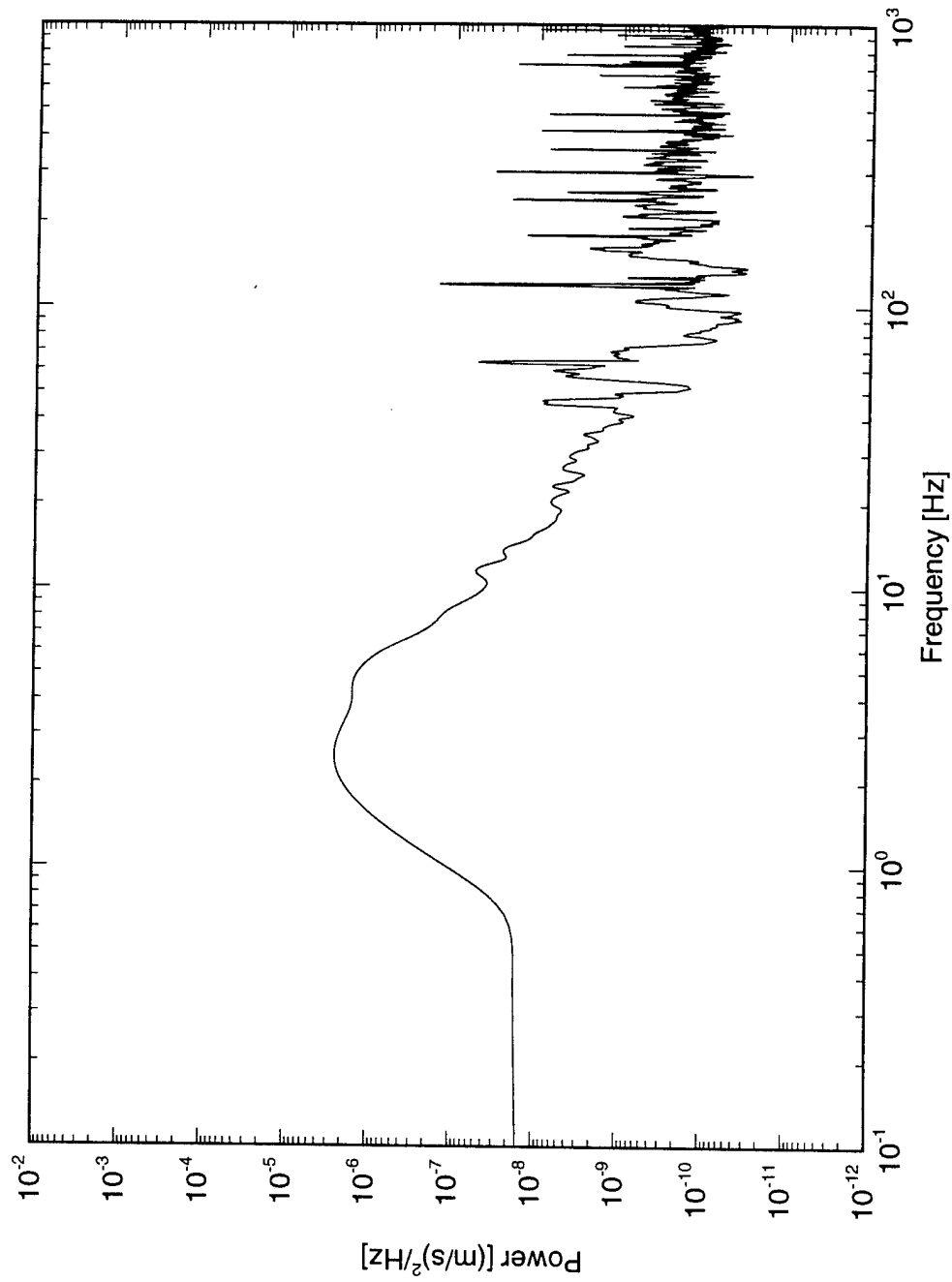


Figure 7.31: Freestream disturbance spectrum at $U_\infty = 8$ m/s with the plenum vented (AC coupled, band pass 2–1000 Hz, Stewart filters). Measurements taken at $\hat{x} = 1.0$ m.

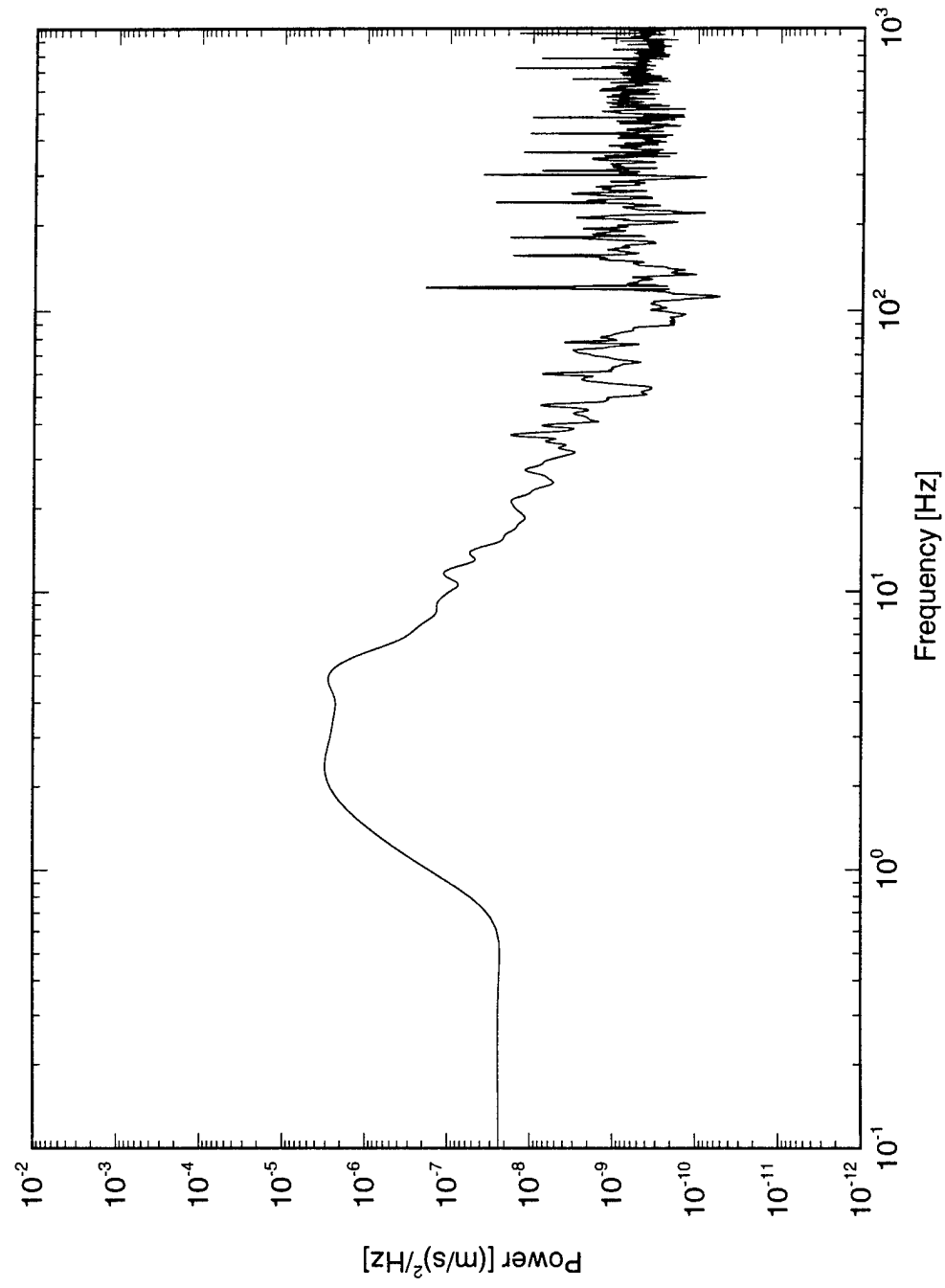


Figure 7.32: Freestream disturbance spectrum at $U_\infty = 10 \text{ m/s}$ with the plenum vented (AC coupled, band pass 2–1000 Hz, Stewart filters). Measurements taken at $\hat{x} = 1.0 \text{ m}$.

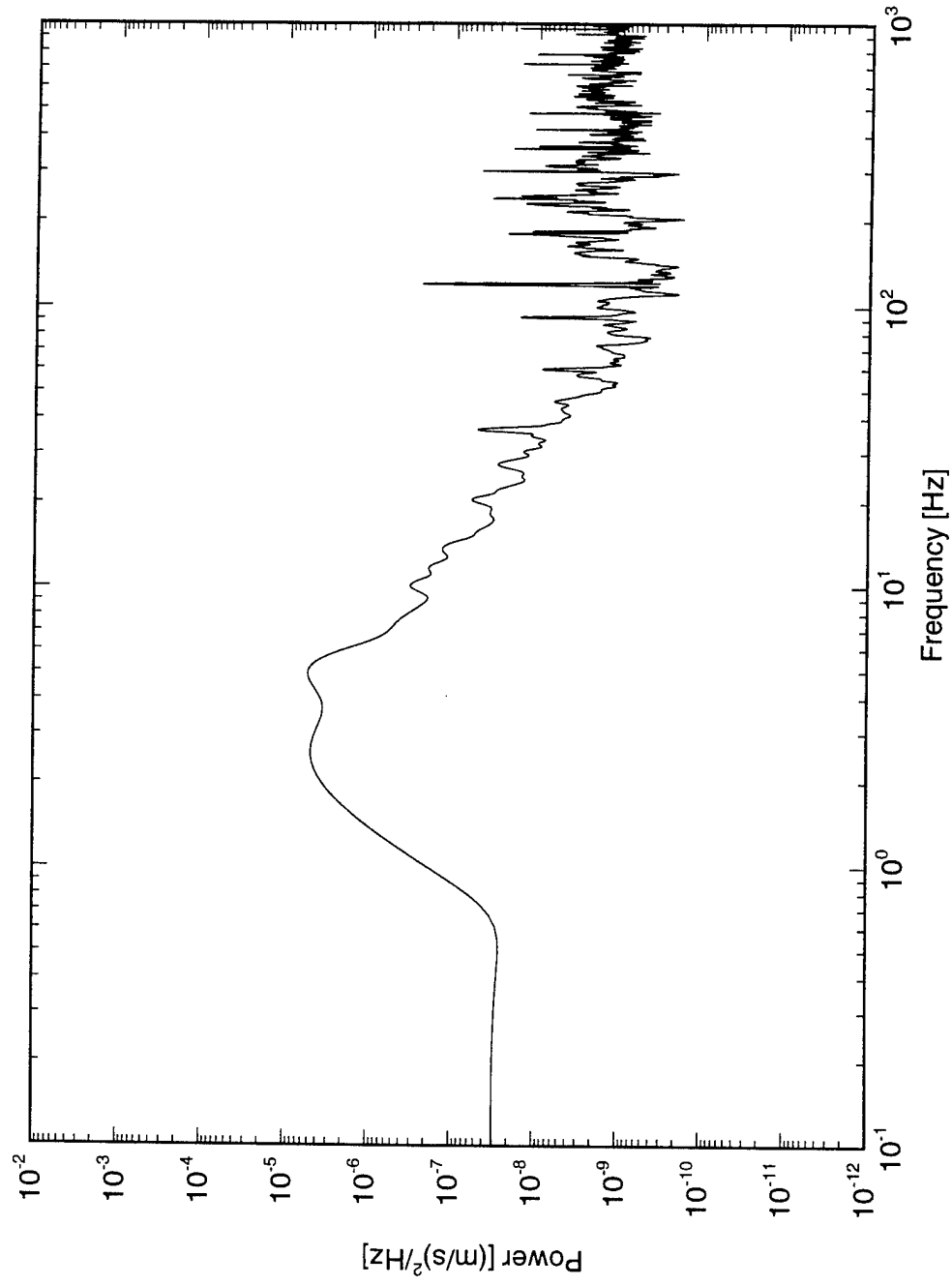


Figure 7.33: Freestream disturbance spectrum at $U_\infty = 12$ m/s with the plenum vented (AC coupled, band pass 2–1000 Hz, Stewart filters). Measurements taken at $\hat{x} = 1.0$ m.

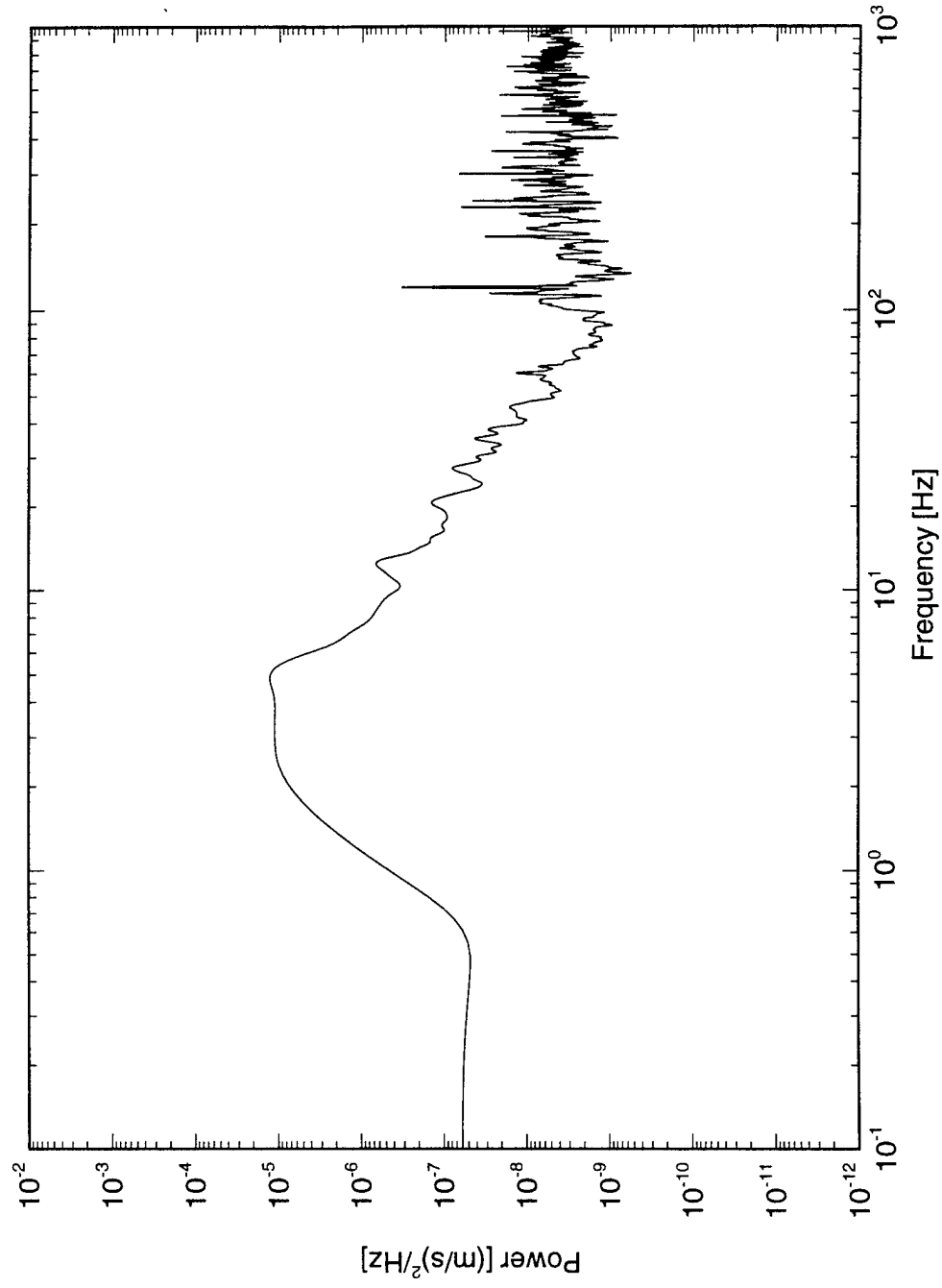


Figure 7.34: Freestream disturbance spectrum at $U_\infty = 15 \text{ m/s}$ with the plenum vented (AC coupled, band pass 2–1000 Hz, Stewart filters). Measurements taken at $\hat{x} = 1.0 \text{ m}$.

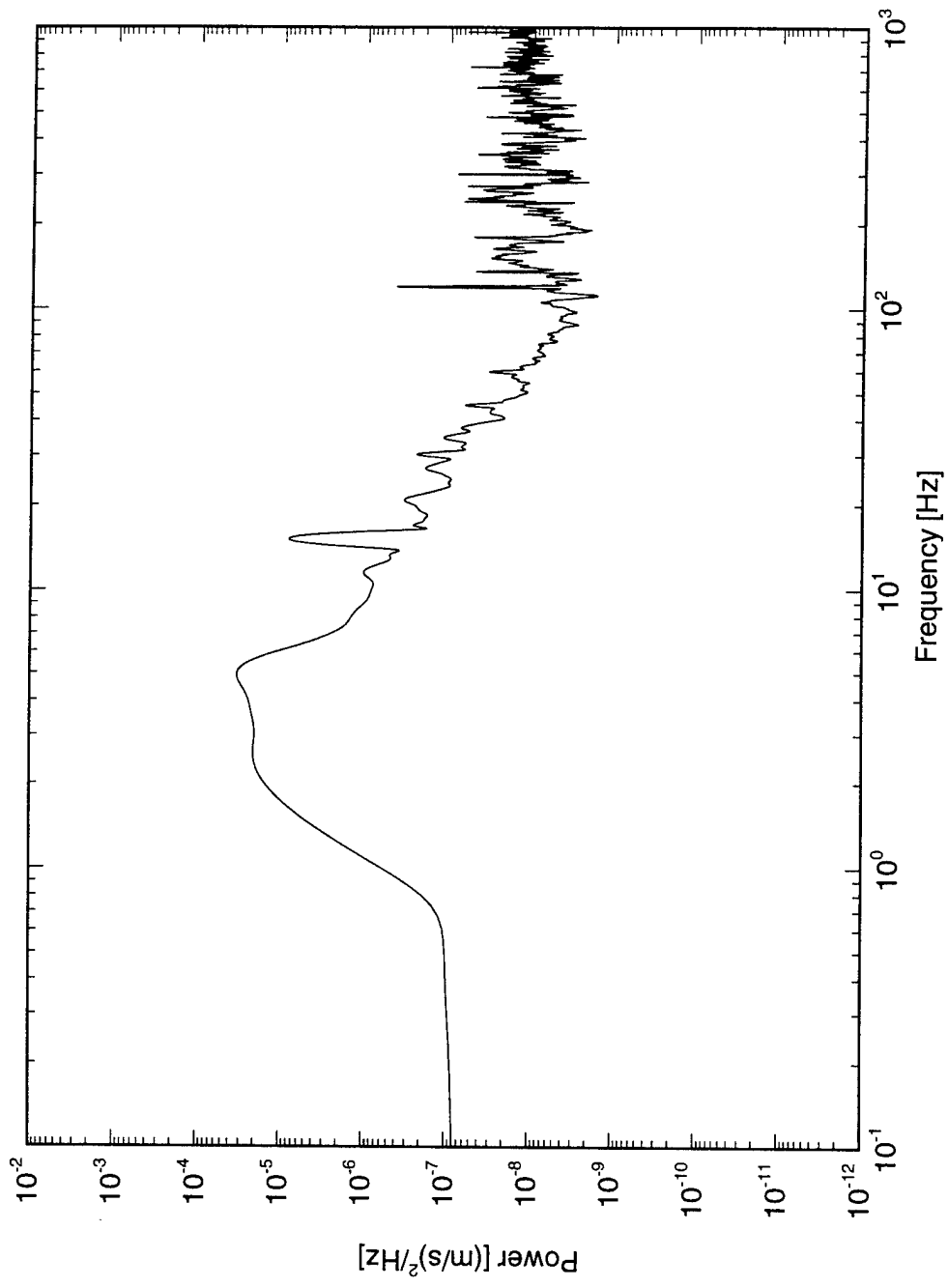


Figure 7.35: Freestream disturbance spectrum at $U_\infty = 18 \text{ m/s}$ with the plenum vented (AC coupled, band pass 2–1000 Hz, Stewart filters). Measurements taken at $\hat{x} = 1.0 \text{ m}$.

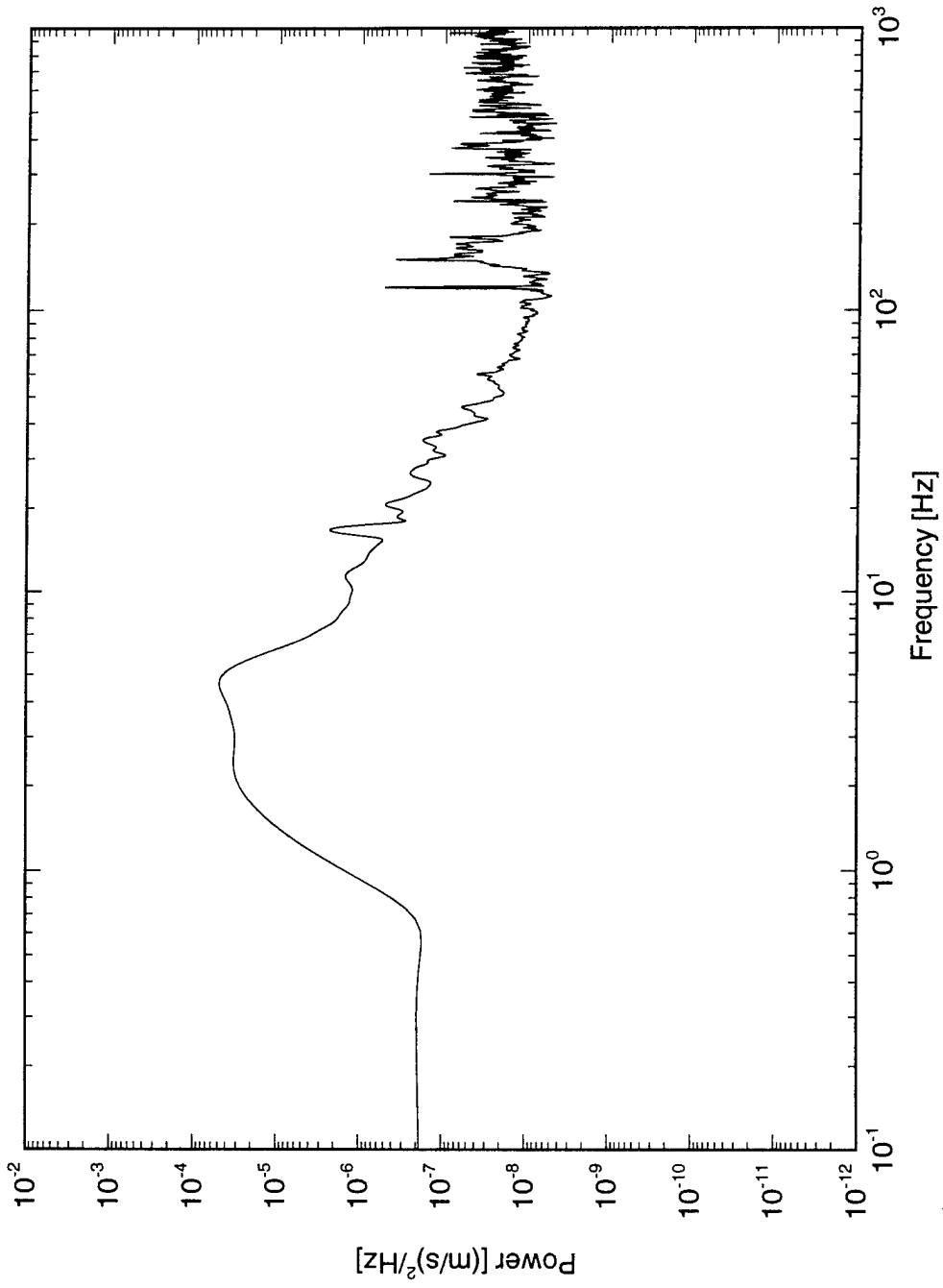


Figure 7.36: Freestream disturbance spectrum at $U_\infty = 20$ m/s with the plenum vented (AC coupled, band pass 2–1000 Hz, Stewart filters). Measurements taken at $\hat{x} = 1.0$ m.

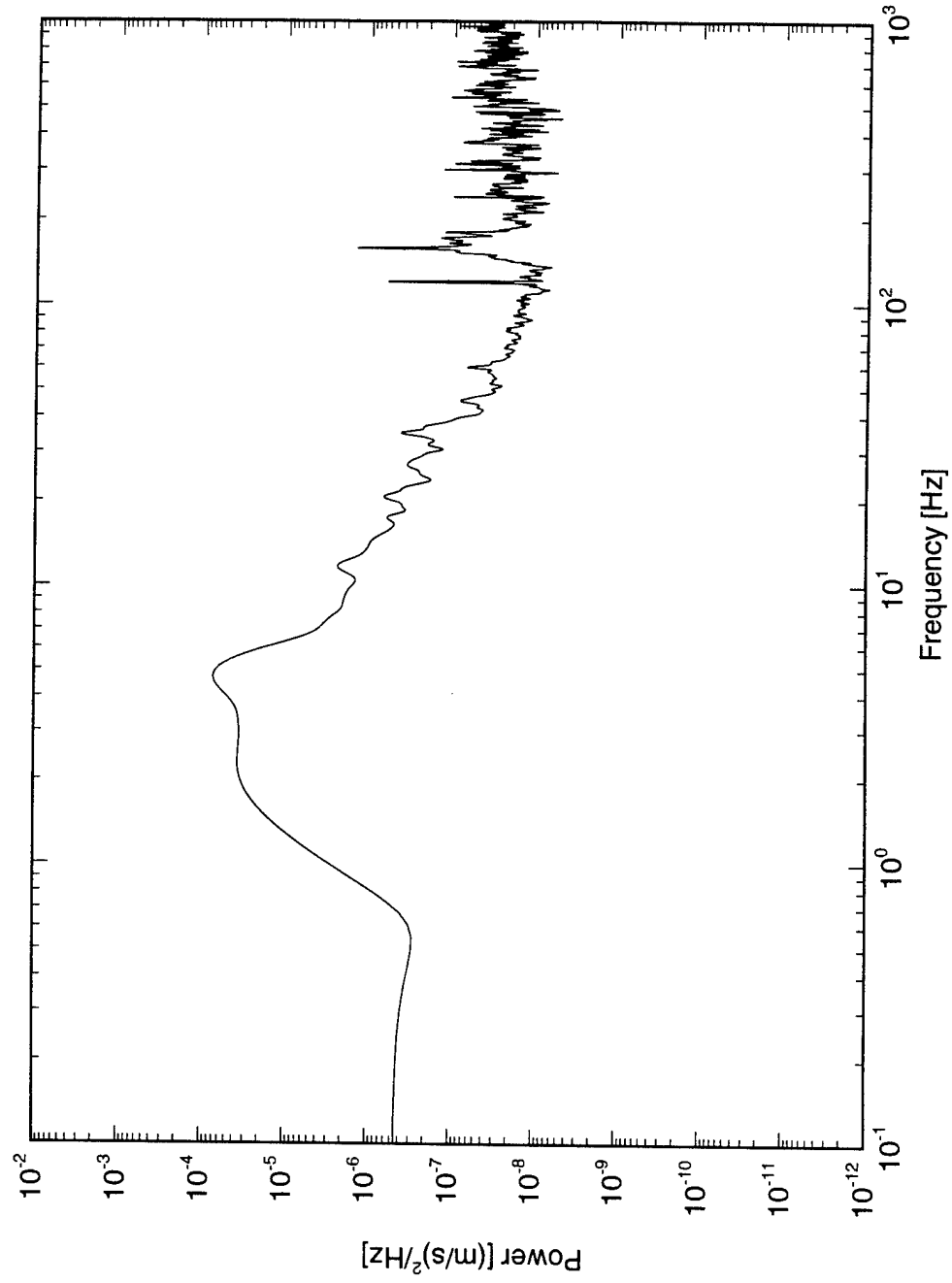


Figure 7.37: Freestream disturbance spectrum at $U_\infty = 21$ m/s with the plenum vented (AC coupled, band pass 2–1000 Hz, Stewart filters). Measurements taken at $\hat{x} = 1.0$ m.

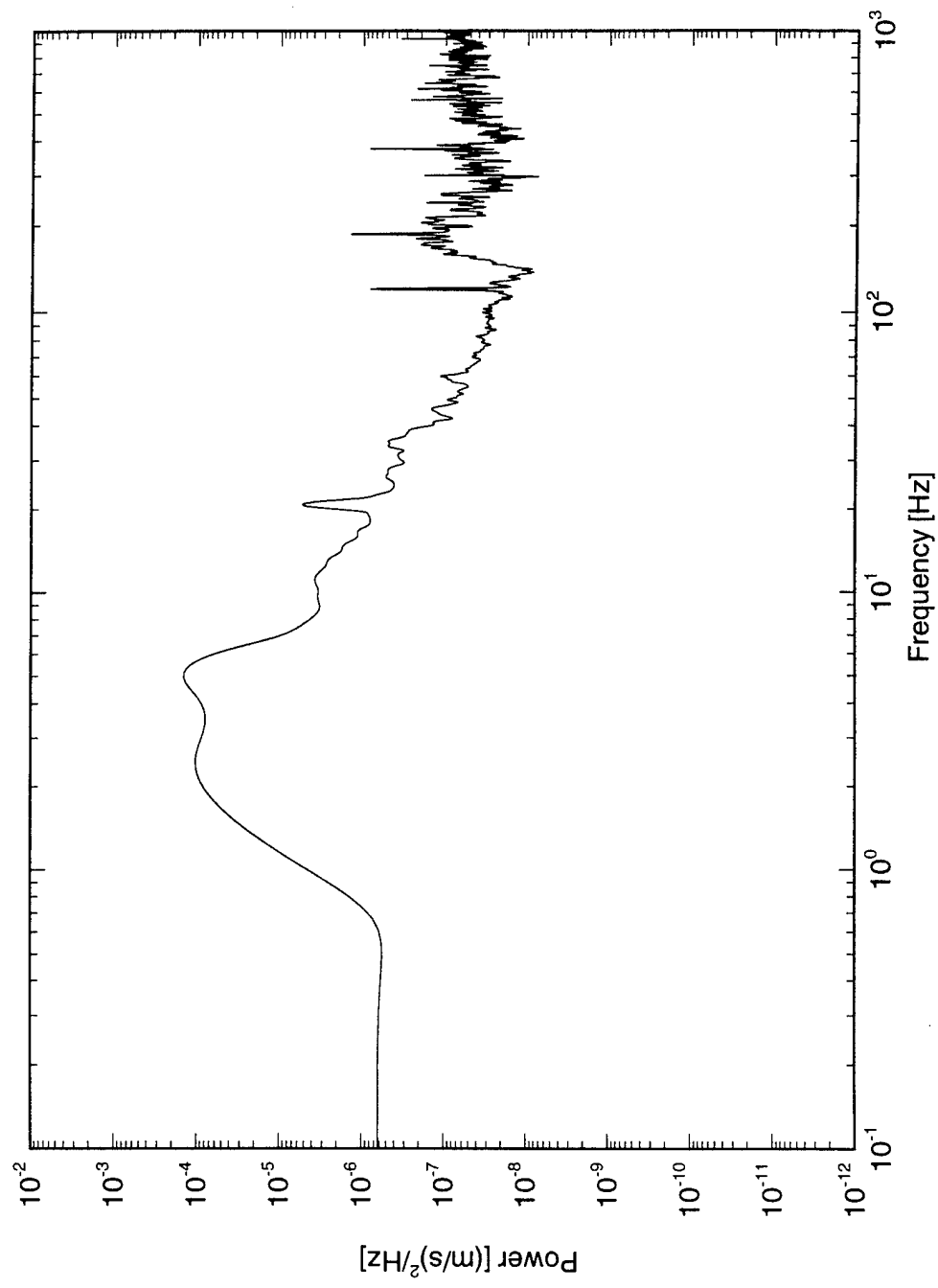


Figure 7.38: Freestream disturbance spectrum at $U_\infty = 25 \text{ m/s}$ with the plenum vented (AC coupled, band pass 2–1000 Hz, Stewart filters). Measurements taken at $\hat{x} = 1.0 \text{ m}$.

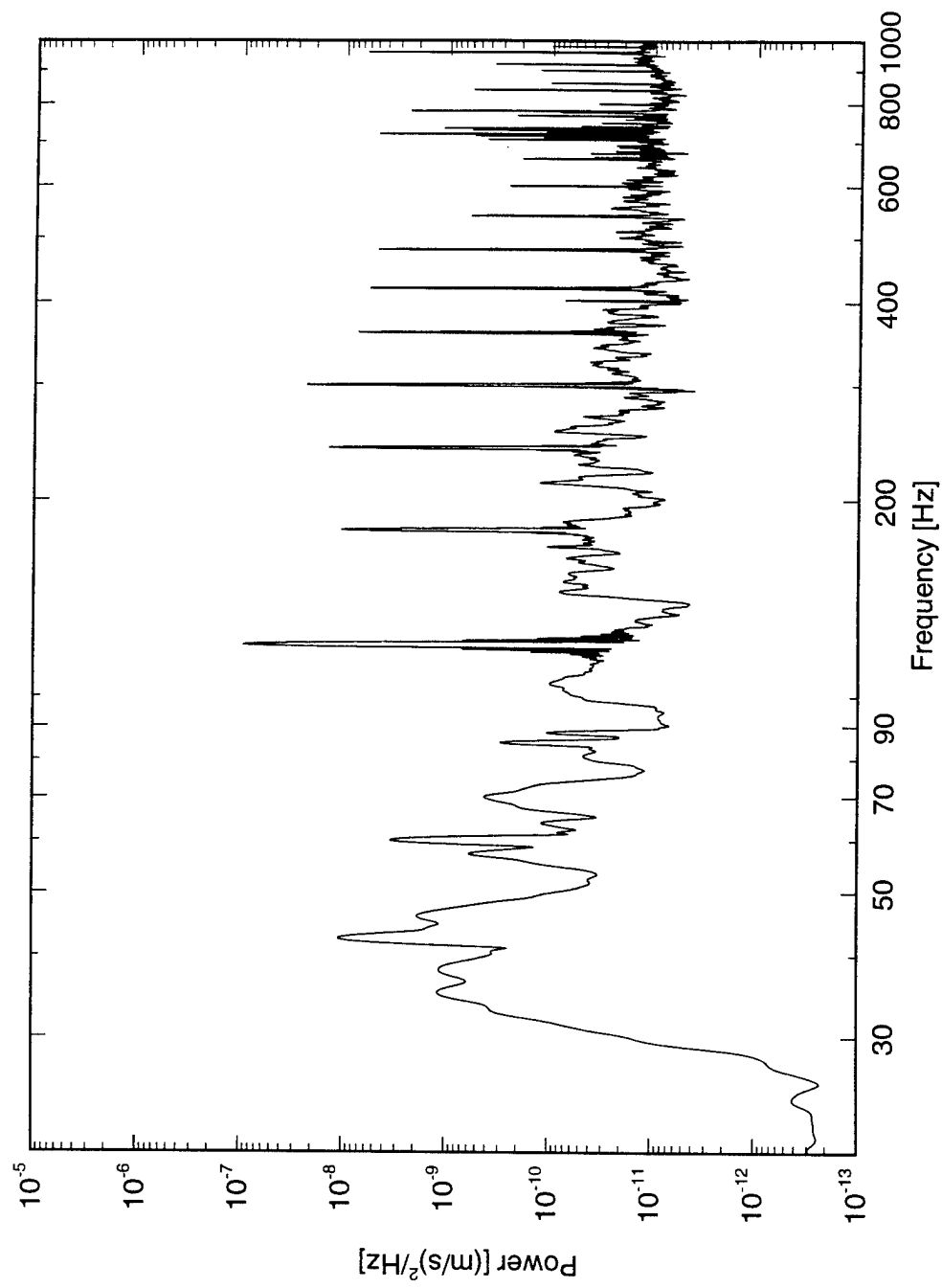


Figure 7.39: Freestream disturbance spectrum at $U_\infty = 5 \text{ m/s}$ with the plenum vented (AC coupled, band pass 35–1000 Hz, Stewart filters). Measurements taken at $\hat{x} = 1.0 \text{ m}$.

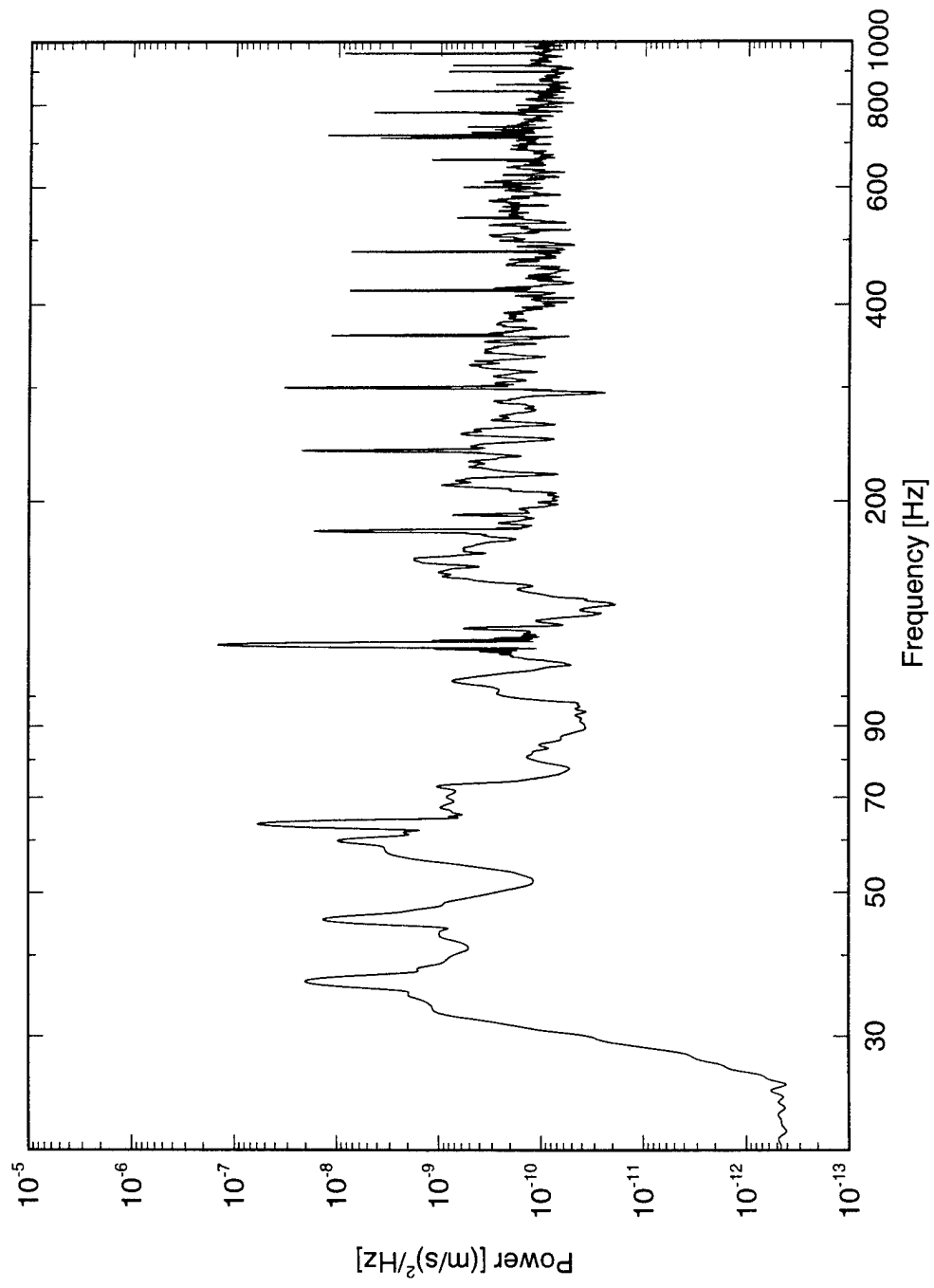


Figure 7.40: Freestream disturbance spectrum at $U_\infty = 8 \text{ m/s}$ with the plenum vented (AC coupled, band pass 35–1000 Hz, Stewart filters). Measurements taken at $\hat{x} = 1.0 \text{ m}$.

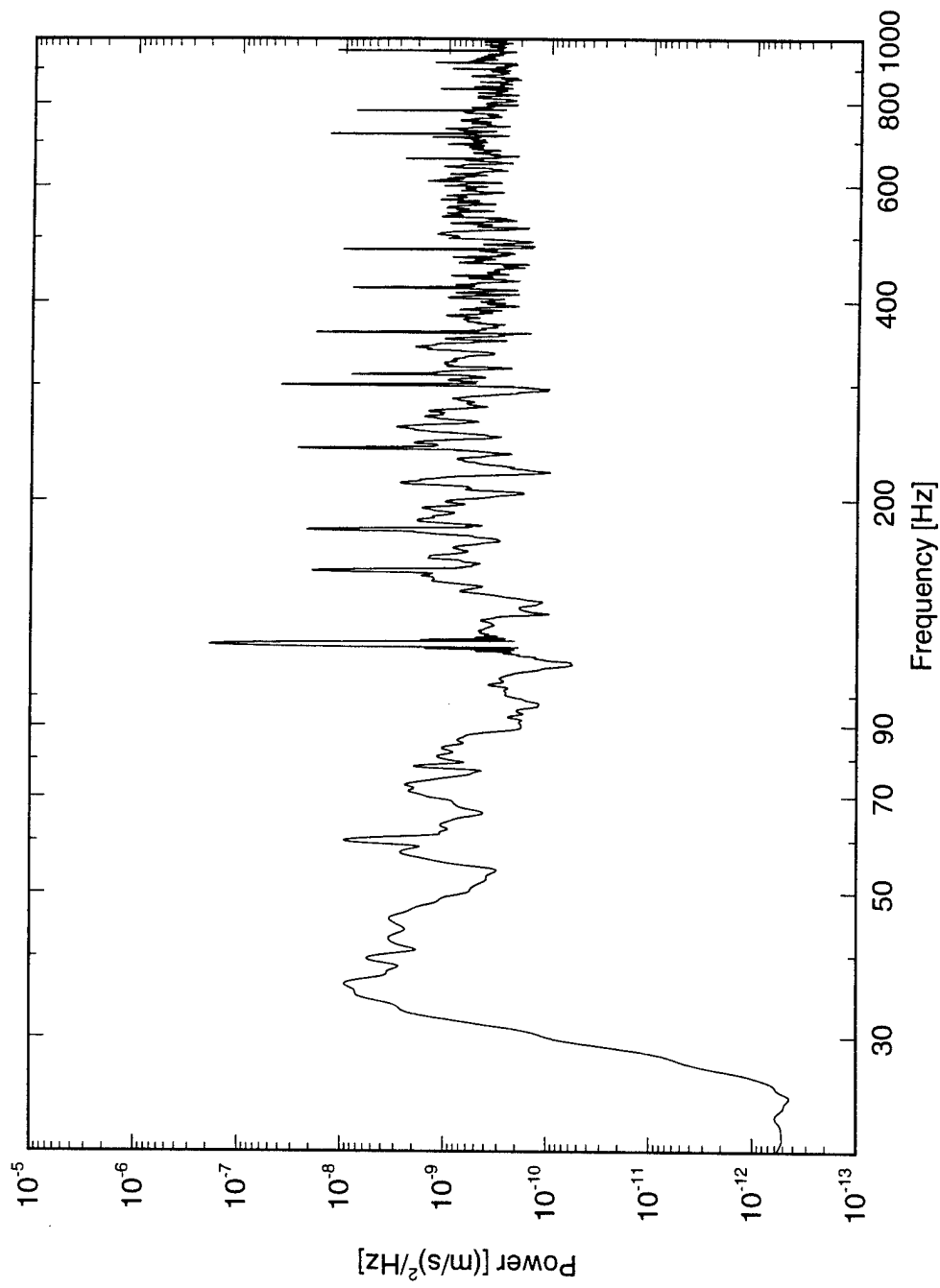


Figure 7.41: Freestream disturbance spectrum at $U_\infty = 10 \text{ m/s}$ with the plenum vented (AC coupled, band pass 35–1000 Hz, Stewart filters). Measurements taken at $\hat{x} = 1.0 \text{ m}$.

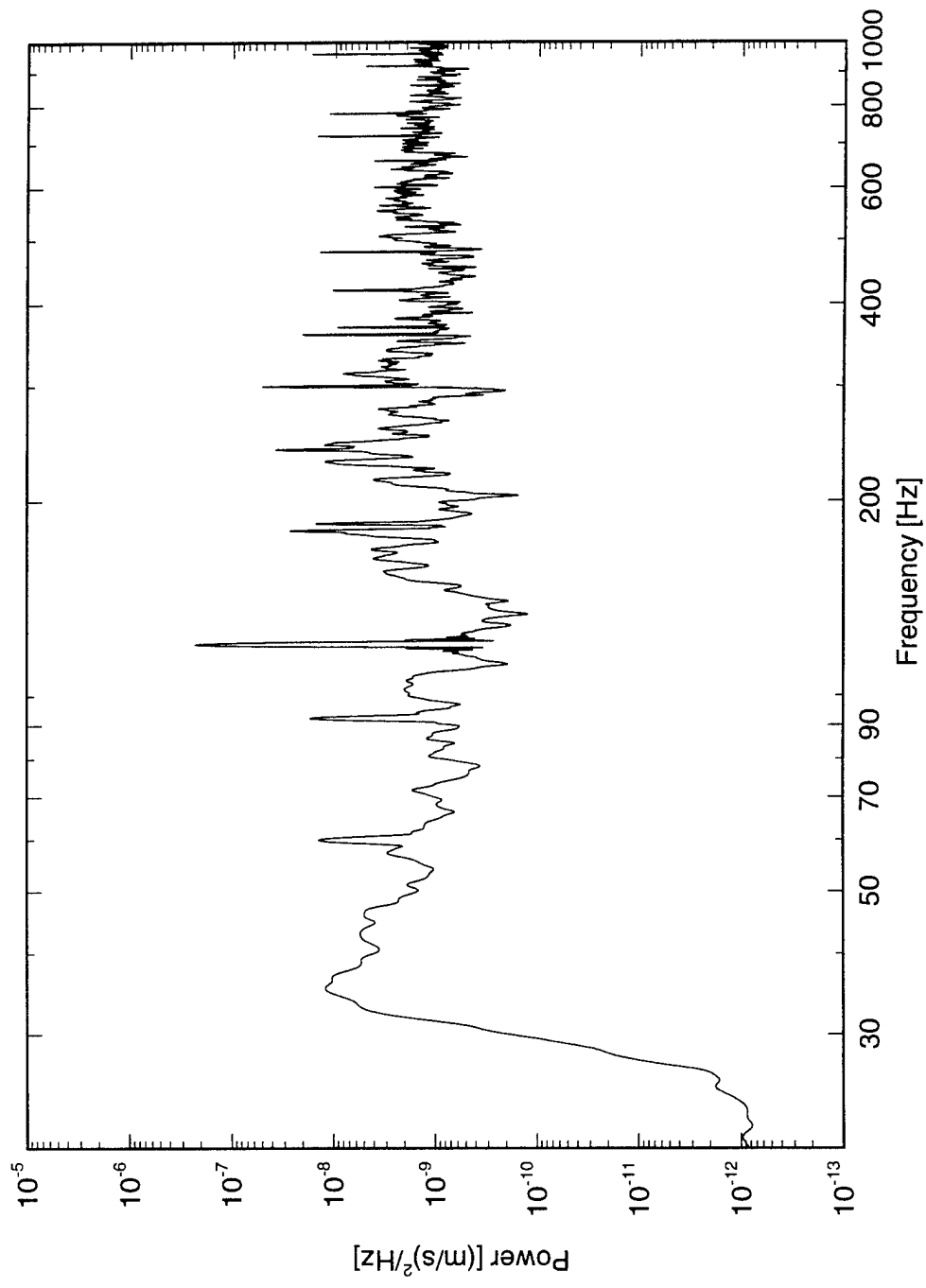


Figure 7.42: Freestream disturbance spectrum at $U_\infty = 12 \text{ m/s}$ with the plenum vented (AC coupled, band pass 35–1000 Hz, Stewart filters). Measurements taken at $\hat{x} = 1.0 \text{ m}$.

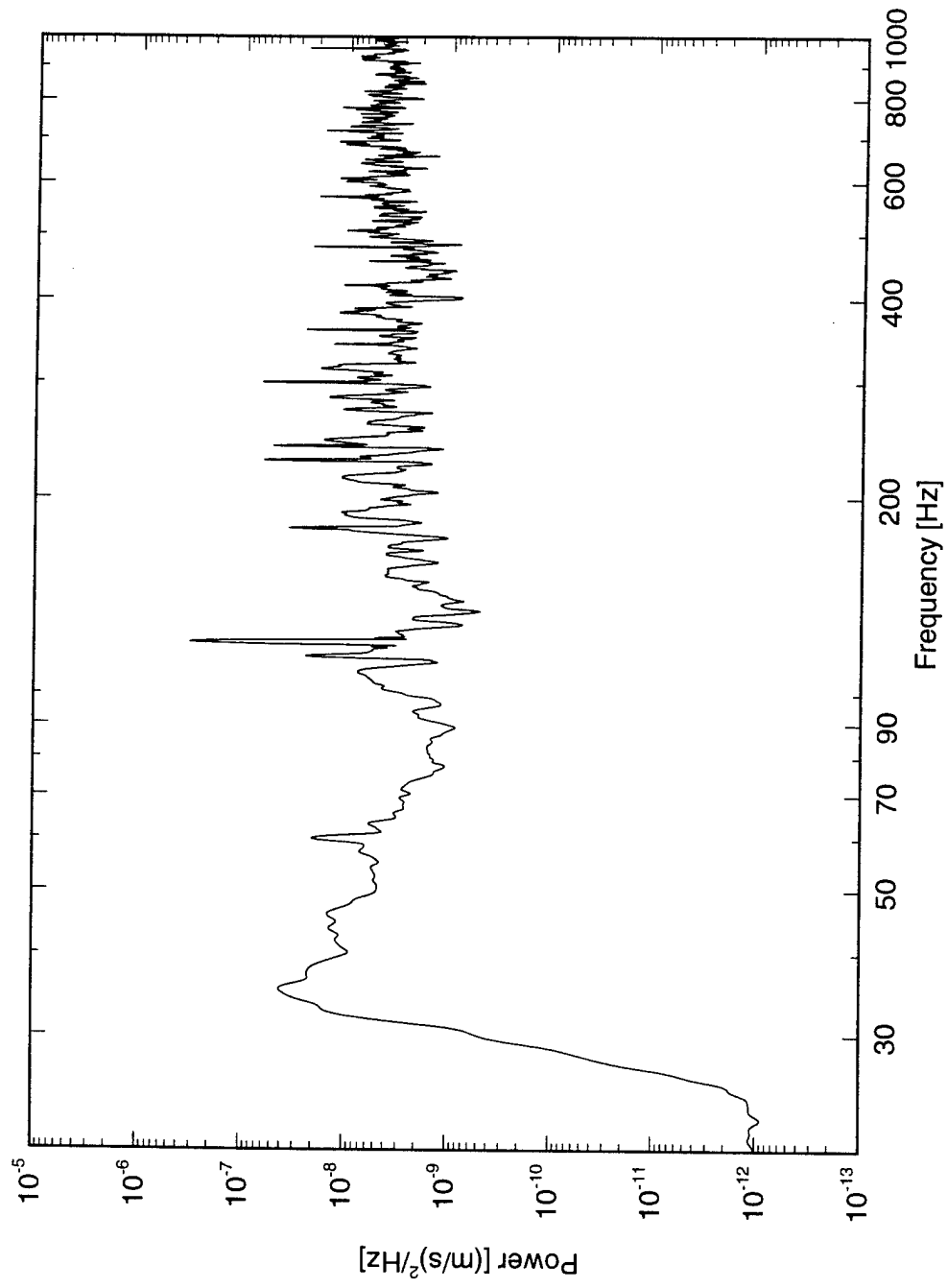


Figure 7.43: Freestream disturbance spectrum at $U_\infty = 15 \text{ m/s}$ with the plenum vented (AC coupled, band pass 35–1000 Hz, Stewart filters). Measurements taken at $\hat{x} = 1.0 \text{ m}$.

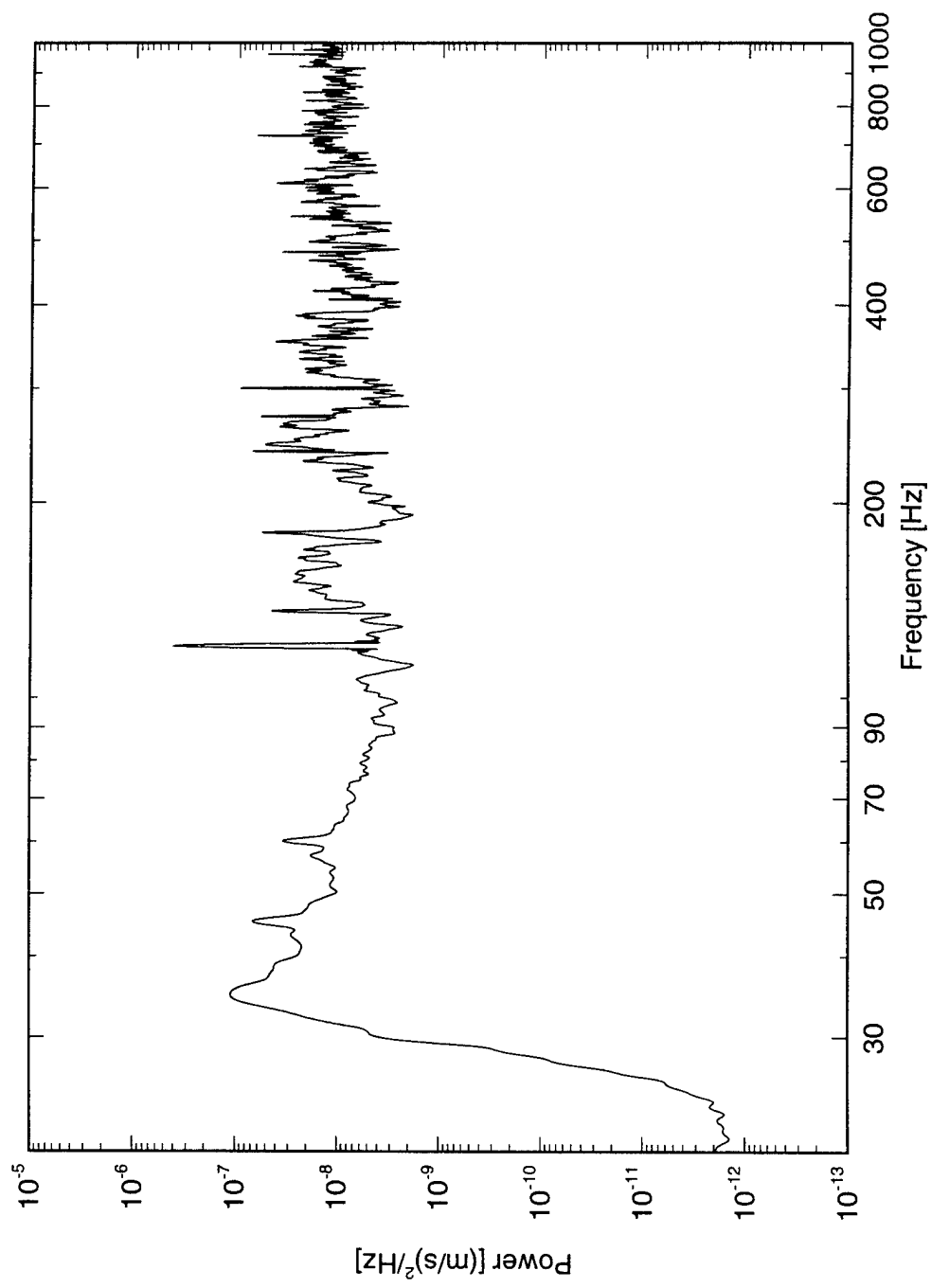


Figure 7.44: Freestream disturbance spectrum at $U_\infty = 18$ m/s with the plenum vented (AC coupled, band pass 35–1000 Hz, Stewart filters). Measurements taken at $\hat{x} = 1.0$ m.

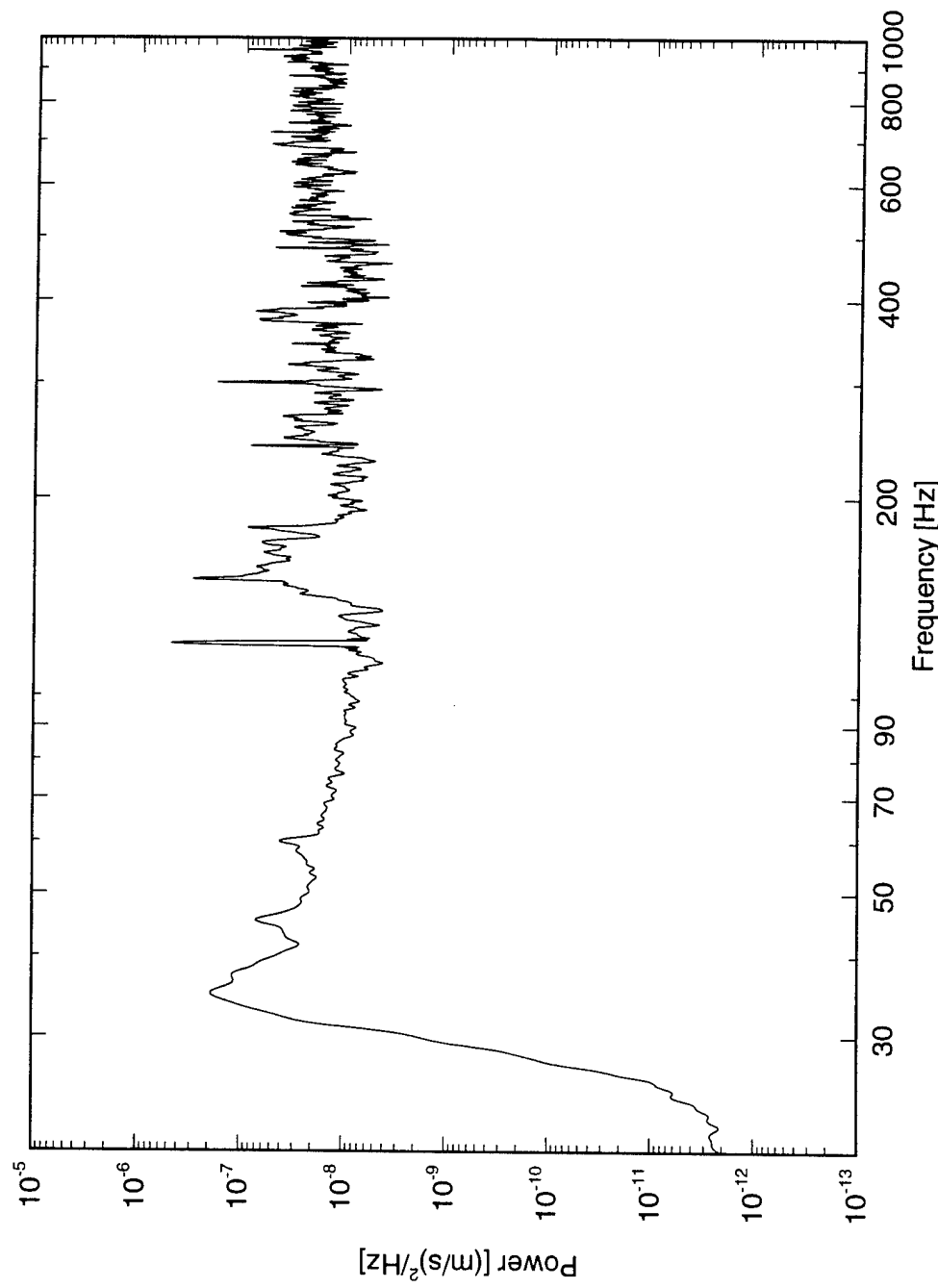


Figure 7.45: Freestream disturbance spectrum at $U_\infty = 20 \text{ m/s}$ with the plenum vented (AC coupled, band pass 35–1000 Hz, Stewart filters). Measurements taken at $\hat{x} = 1.0 \text{ m}$.

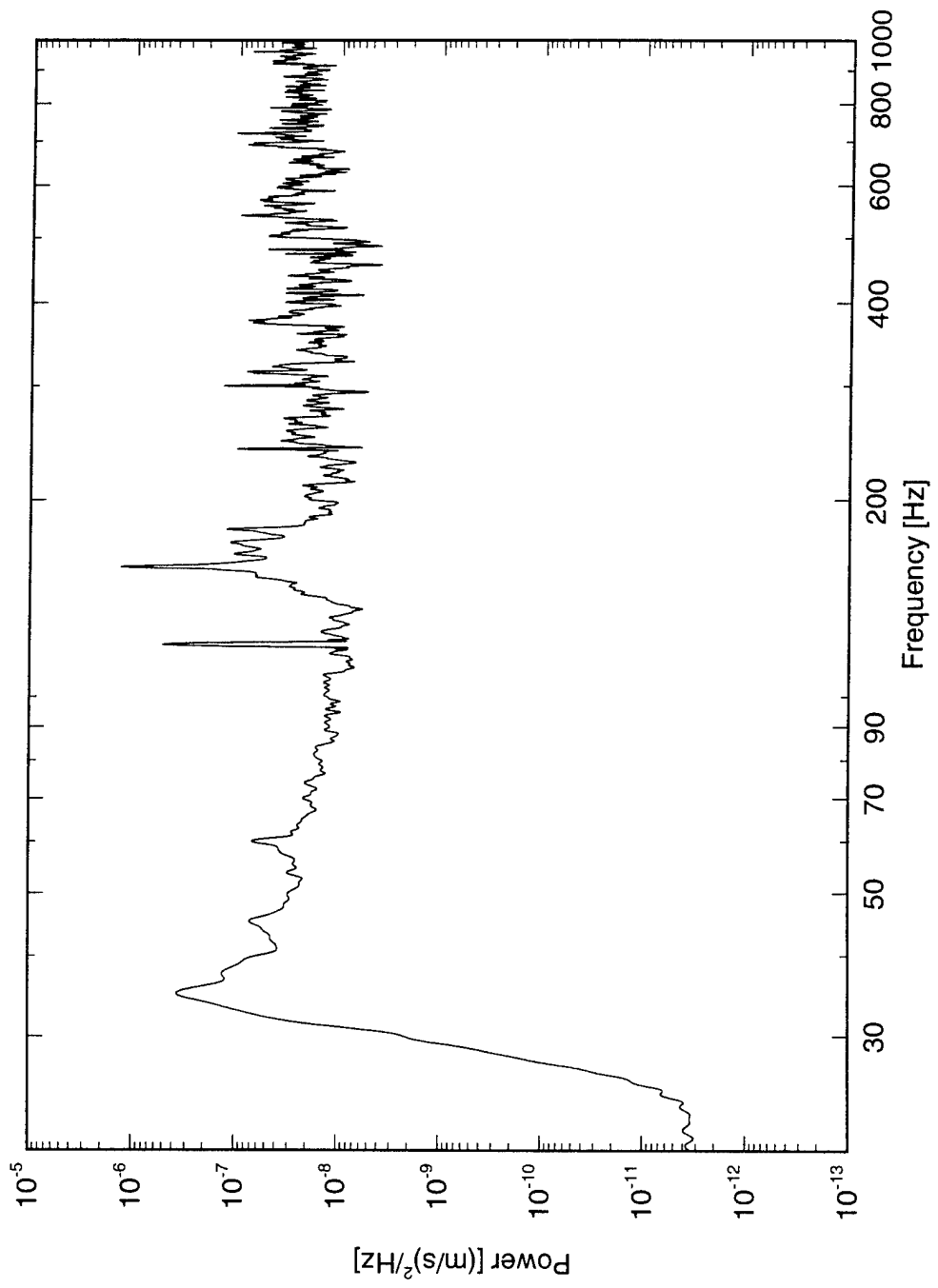


Figure 7.46: Freestream disturbance spectrum at $U_{\infty} = 21$ m/s with the plenum vented (AC coupled, band pass 35–1000 Hz, Stewart filters). Measurements taken at $\hat{x} = 1.0$ m.

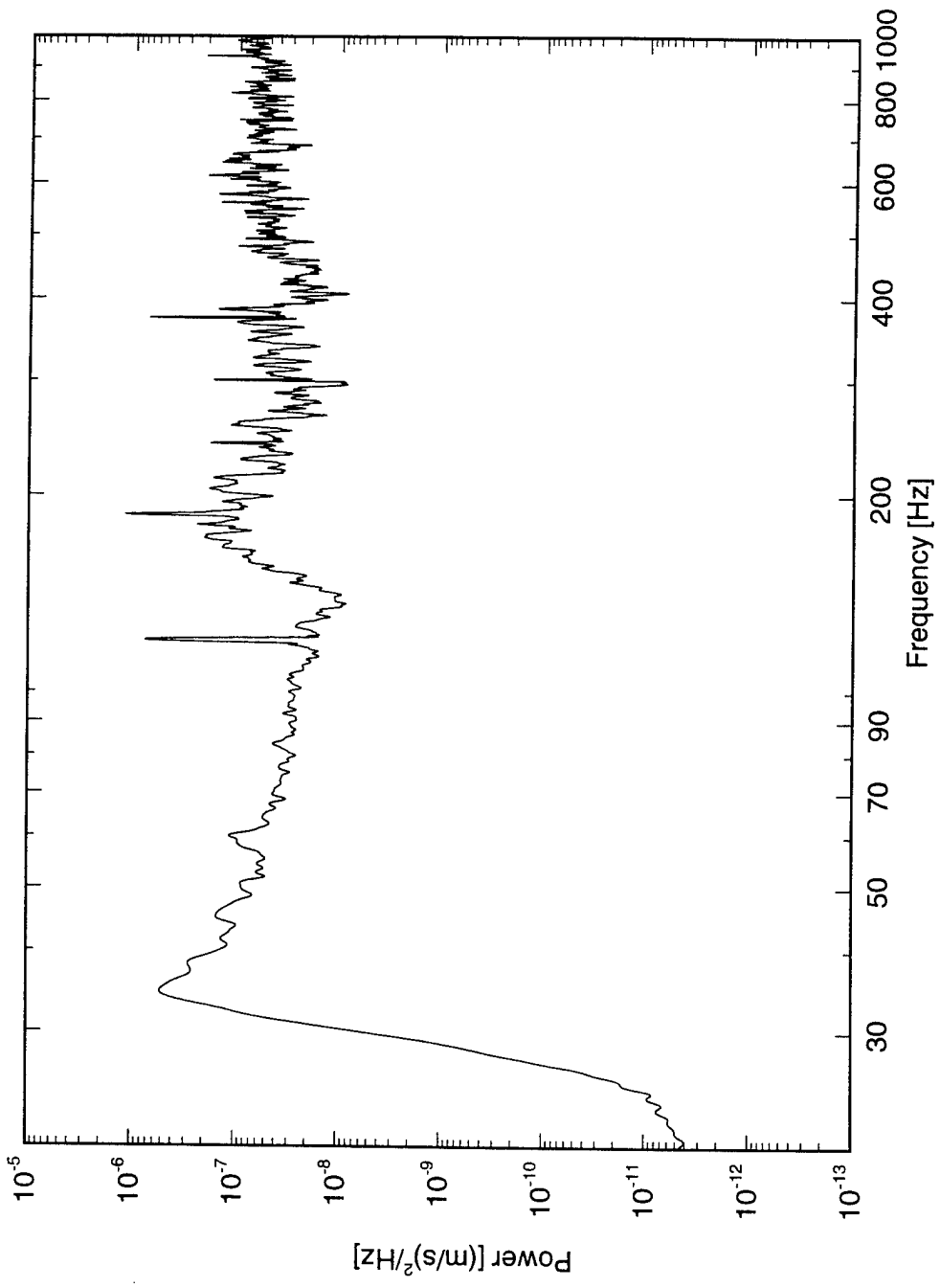


Figure 7.47: Freestream disturbance spectrum at $U_\infty = 25 \text{ m/s}$ with the plenum vented (AC coupled, band pass 35–1000 Hz, Stewart filters). Measurements taken at $\hat{x} = 1.0 \text{ m}$.

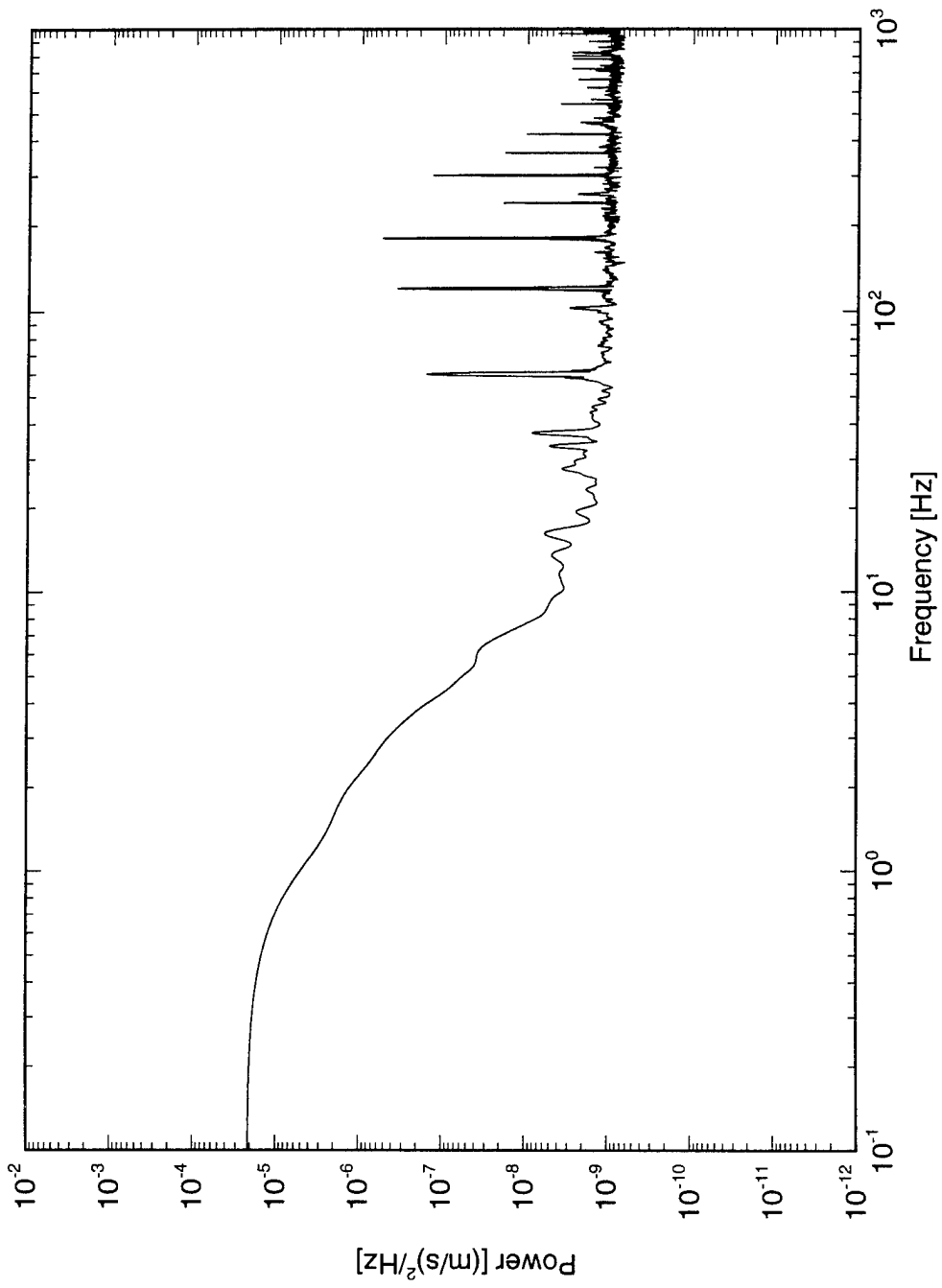


Figure 7.48: Freestream disturbance spectrum at $U_\infty = 5 \text{ m/s}$ with the mixing region vented (DC coupled, band pass 0.1–1000 Hz, Tektronix filters). Measurements taken at $\hat{x} = 1.0 \text{ m}$.

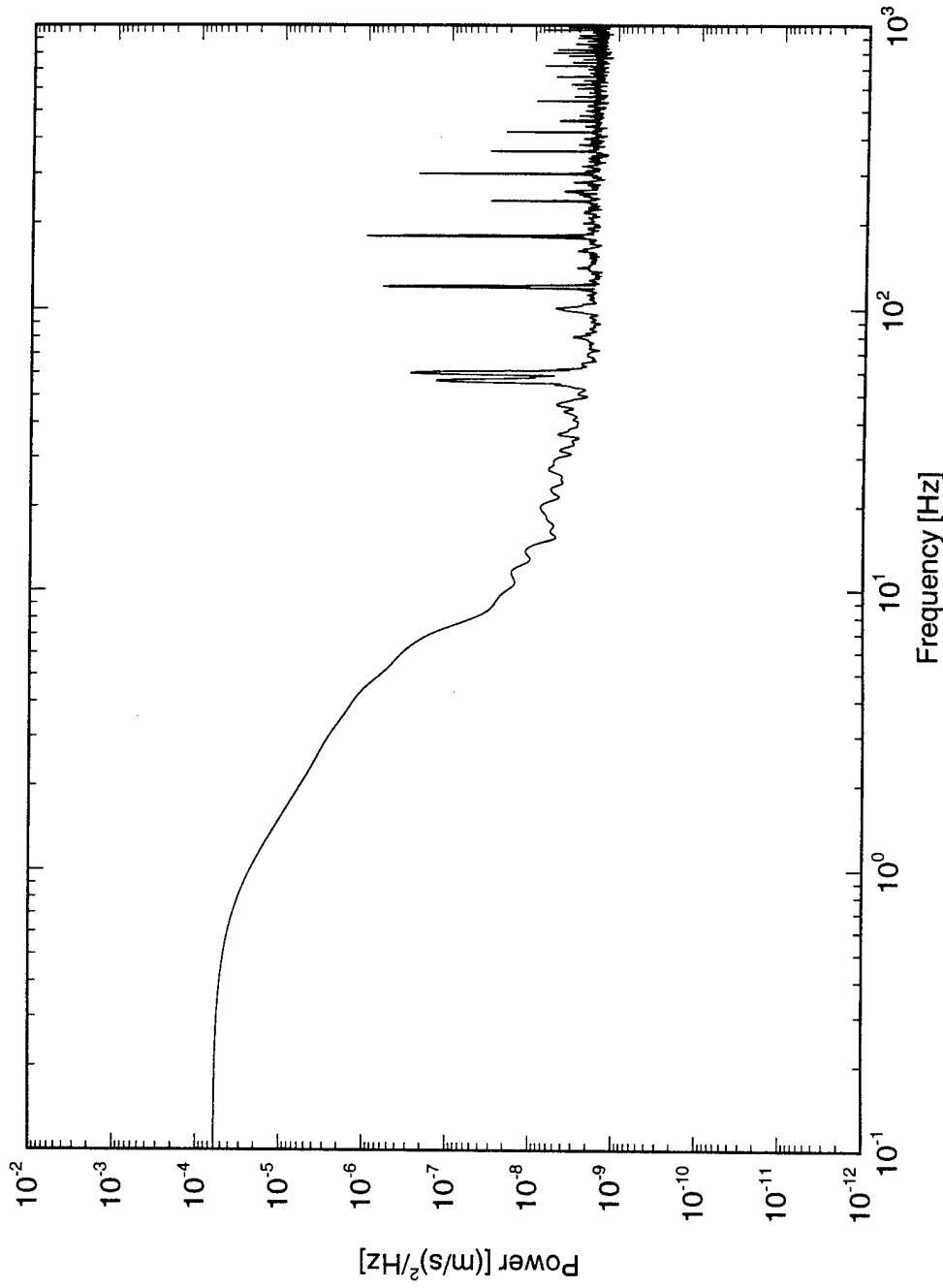


Figure 7.49: Freestream disturbance spectrum at $U_\infty = 8 \text{ m/s}$ with the mixing region vented (DC coupled, band pass 0.1–1000 Hz, Tektronix filters). Measurements taken at $\hat{x} = 1.0 \text{ m}$.

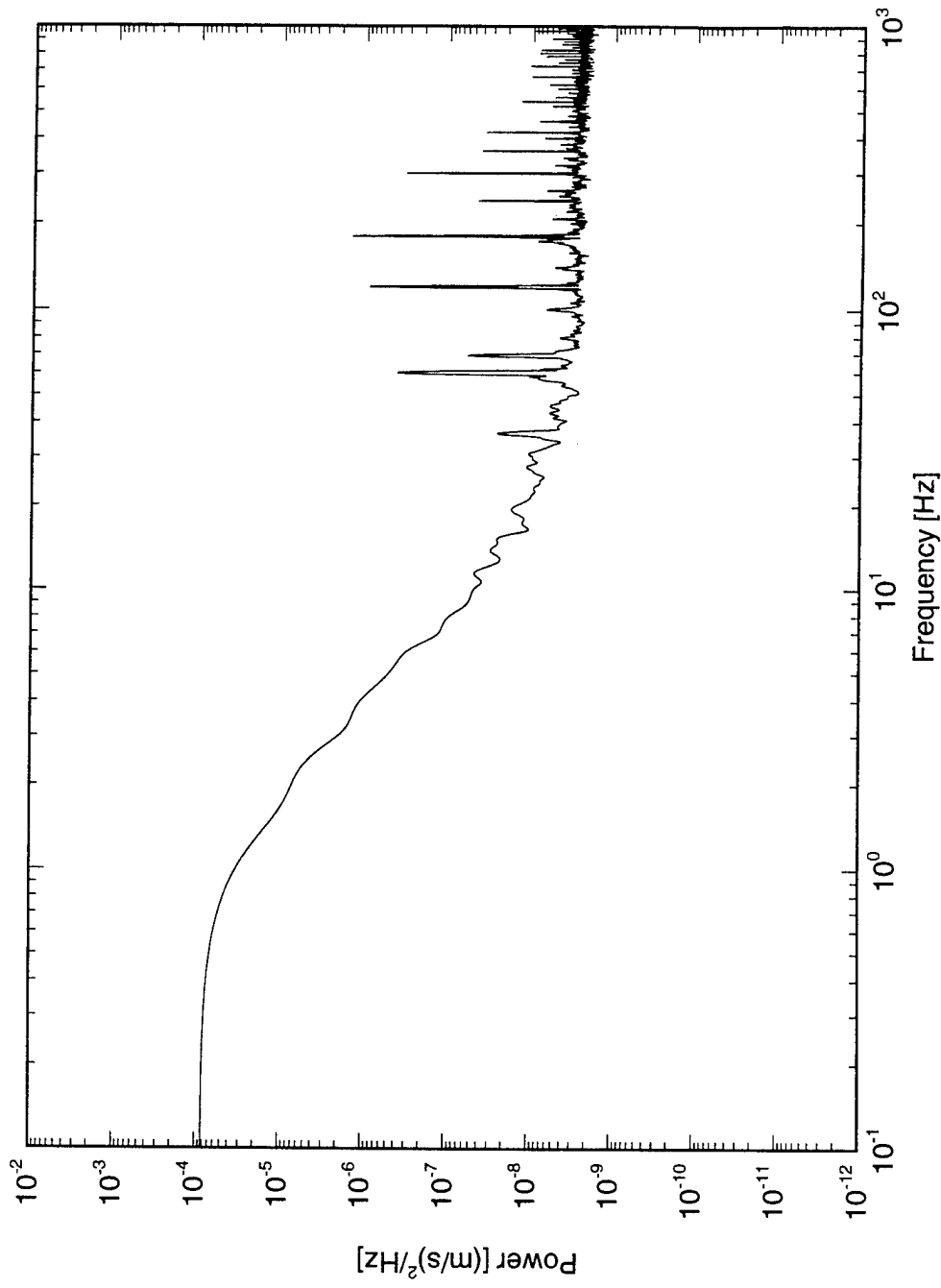


Figure 7.50: Freestream disturbance spectrum at $U_\infty = 10$ m/s with the mixing region vented (DC coupled, band pass 0.1–1000 Hz, Tektronix filters). Measurements taken at $\hat{x} = 1.0$ m.

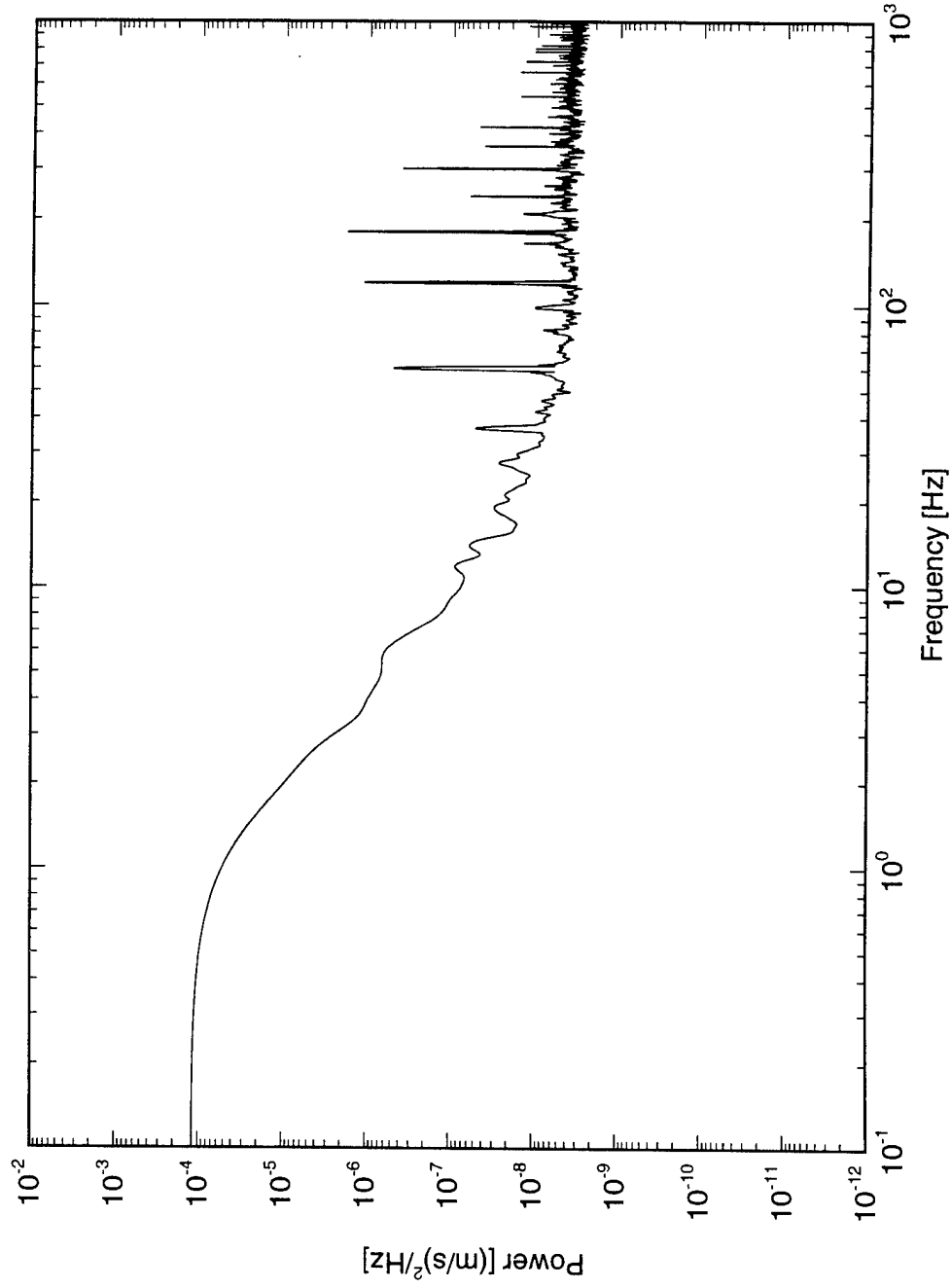


Figure 7.51: Freestream disturbance spectrum at $U_\infty = 12 \text{ m/s}$ with the mixing region vented (DC coupled, band pass 0.1–1000 Hz, Tektronix filters). Measurements taken at $\hat{x} = 1.0 \text{ m}$.

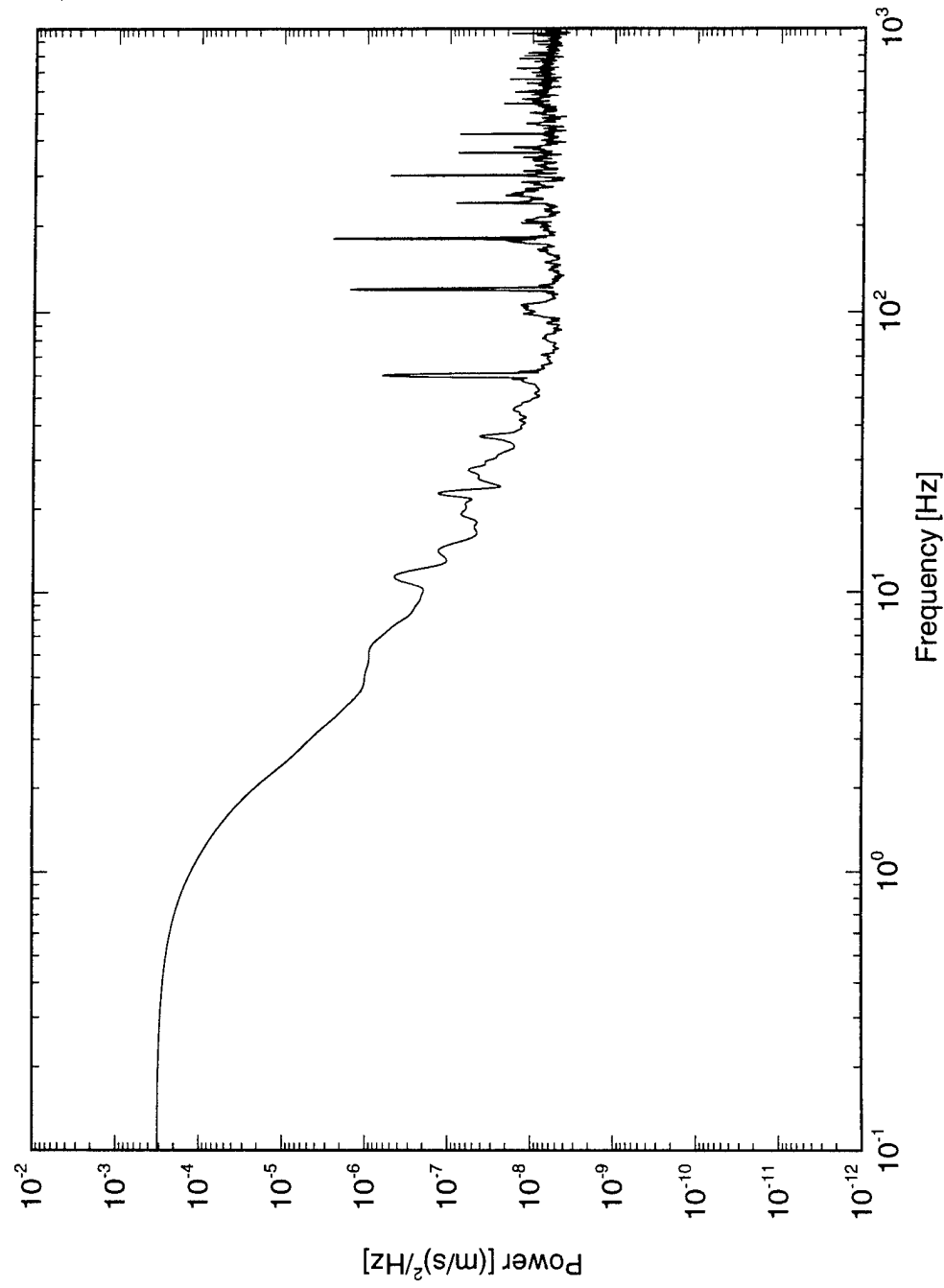


Figure 7.52: Freestream disturbance spectrum at $U_\infty = 15 \text{ m/s}$ with the mixing region vented (DC coupled, band pass 0.1–1000 Hz, Tektronix filters). Measurements taken at $\hat{x} = 1.0 \text{ m}$.

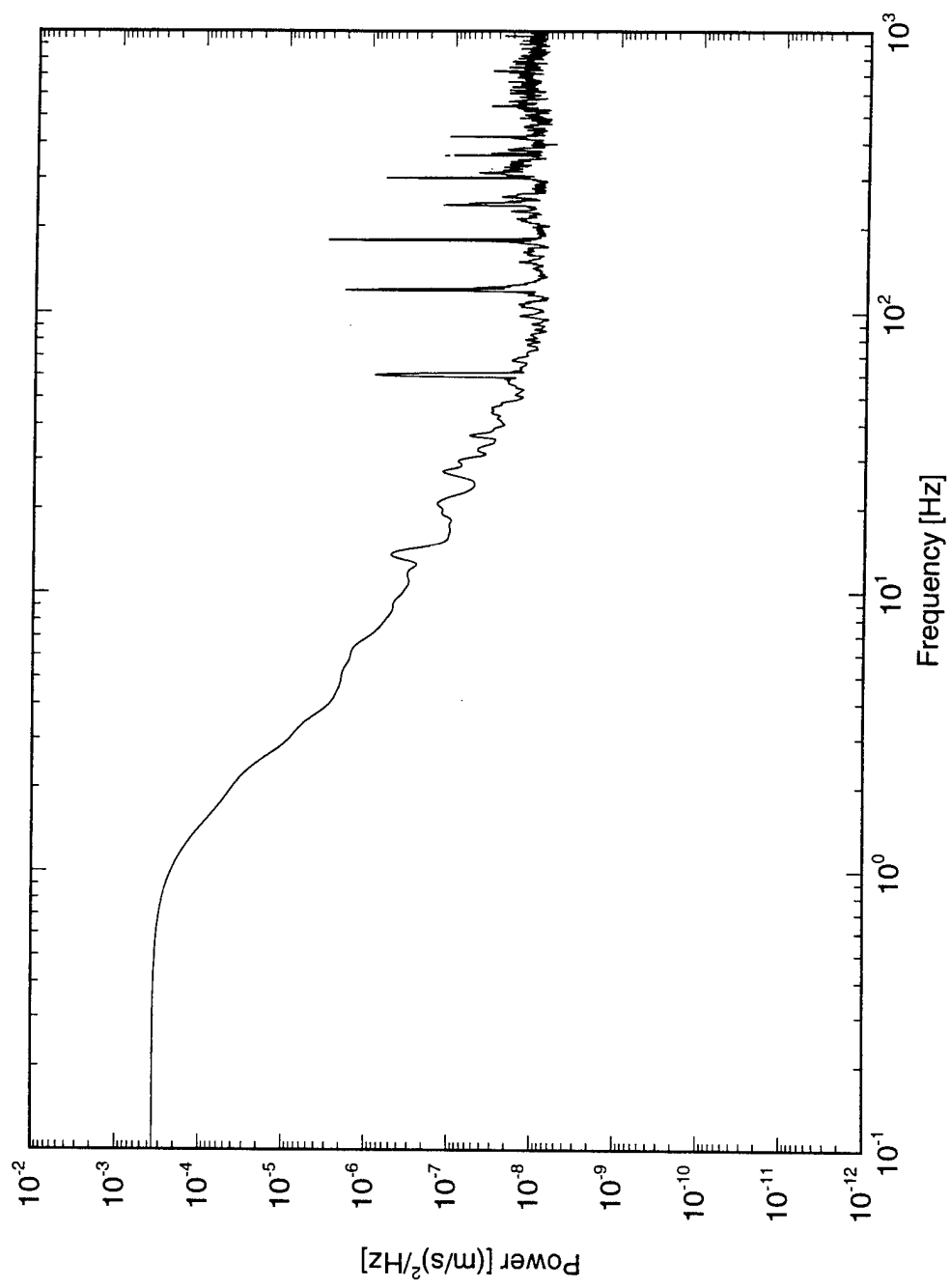


Figure 7.53: Freestream disturbance spectrum at $U_\infty = 18 \text{ m/s}$ with the mixing region vented (DC coupled, band pass 0.1–1000 Hz, Tektronix filters). Measurements taken at $\hat{x} = 1.0 \text{ m}$.

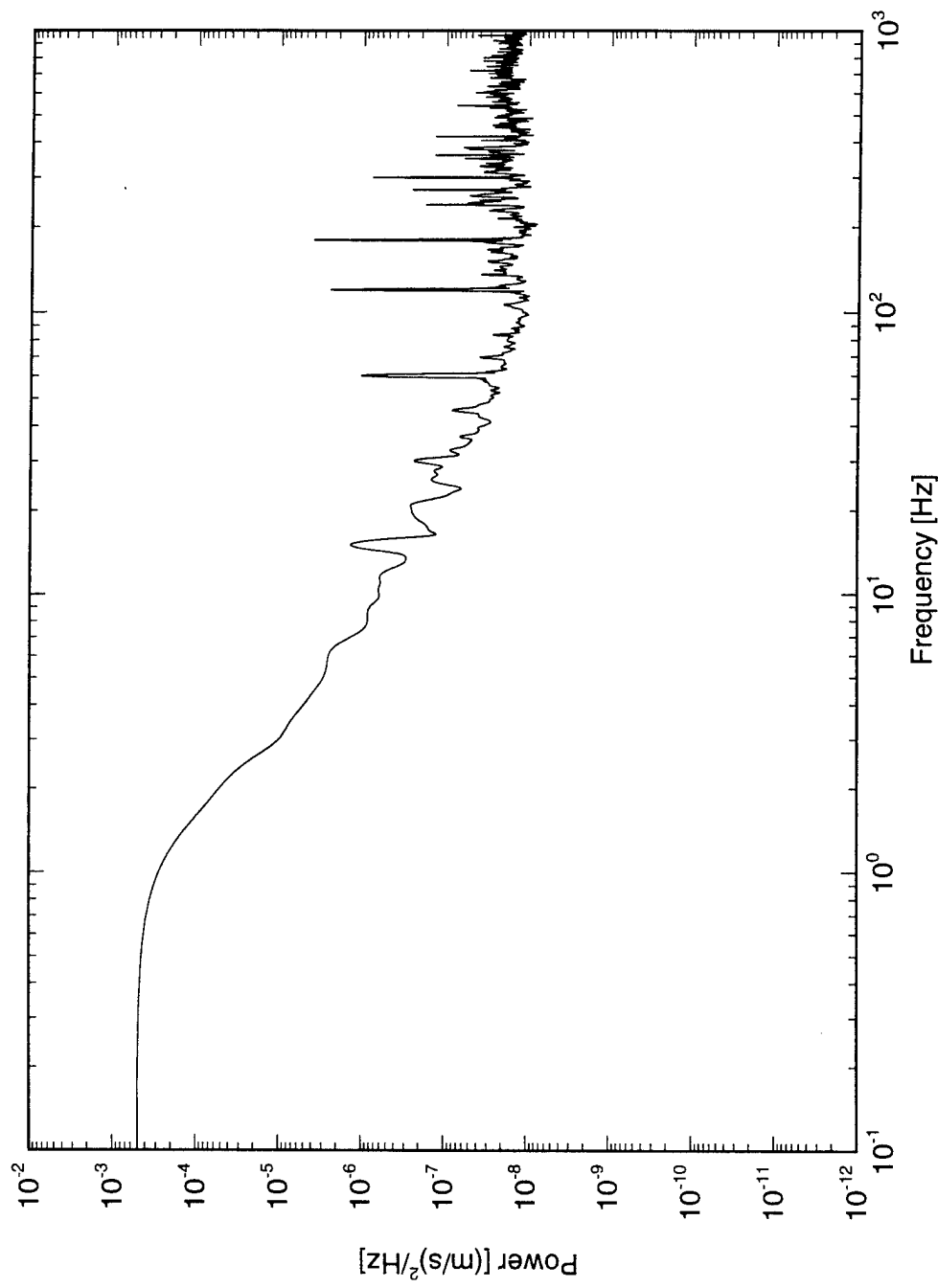


Figure 7.54: Freestream disturbance spectrum at $U_\infty = 20 \text{ m/s}$ with the mixing region vented (DC coupled, band pass 0.1–1000 Hz, Tektronix filters). Measurements taken at $\hat{x} = 1.0 \text{ m}$.

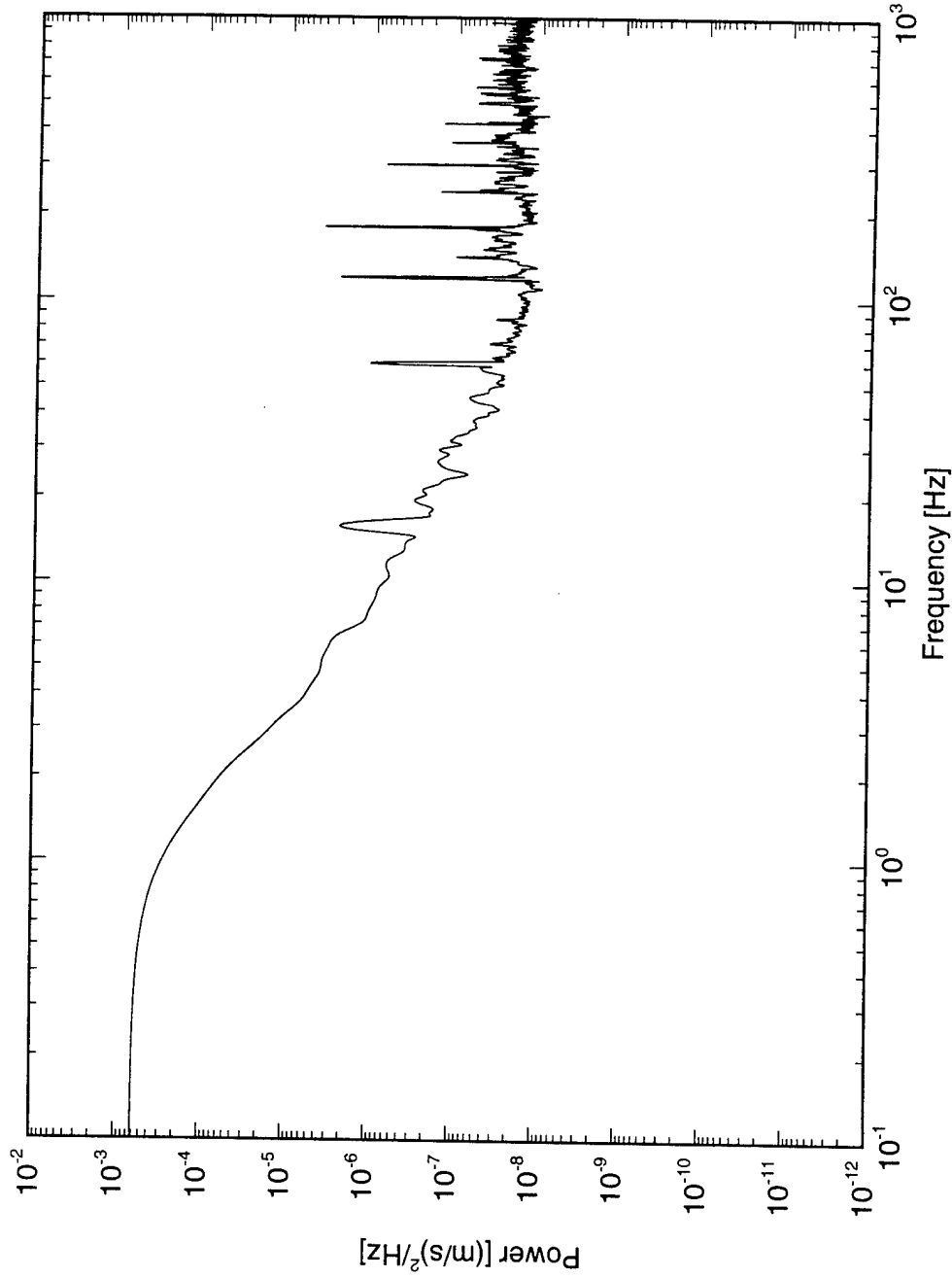


Figure 7.55: Freestream disturbance spectrum at $U_{\infty} = 21$ m/s with the mixing region vented (DC coupled, band pass 0.1–1000 Hz, Tektronix filters). Measurements taken at $\hat{x} = 1.0$ m.

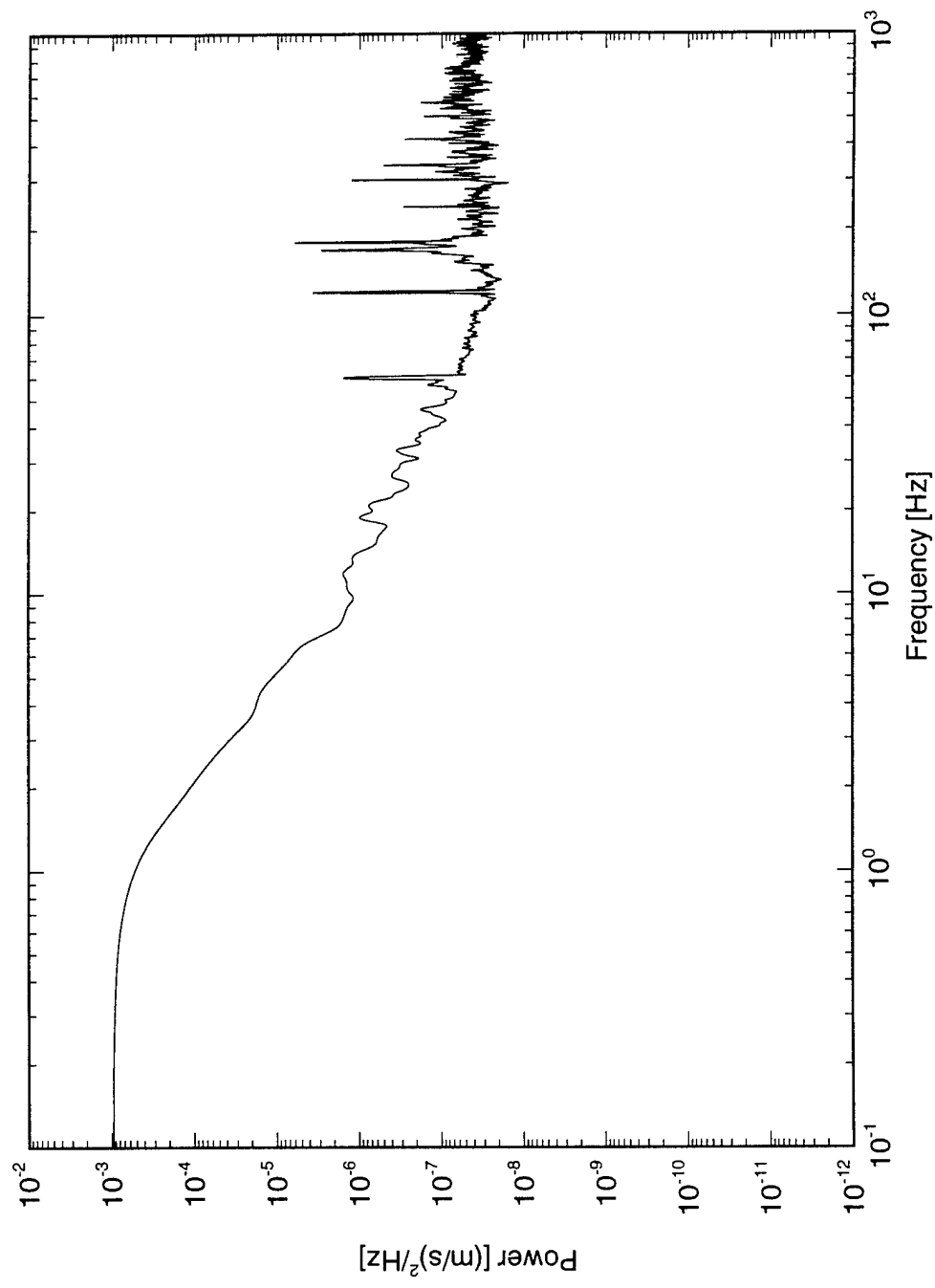


Figure 7.56: Freestream disturbance spectrum at $U_\infty = 25 \text{ m/s}$ with the mixing region vented (DC coupled, band pass 0.1–1000 Hz, Tektronix filters). Measurements taken at $\hat{x} = 1.0 \text{ m}$.

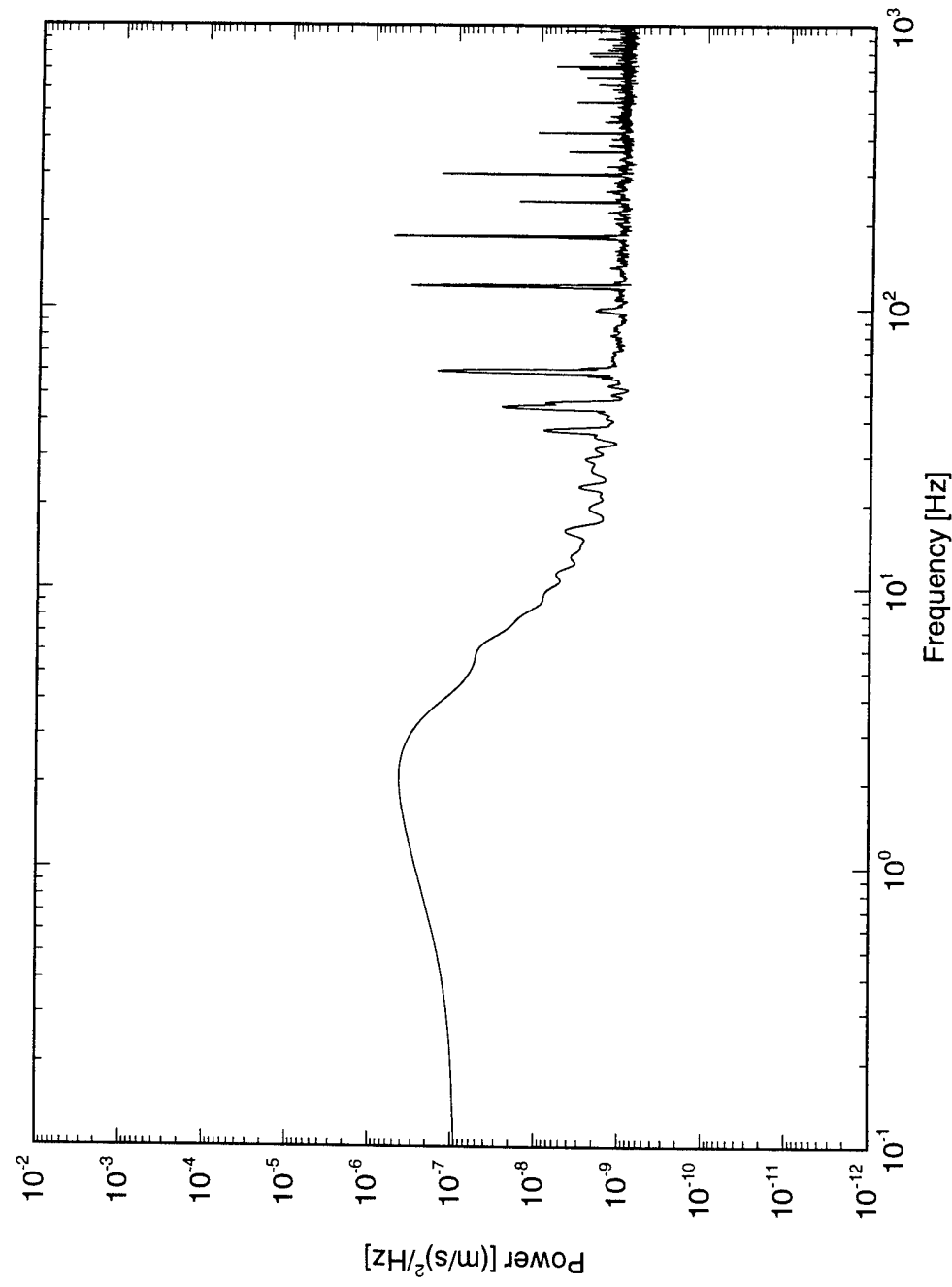


Figure 7.57: Freestream disturbance spectrum at $U_\infty = 5$ m/s with the mixing region vented (AC coupled, band pass 2–1000 Hz, Tektronix filters). Measurements taken at $\hat{x} = 1.0$ m.

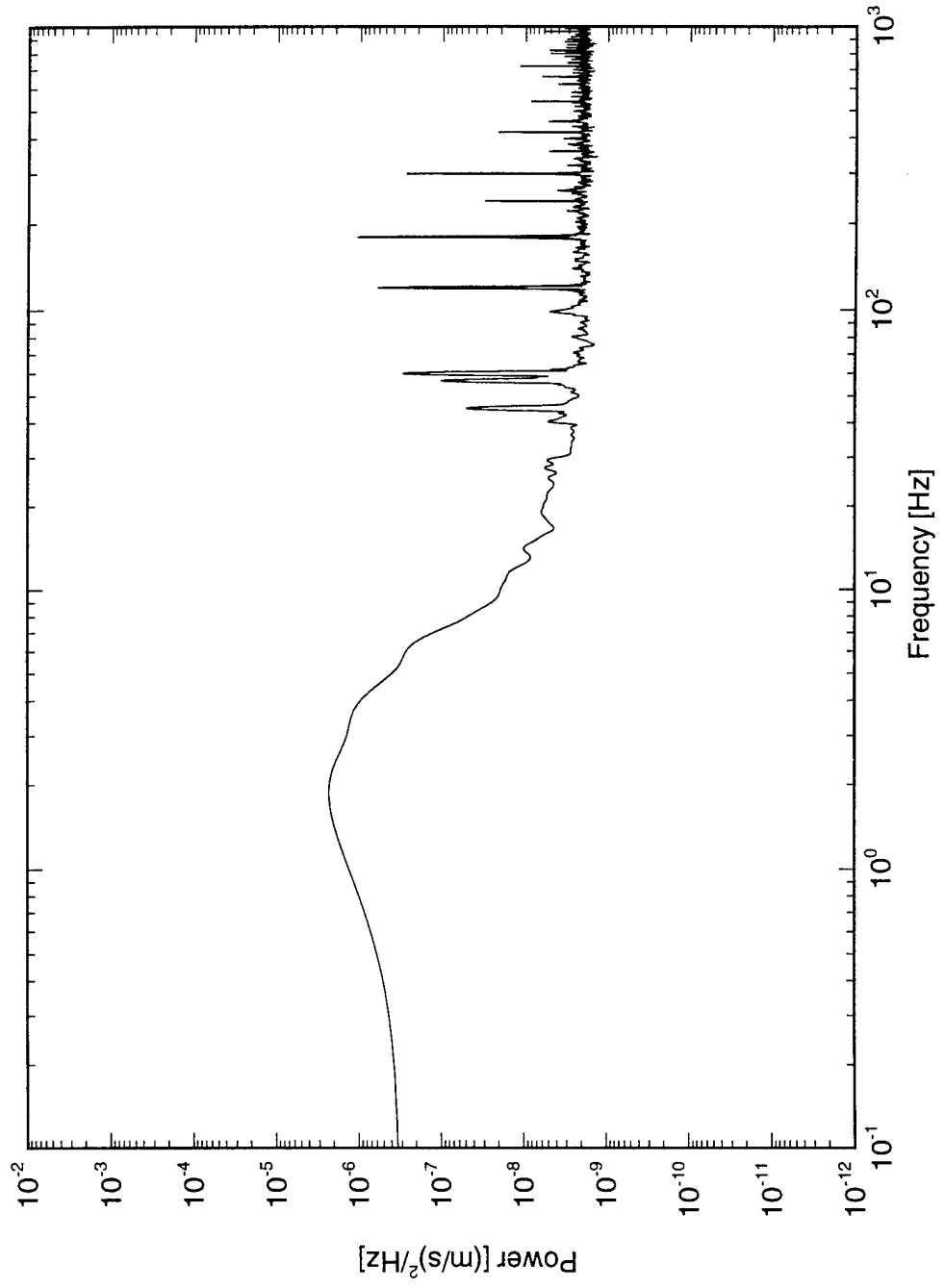


Figure 7.58: Freestream disturbance spectrum at $U_\infty = 8 \text{ m/s}$ with the mixing region vented (AC coupled, band pass 2–1000 Hz, Tektronix filters). Measurements taken at $\hat{x} = 1.0 \text{ m}$.

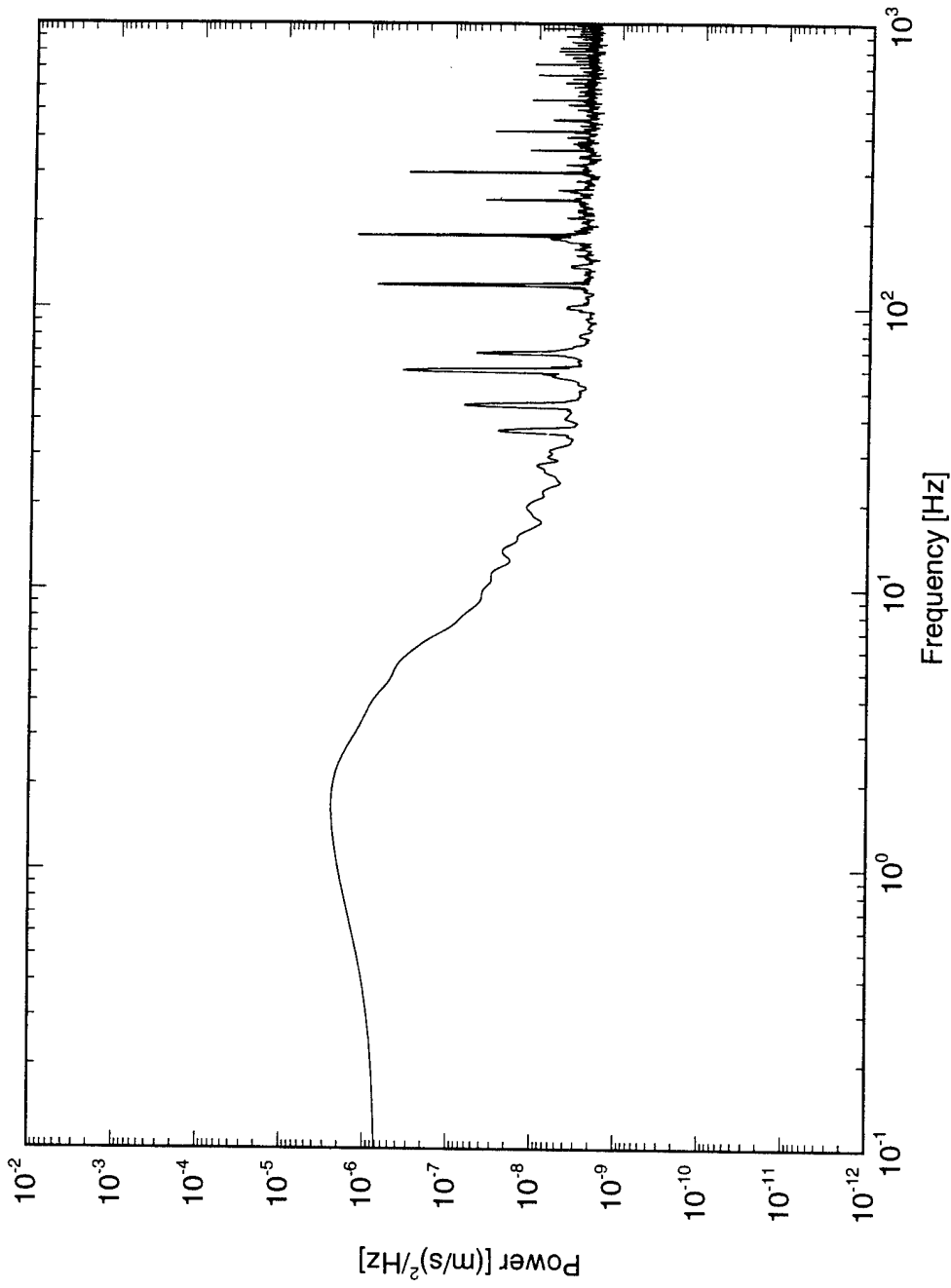


Figure 7.59: Freestream disturbance spectrum at $U_\infty = 10 \text{ m/s}$ with the mixing region vented (AC coupled, band pass 2–1000 Hz, Tektronix filters). Measurements taken at $\hat{x} = 1.0 \text{ m}$.

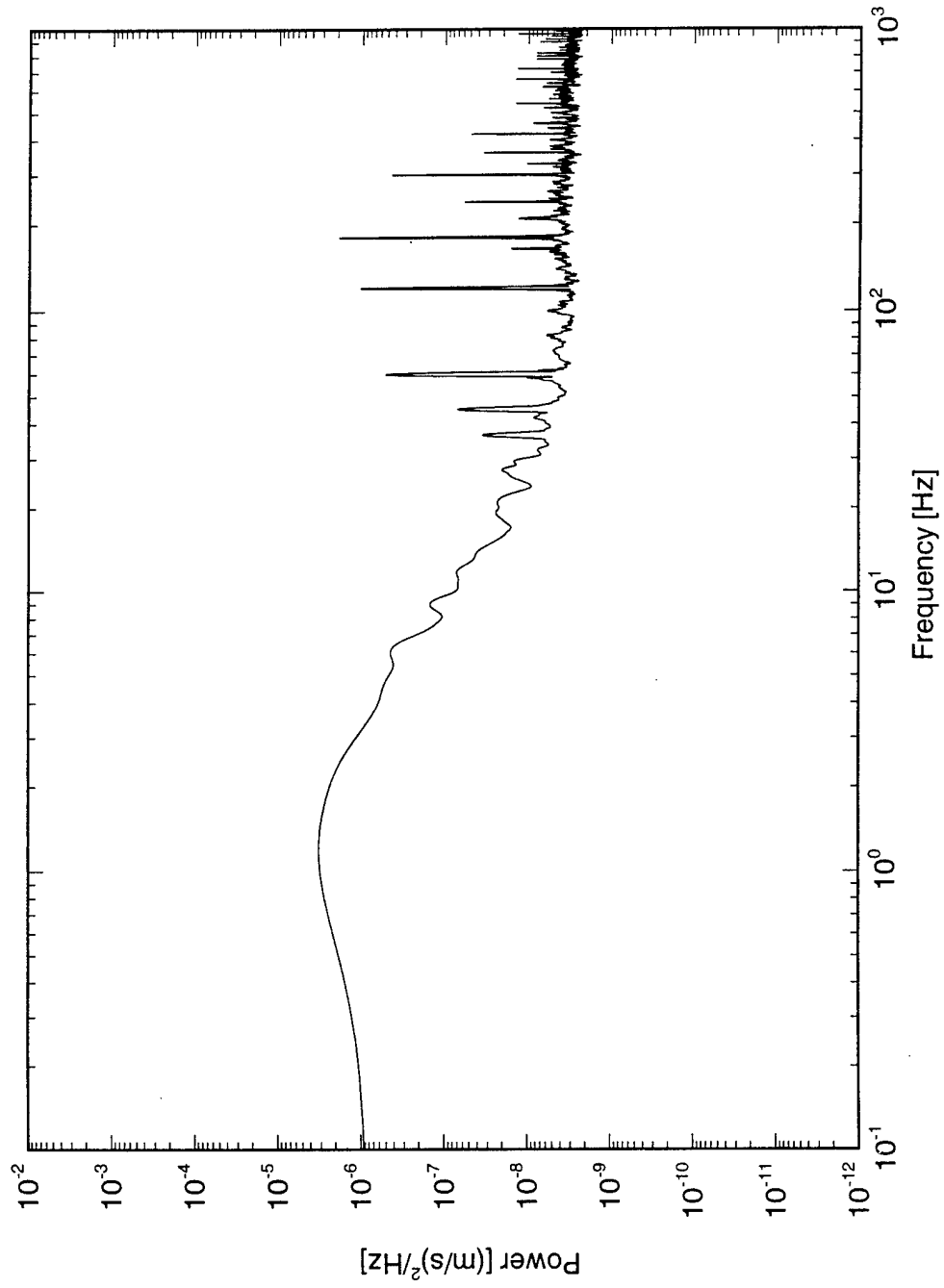


Figure 7.60: Freestream disturbance spectrum at $U_\infty = 12$ m/s with the mixing region vented (AC coupled, band pass 2–1000 Hz, Tektronix filters). Measurements taken at $\hat{x} = 1.0$ m.

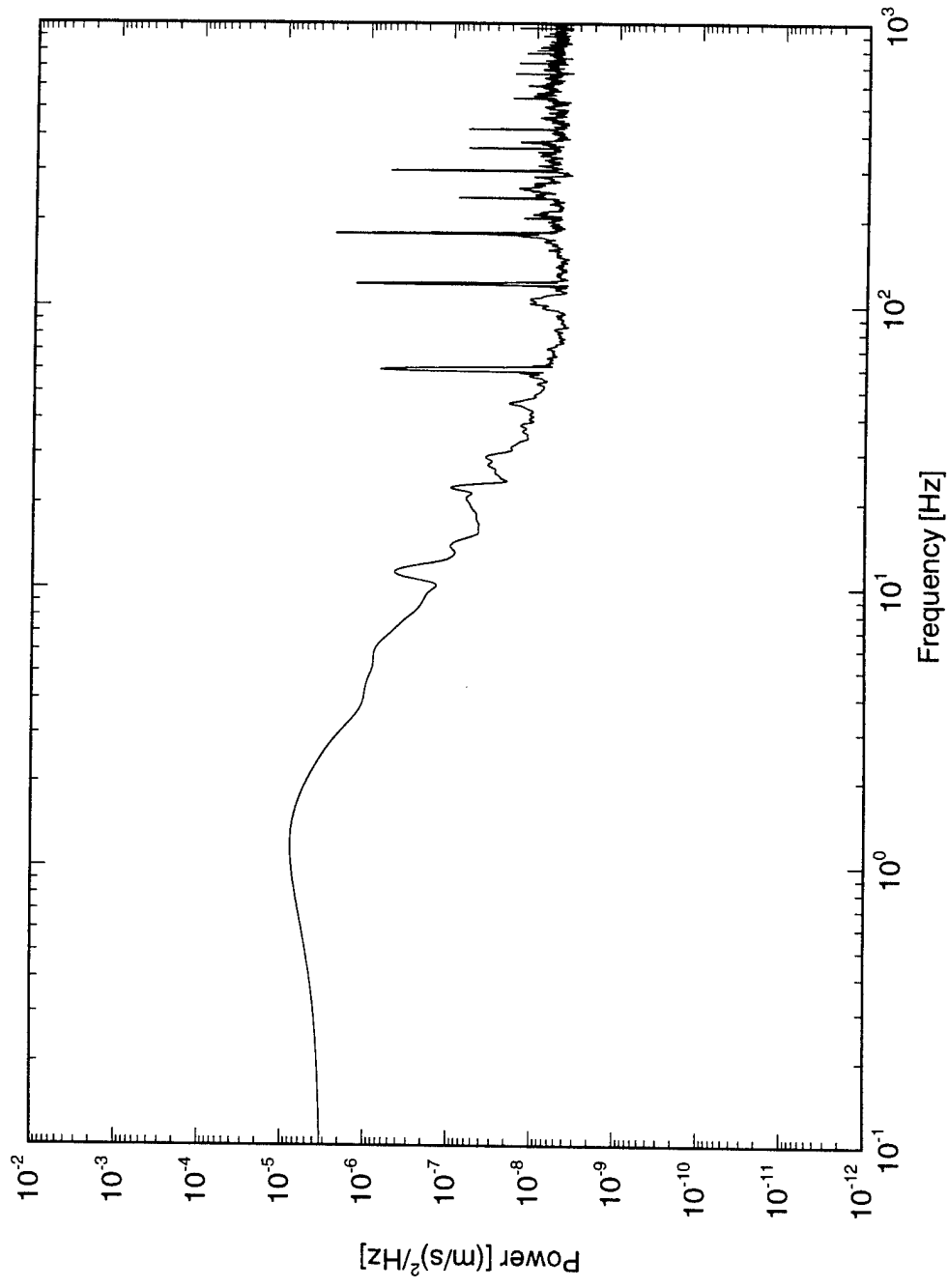


Figure 7.61: Freestream disturbance spectrum at $U_\infty = 15 \text{ m/s}$ with the mixing region vented (AC coupled, band pass 2–1000 Hz, Tektronix filters). Measurements taken at $\hat{x} = 1.0 \text{ m}$.

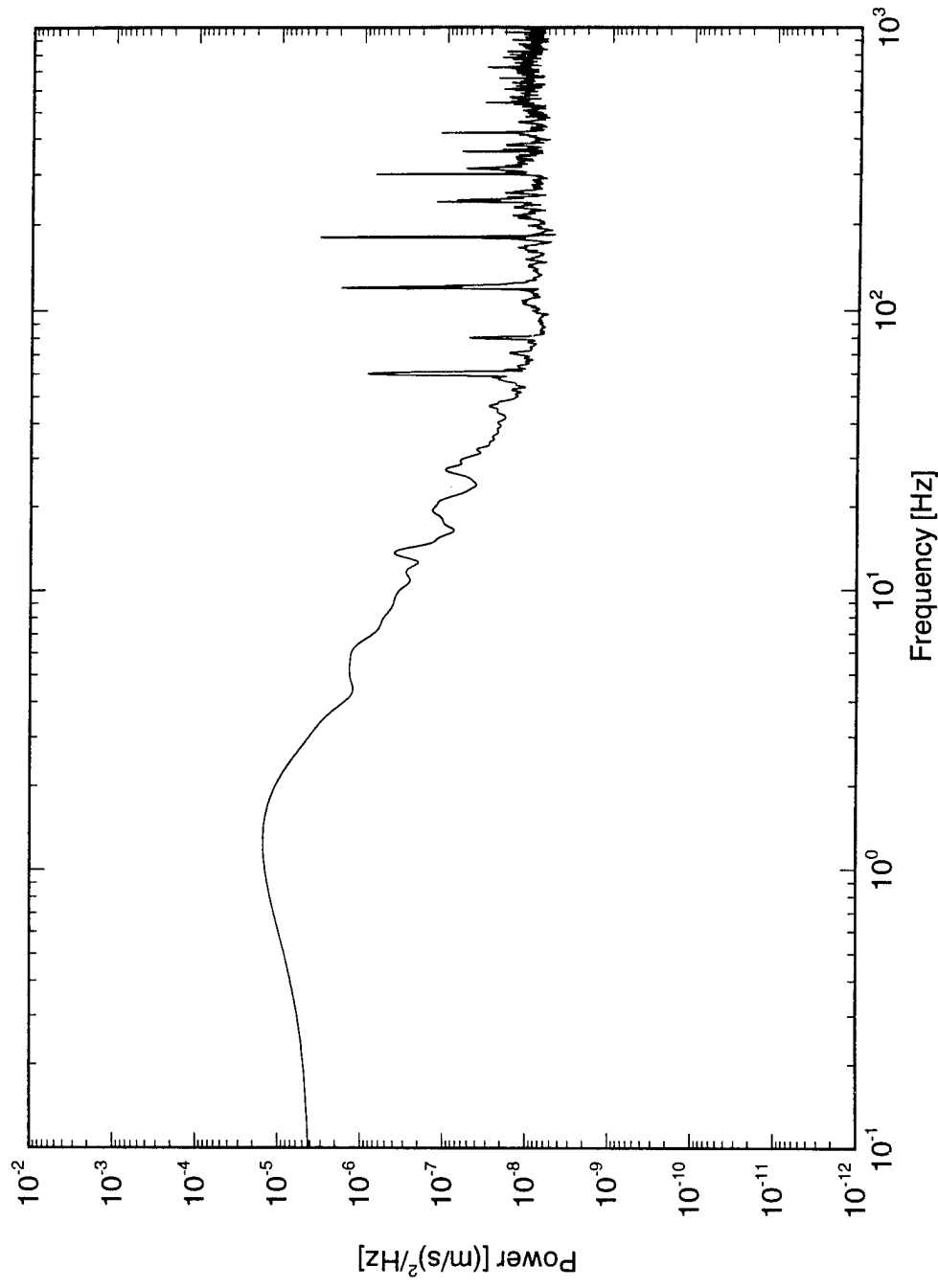


Figure 7.62: Freestream disturbance spectrum at $U_\infty = 18 \text{ m/s}$ with the mixing region vented (AC coupled, band pass 2–1000 Hz, Tektronix filters). Measurements taken at $\hat{x} = 1.0 \text{ m}$.

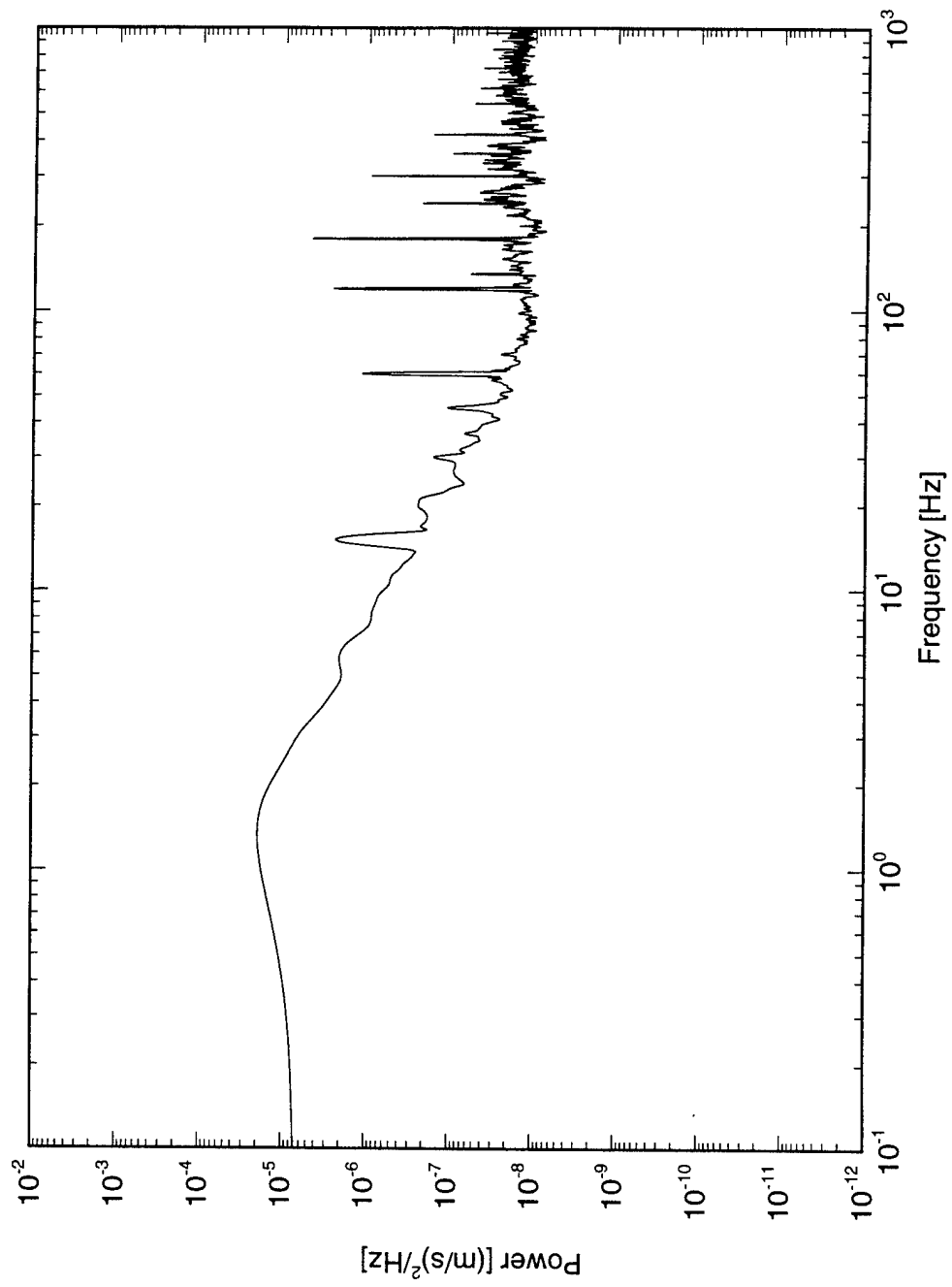


Figure 7.63: Freestream disturbance spectrum at $U_\infty = 20$ m/s with the mixing region vented (AC coupled, band pass 2–1000 Hz, Tektronix filters). Measurements taken at $\hat{x} = 1.0$ m.

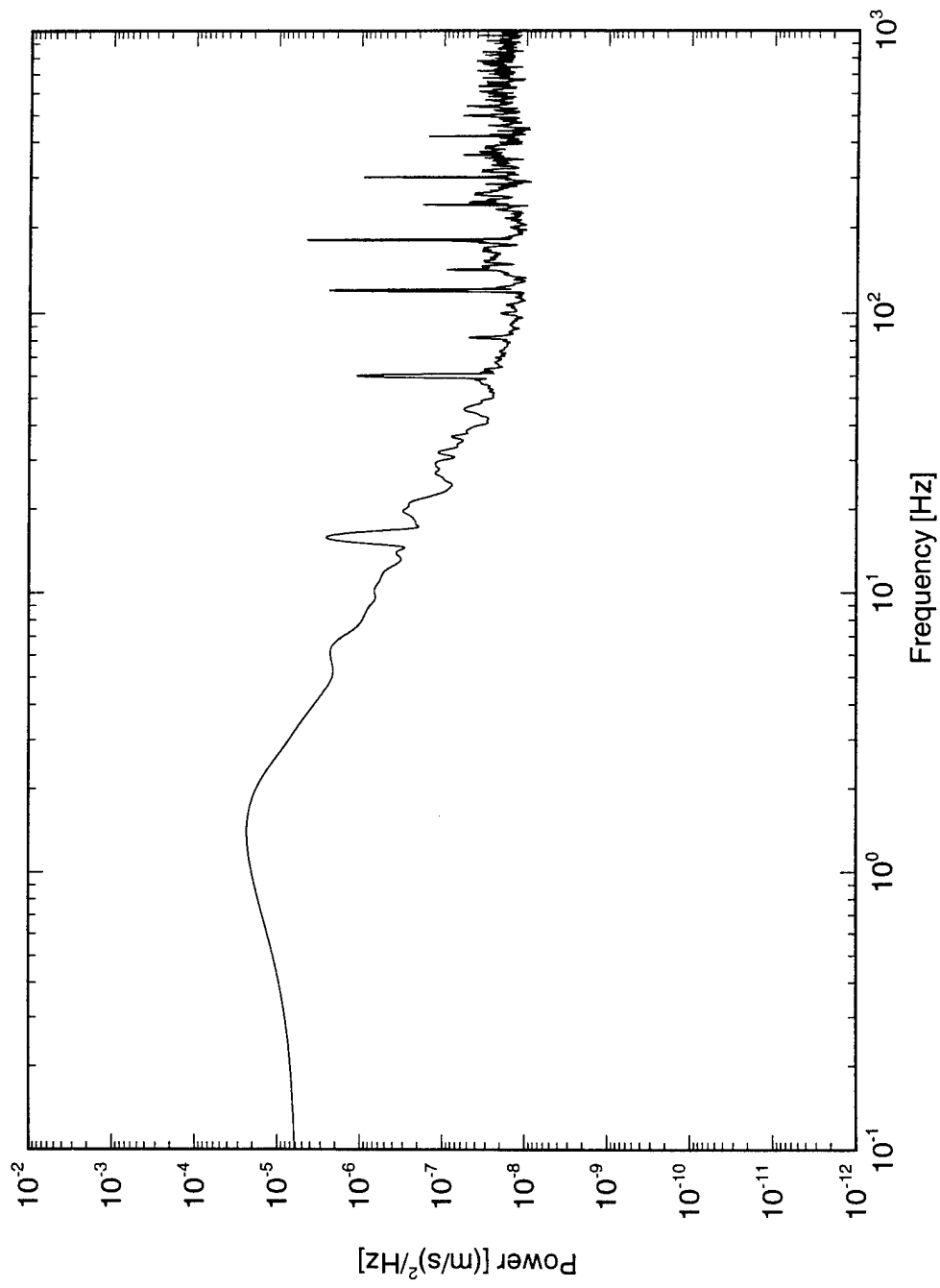


Figure 7.64: Freestream disturbance spectrum at $U_\infty = 21 \text{ m/s}$ with the mixing region vented (AC coupled, band pass 2–1000 Hz, Tektronix filters). Measurements taken at $\hat{x} = 1.0 \text{ m}$.

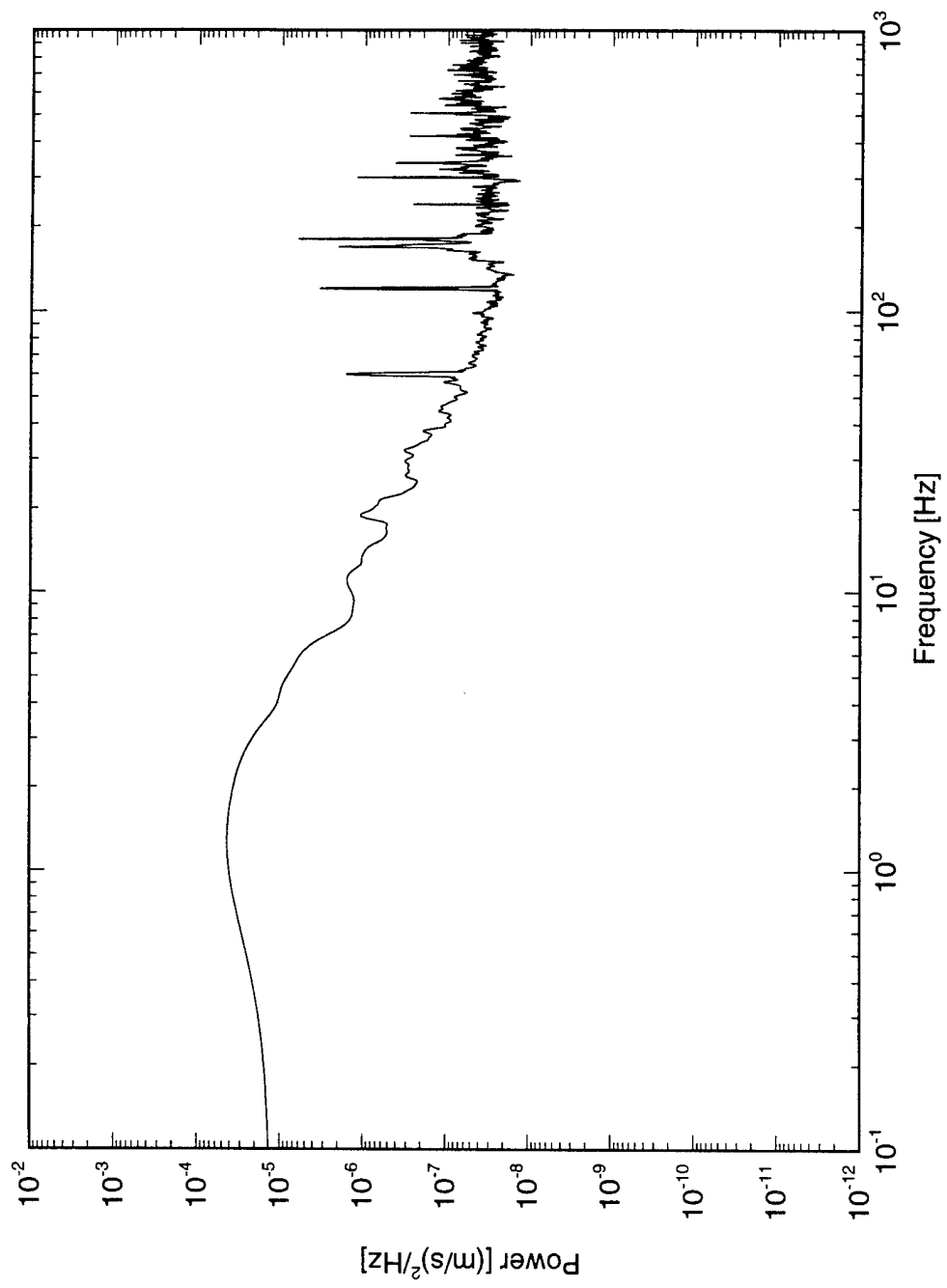


Figure 7.65: Freestream disturbance spectrum at $U_\infty = 25$ m/s with the mixing region vented (AC coupled, band pass 2–1000 Hz, Tektronix filters). Measurements taken at $\hat{x} = 1.0$ m.

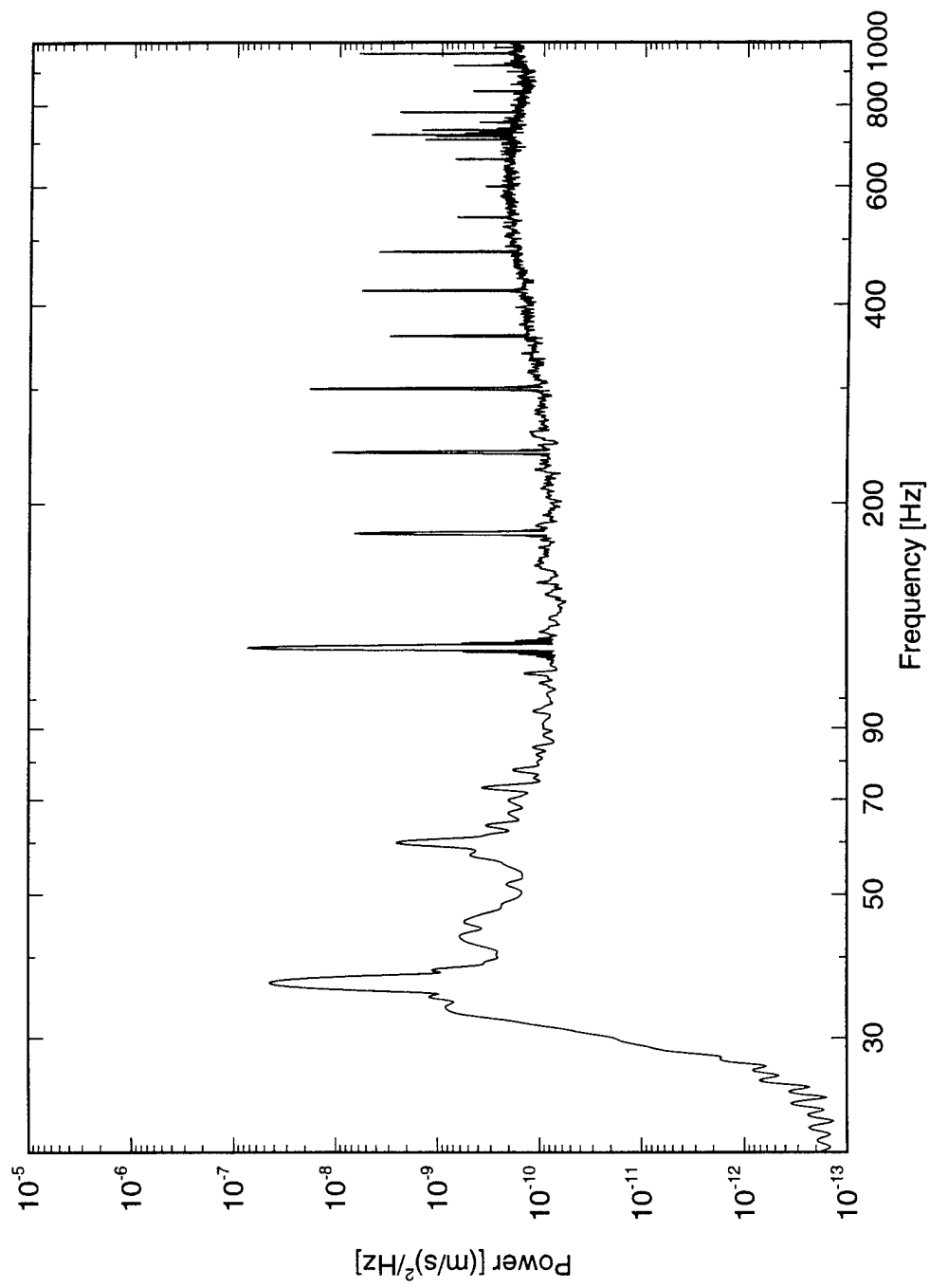


Figure 7.66: Freestream disturbance spectrum at $U_\infty = 5 \text{ m/s}$ with the mixing region vented (AC coupled, band pass 35–1000 Hz, Stewart filters). Measurements taken at $\hat{x} = 1.0 \text{ m}$.

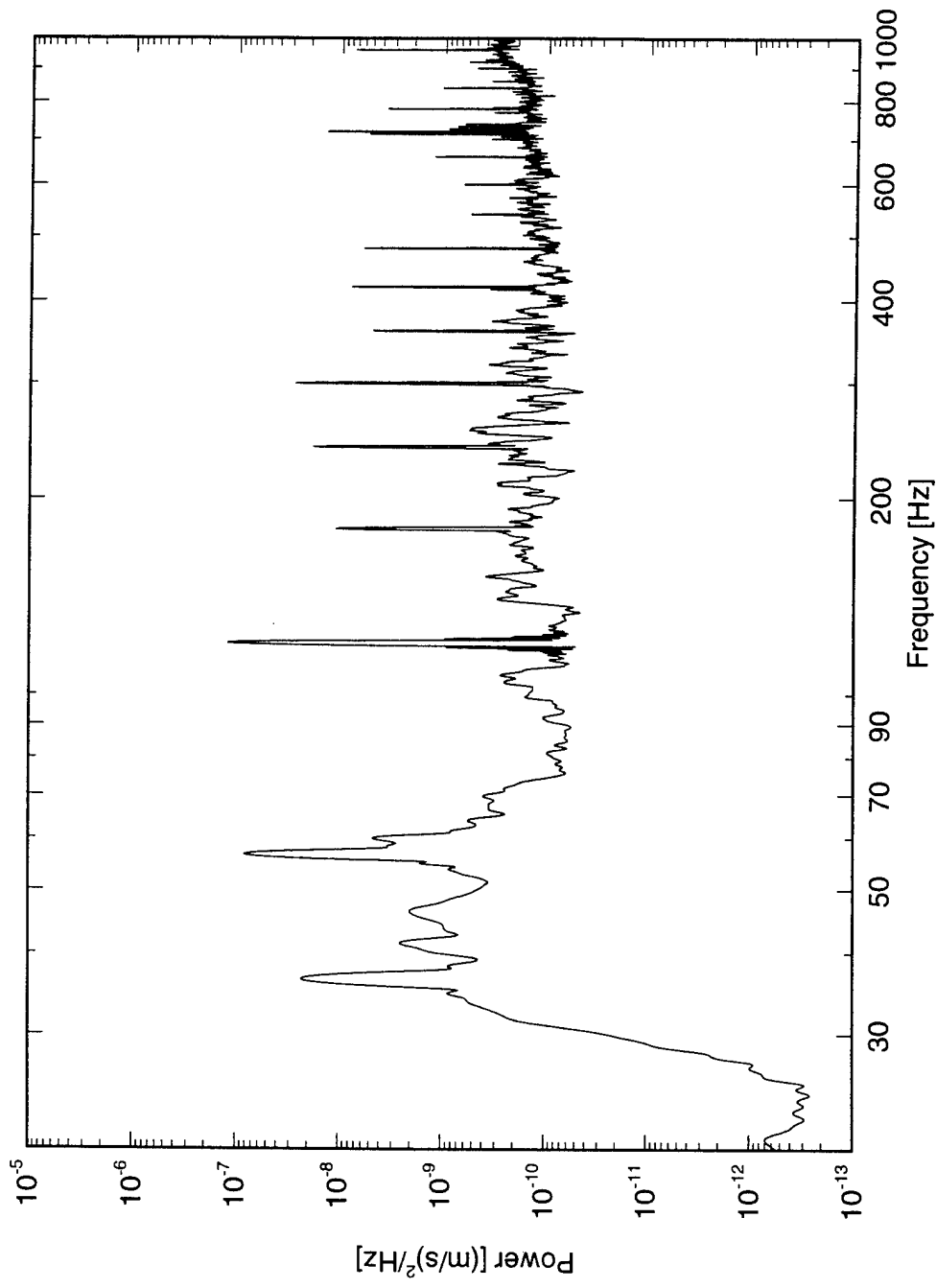


Figure 7.67: Freestream disturbance spectrum at $U_\infty = 8 \text{ m/s}$ with the mixing region vented (AC coupled, band pass 35–1000 Hz, Stewart filters). Measurements taken at $\hat{x} = 1.0 \text{ m}$.

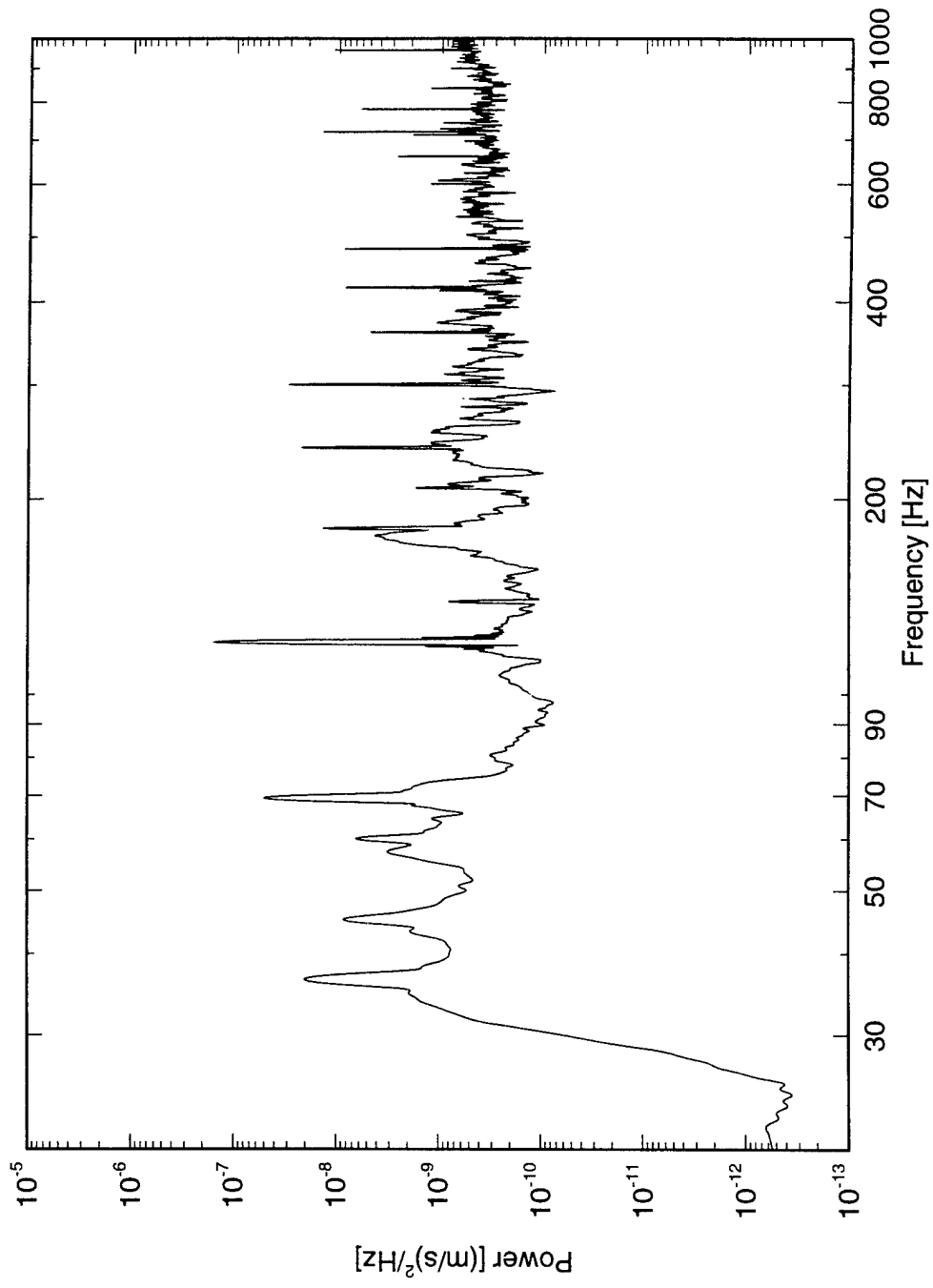


Figure 7.68: Freestream disturbance spectrum at $U_{\infty} = 10$ m/s with the mixing region vented (AC coupled, band pass 35–1000 Hz, Stewart filters). Measurements taken at $\hat{x} = 1.0$ m.

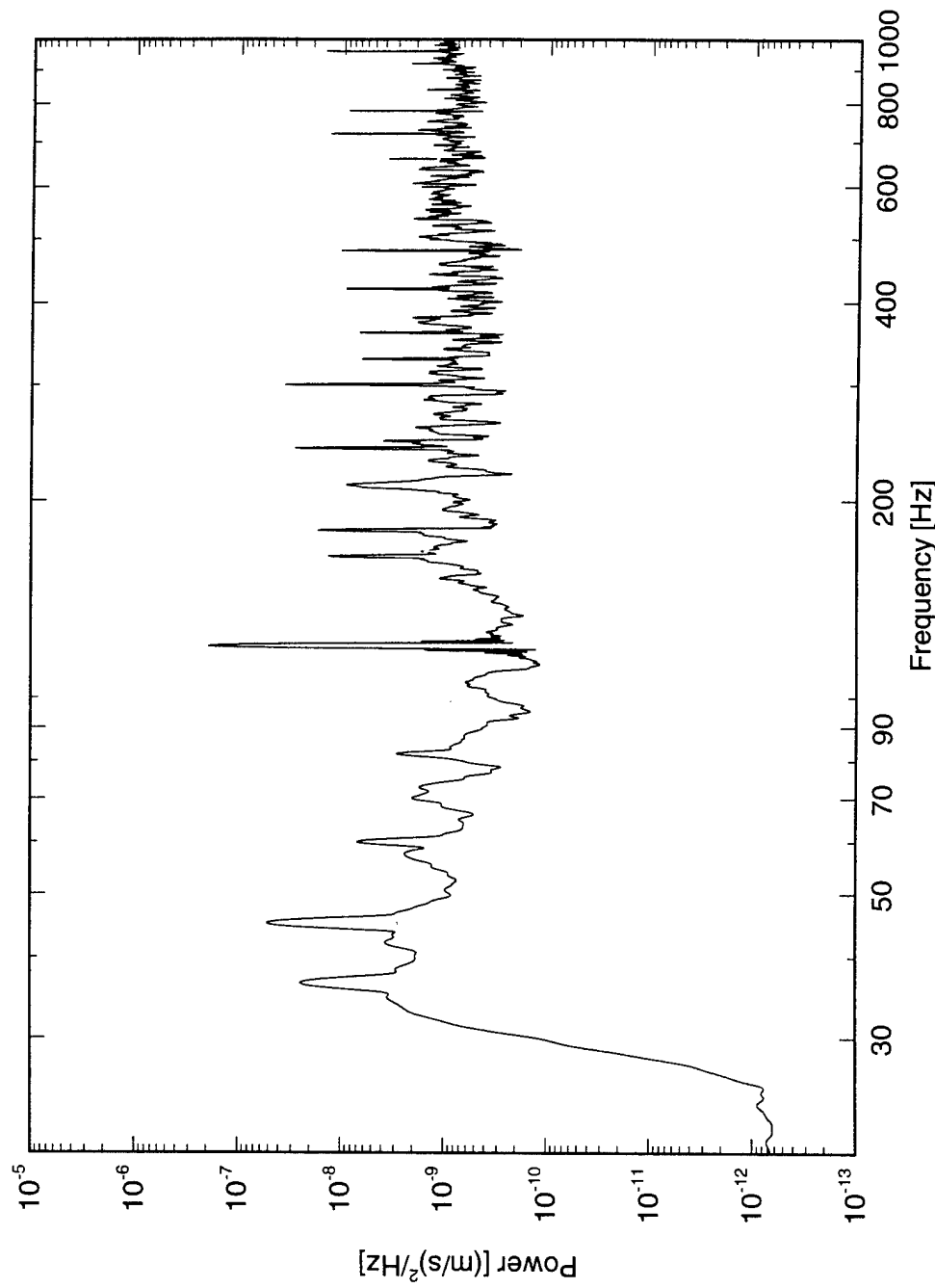


Figure 7.69: Freestream disturbance spectrum at $U_\infty = 12 \text{ m/s}$ with the mixing region vented (AC coupled, band pass 35–1000 Hz, Stewart filters). Measurements taken at $\hat{x} = 1.0 \text{ m}$.

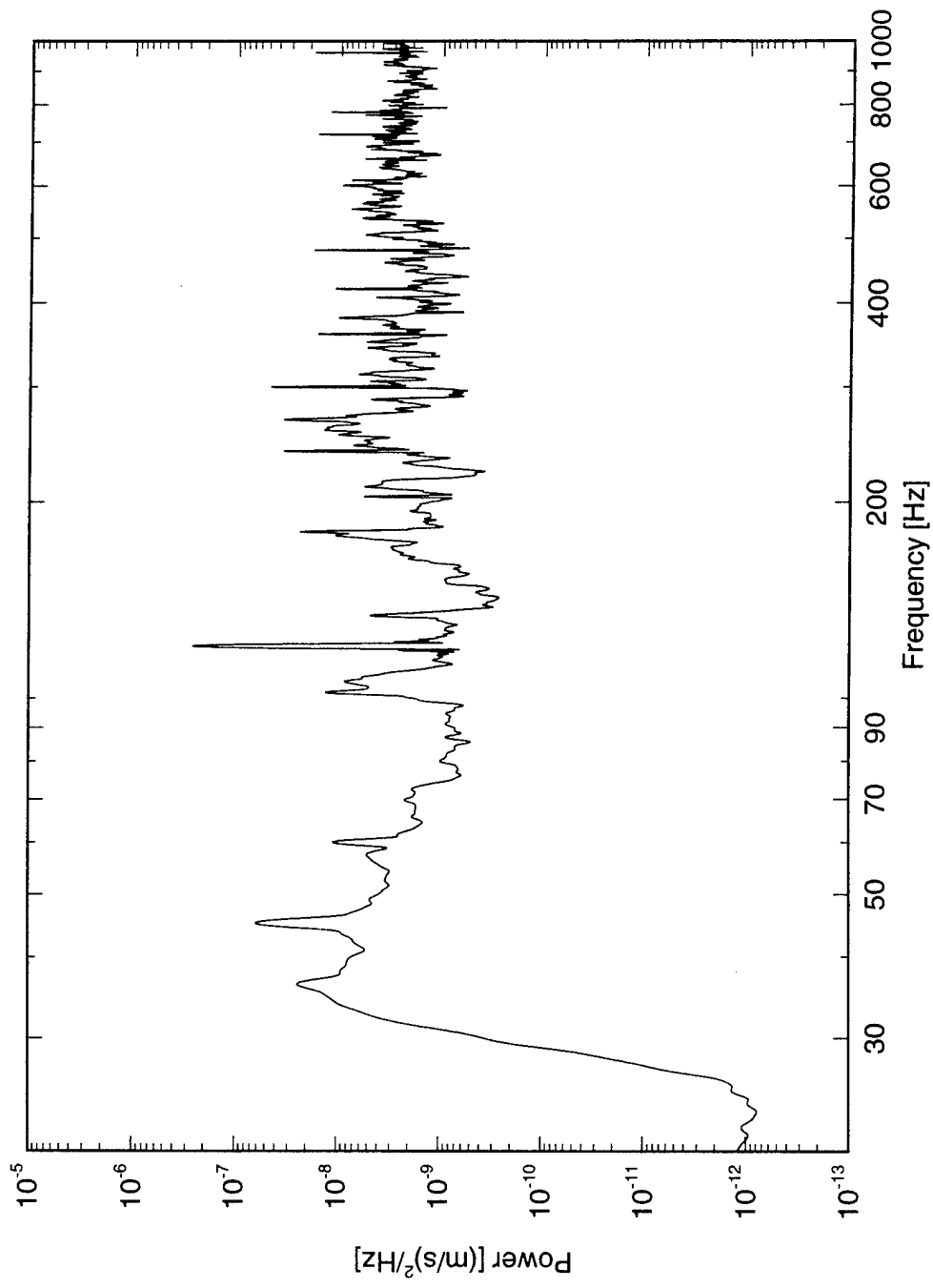


Figure 7.70: Freestream disturbance spectrum at $U_\infty = 15$ m/s with the mixing region vented (AC coupled, band pass 35–1000 Hz, Stewart filters). Measurements taken at $\hat{x} = 1.0$ m.

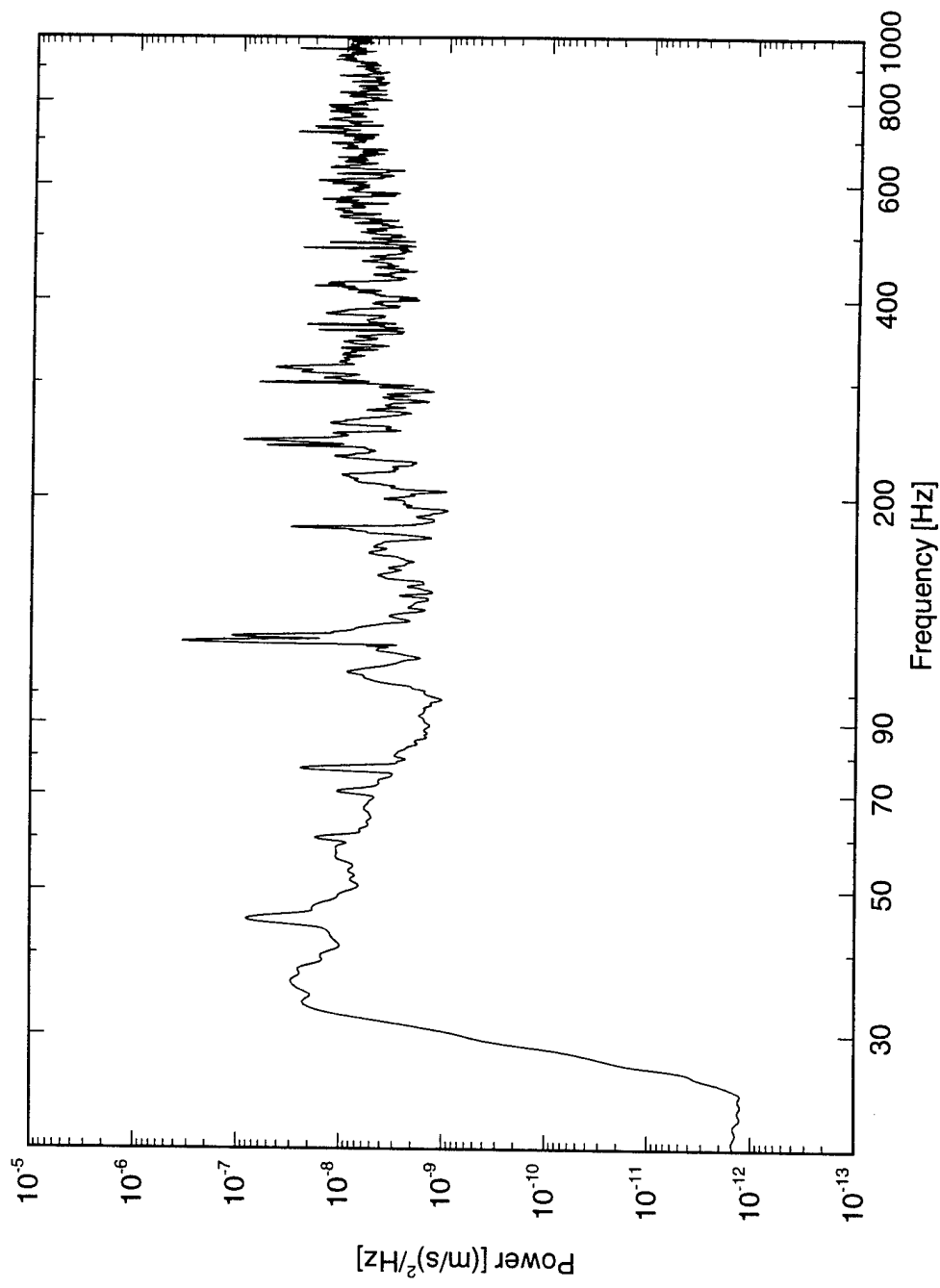


Figure 7.71: Freestream disturbance spectrum at $U_\infty = 18 \text{ m/s}$ with the mixing region vented (AC coupled, band pass 35–1000 Hz, Stewart filters). Measurements taken at $\hat{x} = 1.0 \text{ m}$.

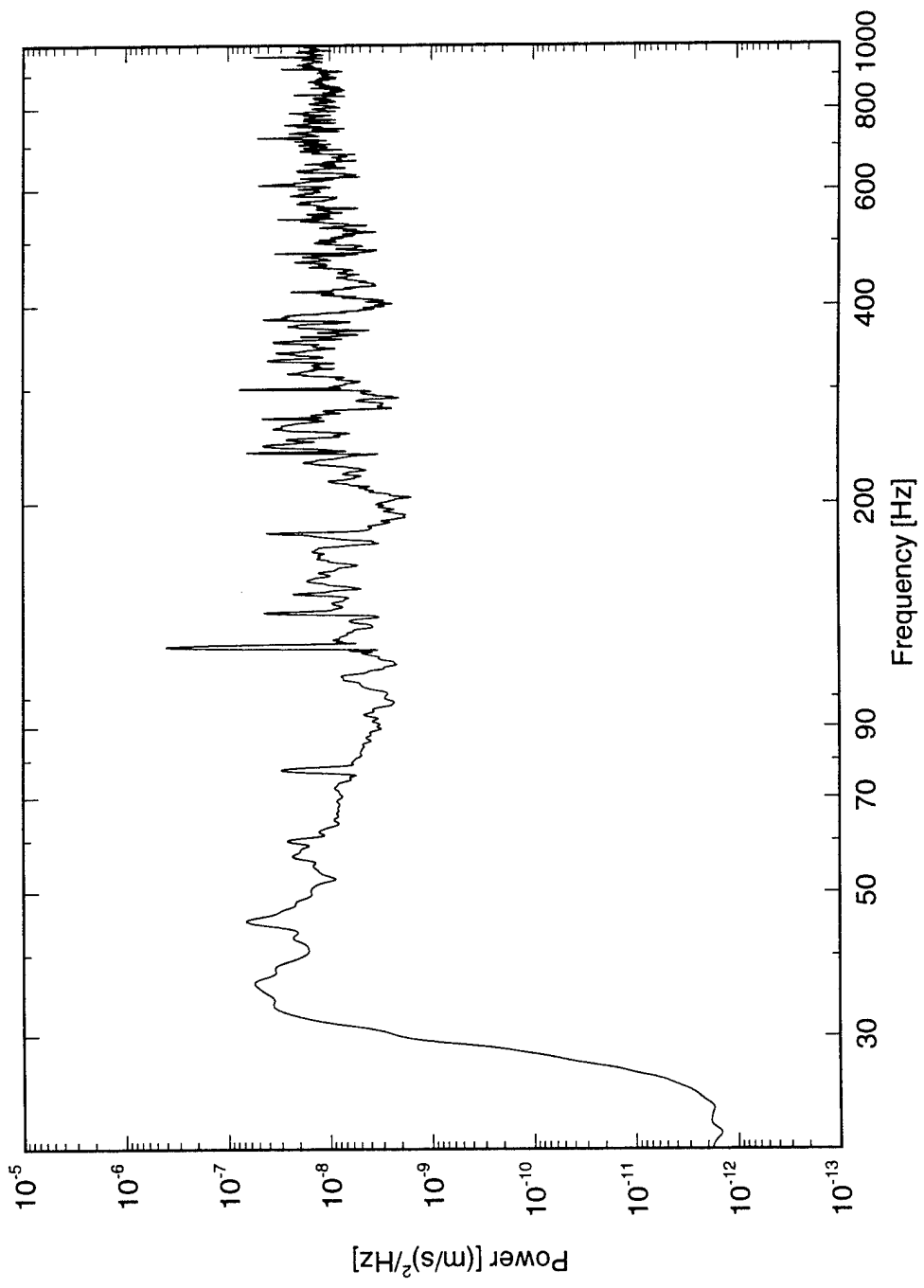


Figure 7.72: Freestream disturbance spectrum at $U_\infty = 20 \text{ m/s}$ with the mixing region vented (AC coupled, band pass 35–1000 Hz, Stewart filters). Measurements taken at $\hat{x} = 1.0 \text{ m}$.

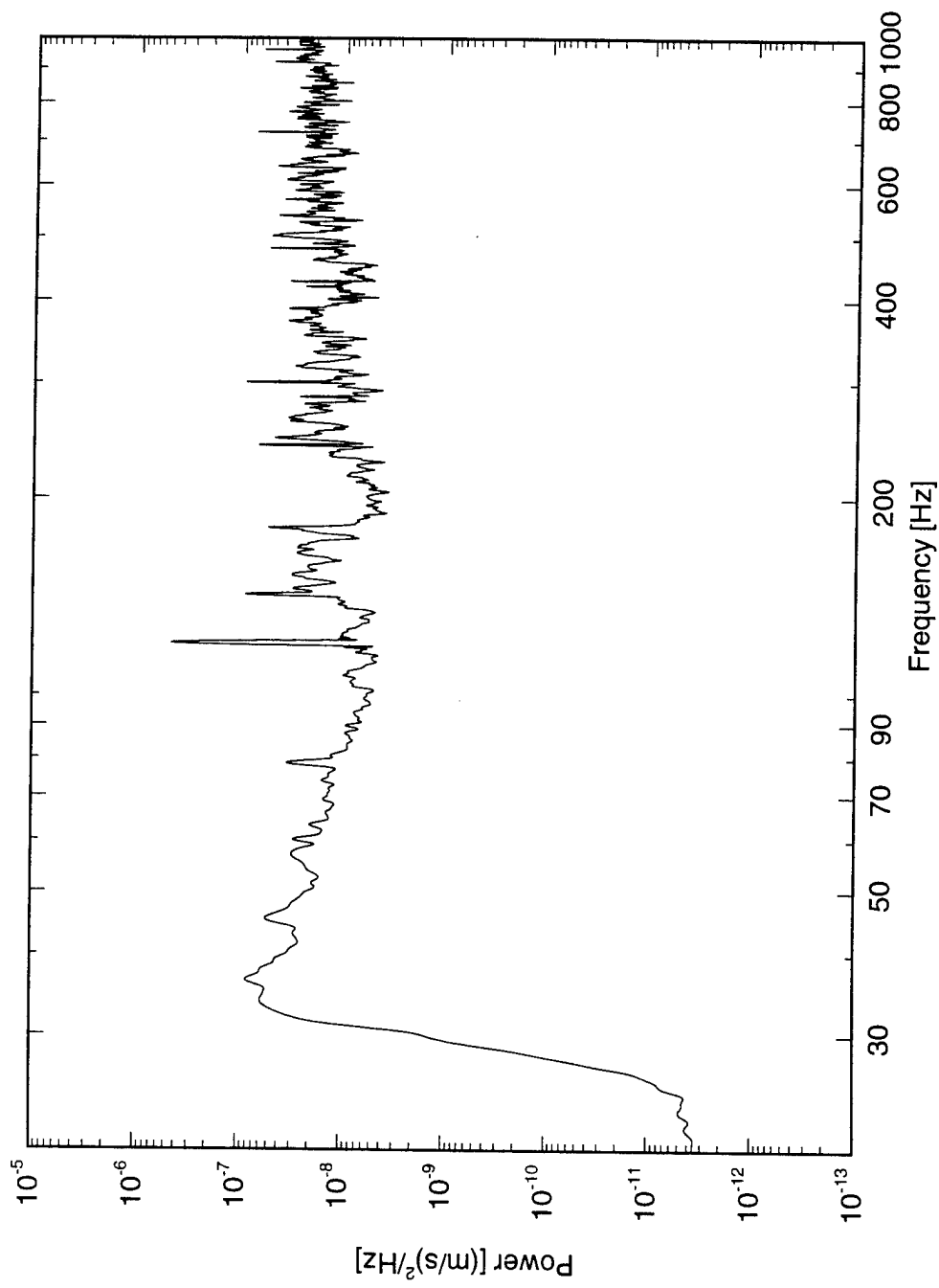


Figure 7.73: Freestream disturbance spectrum at $U_\infty = 21 \text{ m/s}$ with the mixing region vented (AC coupled, band pass 35–1000 Hz, Stewart filters). Measurements taken at $\hat{x} = 1.0 \text{ m}$.

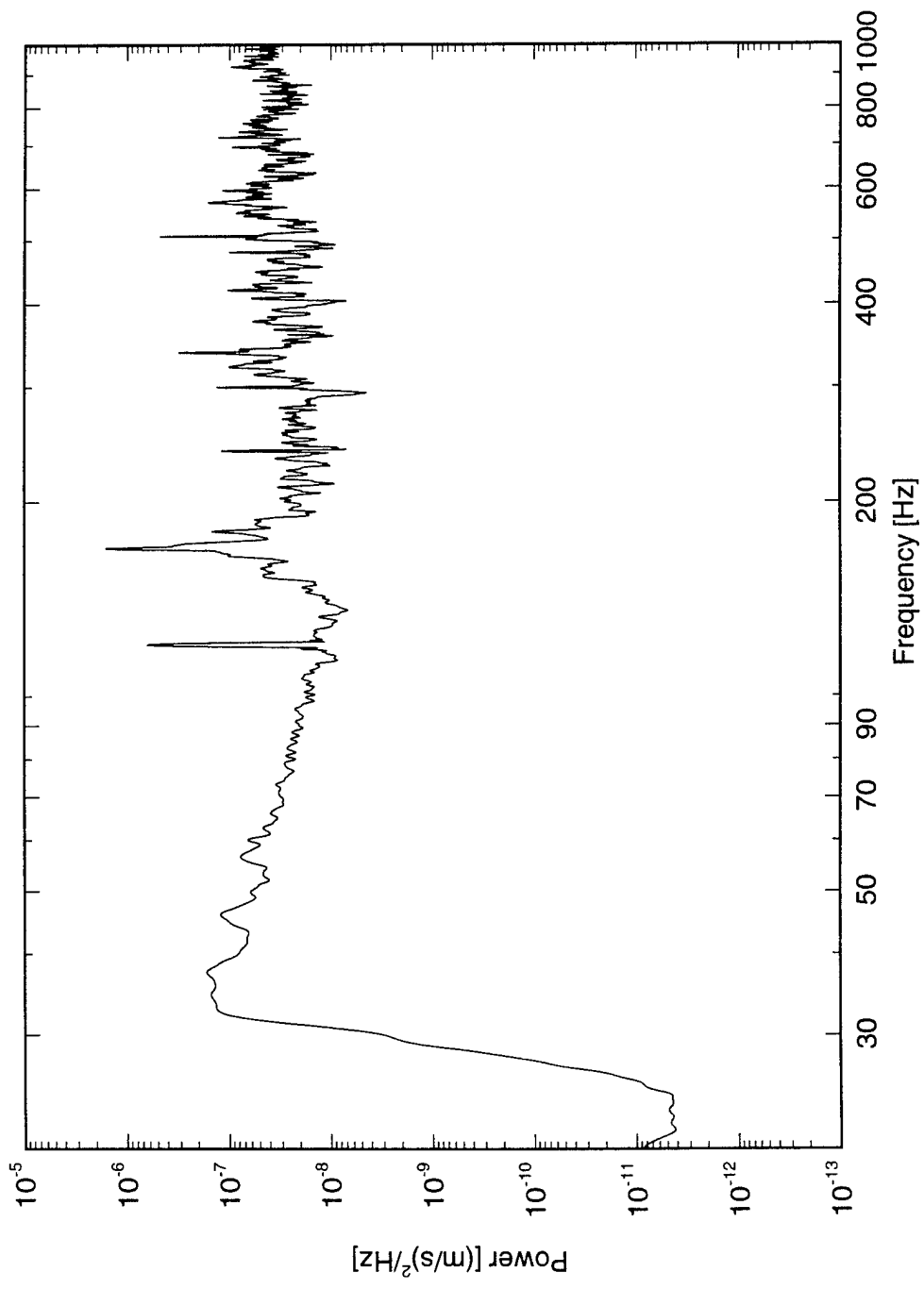


Figure 7.74: Freestream disturbance spectrum at $U_\infty = 25$ m/s with the mixing region vented (AC coupled, band pass 35–1000 Hz, Stewart filters). Measurements taken at $\hat{x} = 1.0$ m.

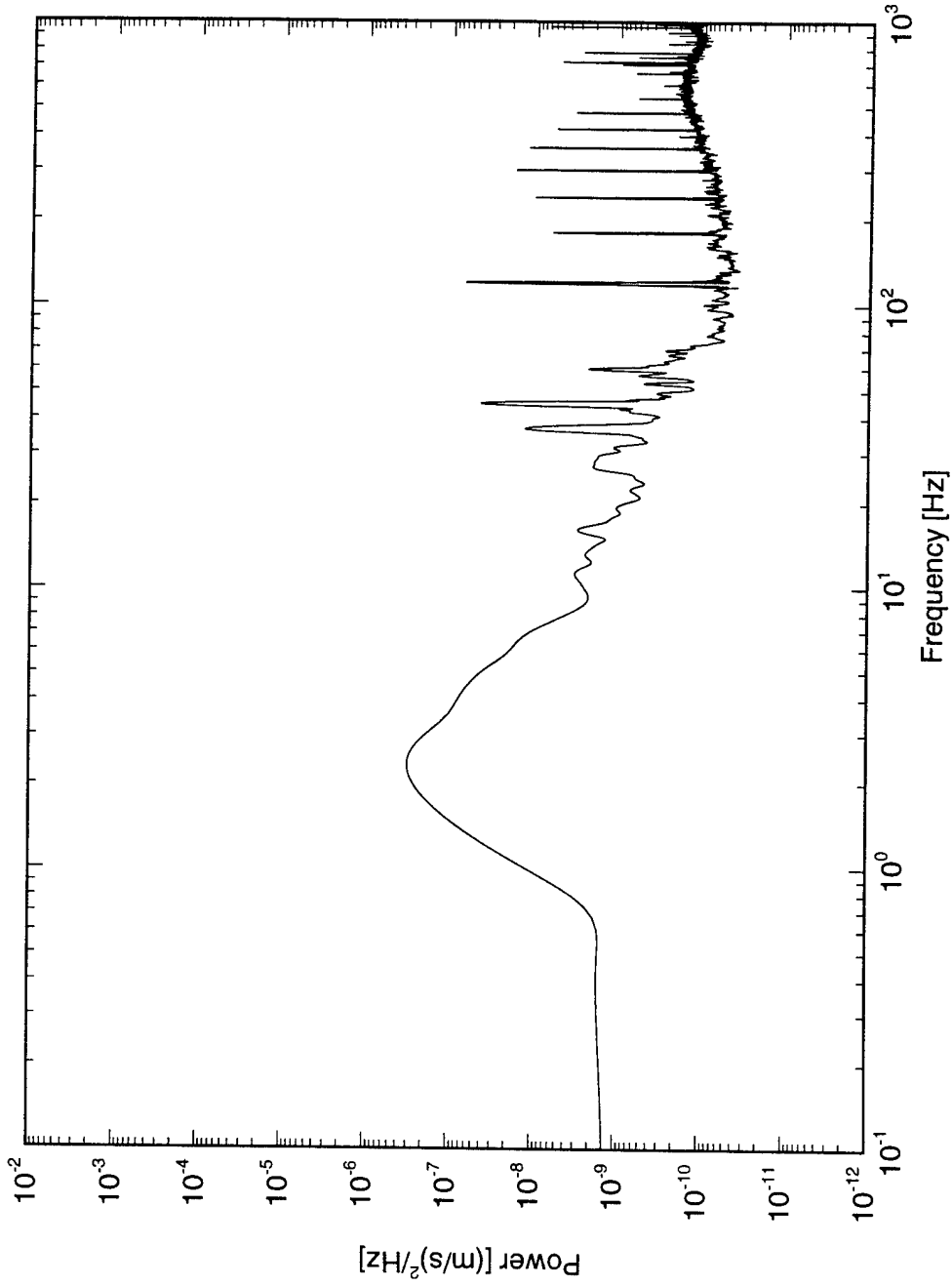


Figure 7.75: Freestream disturbance spectrum at $U_\infty = 5 \text{ m/s}$ with the mixing region vented (AC coupled, band pass 2–1000 Hz, Stewart filters). Measurements taken at $\hat{x} = 1.0 \text{ m}$.

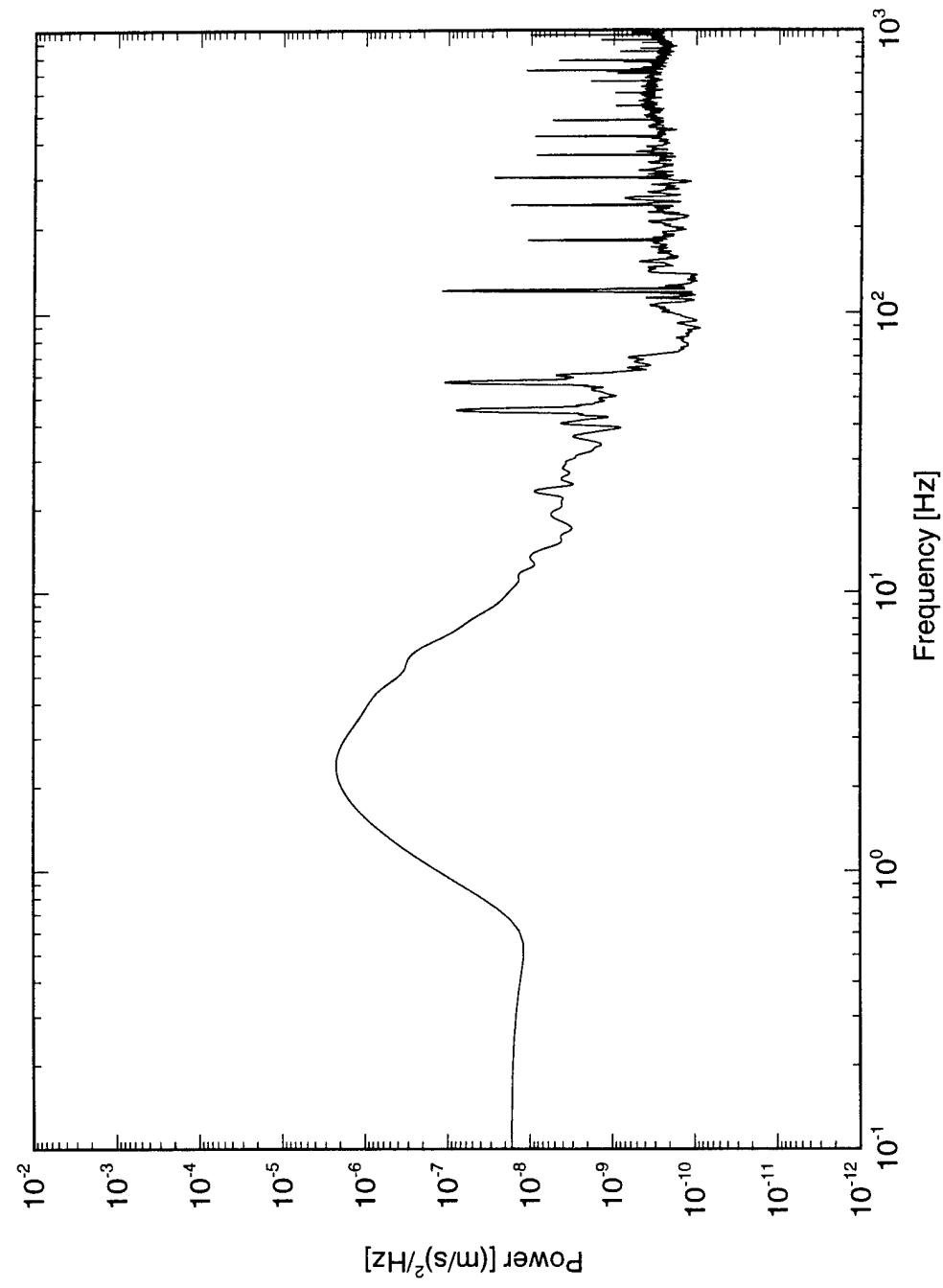


Figure 7.76: Freestream disturbance spectrum at $U_\infty = 8 \text{ m/s}$ with the mixing region vented (AC coupled, band pass 2–1000 Hz, Stewart filters). Measurements taken at $\hat{x} = 1.0 \text{ m}$.

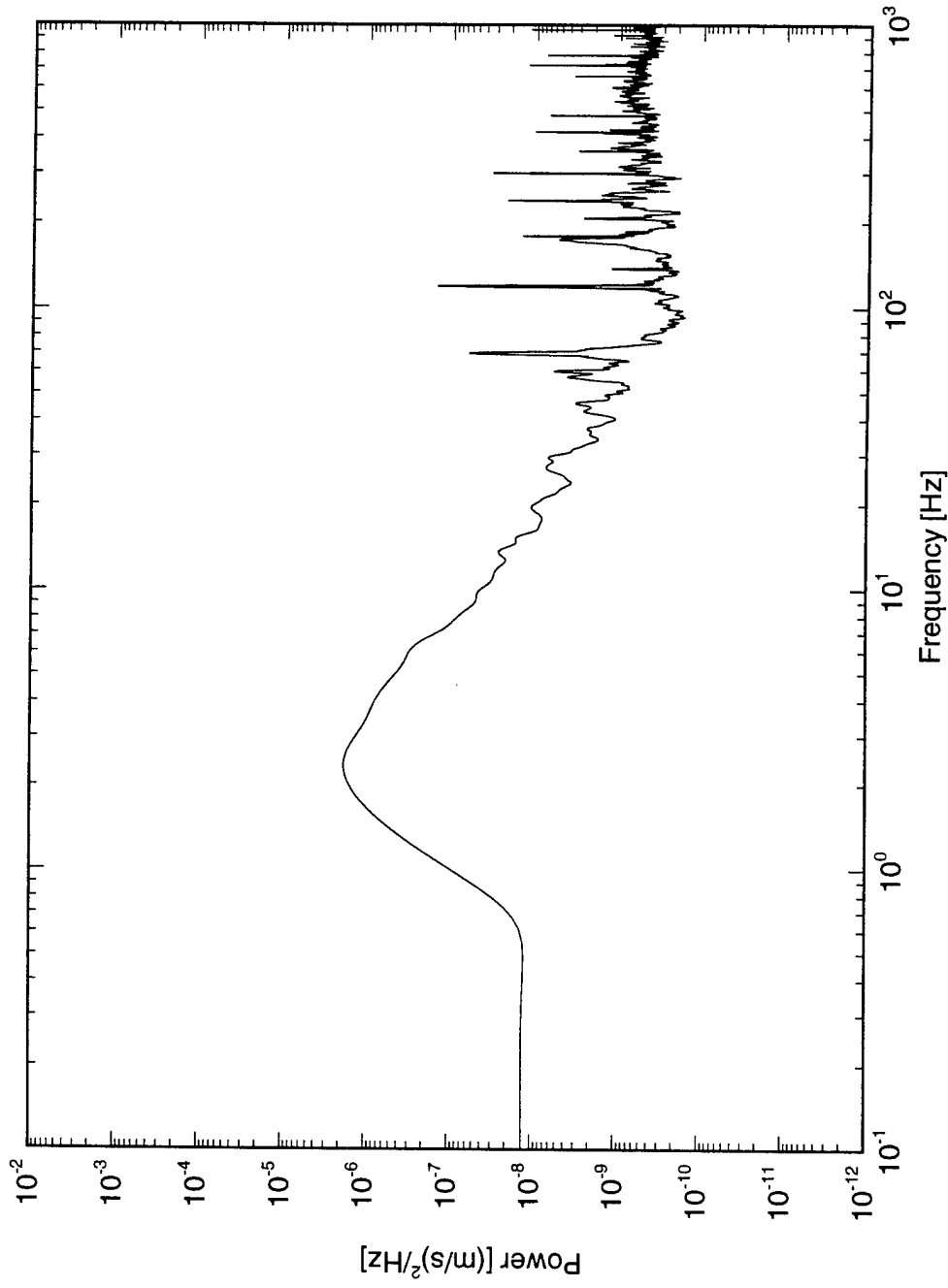


Figure 7.77: Freestream disturbance spectrum at $U_\infty = 10 \text{ m/s}$ with the mixing region vented (AC coupled, band pass 2–1000 Hz, Stewart filters). Measurements taken at $\hat{x} = 1.0 \text{ m}$.

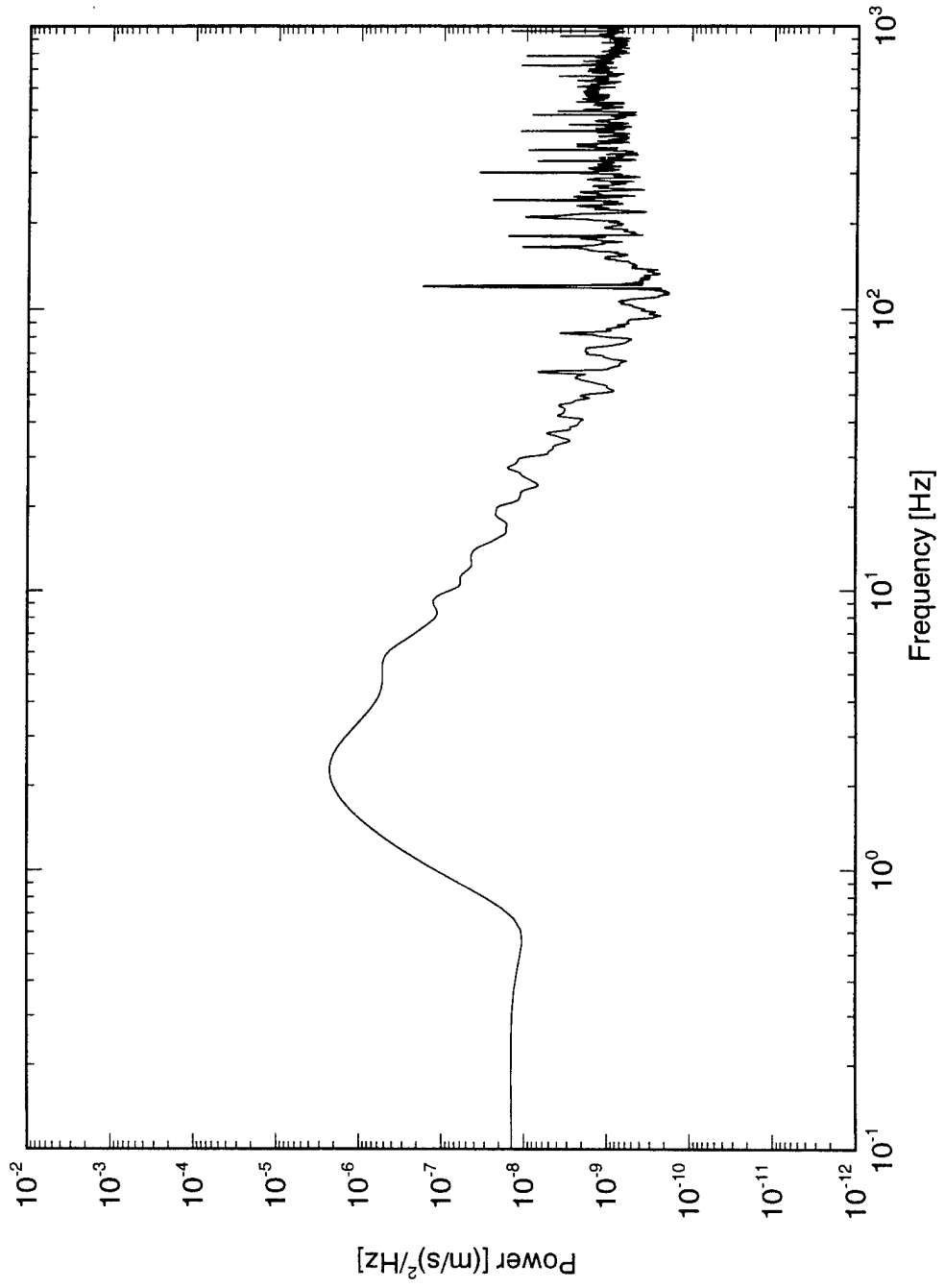


Figure 7.78: Freestream disturbance spectrum at $U_\infty = 12$ m/s with the mixing region vented (AC coupled, band pass 2–1000 Hz, Stewart filters). Measurements taken at $\hat{x} = 1.0$ m.

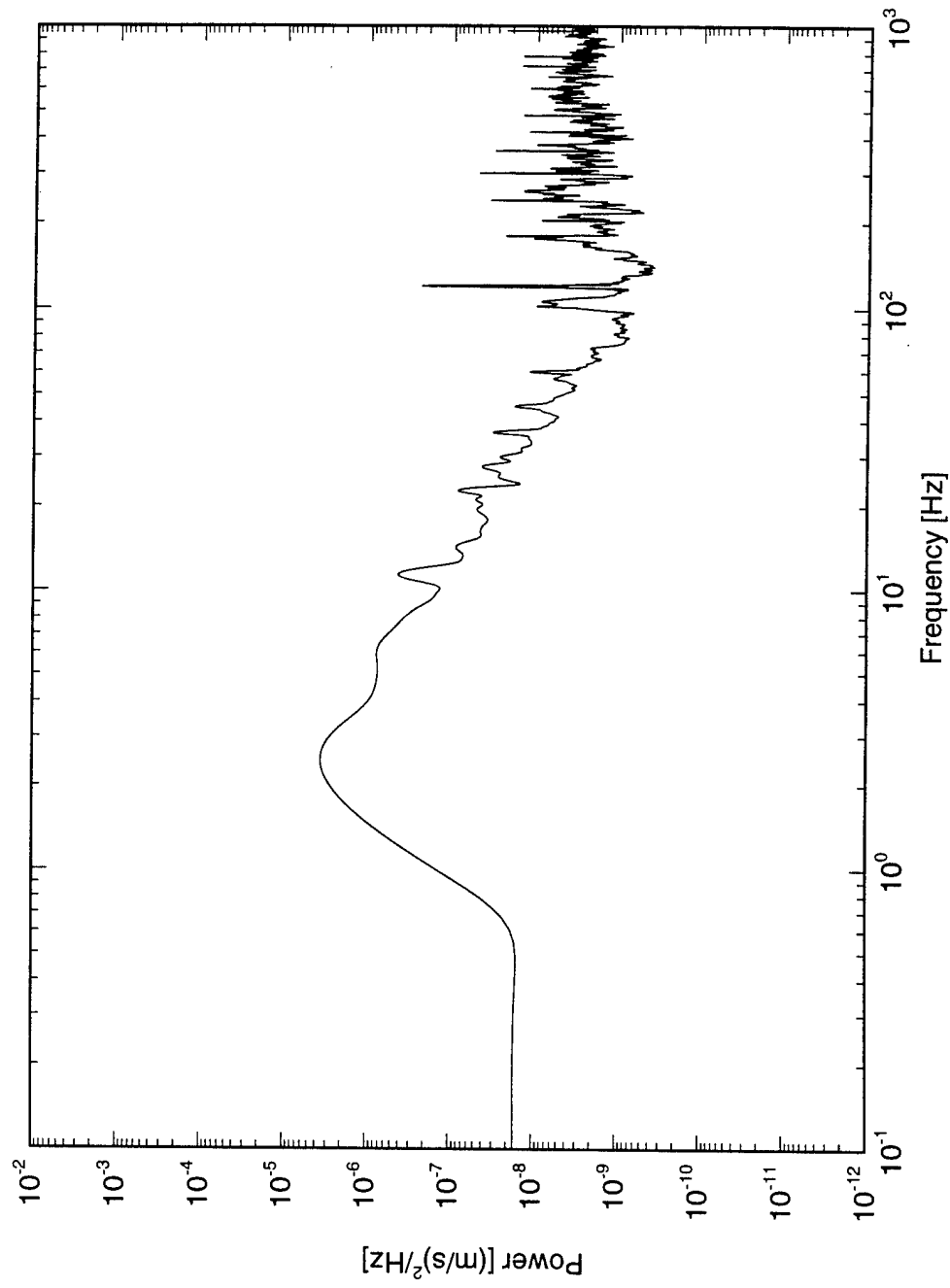


Figure 7.79: Freestream disturbance spectrum at $U_{\infty} = 15 \text{ m/s}$ with the mixing region vented (AC coupled, band pass 2–1000 Hz, Stewart filters). Measurements taken at $\hat{x} = 1.0 \text{ m}$.

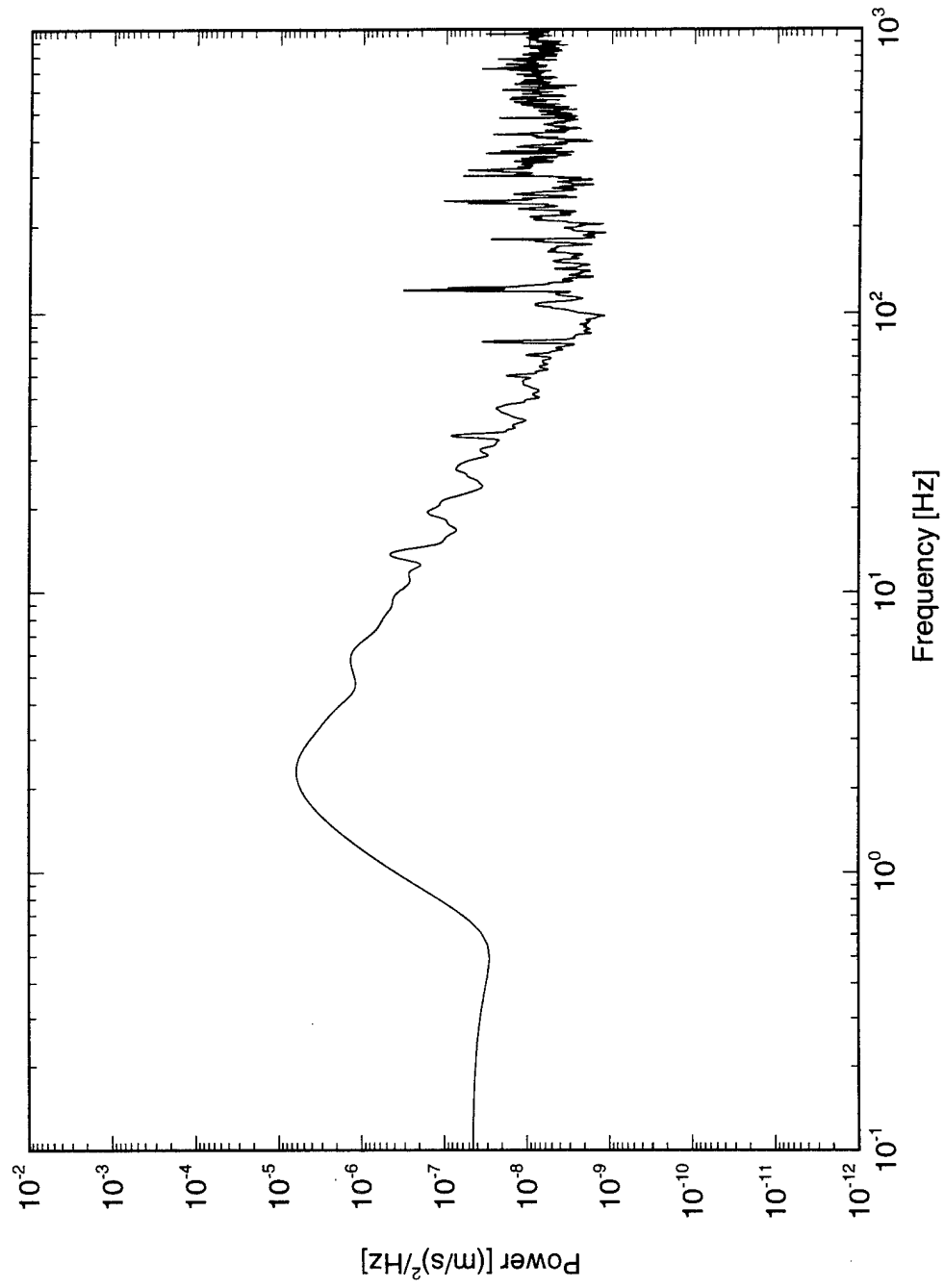


Figure 7.80: Freestream disturbance spectrum at $U_\infty = 18 \text{ m/s}$ with the mixing region vented (AC coupled, band pass 2–1000 Hz, Stewart filters). Measurements taken at $\hat{x} = 1.0 \text{ m}$.

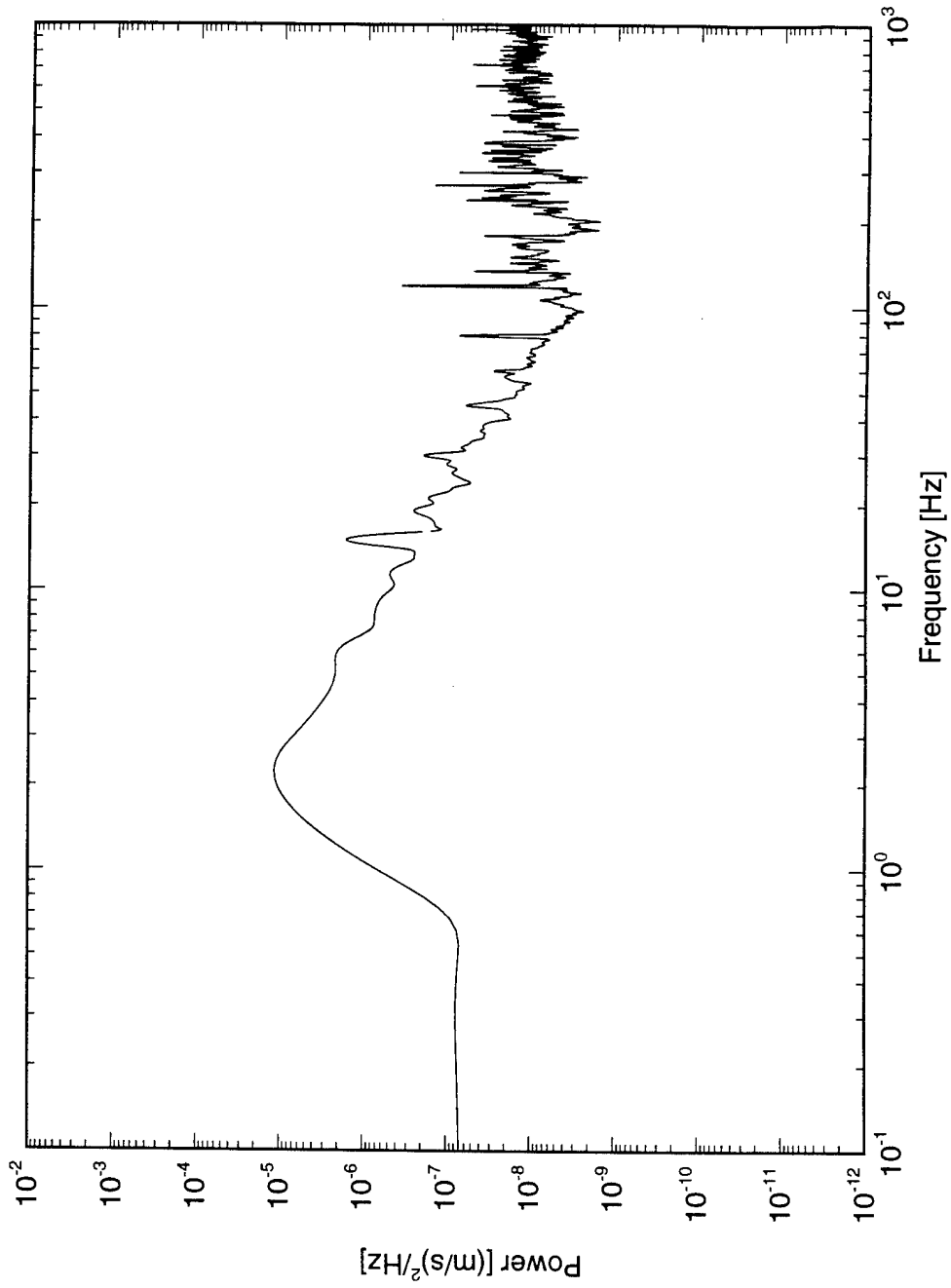


Figure 7.81: Freestream disturbance spectrum at $U_{\infty} = 20 \text{ m/s}$ with the mixing region vented (AC – coupled, band pass 2–1000 Hz, Stewart filters). Measurements taken at $\hat{x} = 1.0 \text{ m}$.

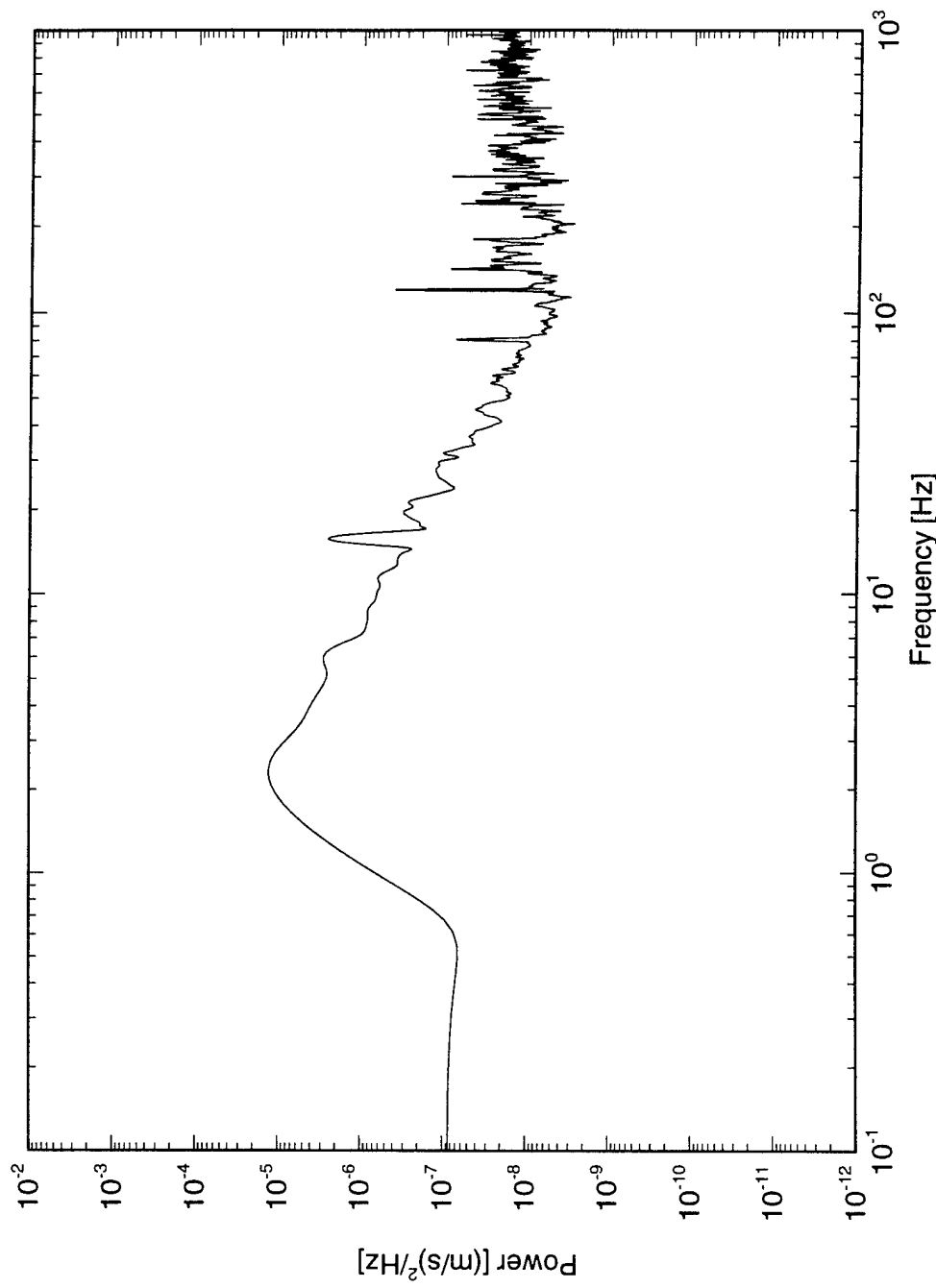


Figure 7.82: Freestream disturbance spectrum at $U_\infty = 21 \text{ m/s}$ with the mixing region vented (AC coupled, band pass 2–1000 Hz, Stewart filters). Measurements taken at $\hat{x} = 1.0 \text{ m}$.

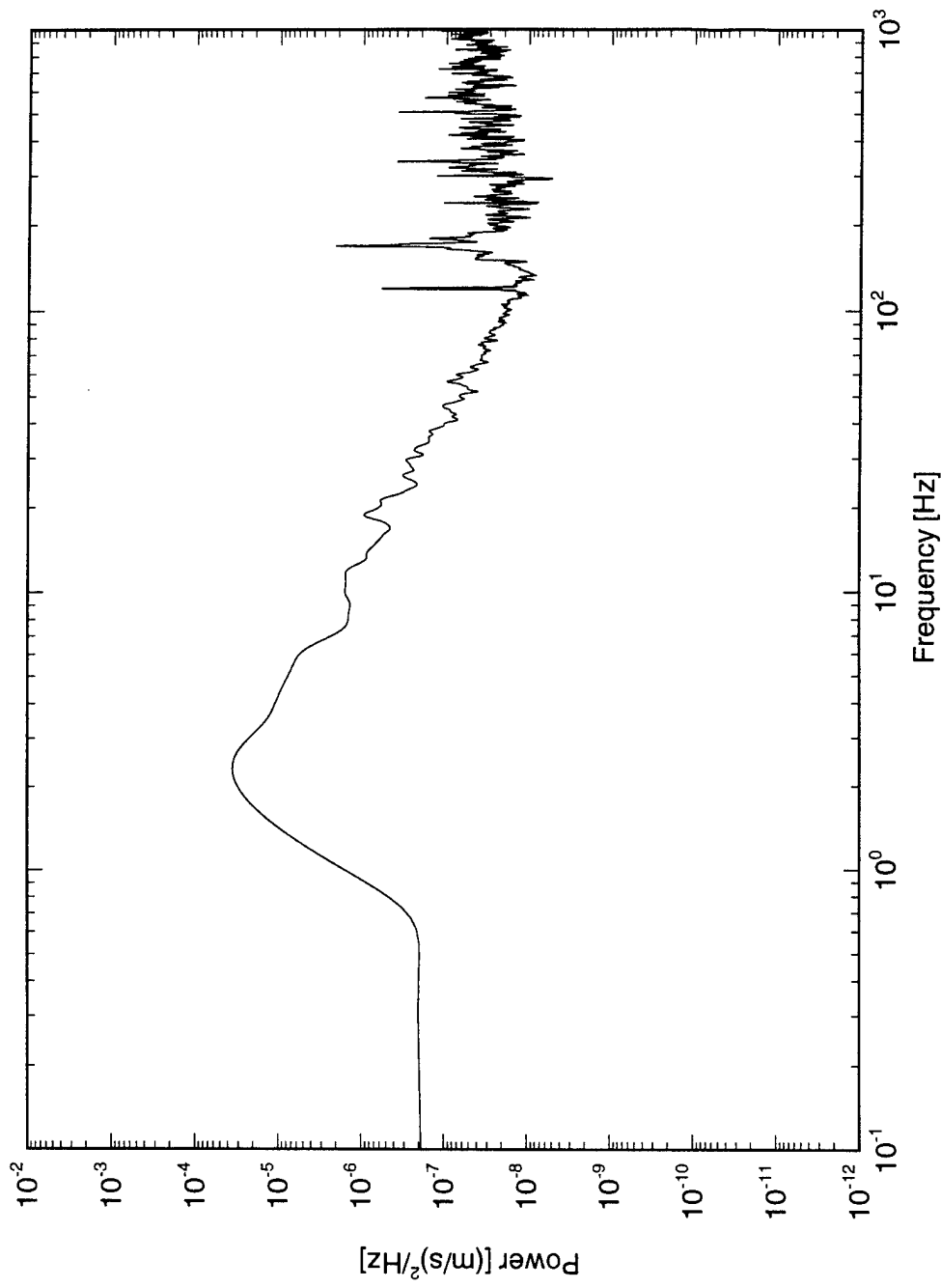


Figure 7.83: Freestream disturbance spectrum at $U_\infty = 25$ m/s with the mixing region vented (AC coupled, band pass 2–1000 Hz, Stewart filters). Measurements taken at $\hat{x} = 1.0$ m.

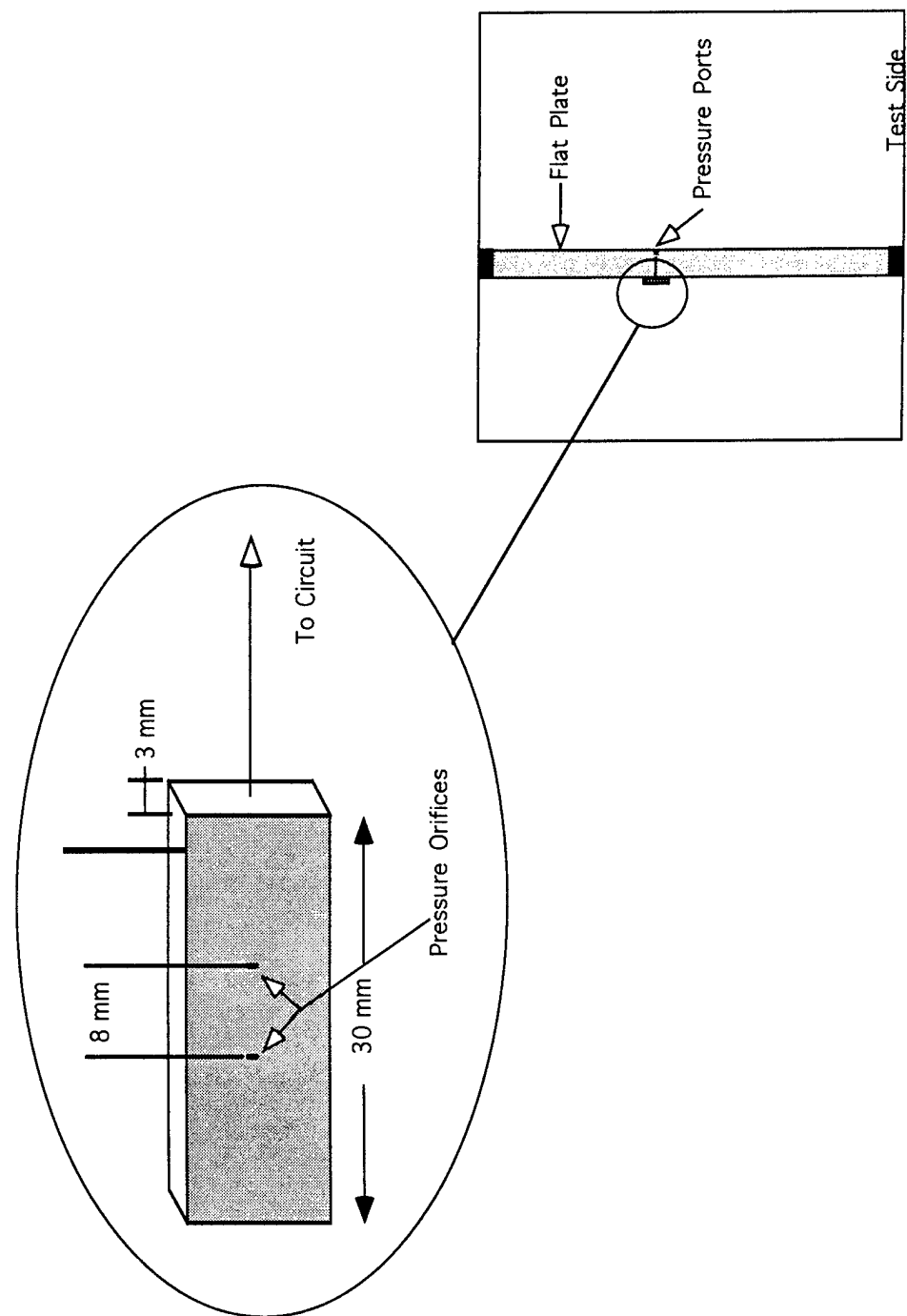


Figure 8.1: The Kendall gauge

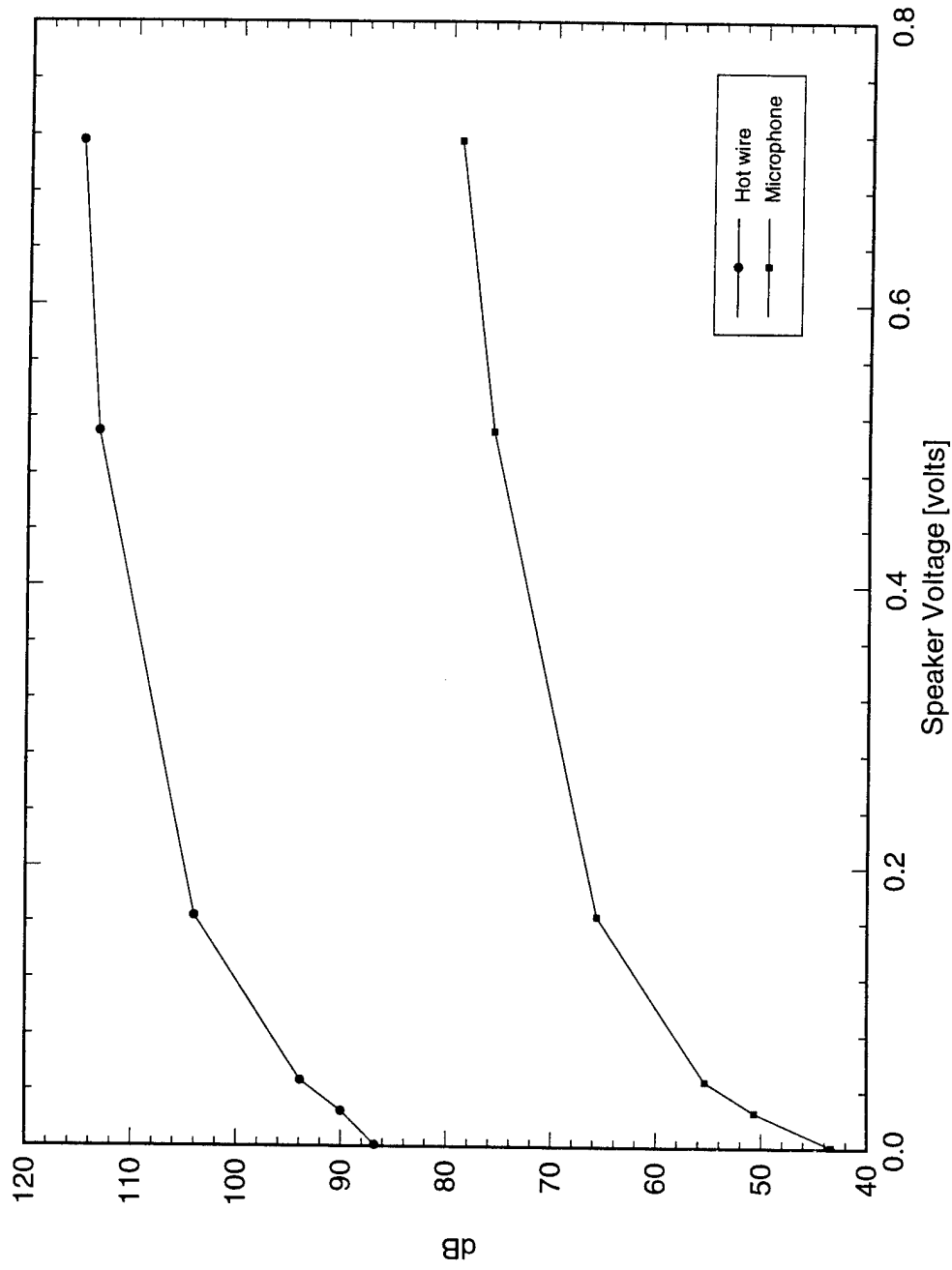


Figure 8.2: Hot-wire and Kendall-gauge response with sound amplitude.

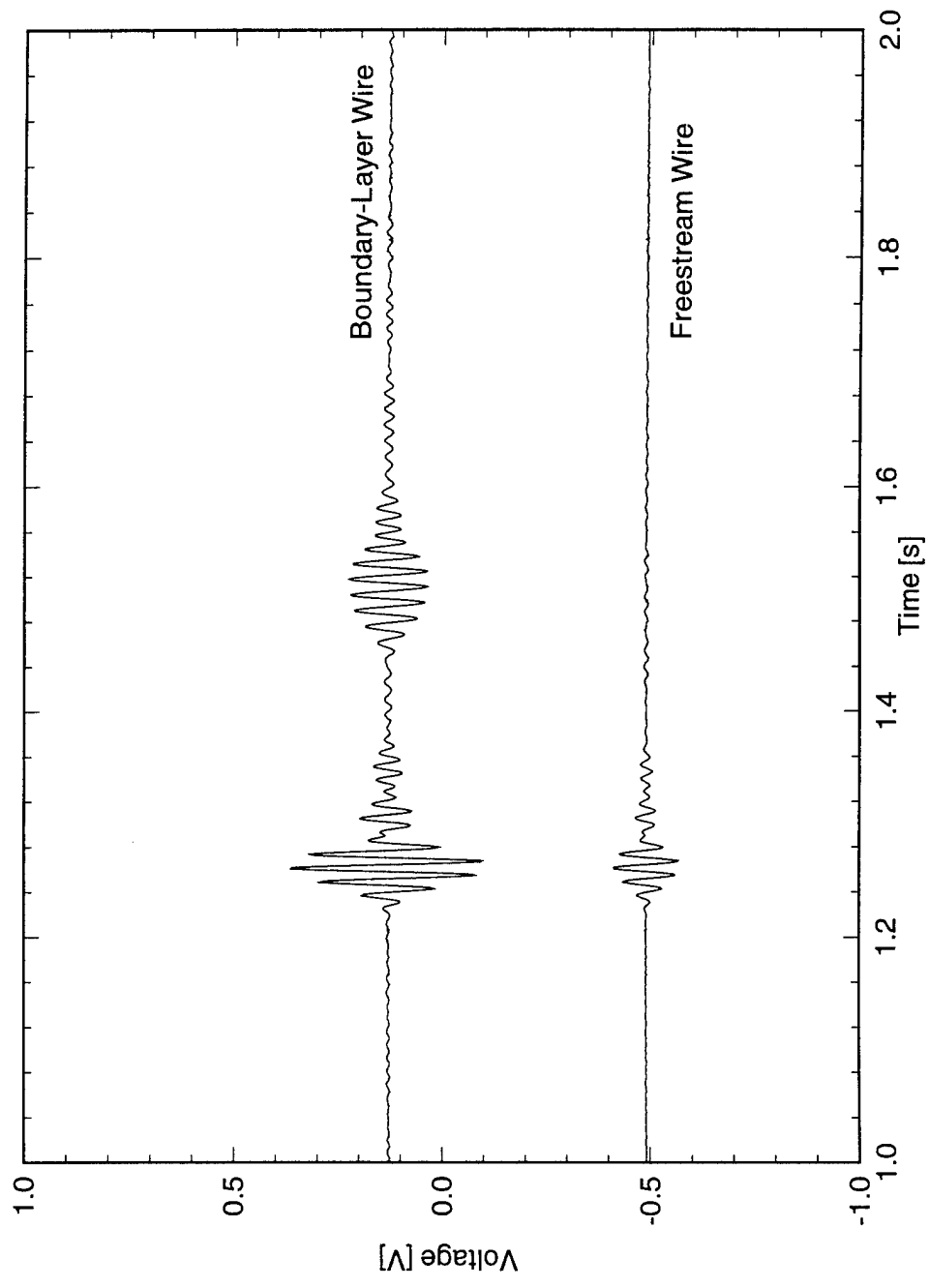


Figure 8.3: Time trace using sound-burst technique for $R = 1140$, $F = 56$, $f = 80$ Hz, and $\hat{x} = 1.8$ m.

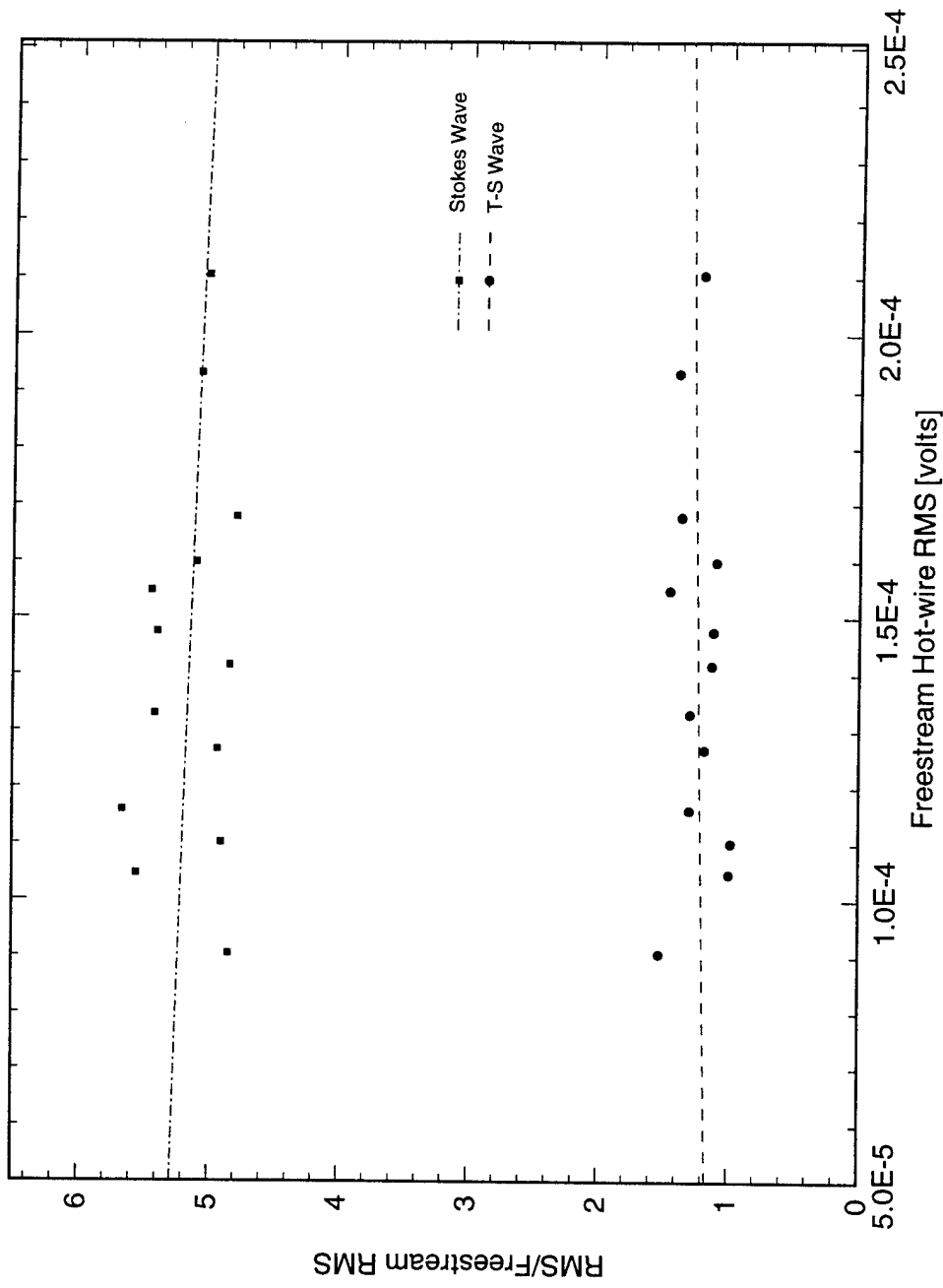


Figure 8.4: Stokes wave and T-S wave growth with band-passed random noise for increasing sound amplitude.

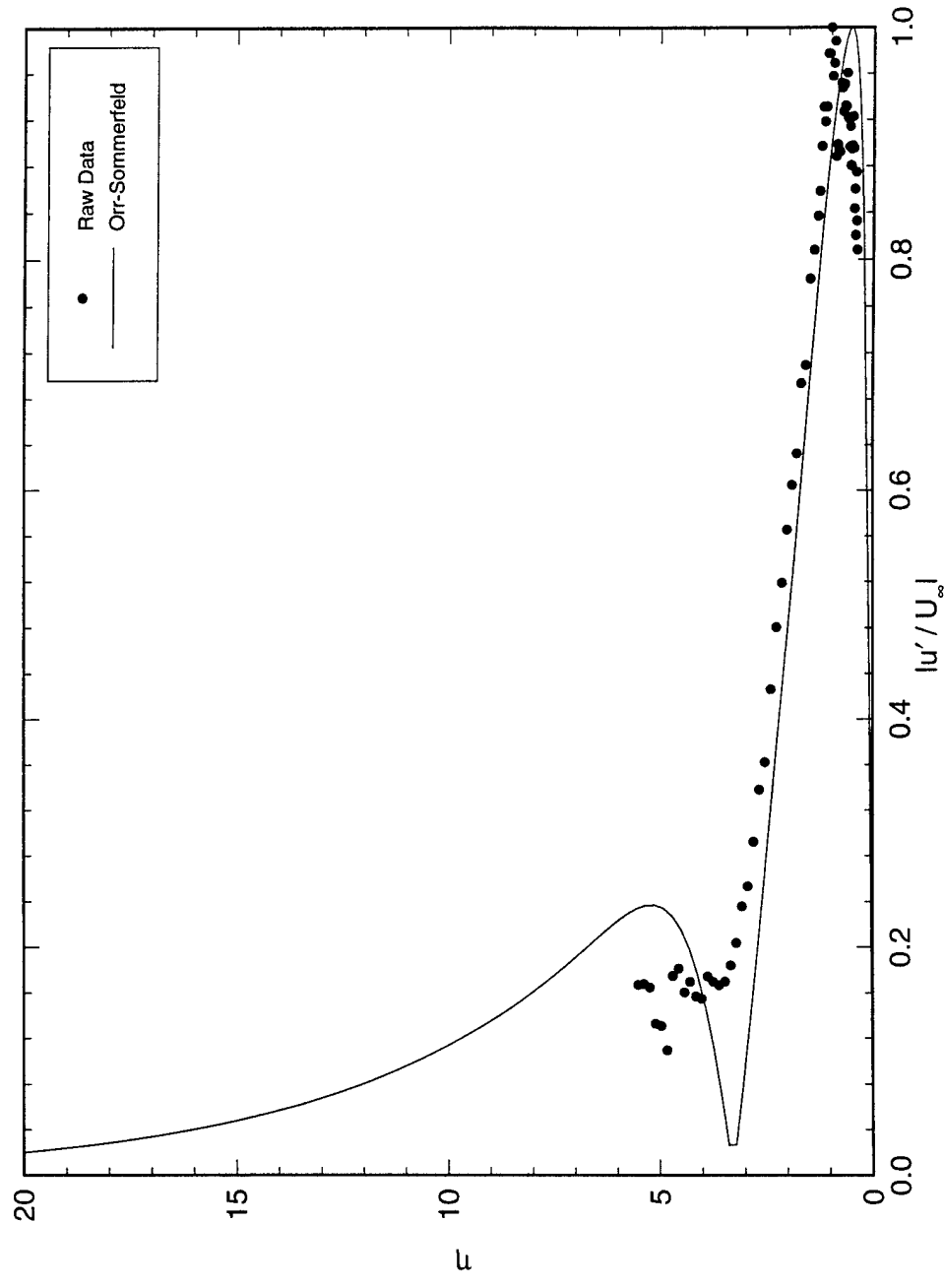


Figure 8.5: Boundary-layer scan disturbance profile (raw signal). Measurements taken at $\hat{x} = 1.753$ m, $R = 1048$, $F = 55$, $U_\infty = 12$ m/s, $f = 75$ Hz, and SPL = 100 dB.

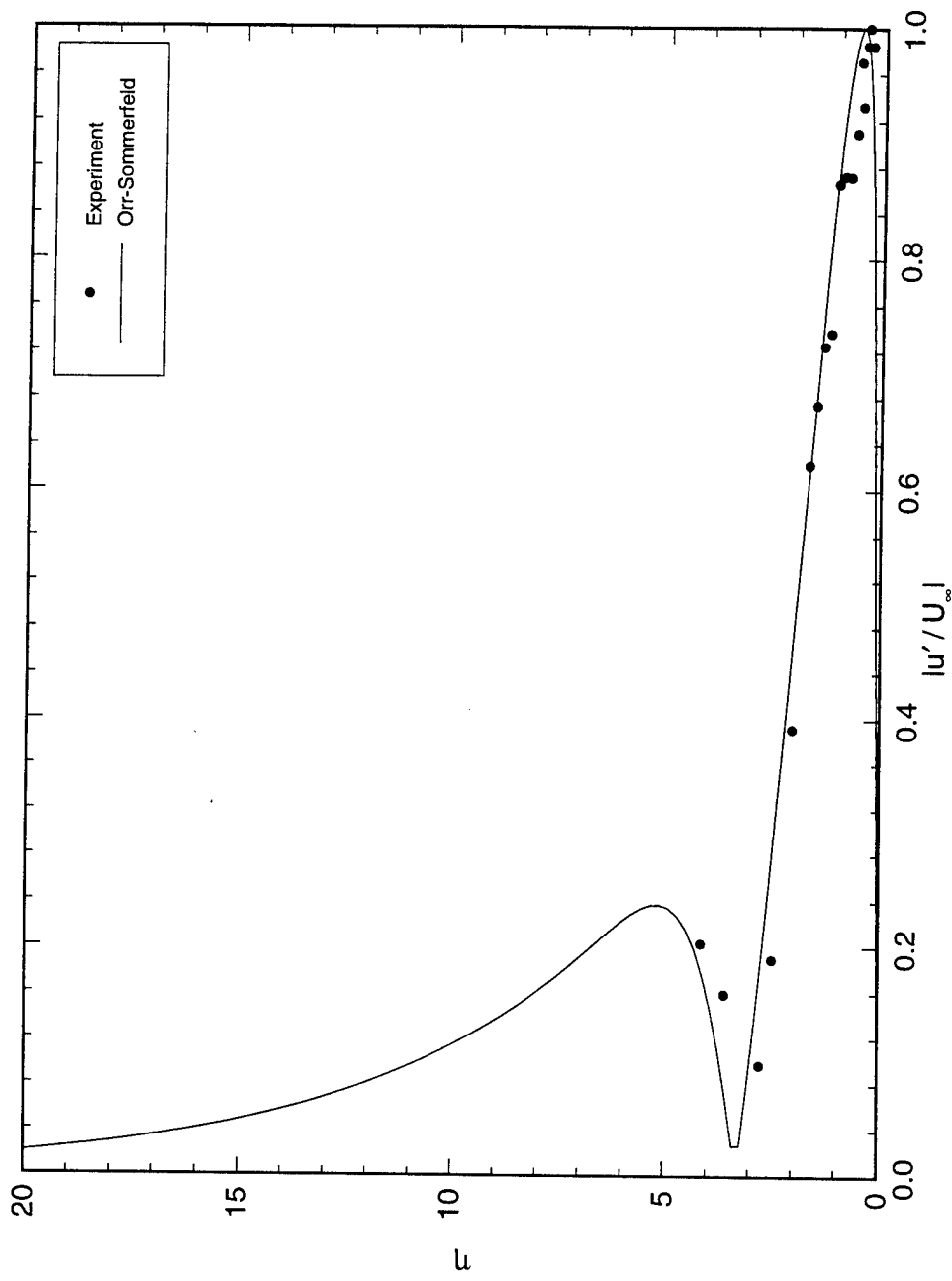


Figure 8.6: Boundary-layer scan disturbance profile after signal separation. Measurements taken at $\hat{x} = 1.753$ m, $R = 1048$, $F = 55$, $U_\infty = 12$ m/s, $f = 75$ Hz, and SPL = 100 dB.

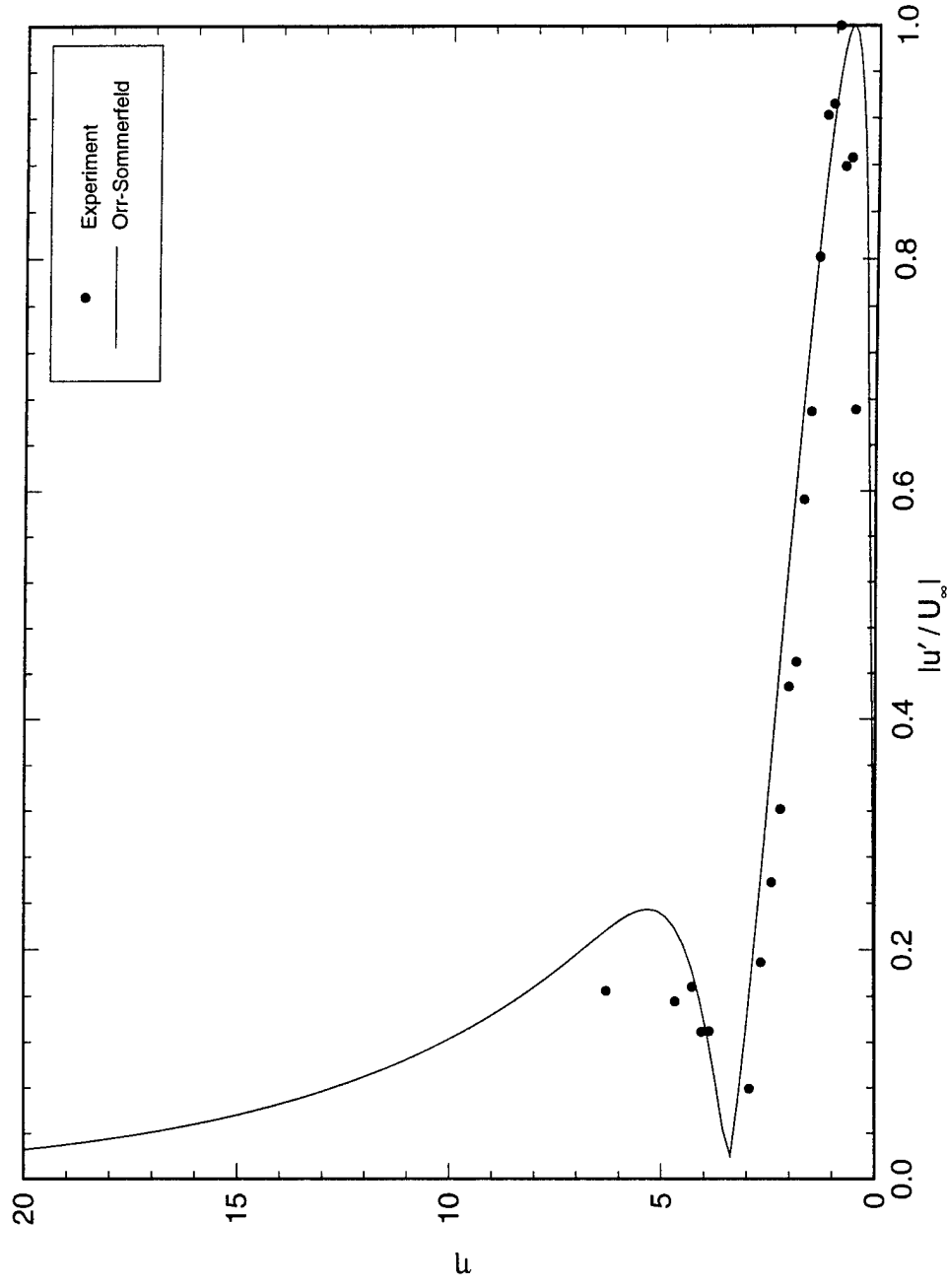


Figure 8.7: Boundary-layer scan disturbance profile after signal separation. Measurements taken at $\hat{x} = 1.753$ m, $R = 1025$, $F = 50$, $U_\infty = 12$ m/s, $f = 68$ Hz, and $\text{SPL} = 101$ dB.

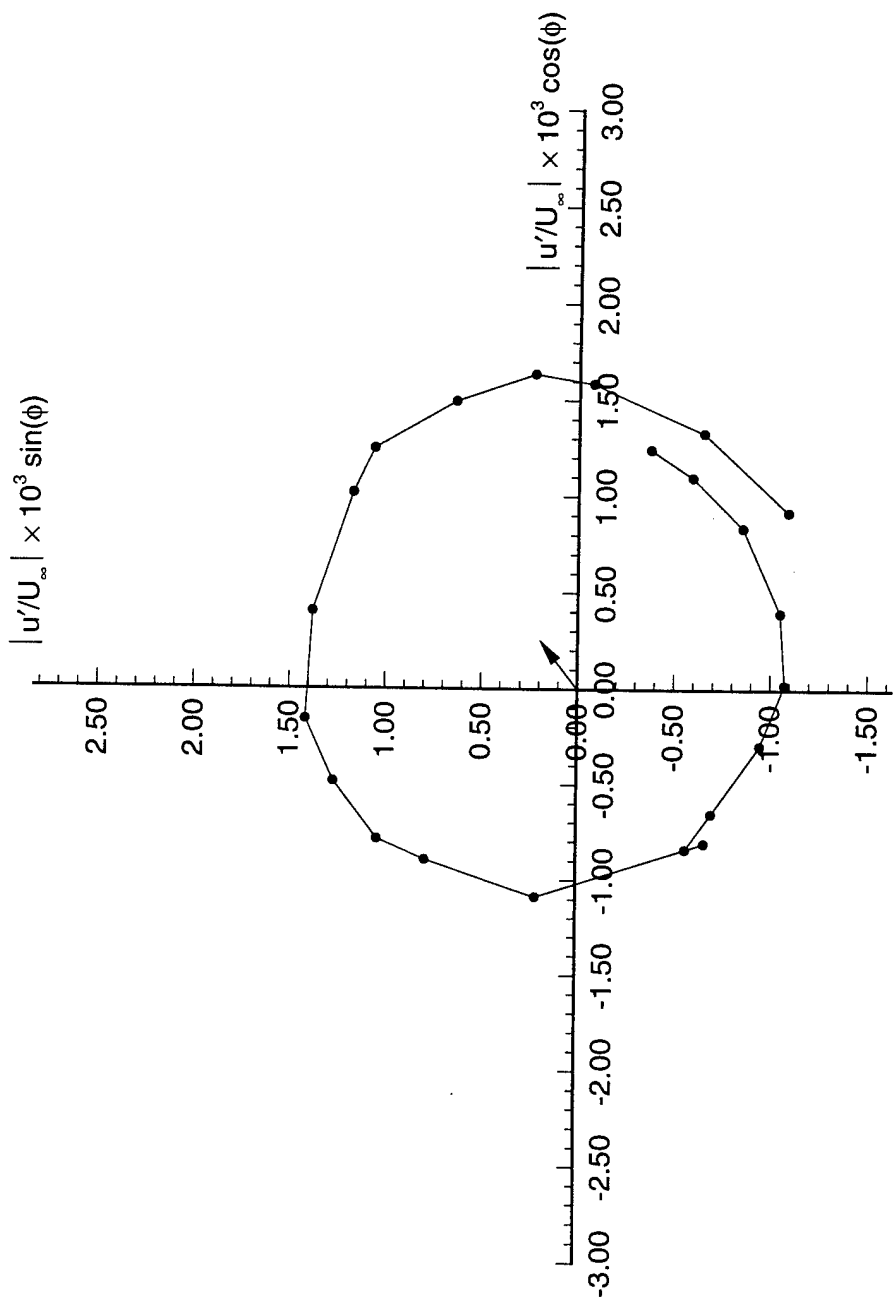


Figure 8.8: Complex polar plot obtained from streamwise scan. Measurements taken at $\hat{x}_{\text{avg}} = 1.763$ m, $R = 1115$, $F = 48$, $U_{\infty} = 48$ m/s, $f = 88$ Hz, and SPL = 89 dB.

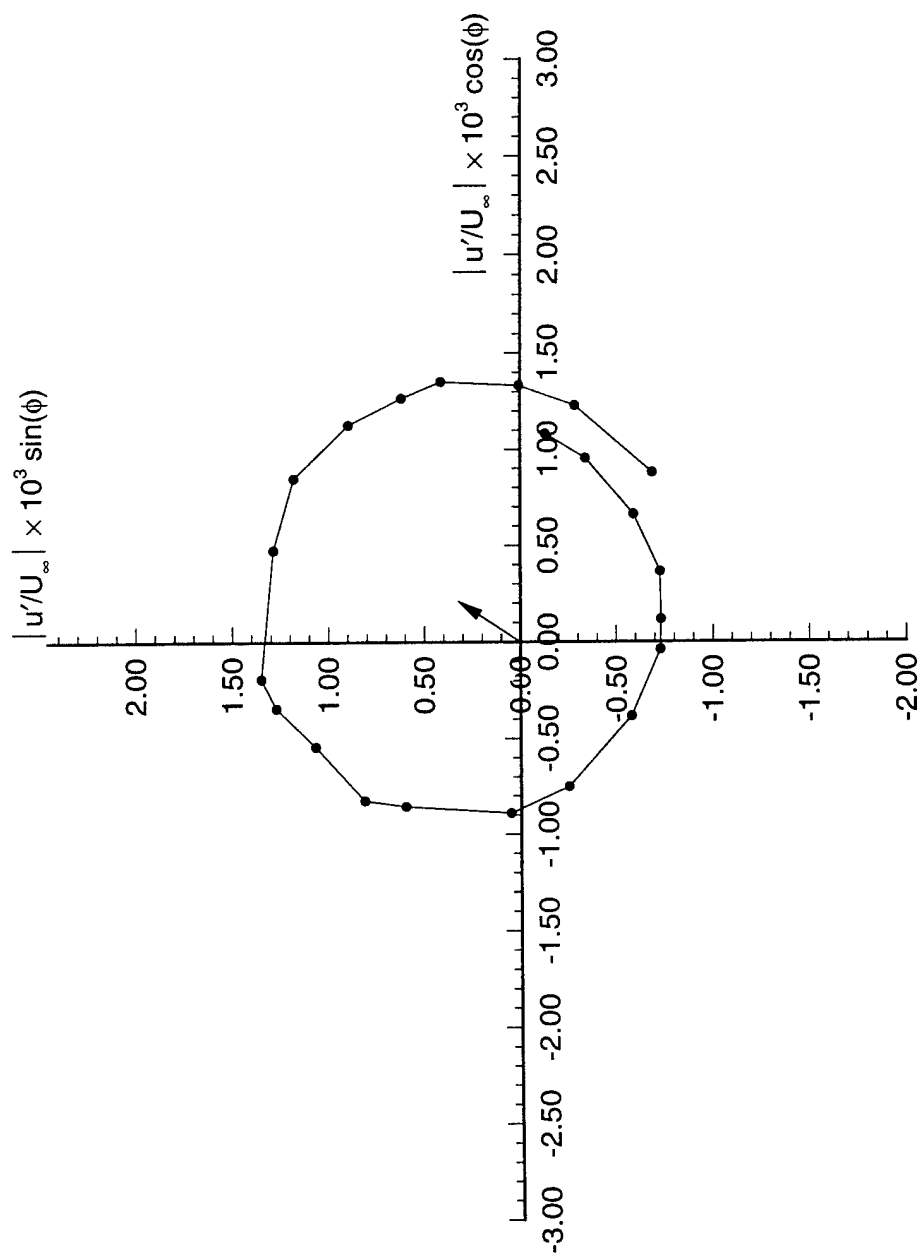


Figure 8.9: Complex polar plot obtained from streamwise scan. Measurements taken at $\hat{x}_{\text{avg}} = 1.763 \text{ m}$, $R = 1105$, $F = 49$, $U_\infty = 13.9 \text{ m/s}$, $f = 87 \text{ Hz}$, and $\text{SPL} = 89 \text{ dB}$.

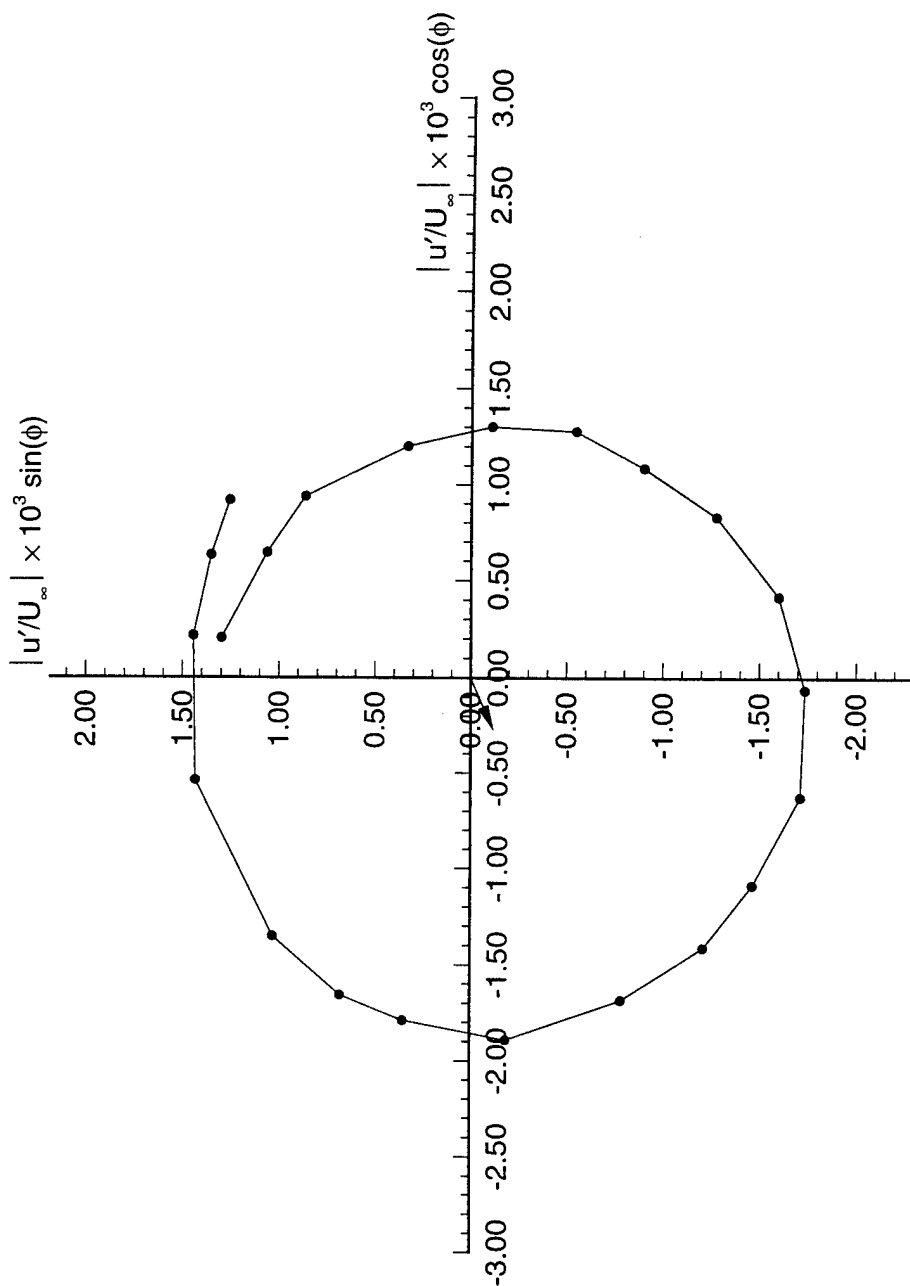


Figure 8.10: Complex polar plot obtained from streamwise scan. Measurements taken at $\hat{x}_{\text{avg}} = 1.763$ m, $R = 1107$, $F = 50$, $U_{\infty} = 13.9$ m/s, $f = 90$ Hz, and SPL = 93 dB.

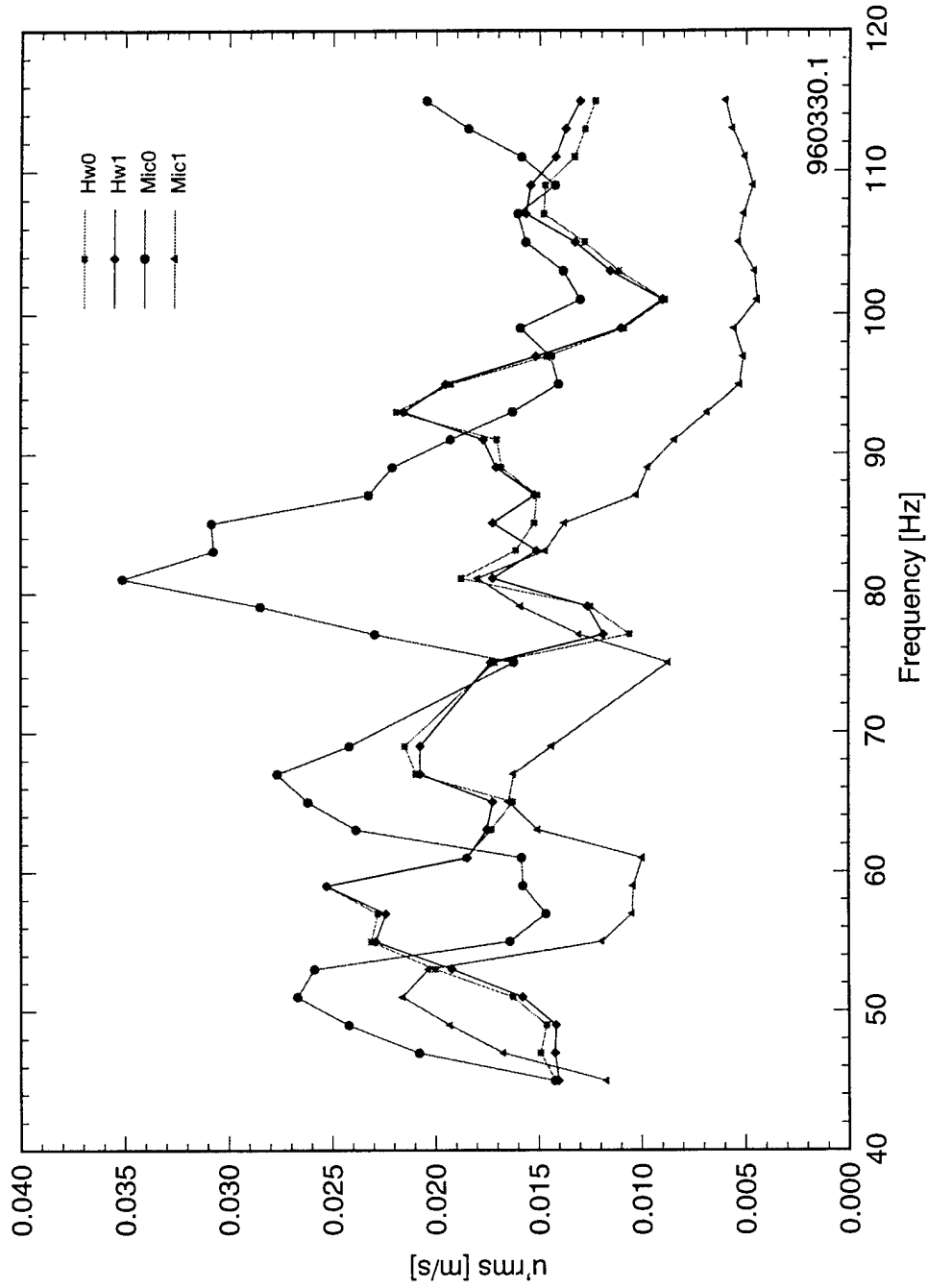


Figure 8.11: First configuration to correlate the hot-wire and microphone response at $\hat{x} = 0.5$ m. Hw0 is located on the sting ≈ 12 mm over flush-mounted microphone, Hw1 is on the sting all the way out, Mic0 is mounted flush at $\hat{x} = 0.5$ m, and Mic1 is attached to the bottom leading-edge static pressure port.

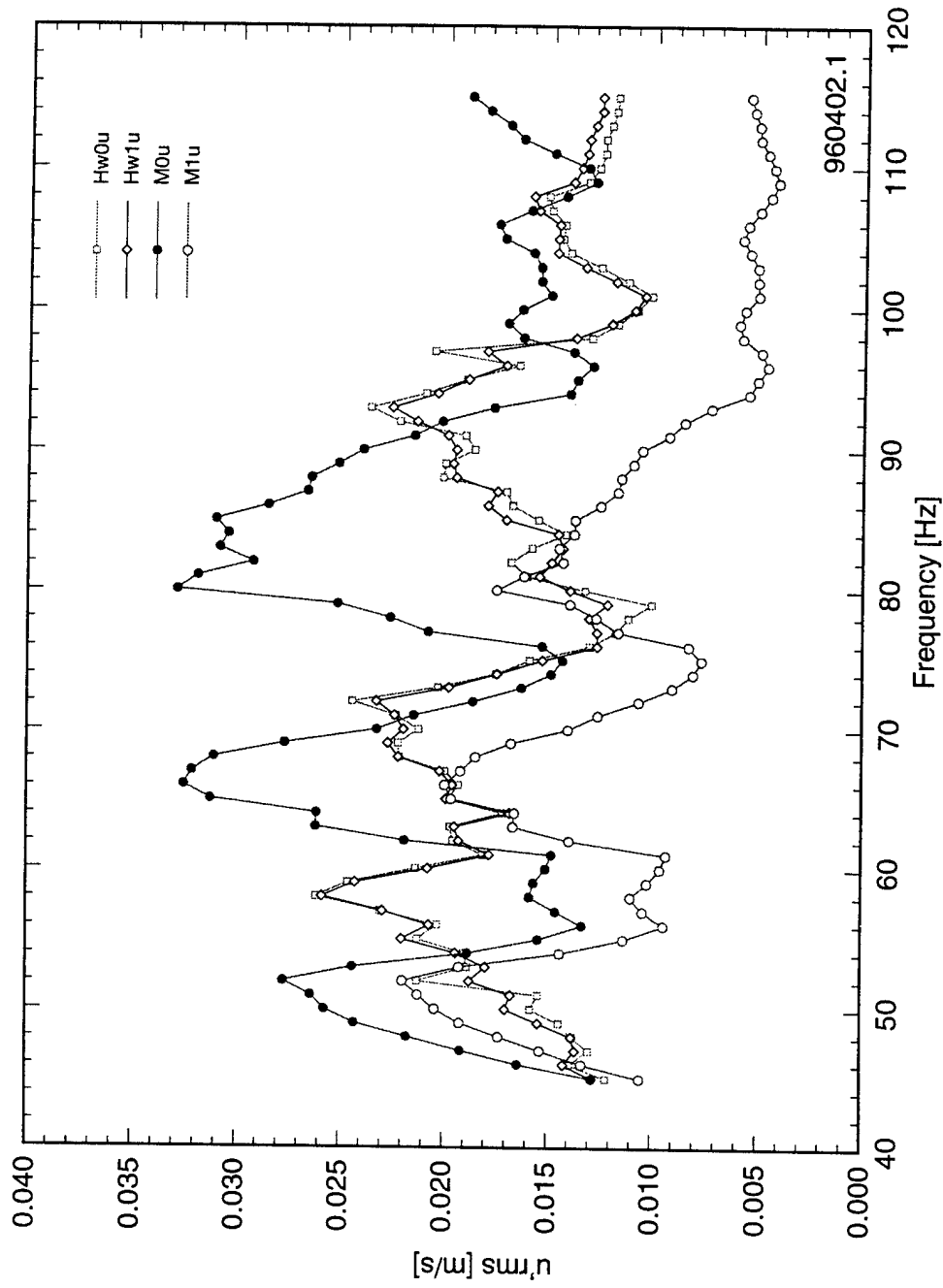


Figure 8.12: Second configuration to correlate the hot-wire and microphone response at $\hat{x} = 0.5$ m. Hw0 is located on the sting in the freestream, Hw1 is fixed to the plate and is 25.4 mm from the flush-mounted microphone in the negative spanwise direction. Mic0 is mounted flush at $\hat{x} = 0.5$ m, and Mic1 is attached to the bottom leading-edge static pressure port.

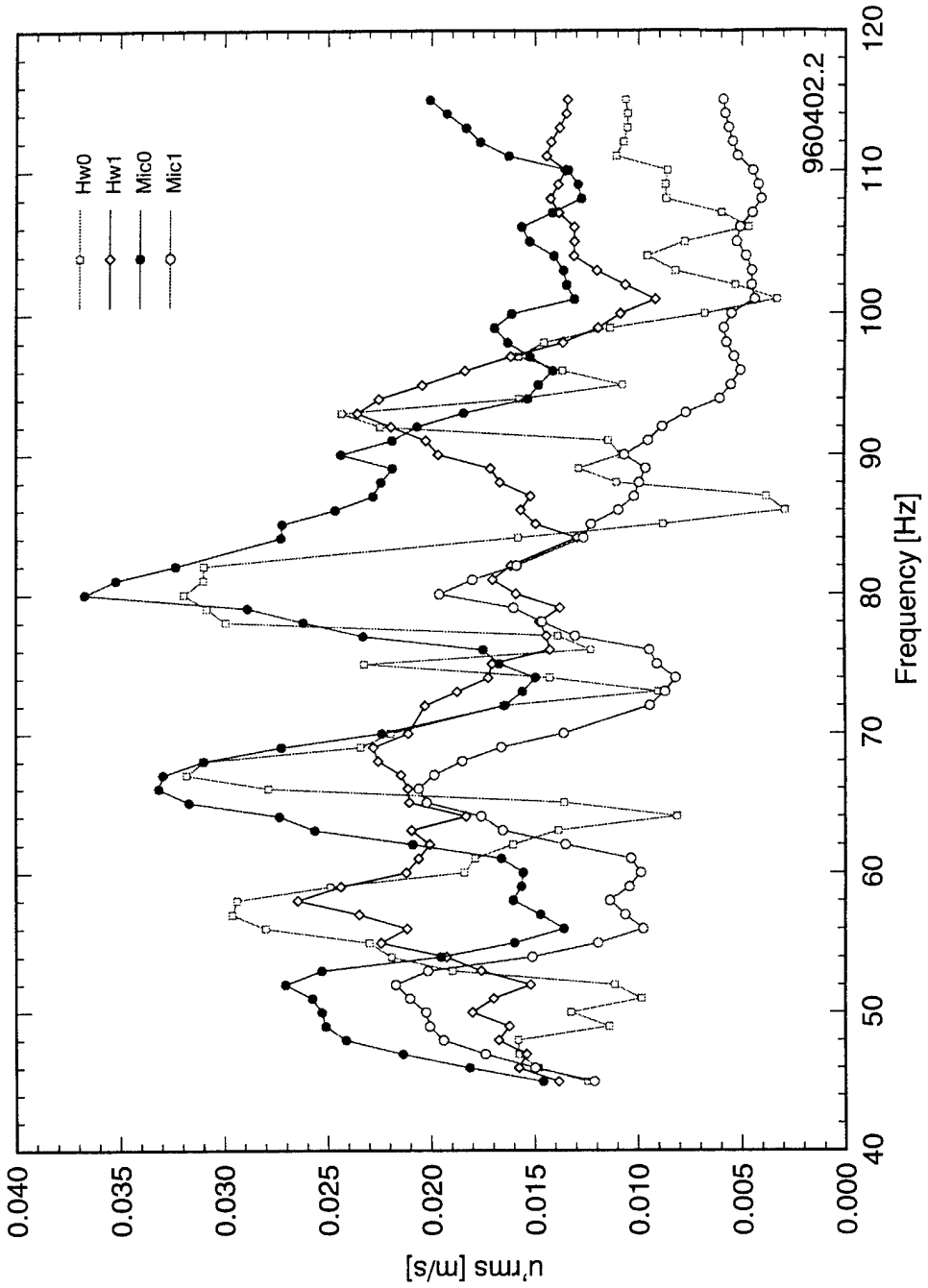


Figure 8.13: Third configuration to correlate the hot-wire and microphone response at $\hat{x} = 0.5$ m. Hw0 is located on the sting over the flush-mounted microphone at $u/U_\infty = 0.16$ and Hw1 is in the freestream at the same streamwise location. Mic0 is mounted flush at $\hat{x} = 0.5$ m, and Mic1 is attached to the bottom leading-edge static pressure port.

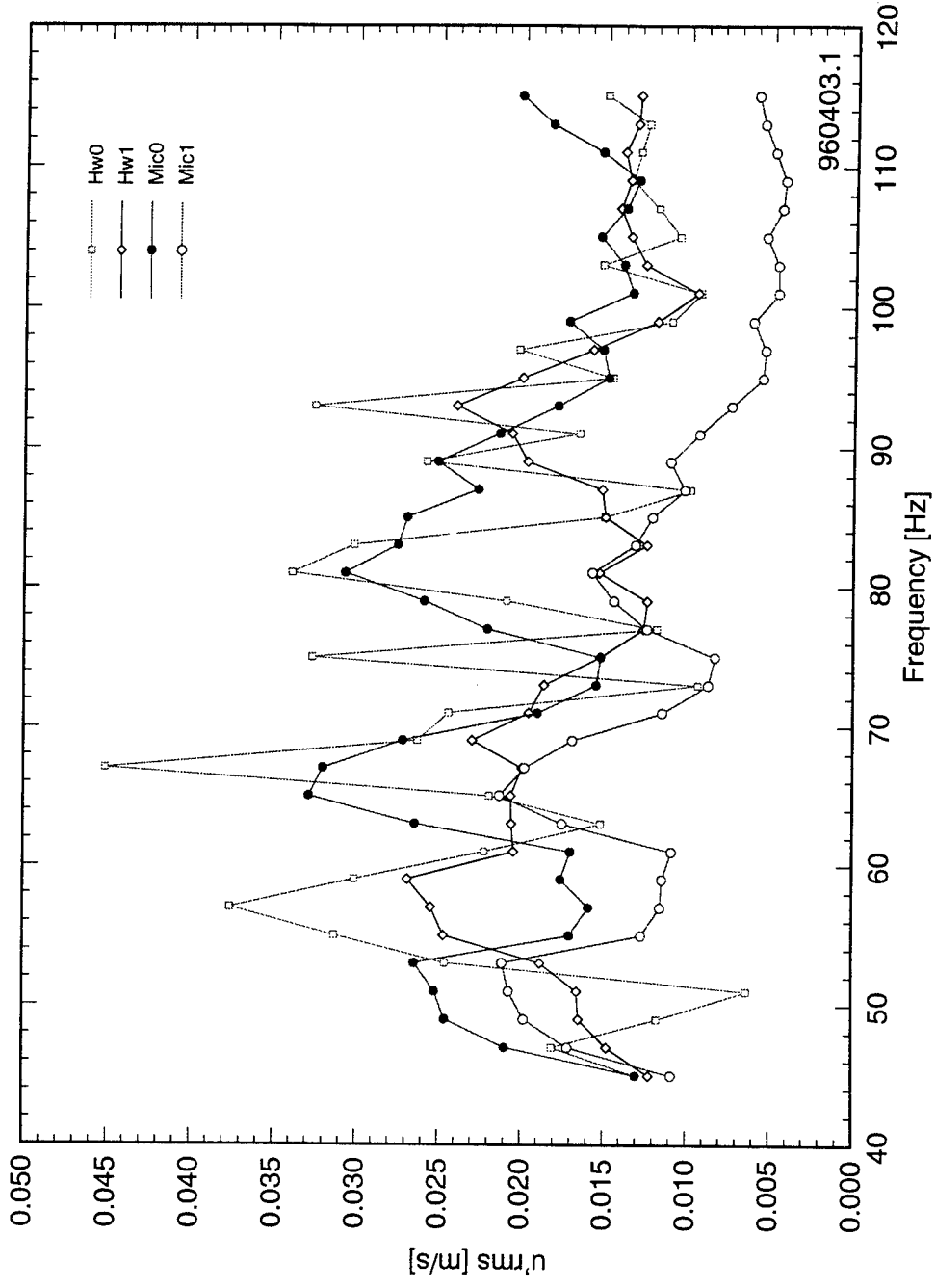


Figure 8.14: Fourth configuration to correlate the hot-wire and microphone response at $\hat{x} = 0.5$ m. Hw0 is located on the sting over the flush-mounted microphone at $u/U_\infty = 0.30$ and Hw1 is in the freestream at the same streamwise location. Mic0 is mounted flush at $\hat{x} = 0.5$ m, and Mic1 is attached to the bottom leading-edge static pressure port.

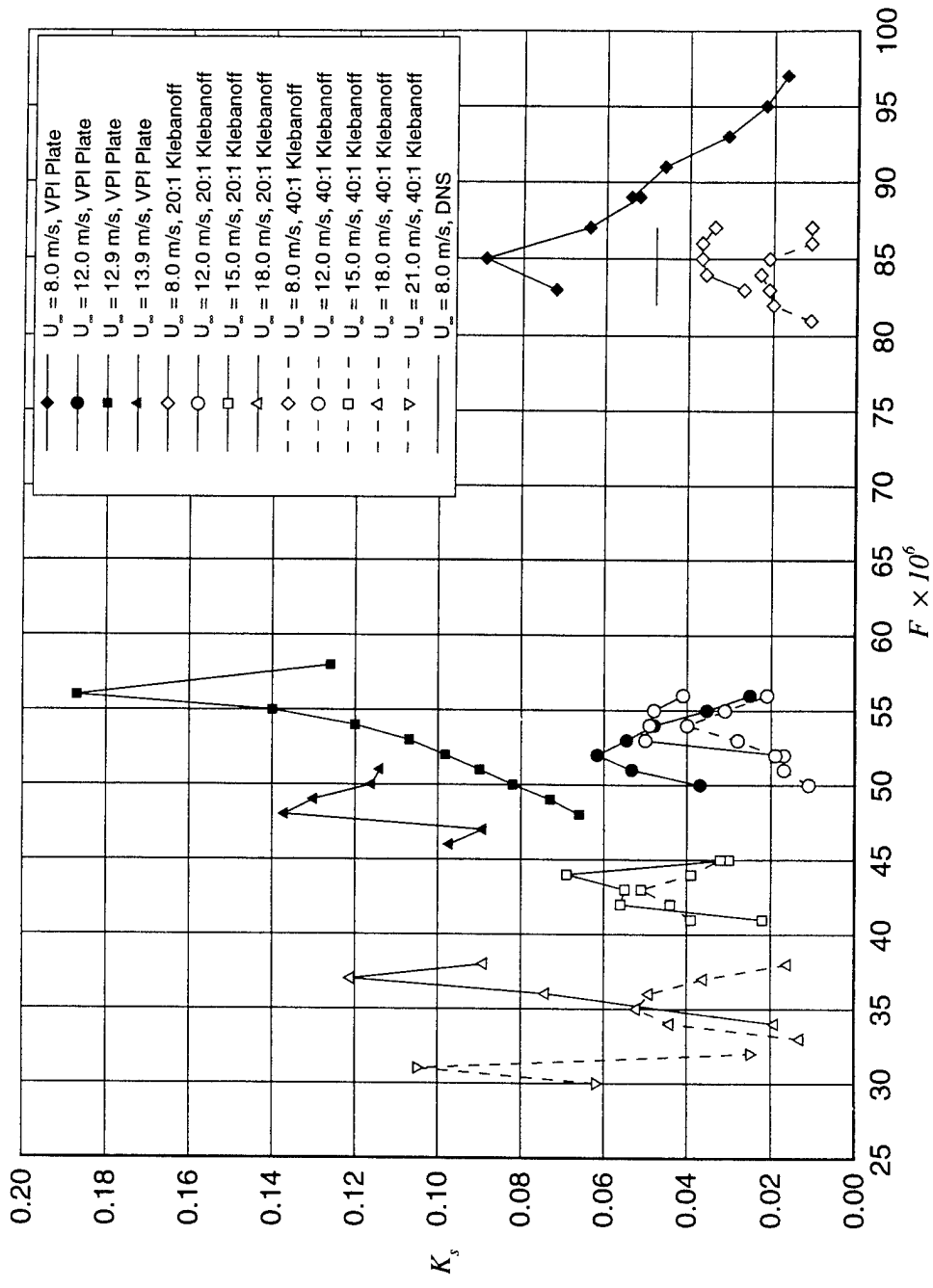


Figure 8.15: Receptivity coefficients (at Branch I) as a function of dimensionless frequency and freestream speed. The 20:1 leading-edge aspect-ratio measurements were performed by Rasmussen (1993) and the 40:1 aspect-ratio measurements were performed by Wei (1994).

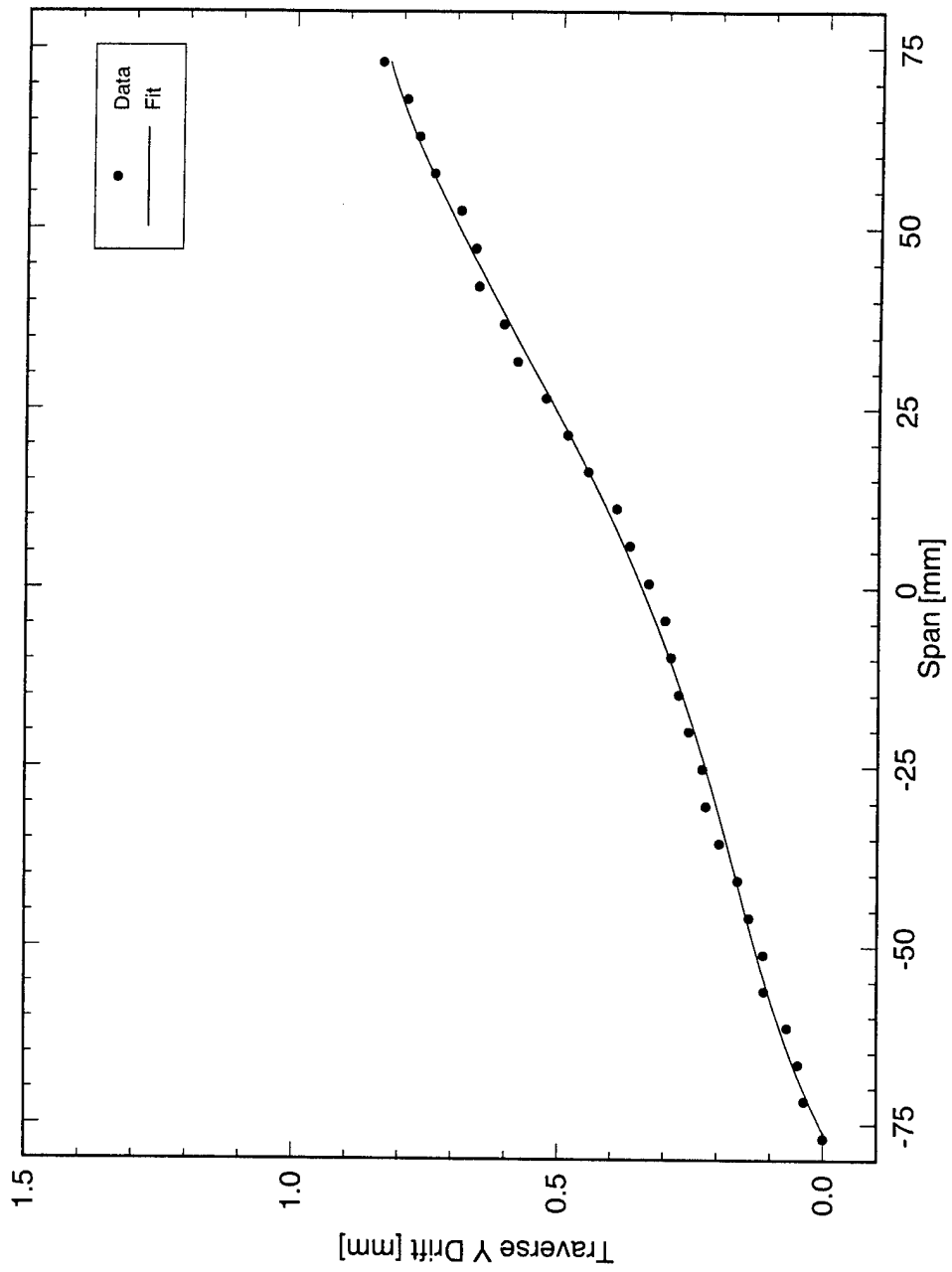


Figure 8.16: Spanwise traverse-alignment scan for $\hat{x} = 1.73$ m, $F = 56$, and $U_\infty = 12.9$ m/s case. The misalignment between the flat plate and the hot-wire traverse is shown by the “drift” in the traverse movement.

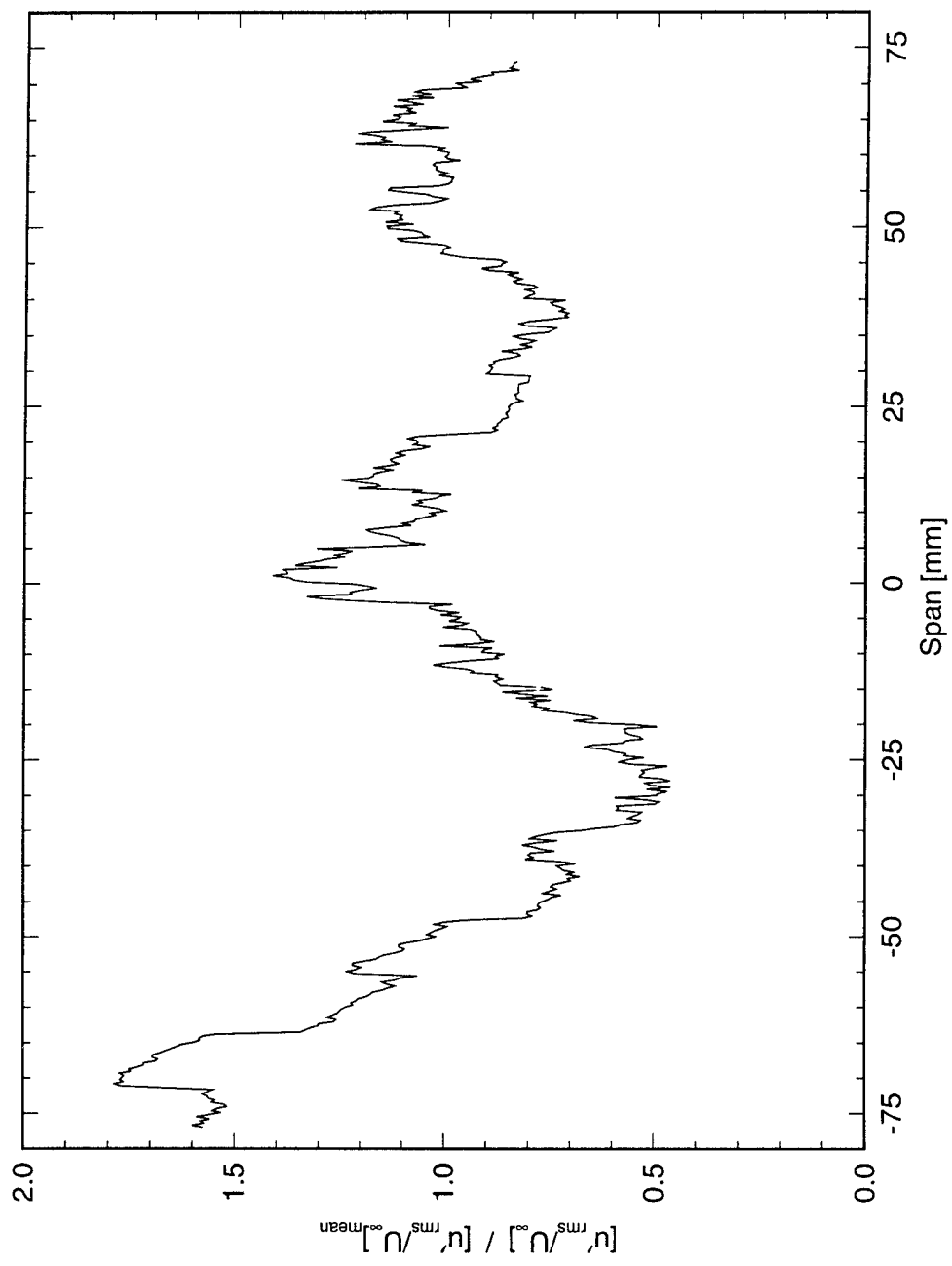


Figure 8.17: Spanwise u'_rms variation for constant- y scans taken at $\hat{x} = 1.73$ m and $\hat{y} = 1.5$ mm,
 $F = 56$, $U_\infty = 12.9$ m/s.

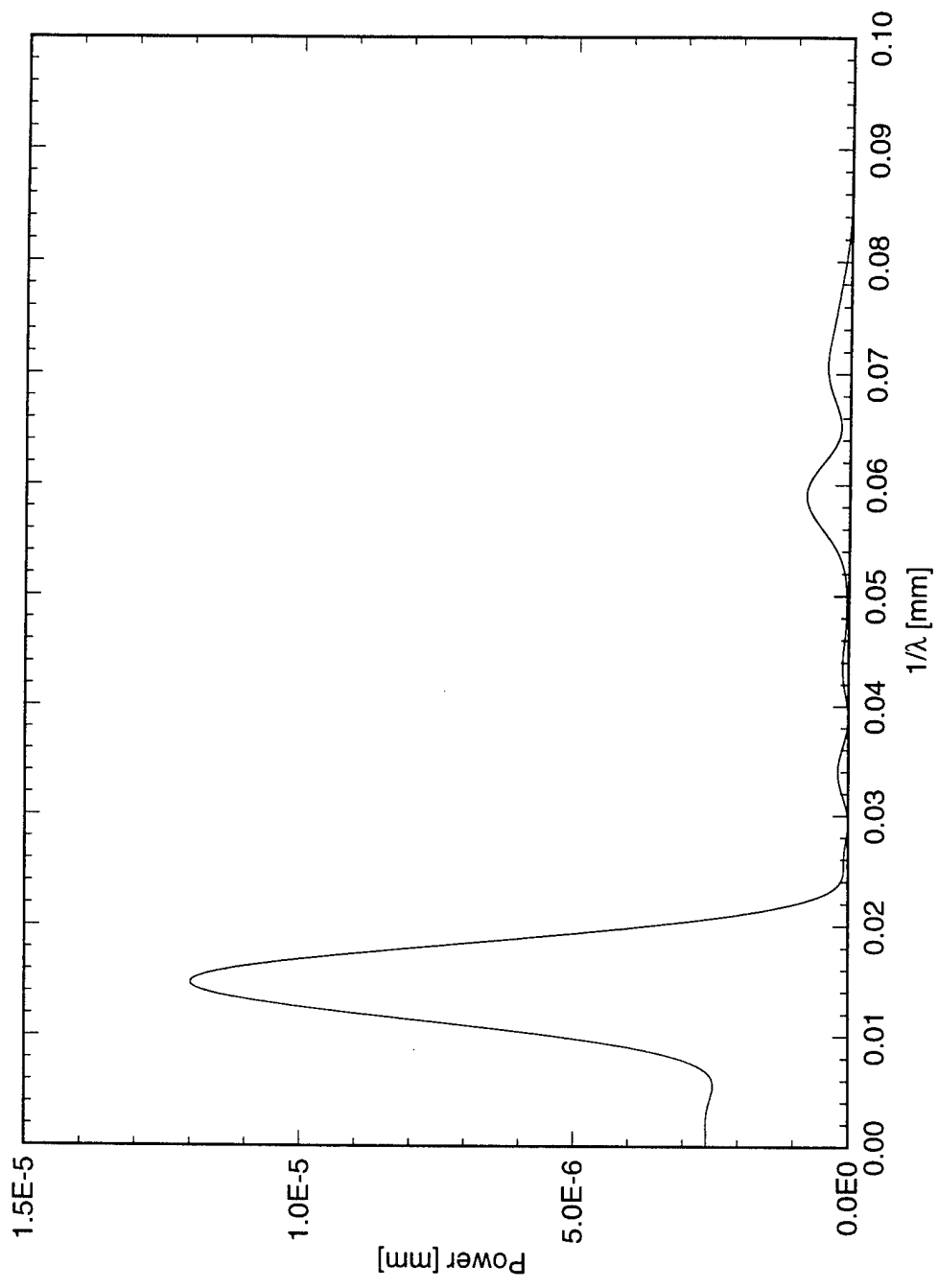


Figure 8.18: Wavenumber spectrum of u'_rms spanwise variation taken at $\hat{x} = 1.73$ m and $\hat{y} = 1.5$ mm,
 $F = 56$, $U_\infty = 12.9$ m/s.

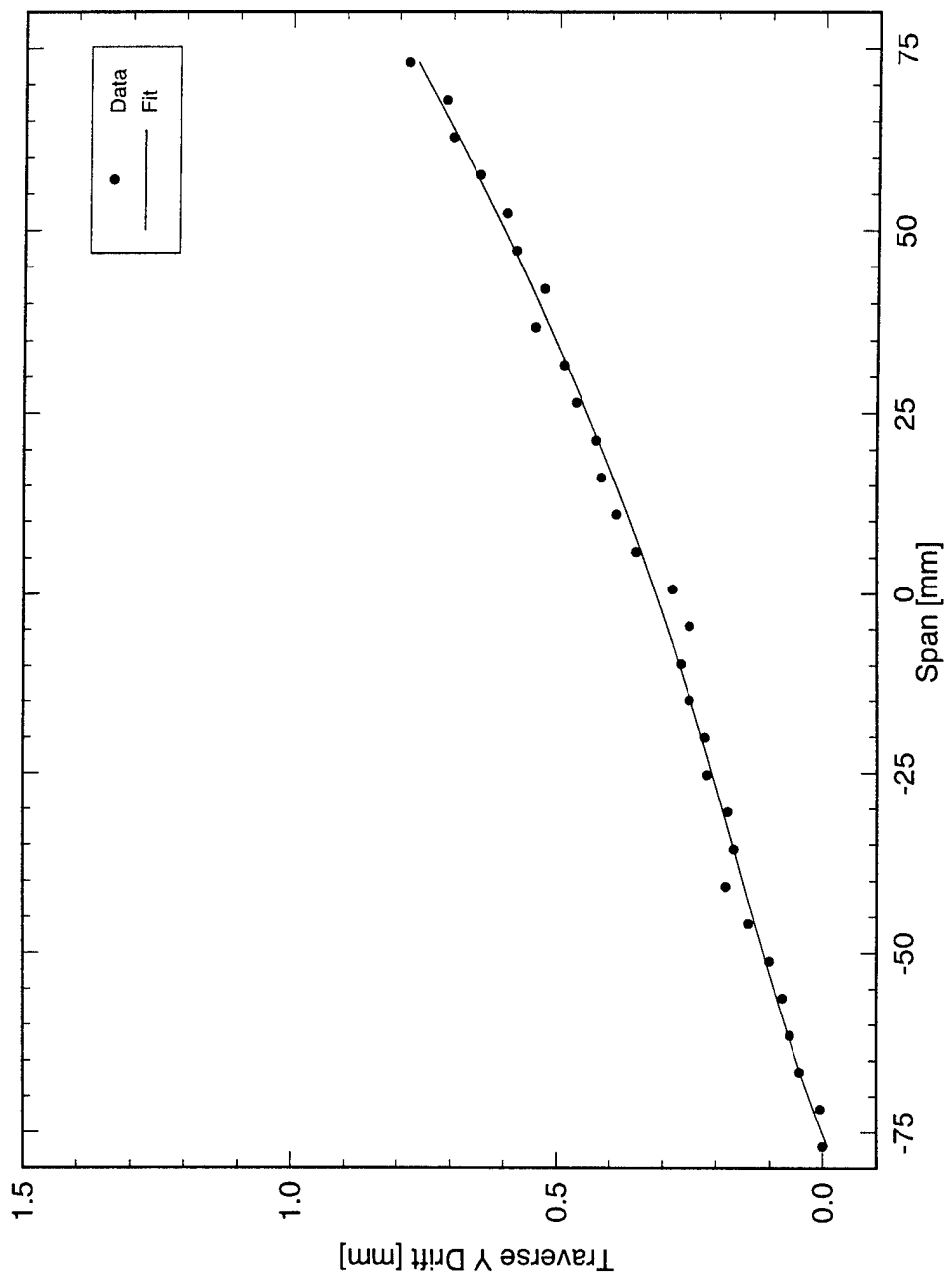


Figure 8.19: Spanwise traverse-alignment scan for $\hat{x} = 1.53$ m, $F = 85$, and $U_\infty = 8.0$ m/s case. The misalignment between the flat plate and the hot-wire traverse is shown by the “drift” in the traverse movement.

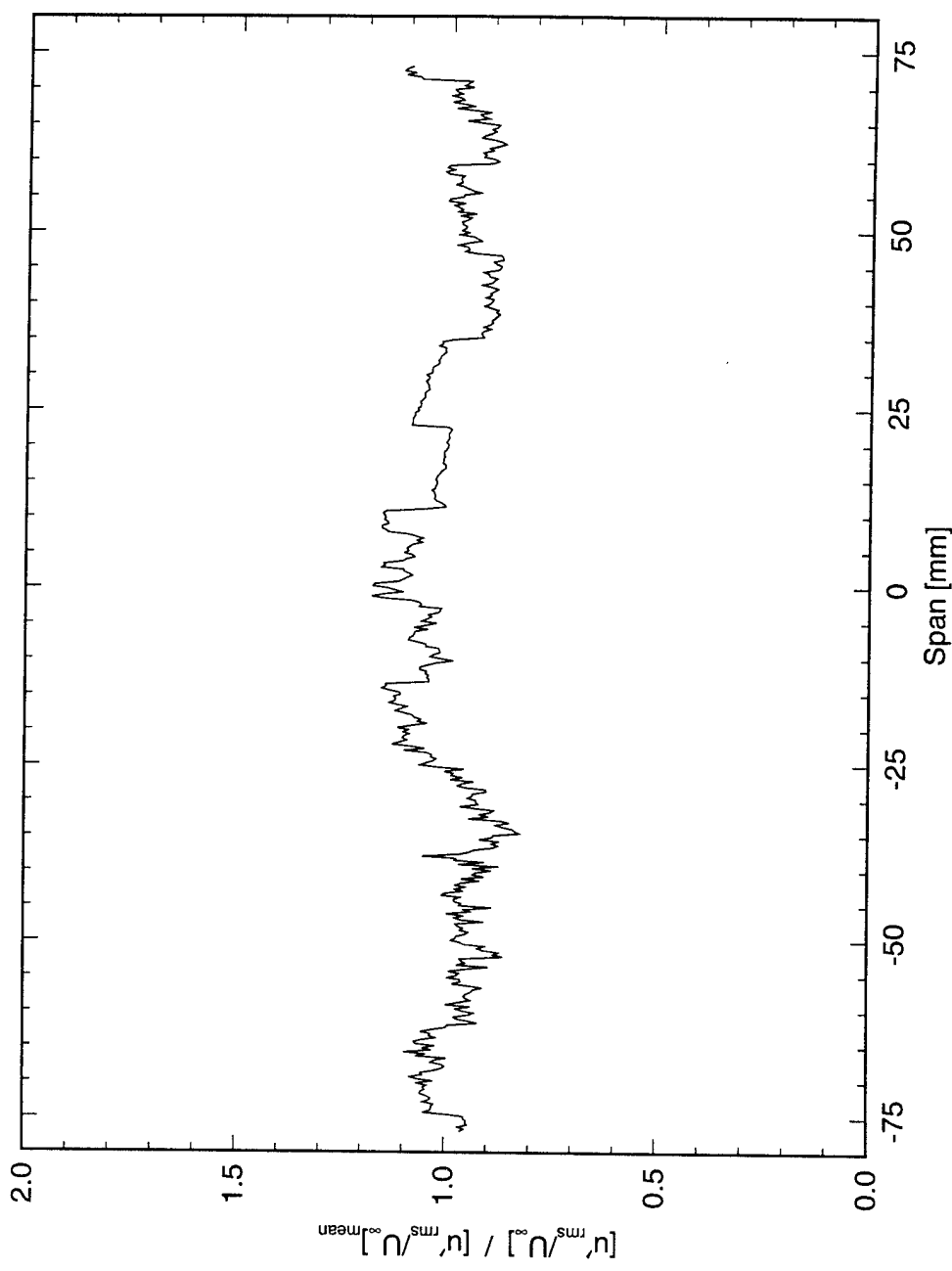


Figure 8.20: Spanwise u'_rms variation for constant-y scans taken at $\hat{x} = 1.53$ m and $\hat{y} = 1.78$ mm,
 $F = 85$, $U_\infty = 8.0$ m/s.

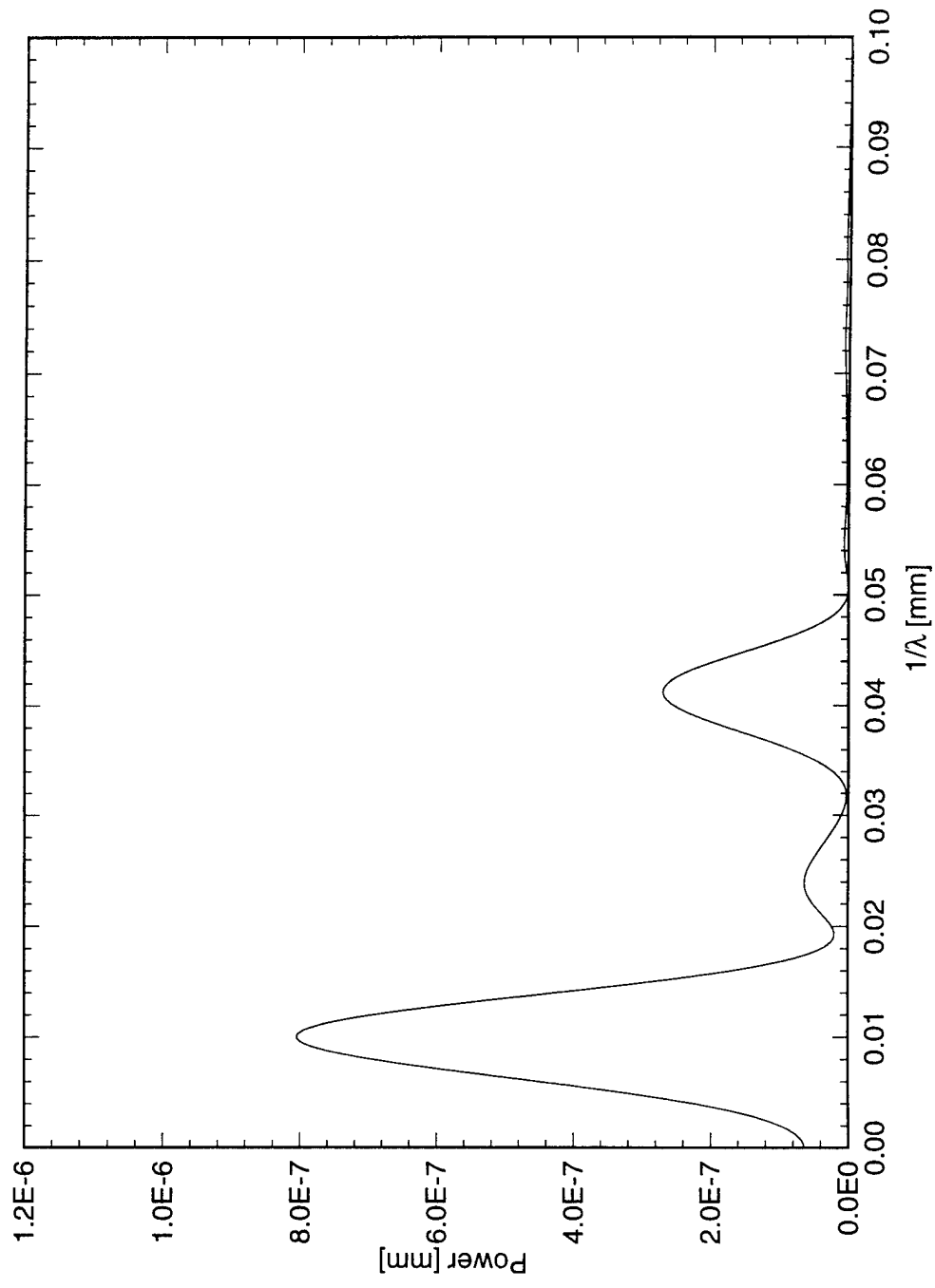


Figure 8.21: Wavenumber spectrum of u'_rms spanwise variation taken at $\hat{x} = 1.53$ m and $\hat{y} = 1.78$ mm,
 $F = 85$, $U_\infty = 8.0$ m/s.

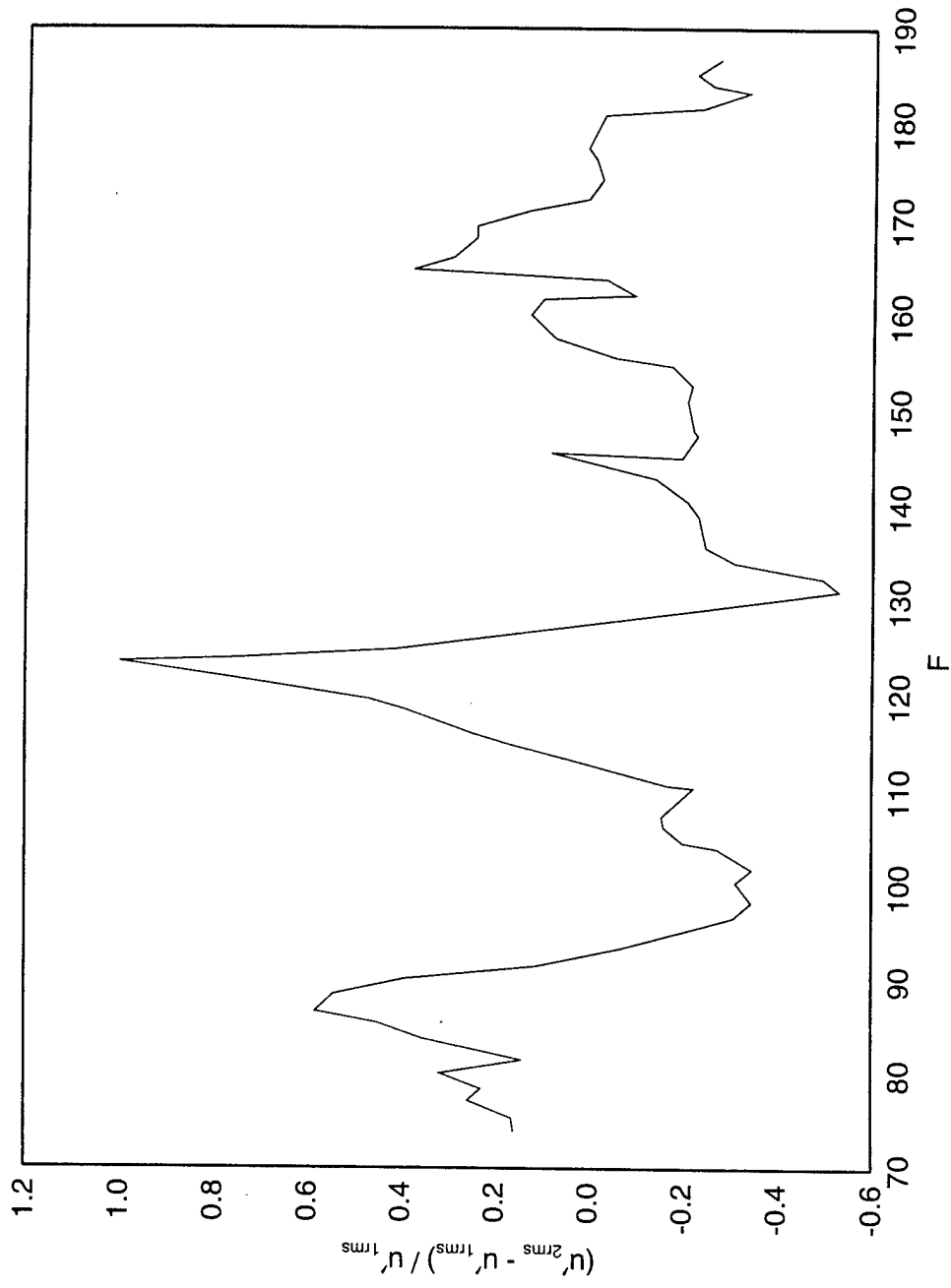


Figure 8.22: Investigation of v' at the leading edge for $U_{\infty} = 8 \text{ m/s}$ and $V_{sp} = 0.5 \text{ volts (rms)}$. Measurements taken at $\hat{x} = 1.7 \text{ m}$, $Re_x = 0.78 \times 10^6$, $T = 302.5 \text{ K}$, $a_{\infty} = 348.5 \text{ m/s}$, band pass $40\text{--}120 \text{ Hz}$.

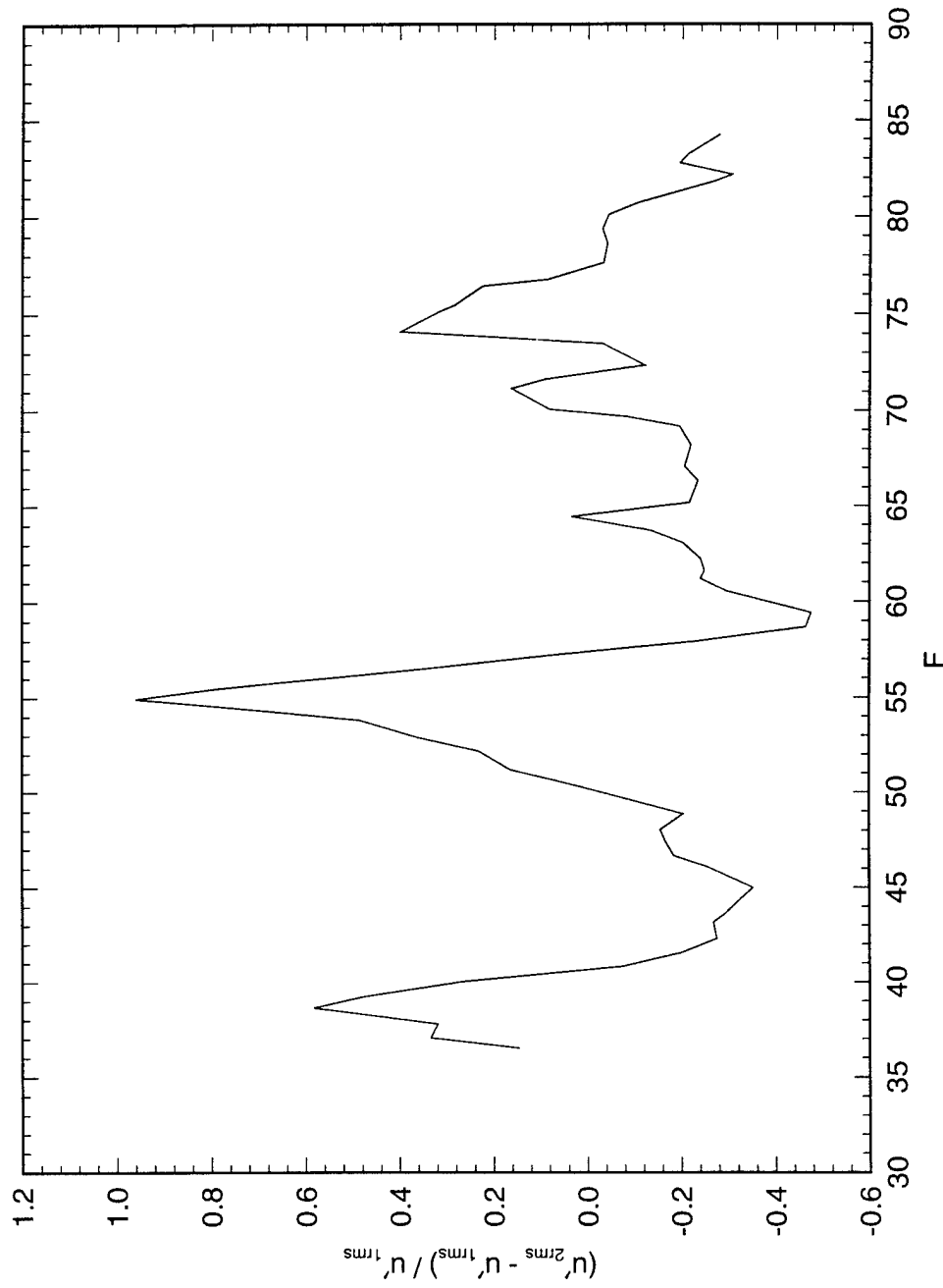


Figure 8.23: Investigation of v' at the leading edge for $U_{\infty} = 12 \text{ m/s}$ and $V_{sp} = 0.5 \text{ volts (rms)}$. Measurements taken at $\hat{x} = 1.7 \text{ m}$, $Re_x = 1.14 \times 10^6$, $T = 304.4 \text{ K}$, $a_{\infty} = 349.08 \text{ m/s}$, band pass 40~120 Hz.

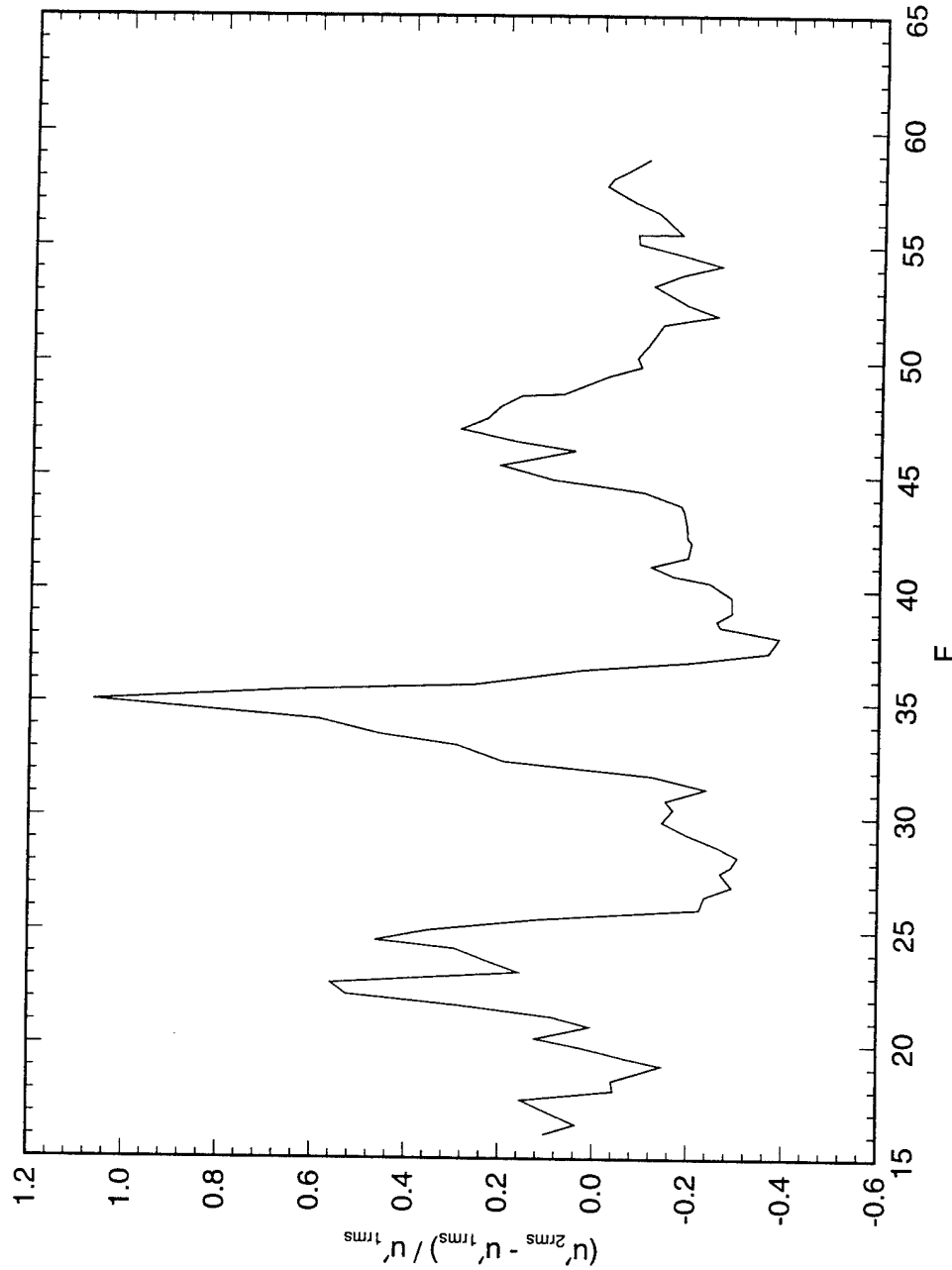


Figure 8.24: Investigation of v' at the leading edge for $U_\infty = 15$ m/s and $V_{sp} = 0.5$ volts (rms). Measurements taken at $\hat{x} = 1.7$ m, $Re_x = 1.52 \times 10^6$, $T = 303.9$ K, $a_\infty = 349.3$ m/s, band pass 30–130 Hz.

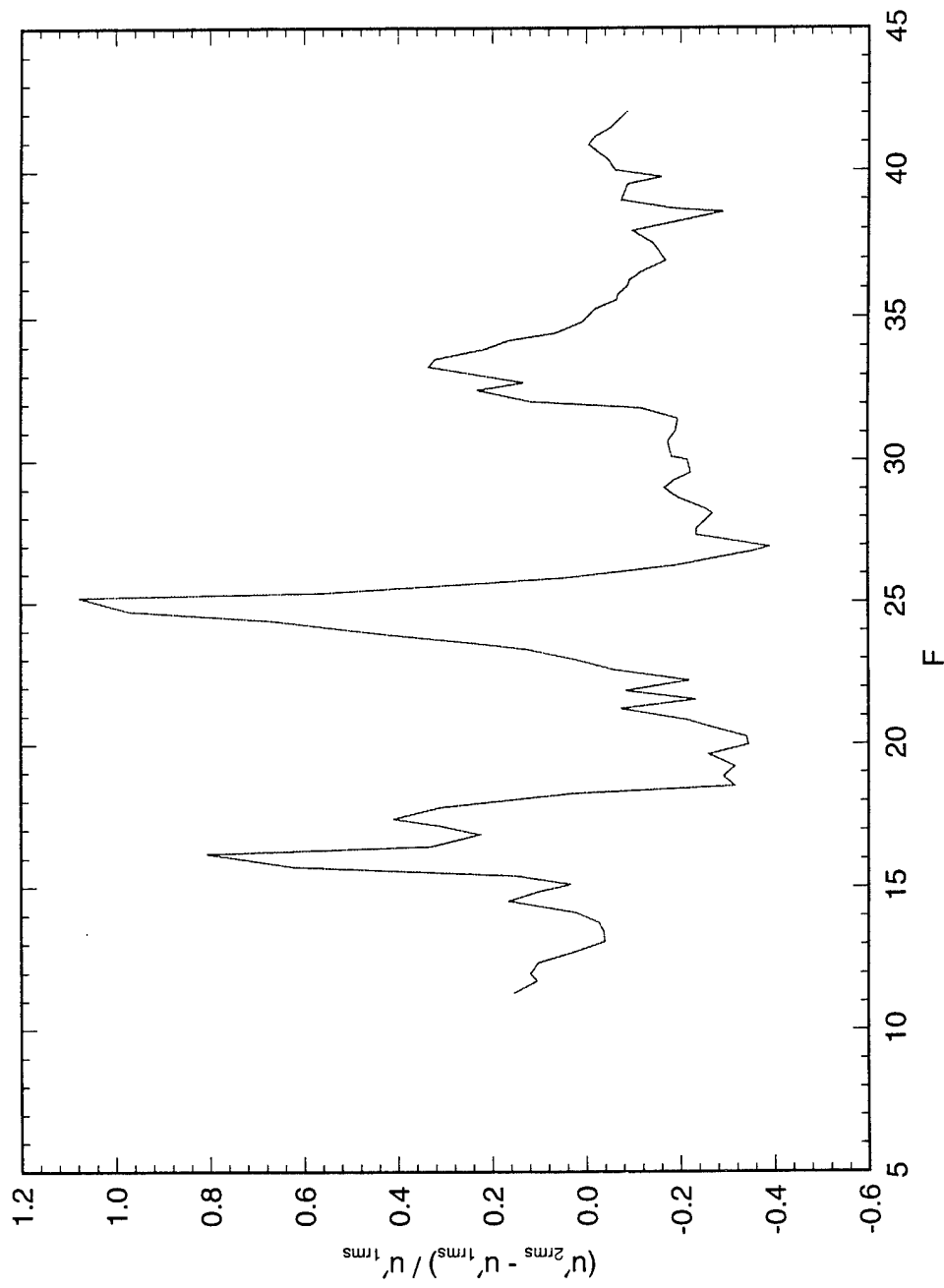


Figure 8.25: Investigation of v' at the leading edge for $U_\infty = 18 \text{ m/s}$ and $V_{sp} = 0.5 \text{ volts (rms)}$. Measurements taken at $\hat{x} = 1.7 \text{ m}$, $Re_x = 1.72 \times 10^6$, $T = 307.4 \text{ K}$, $a_\infty = 351.4 \text{ m/s}$, band pass 30–130 Hz.

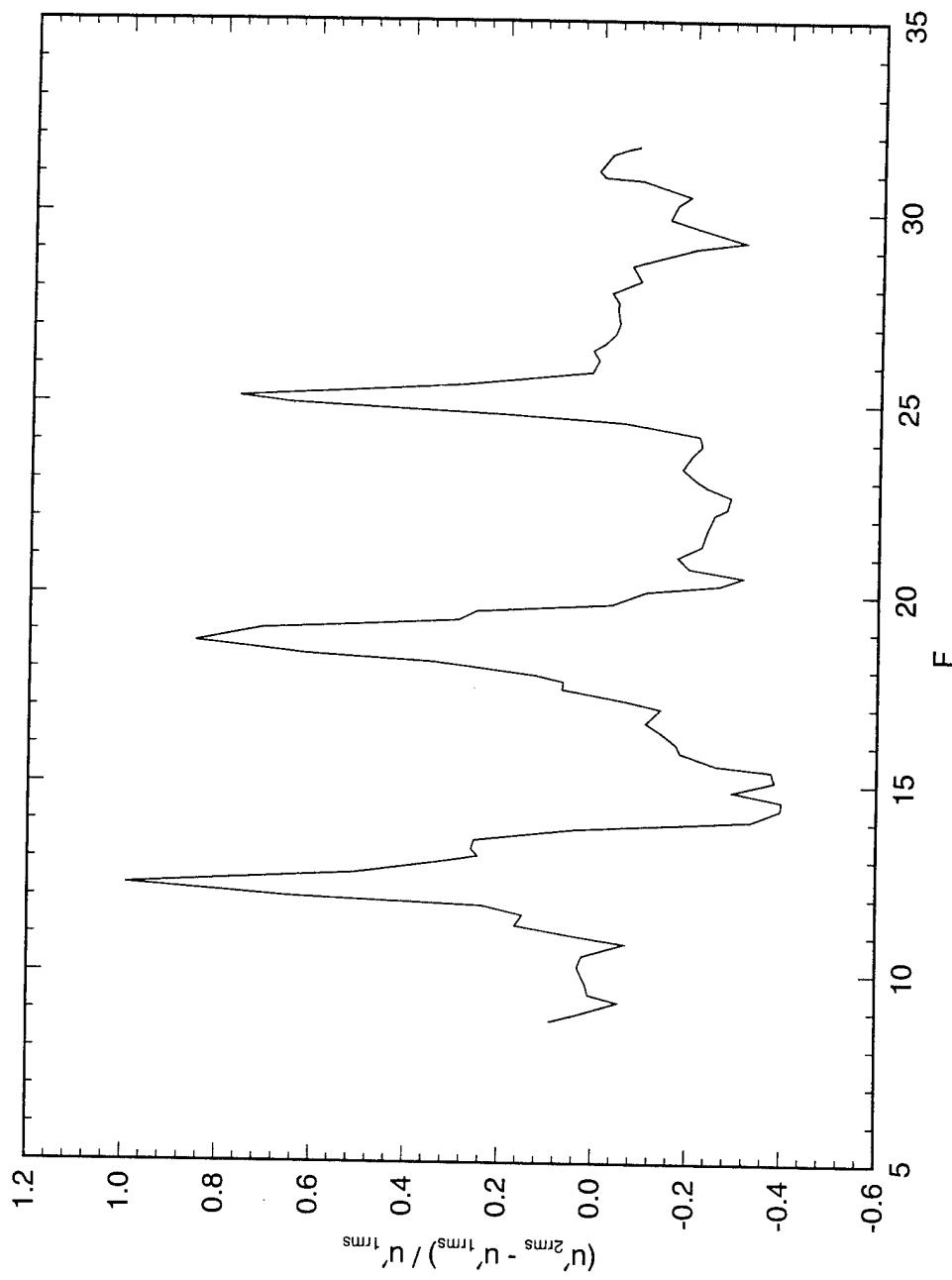


Figure 8.26: Investigation of v' at the leading edge for $U_\infty = 21 \text{ m/s}$ and $V_{sp} = 0.5 \text{ volts (rms)}$. Measurements taken at $\hat{x} = 1.7 \text{ m}$, $Re_x = 2.01 \times 10^6$, $T = 313.7 \text{ K}$, $a_\infty = 354.9 \text{ m/s}$, band pass 30-130 Hz.

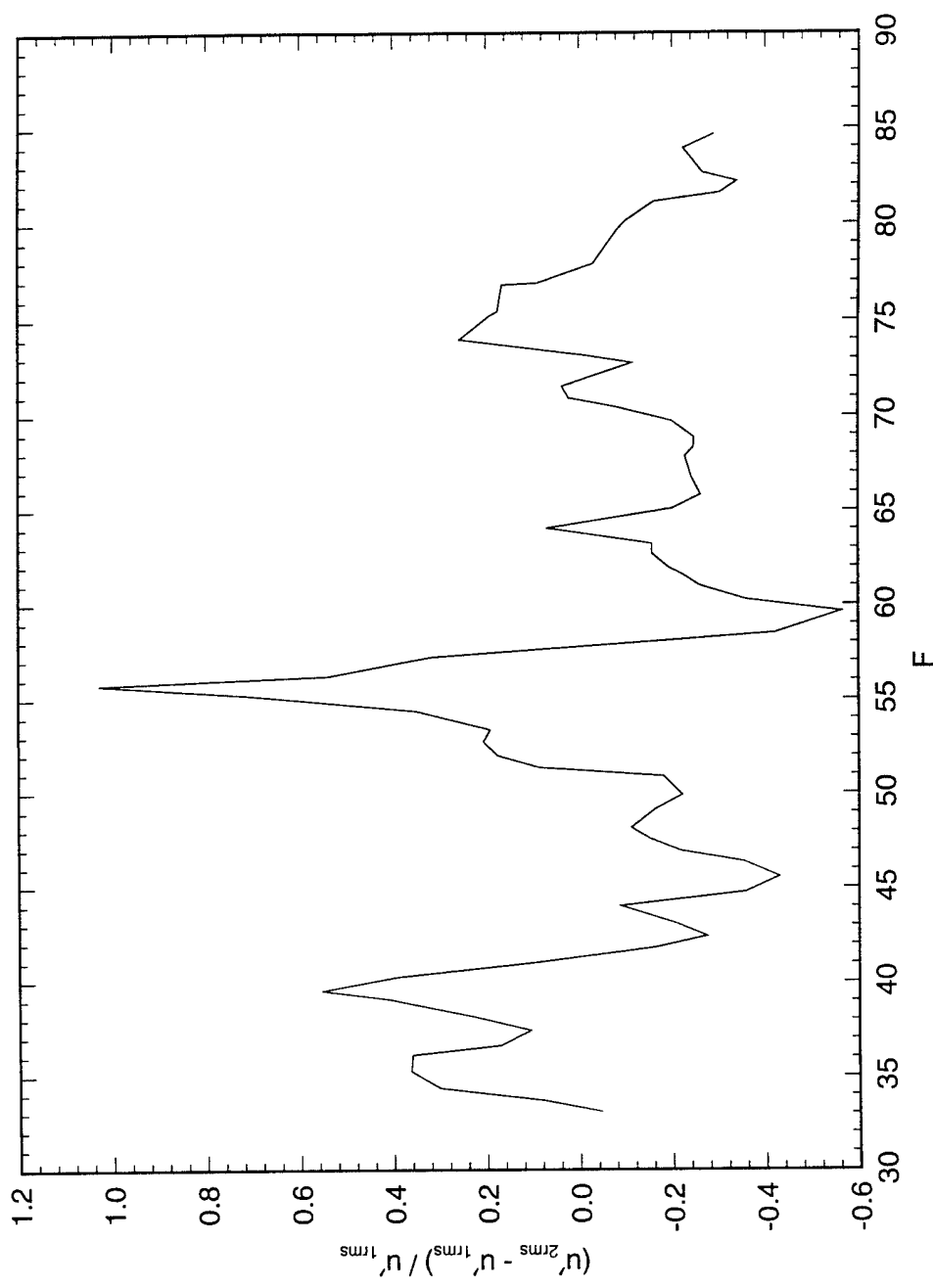


Figure 8.27: Investigation of v' at the leading edge for $U_\infty = 12 \text{ m/s}$ and $V_{sp} = 0.1 \text{ volts (rms)}$. Measurements taken at $\hat{x} = 1.7 \text{ m}$, $Re_x = 1.15 \times 10^6$, $T = 304.0 \text{ K}$, $a_\infty = 349.4 \text{ m/s}$, band pass 40-120 Hz.

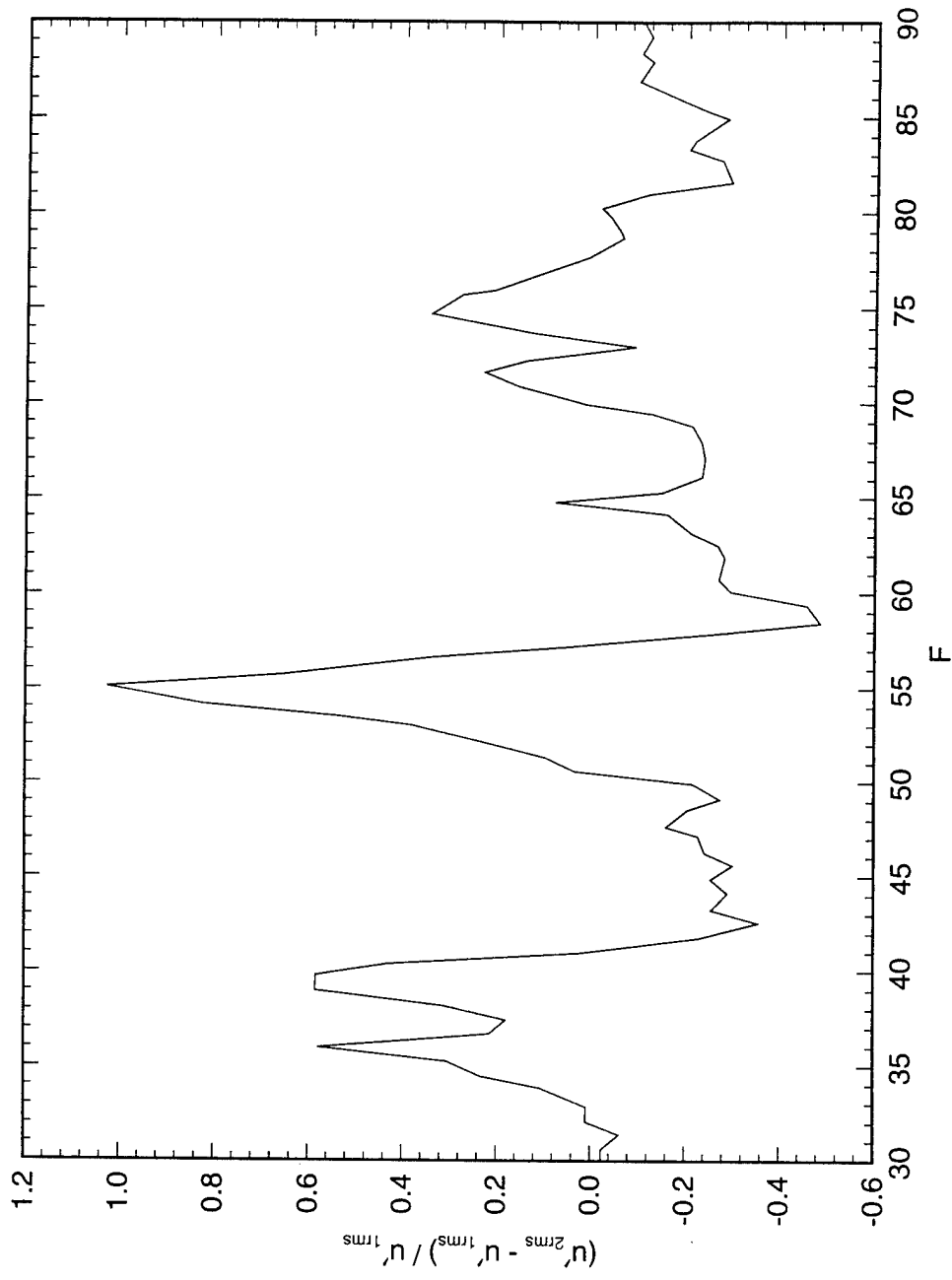


Figure 8.28: Investigation of v' at the leading edge for $U_\infty = 12 \text{ m/s}$, $V_{sp} = 0.5 \text{ volts (rms)}$, and shutters rotated 30° . Measurements taken at $\hat{x} = 1.7 \text{ m}$, $Re_x = 1.22 \times 10^6$, $T = 303.8 \text{ K}$, $a_\infty = 346.18 \text{ m/s}$, band pass 30–45 Hz.